Self-consistent Optomechanical Dynamics and Radiation Forces in Thermal Light Fields

Dissertation

zur Erlangung des akademischen Grades
Doctor of Philosphy

eingereicht an der
Fakultät für Mathematik, Informatik und Physik
der Universität Innsbruck

von

Mag. Matthias Sonnleitner

Betreuung der Dissertation:
Univ.-Prof. Dr. Helmut Ritsch,
Institut für Theoretische Physik,
Universität Innsbruck
und
O. Univ.-Prof. Dr. Monika Ritsch-Marte,
Sektion für Biomedizinische Physik,
Medizinische Universität Innsbruck

Innsbruck, 5. März 2014

für Angelina

Zusammenfassung

Die mechanische Wechselwirkung zwischen neutraler Materie und elektromagnetischer Strahlung bildet die Grundlage vieler Standardverfahren der modernen Physik mit Anwendungen in Biologie, Chemie und Medizin. Die vielseitige Natur dieser Lichtkräfte birgt jedoch weiterhin Raum für unerforschte Phänomene und neue Erkenntnisse. Die vorliegende Arbeit behandelt zwei unterschiedliche Teilaspekte dieses spannenden Themenkreises.

Der erste Teil widmet sich der komplexen Dynamik mehrerer Teilchen, welche gemeinsam mit dem selben Lichtfeld wechselwirken. Dabei bedienen wir uns eines etablierten Modells, bei dem die einzelnen Teilchen als Strahlteiler (beam splitter) angenommen werden, sodass die Wechselwirkung mit einer einfallenden ebenen Welle in einem eindimensionalen Aufbau über Transfermatrizen beschrieben werden kann. Dieses Modell hat den großen Vorteil, dass die Lichtkräfte auf die einzelnen Strahlteiler mit Hilfe des Maxwell'schen Spannungstensors exakt berechnet werden können. Dies erlaubt die selbstkonsistente Beschreibung eines Systems, bei dem einfallende Lichtstrahlen Kräfte auf Teilchen ausüben, diese dabei das Licht jeweils unterschiedlich streuen sodass sich wiederum die Kräfte auf das gesamte Ensemble verändern.

Das beschriebene Transfermatrix-Modell wurde ursprünglich für Atomwolken in optischen Gittern entworfen. In der vorliegenden Arbeit wird untersucht, wie dieses Modell zur Beschreibung der Lichtkräfte im Inneren eines ausgedehnten Dielektrikums verwendet werden kann. Dabei zeigt sich, dass es durch eine geeignete Wahl eines einzelnen Kopplungsparameters möglich ist, die optischen Eigenschaften eines homogenen Mediums exakt durch eine Abfolge unendlich vieler Strahlteiler wiederzugeben. Da die Kräfte auf die einzelnen Strahlteiler bekannt sind, lassen sich so auch die optischen Kräfte im Inneren des Mediums berechnen.

Die selbstkonsistente Natur des Transfermatrix-Modells erlaubt es schließlich, die aus den Lichtkräften im Inneren eines Mediums resultierenden Verformungen zu berücksichtigen. Wir zeigen, wie es nach dem Einschalten eines externen Laserstrahls zu Dichtemodulationen innerhalb eines ursprünglich homogenen Dielektrikums kommt, welche nicht nur zur Dehnung oder Kontraktion des Mediums führen können, sondern auch die Eigenschaften eines solchen Mediums in einer optischen Falle beeinflussen.

Die so gewonnenen Erkenntnisse haben nicht nur Auswirkungen auf akademische Grundsatzfragen zur Natur der Strahlungskräfte in polarisierbaren Materialien, sondern betreffen auch angewandte Forschung im Bereich der Biologie und der Medizin, wo die elastischen Eigenschaften biologischer Zellen und ihre Erforschung mithilfe optomechanischer Methoden von großem Interesse sind.

Auf die ursprünglichen Anwendung hinter der Transfermatrix-Methode auf Atomwolken in optischen Gittern bezieht sich ein weiterer Teilaspekt dieser Arbeit, bei dem eine neue Methode zum Fangen von Teilchen in zwei gegenläufigen Wellen orthogonaler Polarisierung beschrieben wird. Im Gegensatz zu den üblichen optischen Gittern, bei denen sich die Teilchen durch ein vorgegebenes Potential bewegen, erzeugen die Strahlteiler hier selbst ihre Falle aus mehrfach gestreutem Licht. Diese Ergebnisse sind für die weitere Erforschung und Manipulation von Atomwolken oder polarisierbaren Nanoteilchen von großem Interesse.

Im zweiten Teil der vorliegenden Arbeit werden die mechanischen Lichteffekte auf Atome in thermischen Strahlungsfeldern beleuchtet. Experimente zu Lichtkräften setzen üblicherweise auf Laserlicht, da dieses besser kontrollierbar ist und höhere Intensitäten erlaubt. Dennoch ist es erstaunlich, dass Strahlungskräfte aufgrund natürlicher, thermischer Quellen bisher so wenig Beachtung fanden, obwohl die physikalischen Grundlagen zur Wechselwirkung zwischen Materie und Licht bei inkohärenter und breitbandiger Strahlung natürlich genau so auftreten wie bei Laserlicht. Daher entwickeln wir in dieser Arbeit ein Modell zur Beschreibung der Strahlungskräfte zwischen einer heißen Kugel und einem Atom außerhalb dieser Kugel.

Die dabei auftretende Gradientenkraft ist in guter Näherung proportional zur vierten Potenz der Temperatur und kann für kleine Schwarzkörper die Gravitation um einige Größenordnungen übertreffen. Trotz des unterschiedlichen Abstandsverhaltens bleibt die Dominanz der strahlungsinduzierten Gradientenkraft auch für Ensembles kleiner Schwarzkörper erhalten.

Der abstoßende Strahlungsdruck hängt stark vom Absorptionsverhalten der beteiligten Atome ab: so ergibt sich für Wasserstoff, dass der Strahlungsdruck für Temperaturen unter einigen tausend Kelvin vernachlässigbar gering ist, während beispielsweise Lithiumatome schon von wenige hundert Kelvin heißen Schwarzkörpern abgestoßen werden.

In der vorliegenden Arbeit werden diese bisher weitgehend unbeachteten Kräfte anhand einfacher und allgemeiner Modelle untersucht. Besonderes Augenmerk wird dabei auf mögliche Auswirkungen auf astrophysikalische Szenarien gelegt, wo die Wechselwirkung zwischen aufgeheiztem Staub und Atomen, Molekülen oder Nanopartikeln eine wichtige Rolle spielt.

Abstract

The mechanical interaction between neutral matter and electromagnetic radiation is the basis of many modern standard technologies in physics and beyond. But the versatile nature of these light forces ensures that there remain many unexplored phenomena. The present thesis treats two different aspects of this fascinating topic.

The first part addresses the complex dynamics of an ensemble of particles collectively interacting with the same light field. To do so we use a well established model describing the individual particles as beam splitters such that the interaction with the incident plane waves can be described with a transfer-matrix approach, in a one dimensional setup. This model has the great advantage that the light forces on each particle can be exactly calculated using Maxwell's stress tensor. This allows for a self-consistent description of the system where incident light fields accelerate individual particles, which in turn scatter the light and thus change the fields and corresponding forces on the other scatterers.

Originally, this transfer-matrix model was developed to describe atom clouds in one-dimensional optical lattices. In the present thesis we enhance this formalism to describe the optical forces inside an extended dielectric. There we show how a special choice of a single coupling parameter enables us to exactly reproduce the optical properties of a homogeneous object in the limit of an infinite stack of beam splitters. Since the force on each individual beam splitter is known we thus obtain the correct volumetric force density inside the medium.

The self-consistent nature of the transfer-matrix formalism finally enables us to incorporate the strain and deformation induced by the light forces inside the medium. Sending a light field through an initially homogeneous dielectric then results in density modulations which in turn alter the optical properties of this medium. We can show how objects in various radiation fields contract or elongate and how this affects the trapping properties of dielectric media in laser traps.

These results have implications on fundamental research on the nature of radiation forces inside polarizable media as well as on applied technologies in Biology or Medicine, where the elastic properties of biologic cells are routinely probed using optomechanical methods.

In line with the original scope of the transfer-matrix model, i.e. atom clouds in optical lattices, we also present a short work on a novel method to trap particles in two counter-propagating waves of orthogonal polarization. In contrast to typical optical lattices, where particles are trapped in a prescribed periodic potential, the beam splitters here generate their own trap made of multiply scattered light. These results are of great interest for future research and manipulation of atomic ensembles or polarizable nanoparticles.

A second part of the present thesis is concerned with mechanical light-effects on atoms in thermal radiation fields. Typical experiments on light forces use laser light since its coherent nature allows for precise control and high local intensities. But yet it is surprising that radiation forces from natural, thermal sources have received so little attention yet, although the basic physical effects leading to the forces are the same for every source of radiation. We therefore develop a model to describe the radiation forces between a hot sphere and an atom outside that sphere.

For small blackbodies, the emerging gradient force is in good approximation proportional to the fourth power of temperature and may surpass gravity by several orders of magnitude. And despite a different distance behaviour this attractive radiation-induced gradient force prevails also for ensembles of small blackbodies.

The strength of the more familiar repulsive scattering force strongly depends on the absorption spectrum of the involved atoms: for hydrogen we find that the scattering force can be neglected for thermal fields of temperatures below several thousand Kelvin, but lithium atoms, for instance, are repelled even by blackbodies of several hundred Kelvin.

In this thesis these so far widely ignored forces are discussed at hand of generic models. A special emphasis lies on possible implications on astrophysical scenarios where the interactions between heated dust and atoms, molecules or nanoparticles are of crucial interest.

Danksagung

Mein erster Dank gebührt natürlich meinem Betreuerteam aus Univ.-Prof. Dr. Helmut Ritsch und O.Univ.-Prof. Dr. Monika Ritsch-Marte. Beide haben sich stets Zeit für Diskussionen genommen und mich mit fundiertem Wissen sowie umfangreicher Erfahrung gut und freundschaftlich beraten. Ihre Fröhlichkeit und ihr fortwährender Spaß an Forschung und Technik werden mir sicher auch in Zukunft als Motivation und Vorbild dienen.

Dass ich in der Zeit hier als Doktorand so viel Spaß hatte liegt zu einem guten Teil am großartigen Arbeitsumfeld. Gesondert danken möchte ich hier Wolfgang Niedenzu, der mich über die Kaffeerunde schon während meiner Diplomarbeitszeit als U-Boot in die Ritsch-Gruppe geschleust hat. Er war mit seit Studienbeginn nicht nur ein unfassbar umfangreiches Lexikon zu Linux, LaTeX, Matlab, Buchdruck und Physik sondern auch ein wertvoller Freund. Bei Stefan Ostermann möchte ich mich für die tolle Zusammenarbeit beim gemeinsamen Paper bedanken. Auch den weiteren aktuellen und ehemaligen Mitgliedern dieser Gruppe,[1] Erez Boukobza, Claudiu Genes, Tobias Grießer, Torsten Hinkel, Daniela Holzmann, Sebastian Krämer, Thomas Maier, Igor Mekhov, Laurin Ostermann, David Plankensteiner, Kathrin und Raimar Sandner, Valentin Torggler, Dominik Winterauer und Hashem Zoubi danke ich für das freundschaftliche und hilfsbereite Arbeitsklima, die fröhlichen Kaffeepausen, das geteilte Leid in der Mensa und die interessanten Diskussionen über Physik, die Welt et al.

Die räumliche Distanz hat leider dafür gesorgt, dass ich mit den Mitgliedern meiner zweiten Arbeitsgruppe auf der Biomedizinischen Physik, Stefan Bernet, Walter Harm, Alexander Jesacher, Marco Meinschad, Andreas Niederstätter, Lisa Obmascher, Clemens Roider, Ruth Steiger, Viktor Steixner, Gregor Thalhammer, Simon Wieser und Stefan Wieser, viel zu wenig Zeit verbracht habe. In den Seminaren und von den Antworten auf meine naiven Theoretikerfragen habe ich viel gelernt und die weinhaltigen Abende in Obergurgl bzw. bei den Weihnachtsfeiern werde ich stets in bester Erinnerung behalten.

Da auch Forschung nur mit funktionierender Infrastruktur möglich ist, möchte ich mich ganz herzlich bei Ute Thurner auf der Biomedizinischen Physik sowie Hans Embacher, Lidija Infeld, Birgit Laimer und Elke Wölflmaier auf der Theorie dafür bedanken, dass sie alle Räder am Laufen hielten.

Natürlich besteht das Leben nicht nur aus Arbeit und es ist mir eine besondere Freude, mich bei meiner großartigen Familie und Schwiegerfamilie für die umfangreiche Unterstützung und die aufmunternden Worte zu bedanken. Es ist ein schönes

---

[1] Die von hier an folgenden Aufzählungen sind in alphabetischer Reihenfolge und ich verzichte bewusst auf Titel.

Gefühl, wenn einem von so vielen tollen Menschen der Rücken gestärkt wird.

Meinen zahlreichen lieben Freunden möchte ich für die fröhlichen Abende und Wochenenden voller Scherze, Diskussionen, Spielen, Sport und Getränken danken. Vor allem durch diesen wertvollen Ausgleich zur täglichen Arbeit haben sie einen unverzichtbaren Beitrag zum Gelingen dieser Dissertation geleistet.

Ich möchte mir gar nicht vorstellen, wie und wann ich diese Arbeit abgeschlossen hätte, wenn ich nicht die wundervollste und großartigste aller Frauen an meiner Seite gehabt hätte. Meine tiefste Dankbarkeit für Angelinas aufopfernde Unterstützung und ihre perfekte Mischung aus Geduld und Motivationskraft kann leider nicht in Worte gefasst werden, soll aber durch die Widmung dieser Arbeit zum Ausdruck gebracht werden.

Es gibt noch sehr viele freundliche und hilfsbereite Menschen, welche meinen Weg in den letzten Jahren begleitet haben und die ich hier vergessen oder zu wenig gewürdigt habe. Ihnen allen sei hiermit ein kollektives aber nicht minder herzliches Dankeschön ausgesprochen.

Contents

Zusammenfassung **v**

Abstract **vii**

Danksagung **ix**

1 General Introduction **1**
- 1.1 The physics and history of radiation forces in a nutshell 1
- 1.2 A transfer-matrix approach to self-consistent optomechanical dynamics 3
- 1.3 Radiation forces induced by thermal light 4
- 1.4 Overview 5

I A Transfer-Matrix Approach to Self-consistent Optomechanical Dynamics **7**

2 Background: Multiple scattering approach to optical manipulation of elastic media **9**

3 Publication: Optical forces, trapping and strain on extended dielectric objects **13**
- 3.1 Introduction 14
- 3.2 A homogeneous medium approximated by a sequence of beam splitters 14
- 3.3 Forces on and within a dielectric medium 17
- 3.4 Central results and examples 19
- 3.5 Conclusions and Outlook 24

4 Publication: Optomechanical deformation and strain in elastic dielectrics **27**
- 4.1 Introduction 28
- 4.2 Multiple scattering model of light propagation in inhomogeneous media 29
- 4.3 Light forces in an inhomogeneous medium 34
- 4.4 Self-consistent balancing of optical force and elastic back-action 37
- 4.5 Examples and physical interpretation 39
- 4.6 Estimating the deformation by computing the photon momentum transfer on a surface 45
- 4.7 Conclusions 48
- Appendix 4.A General features of transfer matrices 49

Appendix 4.B Analytical approximations for electric fields and forces for small deformations . . . 50

5 Preprint: Scattering approach to two-colour light forces and self-ordering of polarizable particles 53

5.1 Introduction . . . 54
5.2 Multiple scattering approach to multicolour light propagation in linearly polarizable media . . . 55
5.3 Light forces in counter-propagating beams with orthogonal polarization 57
5.4 Tailored long-range interactions in a bichromatic optical lattice . . . 63
5.5 Conclusions . . . 69
Appendix 5.A Distance control for two particles . . . 71
Appendix 5.B Linearisation of the forces on two beam splitters in a bichromatic optical lattice . . . 72

II Light forces induced by sources of thermal radiation 73

6 Background: forces on atoms in thermal radiation fields 75

6.1 The dynamic Stark shift for an atom in a thermal bath . . . 75
6.2 The dynamic Stark shift for an atom close to a hot sphere . . . 80
6.3 Absorption rate and radiation pressure induced by blackbody radiation 82
6.4 Limits of our model . . . 83
Appendix 6.A Energy shift and decay rate in time-dependent perturbation theory . . . 85
Appendix 6.B Planck's law of blackbody radiation . . . 87
Appendix 6.C Poynting vectors and energy densities for incoherent electromagnetic fields . . . 89

7 Publication: Attractive optical forces from blackbody radiation 91

8 Additional calculations on optical forces from blackbody radiation 101

8.1 Estimating the scattering cross section for atom-sphere collisions . . . 101
8.2 Estimating the radiation forces between a hot and a cold dust particle 102
8.3 Averaged interactions for ensembles of small spheres . . . 104
8.4 Coupled dynamics of gas and hot dust . . . 109

Curriculum Vitae 121

Bibliography 123

1 General Introduction

The present thesis summarises my work on two different topics in the field of mechanical light effects. The first part mainly concerns the internal strain and deformation of an initially homogeneous dielectric due to local variations of radiation forces. The second part explores the forces experienced by a polarizable particle in the incoherent thermal field emitted by a small hot object.

Since the two topics are very distinct, this chapter will first provide a short overview on the general field of optical forces. More specific introductions on the two topics will follow in sections 1.2 and 1.3.

1.1 The physics and history of radiation forces in a nutshell

The first notion of radiation forces apparently came from Johannes Kepler (Kepler 1619) (as cited in (Aspelmeyer *et al.* 2013)) who noted that a comet's tail always points away from the sun. By the end of the nineteenth century, after the development of classical electrodynamics, this idea was confirmed in experiments by Nichols and Hull (Nichols *et al.* 1901) and Lebedev (Lebedev 1901). However, the measured forces remained very minute and so it was not until after the invention of the laser that Arthur Ashkin proposed and demonstrated the first optical trap of small particles and laid the foundation of the field of optical manipulation (Ashkin 1970).

For objects small compared to the used wavelength, the processes leading to radiation forces can be easily understood: first, there is a *scattering force* or *radiation pressure*[1] linked to the absorption of light. Whenever an object absorbs an incoming photon it receives a kick of momentum $\hbar\mathbf{k}$, where $\mathbf{k}$ is the wavevector of the photon. After a while the object will spontaneously reemit one or several photons, but this will happen in a random direction and will–on average–not produce a net recoil. The scattering force is thus directly proportional to the absorption rate of photons and their momentum. A beam of light will therefore push an object in the direction of light propagation, i.e. the direction of the Poynting vector.

Simultaneously, an electric field applied to a small polarizable medium perturbs the internal molecular structure and induces a dipole moment proportional to the incident field. From the simple picture of a dipole consisting of two separated charges it is apparent that a homogeneous electric field will generate a Lorentz force of equal magnitude but opposing direction on both charges, hence the net force in

---

[1] Note that the term *radiation pressure* is often used to describe the whole phenomenon of *radiation forces*. In the present work *radiation pressure* shall be used only as a synonym for the scattering force. Also note that we use the terms *optical forces*, *light forces* and *radiation forces* as synonyms, even if the frequencies involved are not in the visible range of the electromagnetic spectrum.

a homogeneous field is zero. An inhomogeneous field, however, will result in a nonzero *dipole* or *gradient force* in the direction of the intensity-gradient of the applied field. The probably most striking example of this force are optical tweezers where the gradient force of a tightly focused Gaussian beam typically traps particles at the intensity maximum, with a slight displacement due to the scattering force component (Ashkin *et al.* 1986).

For larger objects both processes happen throughout the whole medium such that the radiation field inducing forces in one volume element is influenced by the presence of the surrounding medium. Therefore, radiation forces on larger objects are generally not strictly separable into a scattering- and dipole-force component.

It is essential that the object in an optical trap is not a passive "victim" of radiation forces but actively interacts with the electromagnetic field. In fact, it is just this active interaction that creates the force. In theory, this fact is visible in the calculation of forces using the Maxwell stress tensor where the self-consistent field is required to calculate the resulting force. An exciting display of this feature is optical binding where one trapped particle changes the surrounding field to modify the trapping positions of subsequent particles (Čižmár *et al.* 2010).

Optical tweezers soon became a cross-disciplinary tool as the control and manipulation of microscopic objects is of broad interest, especially in biology. If care is taken to adjust the laser wavelength to a range of low absorption–the 1064 nm Nd:YAG-laser is common–one can trap living cells, bacteria or viruses for long times without harm. In combination with adequate visualisation techniques this allows one to study also microchemical or mechanical processes within the object. A subject of continuous research is also the improvement of the force measurement within the tweezers. The high sensitivity achieved there is successfully used to probe material properties of biological samples, Brownian motion, streaming properties in microfluidics, the forces involved in molecular motors or the elasticity of DNA-strands (Ashkin 2006).

The explanation and examples above were given for micro- to nanometre sized particles, but the most fundamental scientific progress was achieved on the atomic level. Although the principles behind the forces remain the same, an accurate quantum mechanical description of optical forces on atoms results in various effects not found in the classical regime. For instance, the level structure of atoms and molecules ensures that the absorption process involved in the scattering force is possible only if the frequency and polarization of the incoming radiation matches an atomic transition. This level structure is also responsible for the dispersive nature of the dipole force which changes sign and pulls atoms towards intensity minima, if the laser frequency is larger than the atomic transition energy.[2] Also, when the dipole force on atoms is expressed as a dynamic Stark-shift of the current atomic state, one

---

[2] For typical macroscopic transparent materials this does not happen. The fact that an object is transparent in the optical or infrared regime implies that the band gap of this material is too large for these frequencies, otherwise the photons could be absorbed. Hence, when interacting with a transparent object, laser light is always red detuned and the particle seeks maxima of intensity. However, transparent objects can be drawn towards minimal intensity if the surrounding medium has a higher refractive index.

has to keep track of the change of this state if the atom moves through the applied resonant field. And, as a last but not exhaustive example of unique quantum effects in radiation forces, also quantum fluctuations of the atom-field interactions can play a crucial role (Cohen-Tannoudji 1992; Gordon *et al.* 1980).

It was soon discovered that the described features in combination with the Doppler effect can be used to cool atoms (Dalibard *et al.* 1989; Hänsch *et al.* 1975) which paved the way to today's unmatched control of quantum systems. Using additional evaporative cooling allowed for the creation of Bose-Einstein condensates (Anderson *et al.* 1995; Davis *et al.* 1995) which have become such a standard tool of quantum optics that their production process is hardly worth a sentence in many modern experimental publications.

Another powerful tool is the optical lattice where atoms are trapped in the periodic potential generated by a standing wave field. This allows the realisation of several textbook experiments on quantum physics, simulations of condensed matter theories and the exploration of exotic quantum states of bosonic and/or fermionic gases (Bloch 2005; Jessen *et al.* 1996).

The interactive nature of radiative forces mentioned earlier is the key element of optical cavities, where the multiple interaction of atoms with the same photons results in intriguing effects including, but not limited to, self-organisation of atoms in light fields (Domokos *et al.* 2003; Ritsch *et al.* 2013).

To conclude this broad overview let us note that the techniques of atom optics and the afore mentioned classical applications of radiation forces meet in the field of optomechanics. One of the goals here is to cool nano- and micrometre-sized objects to the lowest vibrational states to gain, for instance, new fundamental insights on macroscopic quantum states as well as new highly sensitive measurement devices for gravitational or magnetic fields (Aspelmeyer *et al.* 2013).

1.2 A transfer-matrix approach to self-consistent optomechanical dynamics

Not long after the invention of optical traps it was reported that radiation forces of a focused Gaussian beam deform the surface of water (Ashkin *et al.* 1973). Already in this first publication the result was linked to the Abraham-Minkowski controversy on the momentum of light propagating inside a dielectric medium. This famous dispute is about the contradicting tensors proposed by Max Abraham and Hermann Minkowski in the early twentieth century to extend Maxwell's stress tensor to polarizable media. One of the consequences is that the photon momentum inside a medium of refractive index n reads $\hbar k/n$ in Abraham's version but $n\hbar k$ in Minkowski's description. More information on that topic, how these different momenta supposedly affect the deformation of an object and various solutions to the problem can be found in (Barnett *et al.* 2010; Pfeifer *et al.* 2007).

Aside from this disturbing fundamental question, the stress and deformation of materials due to radiation forces is also an important topic for applications. As mentioned above, optical tweezers are routinely used to test material properties of biological samples. One result there is that highly elastic human red blood cells start to stretch along the beam axis as soon as they are put in an optical trap (Guck *et al.* 2001; Singer *et al.* 2001). This effect is of great interest for medical usage as it might lead to new diagnostic tools (Lee *et al.* 2007). Some numerical studies therefore attempt to describe the deformation of biological objects, typically by calculating alleged surface forces due to the jump of the photon momentum at the interface between the sample and the surrounding water (Guck *et al.* 2001; Sraj *et al.* 2010).

In the first part of the present work we use a different approach to calculate radiation force-distributions inside dielectric media. The used scheme was introduced by Deutsch et al. to compute the propagation of plane electromagnetic waves through a one-dimensional array of scatterers such as, for instance, thin atomic clouds or micro-membranes (Asbóth *et al.* 2008; Deutsch *et al.* 1995). In this framework, each scatterer is represented by a beam splitter partly reflecting, transmitting or absorbing the incoming light. Fortunately, this process can be described using a transfer-matrix model which allows for the fast calculation of the full, self-consistent dynamics of multiple scattering.

We show that this scheme can be applied to extended dielectrics, since a dense array of beam splitters with properly chosen parameters modifies the electromagnetic field in the same way as a homogeneous dielectric of a given refractive index n. And since the force on each slice is known we are able to calculate the optical force density inside a dielectric medium. This force then generates local stress which in turn leads to the deformation of an elastic object.

At the end of this first part, the transfer-matrix formalism is used to develop a new and self-consistent trapping mechanism for polarizable particles illuminated by two counter-propagating beams of orthogonal polarization and possibly different wavelength. We also show how long-range interactions between different particles in standard optical lattices can be triggered and tuned by additional, orthogonally polarized beams.

1.3 Radiation forces induced by thermal light

Almost all the research mentioned above uses laser light to explore radiation forces on atoms or microparticles. This is because the coherent nature of laser light allows for the tight focusing needed in optical tweezers and the interference needed to generate optical lattices. Also, the narrow linewidth of lasers is useful to control a setup by addressing, for instance, only certain atomic transitions.

Kepler's observation of the radiation pressure effects in comet tails however calls our attention to the optical forces generated by natural sources of light. In astrophysics it is well known that the scattering force is of great importance for the dynamics of gaseous clouds or the stability of stars (Carroll *et al.* 1996). In atomic physics thermal light fields usually play a role as an undesired source of blackbody Stark-shifts, although some recent experiments try to probe atom-surface interactions due to thermal near-fields (Obrecht *et al.* 2007).

And although the sometimes surprisingly versatile thermal emission from small particles has been studied in various contexts (Reiser *et al.* 2013) the framework of attractive gradient forces due to a finite source of thermal radiation has–at least to our knowledge–not been studied yet. In the second part of this thesis we therefore draft a simplified but generic description of the radiative interaction between polarizable particles and spherical blackbodies.

1.4 Overview

This work is organised as follows: The first part is mainly devoted to the application of a transfer-matrix model (Deutsch *et al.* 1995) to the trapping and deformation of a one-dimensional object due to radiation forces. After a short heuristic introduction in chapter 2, we show in a publication (Sonnleitner *et al.* 2011) reprinted in chapter 3 why an array of beam splitters is equivalent to a homogeneous dielectric.

In a second work presented in chapter 4 we extend the formalism to compute the forces in inhomogeneous media (Sonnleitner *et al.* 2012). This allows us to compute the interplay between optical forces and elastic back-action self-consistently. In various examples for different setups, including objects in standing waves, two orthogonally polarized beams and single beams, we show that the deformation of an initially homogeneous medium depends strongly on the initial conditions, such that both elongation and contraction is possible. Furthermore, our results are in stark contrast to the results expected from a simplified notion of a surface force resulting from a sudden jump in photon momentum.

In the preprint (Ostermann *et al.* 2013) presented in chapter 5 we use the beam splitter formalism in its original scope of individual polarizable particles reshaping their optical trapping fields. We present a setup where particles are exposed to two non-interfering beams of orthogonal polarization and different frequency. Multiple scattering between the beam splitters then results in a dynamic reorganisation process where the particles finally trap themselves. We also show how a perturbative beam can be used to mediate interactions between particles trapped in a standard optical lattice.

The second part of this thesis presents our approach to describe the light forces on an atom, molecule or Rayleigh scatterer in the incoherent thermal radiation field of a spherical blackbody. In the introductory chapter 6 we present the basic calculations on how a thermal light field affects an atom and what type of forces arise if this thermal field has a finite source. These results are then extended in the publication (Sonnleitner *et al.* 2013) reprinted in chapter 7 where we show that the attractive gradient force outmatches both the repulsive radiation pressure and gravity for a wide range of parameters.

Chapter 8 contains several additional calculations on this topic, such as an estimation for the forces arising if the atom in the thermal field is replaced by a nanoparticle described as a Rayleigh scatterer. We there also present an extensive calculation of the self-consistent dynamics between small radiating blackbodies and an ensemble of atoms or nanoparticles interacting both gravitationally and via attractive light forces due to thermal radiation.

The thesis concludes with a curriculum vitae and a bibliography. The author's contributions to the publications reprinted in this thesis are indicated by a short note at the beginning of each article.

Part I

A Transfer-Matrix Approach to Self-consistent Optomechanical Dynamics

2 Background: Multiple scattering approach to optical manipulation of elastic media

Imagine a plane electromagnetic wave travelling along the x-axis into a cloud of polarizable particles. A fraction of that wave will be reflected, a fraction will be absorbed and a third fraction will be transmitted and continues its way. If the wave is travelling through an array of such clouds, these scattering events will occur several times and the electromagnetic field will be reshaped by the presence of the polarizable particles acting as beam splitters.

To describe this process we employ the macroscopic Maxwell equations in a region without charges and derive

$$\nabla \times \nabla \times \mathbf{E} + \mu_0 \partial_t^2 \mathbf{D} = 0 \tag{2.1}$$

with the vacuum permeability μ_0 and the electric displacement $\mathbf{D}$ related to the electric field $\mathbf{E}$ and the polarizability $\mathbf{P}$ via $\mathbf{D} = \varepsilon_0 \mathbf{E} + \mathbf{P}$. Assuming time harmonic fields travelling along the x-direction we set $\mathbf{E}(\mathbf{x}, t) = \mathrm{Re}[E(x)\exp(-i\omega t)\mathbf{e}_z]$.

As mentioned above and illustrated in figure 2.1, this wave shall propagate through N identical clouds of particles with polarizabilities α such that $\mathbf{P}(\mathbf{x}, t) = \eta(x)\alpha\mathbf{E}(\mathbf{x}, t)$. Within each cloud the particles shall be distributed according to a Gaussian distribution such that the total particle density reads

$$\eta(x) = \eta_0 \sum_{i=1}^{N} \frac{1}{\sqrt{2\pi\sigma^2}} e^{-\frac{(x-x_i)^2}{2\sigma^2}}. \tag{2.2}$$

The total number of particles is then given as $\iiint \eta(x)\mathrm{d}x\mathrm{d}y\mathrm{d}z = N\eta_0 A$, with A denoting the area occupied by the clouds in y and z-direction. Equation (2.1) can then be reduced to a scalar equation reading

$$(\partial_x^2 + k^2)E(x) = -k^2 E(x) \frac{\eta_0 \alpha}{\varepsilon_0} \sum_{i=1}^{N} \frac{1}{\sqrt{2\pi\sigma^2}} e^{-\frac{(x-x_i)^2}{2\sigma^2}}. \tag{2.3}$$

If the clouds are well localised we may use $\lim_{\sigma\to 0}(2\pi\sigma^2)^{-1/2}\exp(x^2/(2\sigma^2)) = \delta(x)$ to replace the Gaussian distributions with Dirac delta functions. In figure 2.2 we show an example where this is valid for $k\sigma < 1/20$. Equation (2.3) then reduces to (Deutsch *et al.* 1995)

$$(\partial_x^2 + k^2)E(x) = -2k\zeta E(x) \sum_{i=1} \delta(x - x_i), \tag{2.4}$$

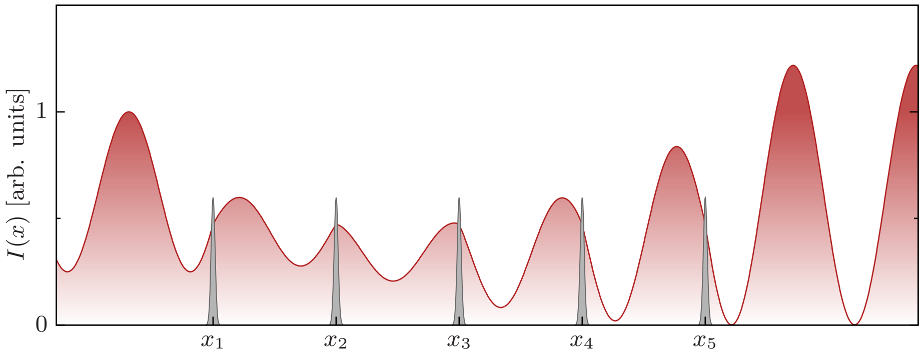

Figure 2.1 Schematic intensity profile of a plane wave interacting with Gaussian clouds of polarizable particles (grey shades) localised at $x_1, \dots, x_5$.

where we defined a coupling parameter $\zeta := k\alpha\eta_0/(2\varepsilon_0)$. This description has the clear advantage that the solutions in the regions $x_i < x < x_{i+1}$ are simple plane waves. The role of the beam splitters at x_i is to impose the boundary conditions $\lim_{x\uparrow x_i} E(x) = \lim_{x\downarrow x_i} E(x)$ and $\lim_{x\uparrow x_i} E'(x) = \lim_{x\downarrow x_i} E'(x) + 2k\zeta \lim_{x\downarrow x_i} E(x)$ for $i = 1, \dots, N$. These boundary conditions can be reshaped into matrix equations which are the foundation of the multiple scattering transfer matrix model (Asbóth *et al.* 2008; Deutsch *et al.* 1995; Ostermann *et al.* 2013; Sonnleitner *et al.* 2011, 2012; Xuereb *et al.* 2009). More details are given in the publications presented in the upcoming chapters 3 and 4, in this chapter we focus on a phenomenological introduction.

In an experiment, the parameter ζ can be calculated after measuring the reflectivity $R := I_{\text{reflected}}/I_{\text{incoming}}$ and the transmittivity $T := I_{\text{transmitted}}/I_{\text{incoming}}$ of a beam splitter as

$$\operatorname{Re}\zeta = \pm\frac{\sqrt{(1+R+T)^2 - 2(R^2+T^2+1)}}{2T}, \qquad \operatorname{Im}\zeta = \frac{1-R-T}{2T}. \tag{2.5}$$

We see that $\operatorname{Im}\zeta$ is proportional to the amount of light being neither reflected nor transmitted. Thus $\operatorname{Im}\zeta$ describes how much power is absorbed by the beam splitter or scattered in other directions.

The transfer-matrix approach allows a fast computation of the optical fields throughout the whole system and using the Maxwell stress tensor this can be used to calculate the light forces acting on each beam splitter.

By design this formalism can be used to calculate the self-consistent dynamics of atom clouds in one-dimensional optical lattices (Asbóth *et al.* 2008). Other systems where this model can be applied include micro-membranes in optical cavities (Jayich *et al.* 2008; Thompson *et al.* 2008; Xuereb *et al.* 2012, 2013), submicron particles in effective 1D geometries (Grass 2013) or atoms interacting with the light travelling through a nearby nanofibre (Chang *et al.* 2013; Schneeweiss *et al.* 2013). All these examples are natural applications of the initial idea of a field propagating through

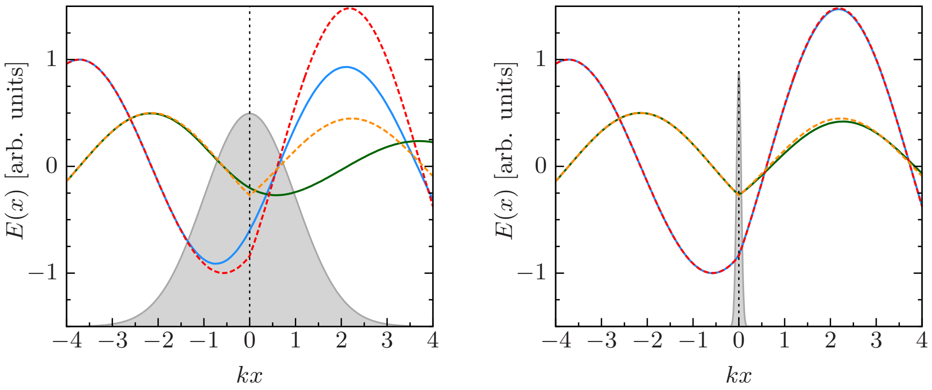

Figure 2.2 Electric fields interacting with different clouds of polarizable particles: The blue and green solid curves represent the real and imaginary parts of solutions to equation (2.3) for a single wide ($k\sigma = 1$, left figure) or thin ($k\sigma = 0.05$, right figure) Gaussian particle distribution resembled by the grey shapes. For comparison the red and orange dashed lines show the real and imaginary parts of an electric field computed using the transfer-matrix method (Deutsch *et al.* 1995). This is obviously a valid approximation for the situation depicted on the right where $k\sigma \ll 1$. Parameters are chosen such that $k\alpha\eta_0/(2\varepsilon_0) = \zeta = 0.5 + 0.3i$; the boundary conditions are fixed as $E(x_0) = 1$ and $E'(x_0) = i/2$ (arbitrary units) with $kx_0 = -10$.

an array of individual scatterers.

To describe light interacting with an extended region of homogeneous density we would set the particle density $\eta(x)$ as a rectangular function ranging, for instance, from $x = 0$ to $x = L$. But it is easy to see that such a rectangular function can again be well approximated by a sum of Gaussian distributions as described in equation (2.2) with a width $\sigma = L/N$ and a uniform spacing $d = x_{i+1} - x_i = L/(N-1)$, provided $L/N \ll 1$.

As illustrated in figure 2.3 a numerical solution of equation (2.3) reproduces the electric field inside a homogeneous medium of refractive index n as long as η_0 is chosen such that ζ fulfils

$$\zeta = \frac{\cos(kd) - \cos(nkd)}{\sin(kd)}. \tag{2.6}$$

This relation is one of the key results of the next chapter 3 and allows us to describe a homogeneous medium by an array of (infinitesimally spaced) beam splitters. We can therefore use the transfer-matrix method to compute the fields and—more importantly—the forces inside an extended dielectric medium.

The volumetric optical forces acting inside an object induce deformations which in turn change the local refractive index. This process can be well understood in the transfer-matrix formalism where the local forces displace the initially equally spaced beam splitters. In chapter 4 we show how this displacement of the beam splitters is linked to the local strain and the resulting inhomogeneous refractive index $n(x)$. As a result we calculate the self-consistent dynamics of a dielectric object where elastic

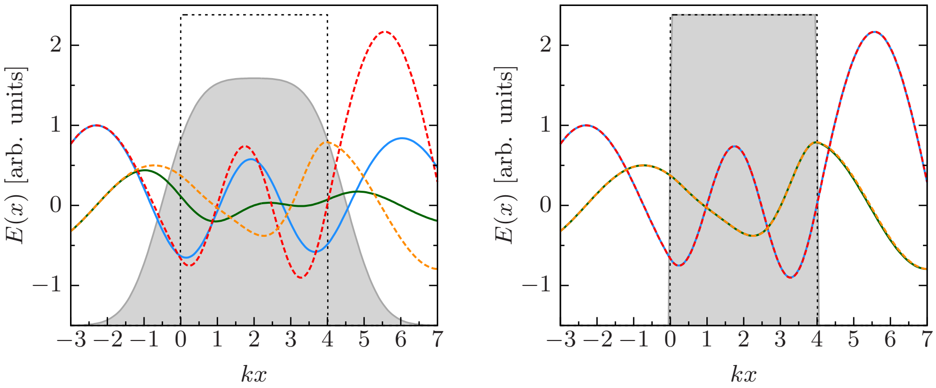

Figure 2.3 Electric field travelling through approximately rectangular particle densities produced by a sum of $N = 5$ (left figure) and $N = 500$ (right figure) Gaussian distributions of width $\sigma = L/N$ and spacing $x_{i+1} - x_i = L/(N-1)$ for $kL = 4$. Blue and green solid lines show the real and imaginary parts of solutions to the corresponding equation (2.3). For comparison, the red and orange dashed lines show the real and imaginary parts of a field travelling through a medium of refractive index $n = 2 + 0.3i$ located in the region $[0, L]$. Since the parameters are chosen such that $\zeta = k\alpha\eta_0/(2\varepsilon_0)$ satisfies equation (2.6) the solutions agree for $N \gg 1$, as can be seen in the right figure. The boundary conditions are fixed as $E(x_0) = 1$ and $E'(x_0) = i/2$ (arbitrary units) with $x_0 = -10L$.

back-action tries to compensate for optomechanical deformations.

Finally, in the preprint article presented in chapter 5 we apply the transfer-matrix method to describe an array of individual nano-particles or atoms. But in contrast to typical standing wave traps we there propose an orthogonal beam trap where particles interact with two counter-propagating waves of orthogonal polarization and possibly different frequency. We show that the light fields then induce an effective interaction between the beam splitters causing them to trap and/or organise themselves in this initially translationally invariant setup. We also explain how a perturbative beam polarized orthogonally to a typical one-dimensional optical lattice can be used to trigger correlated motions between different particles trapped in that lattice.

3 Publication

Optical forces, trapping and strain on extended dielectric objects

M. Sonnleitner*, M. Ritsch-Marte and H. Ritsch

We show that the optical properties of an extended dielectric object are reliably reproduced by a large number of thin slices forming a linear array of beam splitters. In the infinite slice number limit this self-consistent approach allows to calculate light forces within a medium directly from the Maxwell stress tensor for any dielectric with prescribed refractive index distribution. For the generic example of a thick slab in counter-propagating fields the effective force and internal strain distribution strongly depend on the object's thickness and the injected field amplitudes. The corresponding trapping dynamics may even change from high-field-seeking to low-field-seeking behaviour while internal forces lead to pressure gradients and thus imply stretching or compression of an elastic object. Our results bear important consequences for a wide scope of applications, ranging from cavity optomechanics with membranes, size selective optical trapping and stretching of biological objects, light induced pressure gradients in gases, to implementing light control in microfluidic devices.

EPL (Europhys. Lett.) **94**, 34005 (2011) doi: 10.1209/0295-5075/94/34005

---

[*] The author of the present thesis performed all of the calculations in this publication.

3.1 Introduction

Light forces on particles can be understood from the basic principle of redistribution or absorption of the optical momentum. This principle led to the development of physical models appropriate not only for point particles, such as atoms (Cohen-Tannoudji 1992), but also for extended solid objects, such as thin membranes or microbeads (Ashkin 1970). In a recent approach based on a simple model of a series of optical beam splitters (Asbóth *et al.* 2008) it was shown that these two cases can be treated uniformly. Using moving beam splitters (Xuereb *et al.* 2009) one can rederive the dynamics of atoms trapped in optical lattices and well known basic phenomena, such as Doppler cooling of free particles and cavity cooling of nanoscopic mirrors or membranes of negligible thickness.

In this work we generalise this approach to calculate light forces on and within extended dielectric objects, which we treat as the limiting case of a growing number N of more closely spaced layers. Multiple scattering between these layers ensures that the overall refractive index reaches a prescribed continuum value in the limit of $N \to \infty$, which can be performed analytically. By calculating the force on each slice using the Maxwell stress tensor formalism and taking the continuum limit we directly obtain the local forces in the medium as well as the field in a self-consistent form.

Our model can be compared with a previously given approach for polarizable point particles (Cohen-Tannoudji 1992). If the point particles are generalised to be embedded in a dielectric medium and if their modifications of the fields are treated in a self-consistent way, the resulting expressions for the local forces are the same. We will also compare our results with basic but nonetheless controversial arguments using the change of effective photon momentum to estimate light forces on dielectric surfaces.

While freely movable objects will arrange in a force free configuration (Asbóth *et al.* 2008; Singer *et al.* 2003), the averaged force of the field within a rigid or elastic object will lead to differential forces invoking local compression or stretch. This can lead to essential shape modifications as prominently observed for biological objects, such as biological cells (Guck *et al.* 2001), or coupling to vibrational (acoustic) modes of membranes or microspheres (Eichenfield *et al.* 2009; Kippenberg *et al.* 2008; Thompson *et al.* 2008). Our model will allow a microscopic study of this effect for various configurations and density distributions of the particles and can be generalised to dynamic media as fluids or gases.

3.2 A homogeneous medium approximated by a sequence of beam splitters

Let us consider two monochromatic plane-waves propagating in opposite directions at normal incidence through a one dimensional array of thin polarizable layers as sketched in fig. 3.1. This represents an idealised model of a stack of thin slices of

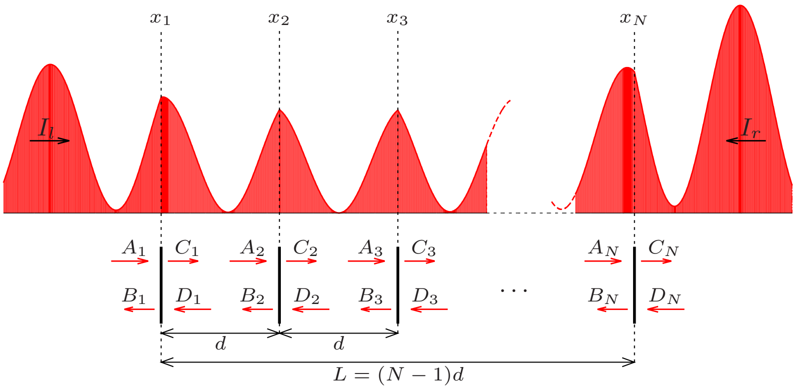

Figure 3.1 N equidistant slices with coupling parameter ζ in a standing-wave field with incoming intensity amplitudes I_l and I_r. Note that the electric field is continuous, but its derivative jumps at each beam splitter position x_j (cf. the boundary conditions of eq. (3.1)). To establish notation, the amplitudes of the plane-wave solutions are displayed below.

dielectric materials (Bhattacharya *et al.* 2008) or trapped clouds of cold atoms in a 1D optical lattice (Deutsch *et al.* 1995). Each layer is characterised by its position x_j ($j = 1, \ldots, N$) and the dimensionless coupling parameter $\zeta = k\eta\alpha/(2\varepsilon_0)$ proportional to the atomic polarizability α and the areal particle density η within the slice. ε_0 is the vacuum permittivity and $k = \omega/c$ the wave number of the optical field. The spatial behaviour of the field $E(x)\exp(-i\omega t)$ is determined by the corresponding 1D Helmholtz-equation (Asbóth *et al.* 2008; Deutsch *et al.* 1995)

$$\left(\partial_x^2 + k^2\right) E(x) = -2k\zeta\, E(x) \sum_{j=1}^{N} \delta(x - x_j) \tag{3.1}$$

with boundary conditions

$$\lim_{x\uparrow x_j} E(x) = \lim_{x\downarrow x_j} E(x) \quad \text{and} \quad \lim_{x\uparrow x_j} E'(x) = \lim_{x\downarrow x_j} E'(x) + 2k\zeta \lim_{x\downarrow x_j} E(x)$$

at each of the N beam splitters.

Between the slices the field propagates freely, i.e. $E_{L,j}(x) := A_j \exp(ik(x - x_j)) + B_j \exp(-ik(x - x_j))$ for $x_{j-1} < x < x_j$ and $E_{R,j}(x) := C_j \exp(ik(x - x_j)) + D_j \exp(-ik(x - x_j))$ for $x_j < x < x_{j+1}$.

Obviously, $E_{R,j}(x) \equiv E_{L,j+1}(x)$ and thus we have $A_{j+1} = C_j \exp(ik(x_{j+1} - x_j))$ and $B_{j+1} = D_j \exp(-ik(x_{j+1} - x_j))$, for $j = 2, \ldots, N-1$. As one can conclude from fig. 3.1 the field amplitudes B_j $\{C_j\}$ are a sum of the reflected $\{$transmitted$\}$ fraction of A_j and the transmitted $\{$reflected$\}$ fraction of D_j. Therefore each slice can be considered as a beam splitter with reflection and transmission amplitudes $r = i\zeta/(1 - i\zeta)$ and $t = 1/(1 - i\zeta)$. The coupling of the field amplitudes can then be

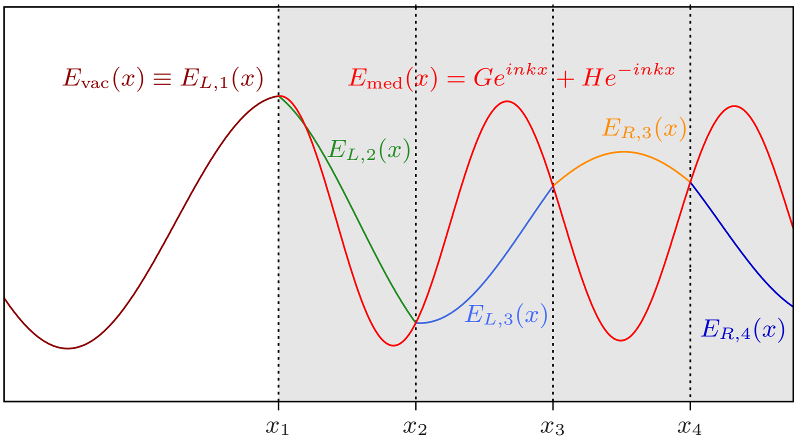

Figure 3.2 Schematic setup: Choosing the coupling parameter ζ as in eq. (3.4) ensures that the electric field at every beam splitter position $x_1, \ldots, x_N$ is the same as the field inside a medium with refractive index n.

rewritten in the transfer-matrix form (Deutsch *et al.* 1995)

$$\begin{pmatrix} C_j \\ D_j \end{pmatrix} = \begin{pmatrix} 1+i\zeta & i\zeta \\ -i\zeta & 1-i\zeta \end{pmatrix} \begin{pmatrix} A_j \\ B_j \end{pmatrix} =: \mathrm{M}_{\mathrm{BS}} \begin{pmatrix} A_j \\ B_j \end{pmatrix}. \tag{3.2}$$

For a distance d between the beam splitters we get with
$\mathrm{P}_d := \operatorname{diag}\left(\exp(ikd), \exp(-ikd)\right)$:

$$\begin{pmatrix} C_j \\ D_j \end{pmatrix} = \mathrm{M}_{\mathrm{BS}}(\mathrm{P}_d \mathrm{M}_{\mathrm{BS}})^{j-1} \begin{pmatrix} A_1 \\ B_1 \end{pmatrix}. \tag{3.3}$$

In the region within an array of N beam splitters, multiple scattering reshapes the resulting field as a function of ζ. Since we are interested in modelling homogeneous dielectric media, we determine the value for ζ such that the field at each beam splitter x_j ($j = 1, \ldots, N$) reproduces the field at this position inside a dielectric with refractive index n, i.e. $E_{\text{med}}(x) = G\exp(ikn(x - x_j)) + H\exp(-ikn(x - x_j))$, as schematically depicted in fig. 3.2. This condition can be met exactly for any finite distance d between the individual slices, if

$$\zeta = \frac{\cos(kd) - \cos(nkd)}{\sin(kd)}. \tag{3.4}$$

Note that the refractive index n can be chosen complex to account for absorption inside the medium (Jackson 1999) and a nonuniform distance d or coupling parameter ζ could model a spatially varying index.

Inserting ζ from eq. (3.4), the eigenvalues of the transfer matrix $\mathrm{M} := \mathrm{P}_d \mathrm{M}_{\mathrm{BS}}$ read $\exp(\pm inkd)$. As shown in refs. (Asbóth *et al.* 2008; Deutsch *et al.* 1995) this allows to directly calculate the amplitudes of the fields generated by a cascade of N beam

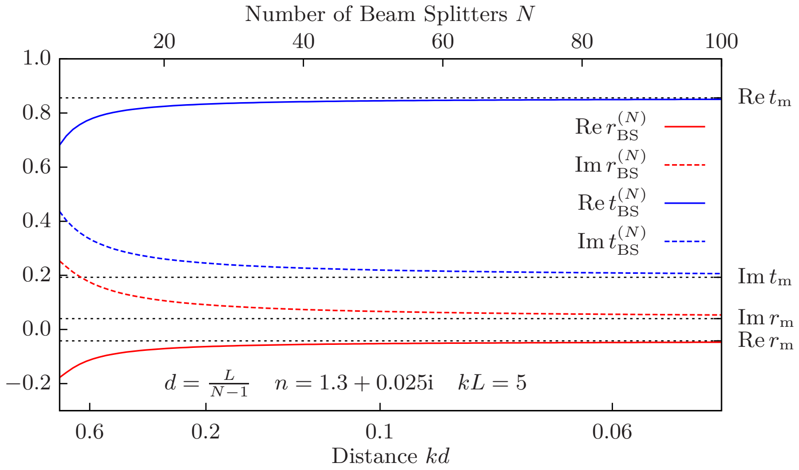

Figure 3.3 The total reflection and transmission coefficients for an object formed by N beam splitters distributed equally over a length L and ζ given by eq. (3.4). Obviously, $r_\mathrm{BS}^{(N)}$ and $t_\mathrm{BS}^{(N)}$ rapidly converge to the values for a homogeneous medium with increasing slice number N.

splitters, which will be our key to compute analytic expressions for the optical force distribution on and inside a dielectric medium.

We first check if our model reproduces the correct reflection and transmission coefficients for a dielectric slab of length L and refractive index n, which for plane-waves at normal incidence are given by (Born *et al.* 1993)

$$r_\mathrm{m} = \frac{(1-n^2)\sin(nkL)}{(n^2+1)\sin(nkL) + 2in\cos(nkL)}, \tag{3.5a}$$

$$t_\mathrm{m} = \frac{2in}{(n^2+1)\sin(nkL) + 2in\cos(nkL)}. \tag{3.5b}$$

For any finite set of N beam splitters the total reflection and transmission coefficients can be read off from $C_N = r_\mathrm{BS}^{(N)} D_N + t_\mathrm{BS}^{(N)} A_1$ and $B_1 = r_\mathrm{BS}^{(N)} A_1 + t_\mathrm{BS}^{(N)} D_N$. In figure 3.3 we show that the corresponding coefficients calculated from eq. (3.3) via $\mathrm{M}_N := \mathrm{M}_\mathrm{BS} \left(\mathrm{P}_d \mathrm{M}_\mathrm{BS}\right)^{N-1}$,

$$r_\mathrm{BS}^{(N)} = \frac{(\mathrm{M}_N)_{1,2}}{(\mathrm{M}_N)_{2,2}}, \qquad t_\mathrm{BS}^{(N)} = \frac{1}{(\mathrm{M}_N)_{2,2}}, \tag{3.6}$$

converge to r_m and t_m as $N \to \infty$, which can be shown analytically.

3.3 Forces on and within a dielectric medium

In earlier works, beam splitters represented atomic clouds or point particles settling at force-free positions with a spacing of $\sim \lambda/2$ (Asbóth *et al.* 2008; Deutsch *et al.*

1995). Here, however, we take the limit of an infinite number of beam splitters concentrated at a finite length L and calculate the optical force on each layer at a predefined fixed position. In general, the total electromagnetic force on an object (i.e. each slice) embedded in vacuum is given by (Jackson 1999)

$$\mathrm{F} = \oint_{\mathcal{A}} \sum_{\beta} \mathrm{T}_{\alpha\beta}\, \mathrm{n}_{\beta}\, \mathrm{d}A, \tag{3.7}$$

where $\mathcal{A}$ denotes the surface of the object, n is the normal to $\mathcal{A}$ and $\mathrm{T}_{\alpha\beta}$ is the Maxwell stress tensor

$$\mathrm{T}_{\alpha\beta} = \varepsilon_0 \mathrm{E}_{\alpha}\mathrm{E}_{\beta} + \tfrac{1}{\mu_0}\mathrm{B}_{\alpha}\mathrm{B}_{\beta} - \tfrac{1}{2}\delta_{\alpha,\beta}\left(\varepsilon_0 \mathrm{E}^2 + \tfrac{1}{\mu_0}\mathrm{B}^2\right). \tag{3.8}$$

Using two planes orthogonal to the direction of propagation (i.e. the x axis) as surface and plane-wave fields as above, the time-averaged optical force per area (pressure) on the j^{th} slice simply reads (Xuereb *et al.* 2009)

$$F_j = \frac{\varepsilon_0}{2}\Big(|A_j|^2 + |B_j|^2 - |C_j|^2 - |D_j|^2\Big). \tag{3.9}$$

Of course the same argument can also be used for the force on an extended object of length L exposed to incoming field amplitudes A and D, i.e.:

$$F_{\text{med}} = \frac{\varepsilon_0}{2}\Big(|A|^2 + |r_{\text{m}}A + t_{\text{m}}D|^2 - |t_{\text{m}}A + r_{\text{m}}D|^2 - |D|^2\Big). \tag{3.10}$$

From above we know that the correct total reflection and transmission coefficients are obtained in the limit of a continuous system, i.e. $\lim N \to \infty$. This guarantees that our discrete model predicts the correct total force on the object. From fig. 3.3 we conclude that the total force and the field distribution within the medium are very well approximated by our beam splitter model even for a moderate number of elements.

To obtain the internal force distribution we rewrite eq. (3.9) using $d = L/(N-1)$ and set $x = (j-1)d$ as the distance between the j^{th} and the first beam splitter. It is also necessary to change notation by $A_1 \to A$, $D_N \to D$ and $\Delta_{AD} := \arg A - \arg D$. After some calculation we find the (volume) force density as limit of the force on more and more closely spaced slices $\mathcal{F}(x) := \lim_{N\to\infty} NF_j/L$ to be

$$\begin{aligned}\mathcal{F}(x) = \frac{2k\varepsilon_0}{|\mathcal{N}|^2}\Big[&|A|^2\,\mathrm{Im}\left[f(L-x)g^*(L-x)\right] - |D|^2\,\mathrm{Im}\left[f(x)g^*(x)\right]\\ &+ |AD|\,\mathrm{Im}\left[e^{-i\Delta_{AD}}f(x)g^*(L-x) - e^{i\Delta_{AD}}f(L-x)g^*(x)\right]\Big]\end{aligned} \tag{3.11}$$

where z^* denotes the complex conjugate of z and

$$\begin{aligned}\mathcal{N} &= (n^2+1)\sin(nkL) + 2in\cos(nkL),\\ f(x) &= (n^2-1)\big(in\cos(nkx) + \sin(nkx)\big),\\ g(x) &= n\big(i\cos(nkx) + n\sin(nkx)\big).\end{aligned} \tag{3.12}$$

One finds that the integrated force density is equal to the total force per unit area derived by the Maxwell stress tensor in eq. (3.10), as required.

With some algebra one can see that the result for the force density in eq. (3.11) can also be obtained by calculating the force on a test-atom in the effective optical field inside a dielectric medium using the well known approach by Cohen-Tannoudji (Cohen-Tannoudji 1992). In this form the optical force on a dipole at the position x_A in the external field $E(x)$ reads

$$F_L = \tfrac{1}{4}\partial_x |E(x_A)|^2 \operatorname{Re}\alpha - \tfrac{1}{2}|E(x_A)|^2 \partial_x \phi(x_A) \operatorname{Im}\alpha\,. \tag{3.13}$$

Here $\phi(x) = -\arg(E(x))$ and α is the polarizability of the dipole. The first term in eq. (3.13) proportional to $\operatorname{Re}\alpha$ is often referred to as *dipole force*, the (dissipative) term proportional to $\operatorname{Im}\alpha$ is called *radiation pressure* or *scattering force* (Cohen-Tannoudji 1992). Note that as we have to insert the effective fields within the medium, the forces in general show a nonlinear dependence on the polarizability induced by multiple scattering within the medium, as found in previous work (Asbóth *et al.* 2008). The agreement between eq. (3.13) and the force from eq. (3.11) is demonstrated in fig. 3.7.

3.4 Central results and examples

Before turning to the discussion of the force distribution within a medium as given by eq. (3.11) to investigate possible light-induced deformations of the objects, let us first treat optical trapping of an extended object as given by eq. (3.10) in a standing-wave configuration.

To provide insight into the role of the position and length of the object, we rewrite eq. (3.10) in terms of the incoming laser intensities I_l and I_r. With x_0 denoting the position of the centre of the object we have $A = |E_l| \exp(i\phi_l) \exp(ik(x_0 - L/2))$, $D = |E_r| \exp(i\phi_r) \exp(-ik(x_0 + L/2))$ and $I_{l,r} = \varepsilon_0 c |E_{l,r}|^2/2$. With $\Delta_{AD} = \phi_l - \phi_r + 2kx_0 =: 2k\xi$ we finally get

$$F_{\mathrm{med}}(L,\xi) = \tfrac{1}{c}(I_l - I_r)u(L) - \tfrac{4}{c}\sqrt{I_l I_r}\, v(L) \sin(2k\xi), \tag{3.14}$$

where we defined $u(L) := 1 + |r_{\mathrm{m}}(L)|^2 - |t_{\mathrm{m}}(L)|^2$ and $v(L) := \operatorname{Im}[r_{\mathrm{m}}(L) t_{\mathrm{m}}^*(L)]$ in terms of the reflection and transmission amplitudes r_{m} and t_{m} given in eq. (3.5).

To trap an object of a given length L in a standing-wave, one needs to find positions ξ_0 with zero average force $F_{\mathrm{med}}(L,\xi_0) = 0$ and a proper restoring force for small excursions, i.e. $F_{\mathrm{med}}(L,\xi) \simeq -\kappa_0(\xi - \xi_0)$ for $k(\xi - \xi_0) \ll 1$ with $\kappa_0 > 0$ being the trap stiffness. Obviously, the first condition is met if

$$\sin(2k\xi_0) = \frac{u(L)}{4v(L)} \frac{I_l - I_r}{\sqrt{I_l I_r}}. \tag{3.15}$$

This equality gives real solutions only if the laser intensities, the object length L and the refractive index n are chosen such that the absolute value of the term on the right hand side is less than one. If this is met, the first zero of the force F_{med} is given by

$$\widetilde{\xi}_0 := \frac{1}{2k}\arcsin\left[\frac{u(L)}{4v(L)}\frac{I_l - I_r}{\sqrt{I_l I_r}}\right]. \tag{3.16}$$

Due to the overall symmetry of the setup, the other zeros of F_{med} satisfy $\xi_0 \in \Xi_+ \cup \Xi_-$,

$$\begin{aligned} \Xi_+ &:= \left\{\tfrac{m\pi}{k} + \widetilde{\xi}_0, m \in \mathbb{Z}\right\}, \\ \Xi_- &:= \left\{\tfrac{(2m-1)\pi}{2k} - \widetilde{\xi}_0, m \in \mathbb{Z}\right\}. \end{aligned} \tag{3.17}$$

Linearising F_{med} in the vicinity of every ξ_0 gives

$$F_{\mathrm{med}}(L,\xi) \simeq -\tfrac{8k}{c}\sqrt{I_l I_r}\, v(L)\cos(2k\xi_0)(\xi - \xi_0). \tag{3.18}$$

Using $\cos(2k\xi_0) = \pm\sqrt{1 - \sin^2(2k\xi_0)}$ with the positive {negative} case referring to $\xi_0 \in \Xi_+$ $\{\xi_0 \in \Xi_-\}$ and eq. (3.15) leads us to the following linear approximations for F_{med}

$$\begin{aligned} F_{0,+}(L,\xi) &= -\kappa_0(L)\operatorname{sgn}[v(L)](\xi - \xi_0) \ \text{ if } \xi_0 \in \Xi_+, \\ F_{0,-}(L,\xi) &= +\kappa_0(L)\operatorname{sgn}[v(L)](\xi - \xi_0) \ \text{ if } \xi_0 \in \Xi_-, \end{aligned} \tag{3.19}$$

where $\operatorname{sgn}(x) := x/|x|$ denotes the signum function and the trap stiffness is given by

$$\kappa_0(L) := \tfrac{2k}{c}\sqrt{16v^2(L)I_l I_r - u^2(L)(I_l - I_r)^2}. \tag{3.20}$$

Hence we conclude that if $v(L) > 0$, then the trapping positions are $\xi_0 \in \Xi_+$ and $F_{0,+}$ describes the restoring force, whereas if $v(L) < 0$, trapping occurs at $\xi_0 \in \Xi_-$ and the force is approximated by $F_{0,-}$. Examples for the trapping properties and the total force F_{med} are depicted in figs. 3.4 and 3.5. Note that $\operatorname{sgn}[v(L)] \simeq -\operatorname{sgn}[\sin(kL\operatorname{Re} n)]$ for $kL\operatorname{Im} n \ll 1$.

For symmetric pump intensities ($I_l = I_r$) we have $\widetilde{\xi}_0 = 0$ and the centre of mass of the object is trapped at positions ξ_0 with $\cos(2k\xi_0) = 1$ for $v(L) > 0$ or $\cos(2k\xi_0) = -1$ for $v(L) < 0$. These are exactly the maxima and minima of the field intensity of a standing-wave in free space. We thus find that, apart from a few singular points, stable trapping positions correspond either to the maximum or the minimum intensity and we observe size-dependent low- or high-field-seeking behaviour. For exactly symmetric input the stability jumps between two positions as function of size, while pump asymmetry allows a continuous shift of the stationary position.

We compared our findings to experimental and numerical works on submicron-sized spheres trapped in a standing-wave field created by interfering evanescent waves (Čižmár *et al.* 2006) or Gaussian beams (Zemánek *et al.* 2003). Despite the differences in the setup, our simple but analytic approach leads to very similar results for the total forces, the trap stiffness, and the size dependent low- or high-field-seeking behaviour.

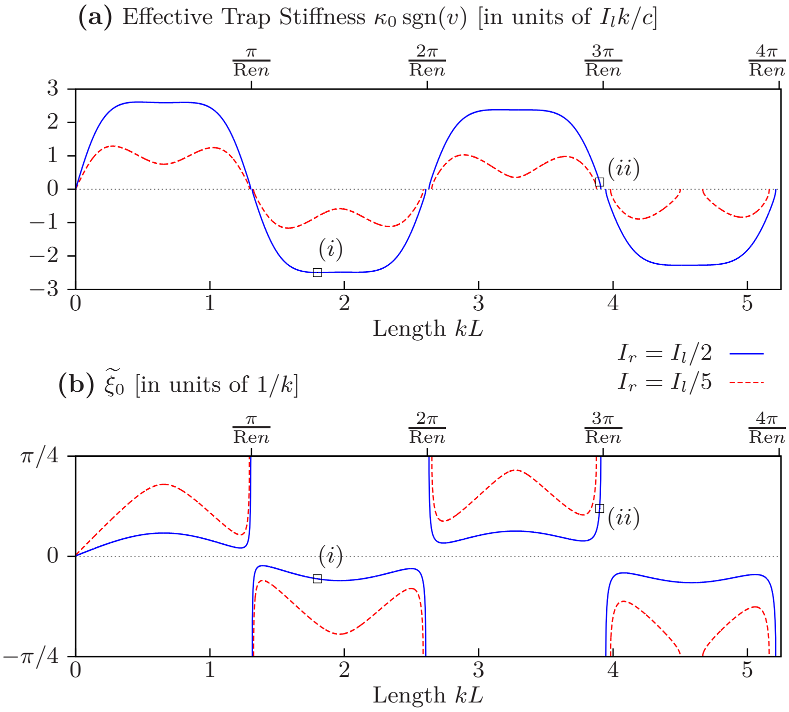

Figure 3.4 The trapping properties for an object with $n = 2.4+0.02i$ in a standing-wave field with asymmetric intensities, $I_r = I_l/2$ (blue, solid line) and $I_r = I_l/5$ (red, dashed line). (a) The effective trap stiffness $\kappa_0(L)\,\mathrm{sgn}[v(L)]$ as used in eq. (3.19). If $\kappa_0\,\mathrm{sgn}(v)$ is positive, trapping occurs at $\xi_0 \in \Xi_+$, else, Ξ_- defines the set of stable trapping positions. (b) The first zero of the total force $\widetilde{\xi}_0$ as defined in eq. (3.16). The labels (i) and (ii) mark the lengths used for the examples in fig. 3.5.

As one can see in eq. (3.15), the total force can only have zeros if $|u(L)(I_l - I_r)| \leq 4|v(L)|\sqrt{I_l I_r}$. For asymmetric pump one can therefore find lengths for which $\widetilde{\xi}_0$ and κ_0 are no longer real values and trapping is impossible. This should have important applications for optical size selection of objects. In fig. 3.4 we observe a contraction of the domains of $\widetilde{\xi}_0$ and κ_0 for larger object lengths. This can be explained as follows: For growing values of $kL\,\mathrm{Im}\,n$, the transmission $t_\mathrm{m}(L)$ goes to zero whereas the reflection $r_\mathrm{m}(L)$ reaches a limit, therefore $v(L)$ also goes to zero and condition (3.15) cannot be fulfilled any more. This simply means that large and/or highly absorbing objects cannot be trapped in an unbalanced standing-wave (i.e. $I_l \neq I_r$).

Forces within an extended medium

Obviously, the total force responsible for the trapping does not act uniformly on each part of the object. In fact the internal force distribution as given by eq. (3.11) even shows sign changes within the object, with local forces possibly much larger than the average force per volume. This of course induces internal strain, which strongly

(i) F_{med} for $kL = 1.8$ [in units of I_l/c]

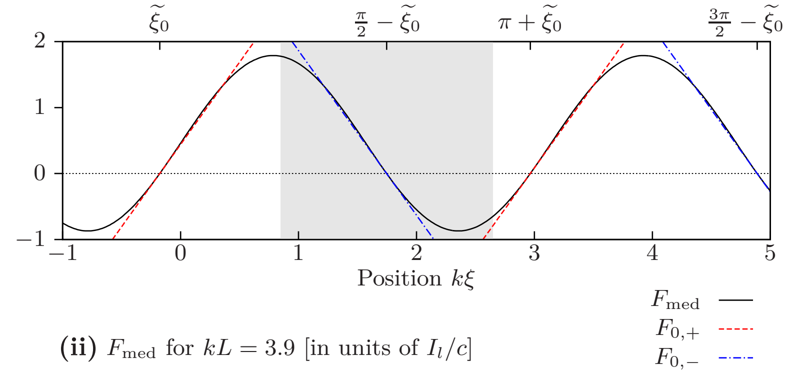

(ii) F_{med} for $kL = 3.9$ [in units of I_l/c]

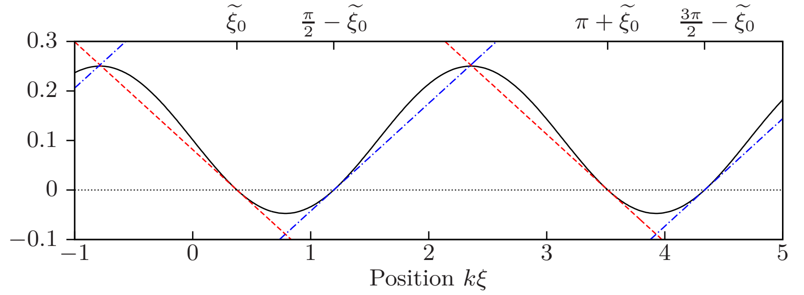

Figure 3.5 The total force F_{med} on an object with $n = 2.4 + 0.02i$ in a standing-wave field with asymmetric intensities ($I_r = I_l/2$) for $kL = 1.8$ (i) and $kL = 3.9$ (ii). The dashed red lines represent the linear approximation $F_{0,+}(L, \xi)$ from eq. (3.19), the dash-dotted blue lines represent $F_{0,-}(L, \xi)$. As one can see in fig. 3.4 $v(L)$ is negative in (i) thus $F_{0,-}$ approximates the trapping force on the object. In (ii) $v(L)$ is positive and trapping is described by $F_{0,+}$. In (i) the extent of an object trapped at position $\pi/2 - \widetilde{\xi}_0$ is highlighted grey.

depends on the object length, on the refractive index and on the incoming intensity amplitudes. The oscillating behaviour of $\mathcal{F}(x)$ originates in the dipole force term of eq. (3.13), which is $\propto \partial_x |E(x)|^2$, as depicted in figs. 3.6 and 3.7. In fig. 3.6 one can observe significant internal forces although the total force on the object vanishes.

Let us point out that we do not find any significant forces appearing specifically at the object's surface. The appearance of such a surface force attributed to the change of the wave-vector (photon momentum) is an issue in the Abraham-Minkowski controversy, reviewed for instance in (Barnett *et al.* 2010), and in optical cell stretchers (Guck *et al.* 2001).

Since such a non-uniform force distribution creates strain, it also possibly leads to a modification of an elastic object's shape or induces microscopic flow in a liquid dielectric. Looking at N slices initially at rest, we expect the distance between the first and the last slice to change as $\partial_t^2 L := \partial_t^2 (x_N - x_1) = (F_N - F_1)/m$, where m denotes the mass of a single slice. In the limit $N \to \infty$, the continuity equation leads

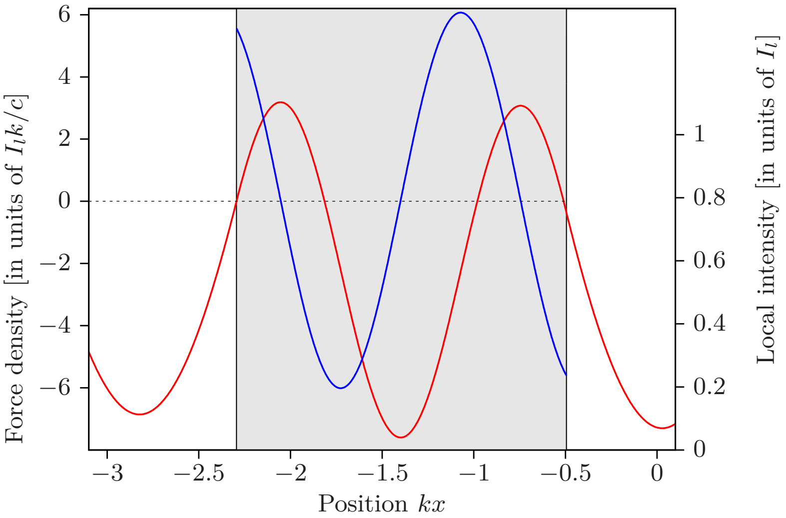

Figure 3.6 Internal force distribution (blue line, left ordinate) and field intensity (red line, right ordinate) for an object with length $kL = 1.8$, refractive index $n = 2.4 + 0.02i$ and incoming intensities $I_r = I_l/2$. The central position $x_0 = \widetilde{\xi}_0 - \pi/2$ is chosen such that $F_{\text{med}} = \int_{x_0-L/2}^{x_0+L/2} \mathcal{F}(x)\,\mathrm{d}x = 0$, cf. fig. 3.5, case (i).

to $\partial_t^2 L = \left(\mathcal{F}(L) - \mathcal{F}(0)\right)/\mu$ or

$$\partial_t^2 L = \tfrac{4k}{c\mu|\mathcal{N}|^2}\Big[\left(I_l + I_r\right)\operatorname{Im}\left[f(0)g^*(0) - f(L)g^*(L)\right] \\ + 2\sqrt{I_l I_r}\cos(2k\xi)\operatorname{Im}\left[f(L)g^*(0) - f(0)g^*(L)\right]\Big]. \quad (3.21)$$

with a mass density μ, and f, g, and $\mathcal{N}$ as given in eq. (3.12).

In fig. 3.6 the parameters are chosen such that the object's central position is trapped and we observe that $(\mathcal{F}(L) - \mathcal{F}(0)) < 0$, indicating contractive strain. But note that one can also find examples of trapped objects with $\partial_t^2 L > 0$.

The above equation (3.21) is valid for homogeneous media only and certainly will not give the correct result for highly compressible material: In the case of elastic media, the internal optical forces will lead to a spatial variation in the material density and refractive index. This again will reshape the local optical fields and thus change the force distribution. We thus expect a complicated nonlinear response of such an object, the detailed investigation of which we will leave to future work.

Up to now we always assumed a standing-wave field i.e. the two counter-propagating beams of equal polarisation and with fixed phase. In the general case of orthogonal directions of polarisation or a random phase of the two beams, the fields cannot interfere. The local intensities and forces are calculated separately for left and right incidence and added up in the end. Therefore, the time-averaged forces are modified by setting the interference terms $\propto \sqrt{I_l I_r}$ in eq. (3.14), (3.21) and $\propto |AD|$ in eq. (3.11), respectively, to zero. Under these circumstances, the forces no longer depend on the object's centre of mass position or the relative phase between the incoming beams.

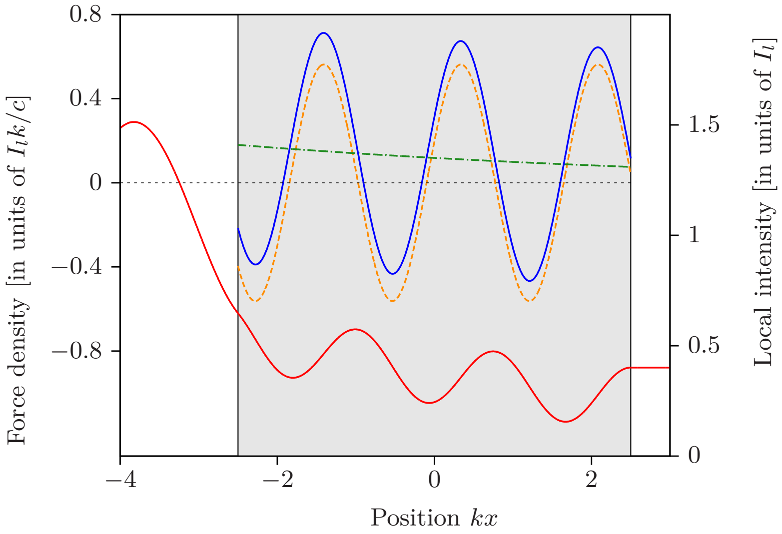

Figure 3.7 Field intensity (red line, right ordinate) and internal force distribution (left ordinate) for $kL = 5$, $n = 1.8 + 0.08i$ and left incidence only (i.e. $I_r = 0$). It is apparent that the total internal force (blue, solid line) is a sum of the dipole force (orange, dashed line) and the scattering force (green, dash-dotted line), as discussed in eq. (3.13).

In fig. 3.7 we show the forces for single side illumination of an extended object. Surprisingly we still find a strong length dependence of the force and the appearance of internal strain. In the chosen example the left and right surfaces are pulled in opposite directions and the object will be stretched in such a field. There are, however, also configurations with different behaviour, if the length is suitably chosen. In fact, for a non-absorbing medium one can read from eq. (3.11) that the force at the rear end will always vanish. Therefore, the expected length change is proportional to $\partial_t^2 L \propto -\mathcal{F}(0)$, which depends on the object's size. Again, a naive argument to derive the force based on effective photon momentum change due to a shift of the wave-vector at the surface will fail qualitatively.

Our findings for the internal force density can be directly compared to the Lorentz force experienced by bound charges and currents inside a dielectric (Mansuripur 2004; Zakharian *et al.* 2005). The results for the force inside a dielectric slab (fig. 1 in (Zakharian *et al.* 2005)) and a semi-infinite dielectric (eq. (3) in (Mansuripur 2004)) match exactly the force distributions obtained from eq. (3.11).

3.5 Conclusions and Outlook

Optical forces in extended media can exhibit quite complex and surprising behaviour even in the most simple 1D geometry and for linearly polarizable rigid objects. Depending on the object size, refractive index and relative pump intensities, our analytic approach predicts interesting trapping features such as a size dependent change from high-field-seeking to low-field-seeking behaviour. Regarding internal forces we described the appearance of compressing or stretching forces on and within the object. Although our model is rather simplistic the results should be qualitatively similar for other shapes such as microspheres or more complex structured objects.

It seems straightforward to generalise our approach in several respects, e.g. to assume a more complicated spatial distribution of the object's refractive index or to include elasticity. Similarly, the effect of using several frequencies or partially coherent light can be included to extend the scope of the results. One very interesting case of course would be the generalisation to liquid or gaseous media, where internal pressure changes would have a strong effect and generate highly nonlinear dynamics. Here the dipole force on a cloud could not only lead to trapping but also compression or expansion of the sample.

Acknowledgements

This work was supported by ESF-FWF I119 N16 and ERC Advanced Grant (catchIT, 247024). Among many others we thank Stefan Bernet, Wolfgang Niedenzu and Tobias Grießer for fruitful discussions.

4 Publication

Optomechanical deformation and strain in elastic dielectrics

M. Sonnleitner*, M. Ritsch-Marte and H. Ritsch

Light forces induced by scattering and absorption in elastic dielectrics lead to local density modulations and deformations. These perturbations in turn modify light propagation in the medium and generate an intricate nonlinear response. We generalize an analytic approach where light propagation in one-dimensional media of inhomogeneous density is modelled as a result of multiple scattering between polarizable slices. Using the Maxwell stress tensor formalism we compute the local optical forces and iteratively approach self-consistent density distributions where the elastic back-action balances gradient- and scattering forces. For an optically trapped dielectric we derive the nonlinear dependence of trap position, stiffness and total deformation on the object's size and field configuration. Generally trapping is enhanced by deformation, which exhibits a periodic change between stretching and compression. This strongly deviates from qualitative expectations based on the change of photon momentum of light crossing the surface of a dielectric. We conclude that optical forces have to be treated as volumetric forces and that a description using the change of photon momentum at the surface of a medium is inappropriate.

New J. Phys. **14**, 103011 (2012) doi: 10.1088/1367-2630/14/10/103011

---

[*] The author of the present thesis performed all of the calculations in this publication.

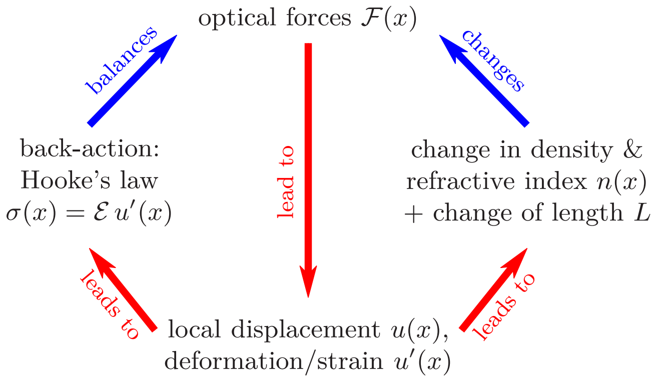

Figure 4.1 Schematic illustration of the interaction between optical forces and local deformations within elastic media.

4.1 Introduction

As light carries momentum besides energy, its propagation through a polarizable medium is accompanied by forces. Although the momentum of a single light quantum is very small, laser light can generate appreciable forces on the microscopic scale. Optical forces are nowadays routinely used to manipulate and trap particles ranging from single atoms and molecules (Ashkin 1970; Hänsch *et al.* 1975; Phillips 1998) to plastic beads, biological cells or microbes up to the size of tens of micrometres (Padgett *et al.* 2011; Stevenson *et al.* 2010; Thalhammer *et al.* 2011). The mechanical motion of even larger objects such as silica mircodisks or suspended mirrors has been damped and cooled by light forces (Kippenberg *et al.* 2008; Wiederhecker *et al.* 2009). While most of the existing work targets the overall effect on the centre of mass of the particles, it has been shown by us as well as by other groups that these forces do not act homogeneously but exhibit distinct patterns within the medium (Mansuripur 2004; Sonnleitner *et al.* 2011; Zakharian *et al.* 2005). For any elastic medium this leads to local compression or stretching. Of course, the modified density also changes the local refractive index and light propagation, which again alters the forces as displayed schematically in figure 4.1. The resulting coupled complex evolution thus obviously requires self-consistent models and solutions (Mansuripur 2010). In addition, as the light mediated interaction is inherently long-range, even a small but periodic variation of the refractive index can have a very large overall collective effect coupling distant areas over a large volume.

This work is organized as follows: in section 4.2 we first present the basic scattering approach to treat the light propagation in an inhomogeneous refractive medium and use a previously developed formalism based on the free space Maxwell stress tensor to calculate the corresponding local force distribution (section 4.3). This method is then used in section 4.4 to develop an iterative scheme to calculate the steady state density and field distribution as a function of geometry and field intensity. In section 4.5

we discuss essential physical consequences predicted by our model at the hand of numerical examples. Finally, in section 4.6 these results are set against common calculations of the total deformation at hand of the change of photon momentum at an interface between two dielectrics.

4.2 Multiple scattering model of light propagation in inhomogeneous media

The effective light propagation in a medium can be seen as the result of multiple individual scattering processes, which in general requires intricate numerical treatments, if one cannot make use of material symmetries. Here we restrict ourselves to the simple but still non-trivial case of two incoming counterpropagating plane waves in a transversely homogeneous and linearly polarizable medium. In this limit only forward and backward scattering add up phase coherently, while all amplitudes for transverse scattering average out. From the viewpoint of the forward and backward propagation directions, transverse scattering thus can just be added to an effective absorption rate in the medium. This is certainly not perfectly fulfilled in an actual setup, but still can be expected to give the correct qualitative behaviour, as long as the transverse extensions are much larger than the wavelength of the light. A more realistic treatment, e.g. in terms of Gaussian transverse beams, is possible, but greatly complicates the model and would obscure many interesting physical phenomena found in this simple approach.

Restricting the dynamics to the forward and backward scattering amplitudes along the propagation directions gives a simple and tractable model for our medium via a one dimensional (1D) array of N thin slices at positions $x_1, \ldots, x_N$. Here the spatial behaviour of the electric field $\mathbf{E}(x,t) = \mathrm{Re}[E(x)\exp(-i\omega t)]\mathbf{e}_y$ is determined by a 1D Helmholtz equation (Asbóth *et al.* 2008; Deutsch *et al.* 1995; Sonnleitner *et al.* 2011)

$$\left(\partial_x^2 + k^2\right) E(x) = -2k\zeta E(x) \sum_{j=1}^{N} \delta(x - x_j). \tag{4.1}$$

The field-induced polarization density at each slice is $P(x) = \alpha\eta_\mathrm{A} E(x) \sum_{j=1}^{N} \delta(x - x_j)$, where we introduced the dimensionless coupling parameter $\zeta = k\eta_\mathrm{A}\alpha/(2\varepsilon_0)$ proportional to the atomic polarizability α and the areal particle density η_A within the slice. ε_0 is the vacuum permittivity and $k = \omega/c$ the wave number of the optical field. Note that we assumed here that the dipoles in each slice can simply be added up coherently for scattering along the propagation direction. As illustrated in figure 4.2, the equation above is satisfied by interconnected plane wave solutions (Deutsch *et al.* 1995), here denoted as

$$E_j(x) := C_j e^{ik(x-x_j)} + D_j e^{-ik(x-x_j)} = A_{j+1} e^{ik(x-x_{j+1})} + B_{j+1} e^{-ik(x-x_{j+1})}, \tag{4.2}$$

for $x_j < x < x_{j+1}$. The amplitudes left and right of a material slice (beam splitter)

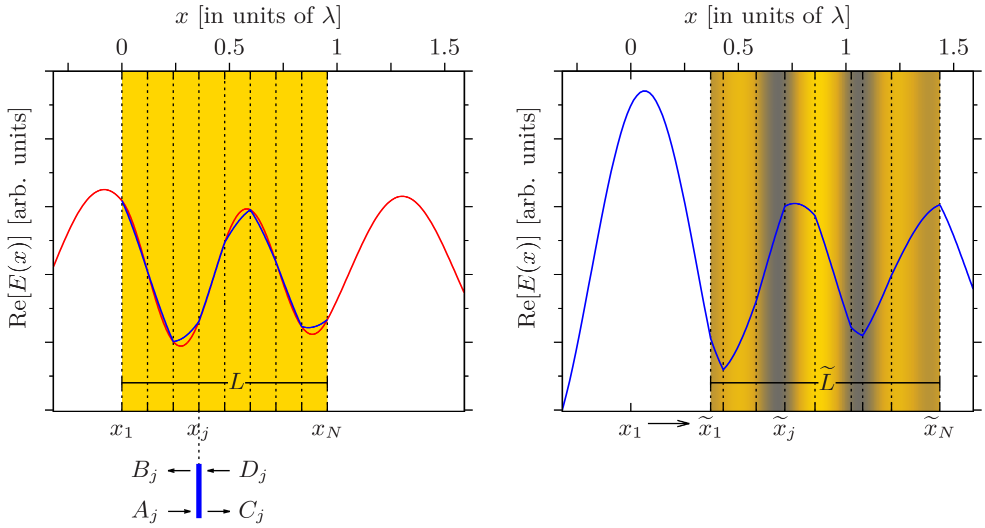

Figure 4.2 Schematic illustration of the displacement and deformation process $x \mapsto \widetilde{x} = x + u(x)$. The initial medium (left figure) occupies the space $[0, L]$, the slices are marked with dotted lines separated by $d_0 = L/(N-1)$. In this case, the field generated by multiple scattering by the beam splitters (blue curve, cf. (4.2)) reproduces the solution for a homogeneous medium with refractive index n (red curve), if the coupling is chosen as in (4.6). On the right hand side we see the displaced medium with irregularly spaced slices of the same coupling ζ and the resulting electric field. The background shading illustrates the change in the distances, i.e. the strain $u'(x) = -(\widetilde{\rho}(x) - \rho)/\rho$, with dark colours indicating regions of higher density.

at position x_j are connected via

$$\begin{pmatrix} C_j \\ D_j \end{pmatrix} = \begin{pmatrix} 1 + i\zeta & i\zeta \\ -i\zeta & 1 - i\zeta \end{pmatrix} \begin{pmatrix} A_j \\ B_j \end{pmatrix} =: \mathrm{M_{BS}} \begin{pmatrix} A_j \\ B_j \end{pmatrix}. \tag{4.3}$$

The amplitudes (A_j, B_j) and (C_{j-1}, D_{j-1}) are coupled by a simple propagation matrix, i.e. $(A_j, B_j)^T = \mathrm{P}_{d_j}(C_{j-1}, D_{j-1})^T$ with $\mathrm{P}_{d_j} := \mathrm{diag}\left(\exp(ikd_j), \exp(-ikd_j)\right)$, with the distance $d_j := x_{j+1} - x_j$, $j = 1, \ldots, N-1$.

Therefore, the amplitudes to the left of the $(j+1)$th slice are obtained by a simple multiplication of the previous transfer matrices

$$\begin{pmatrix} A_{j+1} \\ B_{j+1} \end{pmatrix} = \mathrm{P}_{d_j}\mathrm{M_{BS}} \cdots \mathrm{P}_{d_2}\mathrm{M_{BS}}\mathrm{P}_{d_1}\mathrm{M_{BS}} \begin{pmatrix} A_1 \\ B_1 \end{pmatrix}. \tag{4.4}$$

The amplitudes A_1 and D_N are determined by the amplitudes and phases of waves coming in from the left (i.e. $-\infty$) and from the right ($+\infty$), respectively, and constitute boundary conditions on the solutions for the Helmholtz equation (4.1). B_1 and C_N are obtained by computing the total reflection and transmission amplitudes via

$$\begin{gathered}\frac{1}{t}\begin{pmatrix} t^2 - r_\mathrm{l} r_\mathrm{r} & r_\mathrm{r} \\ -r_\mathrm{l} & 1 \end{pmatrix} = \mathrm{M}_\mathrm{BS}\mathrm{P}_{d_{N-1}}\mathrm{M}_\mathrm{BS}\cdots\mathrm{P}_{d_2}\mathrm{M}_\mathrm{BS}\mathrm{P}_{d_1}\mathrm{M}_\mathrm{BS}, \\ B_1 = r_\mathrm{l} A_1 + t D_N \qquad \text{and} \qquad C_N = t A_1 + r_\mathrm{r} D_N. \end{gathered} \tag{4.5}$$

Note that the reflection coefficients for left or right incidence on an inhomogeneous setup usually do not coincide, i.e. $r_\mathrm{l} \neq r_\mathrm{r}$, but the transmission amplitude t is independent of the direction of propagation. More details on the properties of these generalized transfer matrices are given in appendix 4.A.

For equally spaced, thin polarizable slices we set $x_j = (j-1)d_0$, such that $x_0 = 0$ and $x_N = (N-1)d_0 =: L$ and (4.4) simplifies to $(A_{j+1}, B_{j+1})^T = {\mathrm{T}_\mathrm{h}}^j (A_1, B_1)^T$, with $\mathrm{T}_\mathrm{h} := \mathrm{P}_{d_0}\mathrm{M}_\mathrm{BS}$. In an earlier work (Sonnleitner *et al.* 2011) we showed that choosing a uniform distance d_0 between the slices and setting the coupling parameter

$$\zeta = \frac{\cos(kd_0) - \cos(nkd_0)}{\sin(kd_0)} \tag{4.6}$$

leads to the same optical fields as found inside a medium with refractive index n. A sufficiently dense array of beam splitters with spacing $d_0 = L/(N-1)$ is then in the limit $N \to \infty$ indistinguishable from a homogeneous medium of refractive index n and length L.

A decisive step in this work, which allows us to account for local material density variations, is the introduction of a local *displacement* variable $u(x)$

$$x_j \mapsto \widetilde{x}_j = x_j + u(x_j), \qquad j = 1, \ldots, N. \tag{4.7}$$

As illustrated schematically in figure 4.2, such shifts alter the local fields as well as the total reflection and transmission properties of the object.

The distances between the slices then change as

$$\widetilde{d}_j - d_0 = \widetilde{x}_{j+1} - \widetilde{x}_j - d_0 = u(x_{j+1}) - u(x_j) =: \Delta_j. \tag{4.8}$$

A continuous limit can be consistently defined via $u(x_j) \to u(x)$ for $x \in [0, L]$ to obtain

$$\lim_{N\to\infty} \frac{\Delta_j}{d_0} = \lim_{N\to\infty} \frac{u(x_j + d_0) - u(x_j)}{d_0} = u'(x). \tag{4.9}$$

In analogy with the theory of elastic deformations, we call u' *strain* or *deformation* (Landau *et al.* 1986; Lautrup 2005), and the relative change in the initially homogeneous local material density ρ simply reads

$$\frac{\widetilde{\rho}(x) - \rho}{\rho} = -u'(x). \tag{4.10}$$

Let us here comment on the notation we will use for the rest of this work. As defined in the paragraph above (4.6), our coordinates are chosen such that the unperturbed medium occupies the region $[0, L]$. Introducing a displacement u then shifts the object to $[u(0), L + u(L)]$, with $L + u(L) - u(0) =: \widetilde{L}$. But to ease notation, all the quantities such as the electric field strength E or force F shall remain defined with respect to the original position such that e.g. $E(0)$ $[E(L)]$ always marks the field at the left [right] edge of the medium. The amplitudes at the boundaries then have to be adjusted with corresponding phases, cf. (4.22). This, however, is relevant for mathematical formulations only, physical discussions and figures are unaffected by this detail. In (4.7) we introduced a tilde to distinguish the shifted $\widetilde{x}_j$ from the original x_j. For most other quantities such as the fields or forces, we will omit this tedious notation. Only the changed length $\widetilde{L}$, the inhomogeneous density $\widetilde{\rho}$ (4.10) and refractive index $\widetilde{n}$ (4.19) still have to be distinguished from their original values L, ρ and n.

As mentioned before, defining the coupling ζ as in (4.6) ensures that the solutions of the wave equation (4.1) agree with the field inside a homogeneous dielectric at positions $x_j = (j-1)d_0$, if the fields are assumed to agree at x_1. In the continuous limit $N \to \infty$, the latter requirement is always fulfilled (Sonnleitner *et al.* 2011). Interestingly we still preserve this feature for a model with displaced slices, if we choose the following approach:

Let, as in (4.2), $E_j(x)$ denote the plane wave solution of the Helmholtz equation (4.1) and

$$E_{n_j}(x) = G_j e^{i n_j k (x - x_j)} + H_j e^{-i n_j k (x - x_j)} \qquad \text{for } x_j < x < x_{j+1} \tag{4.11}$$

denote a field defined in the same region, but with a refractive index n_j. To obtain the desired equivalence between a stratified dielectric and a set of irregularly spaced slices, we assume for any given $j \in \{1, \ldots, N-2\}$

$$\lim_{x \downarrow x_j} E_j(x) = \lim_{x \downarrow x_j} E_{n_j}(x) \tag{4.12}$$

and demand that with $E(\uparrow y) \equiv \lim_{x \uparrow y} E(x)$,

$$E_j(\uparrow x_{j+1}) = E_{j+1}(\downarrow x_{j+1}), \qquad E_j'(\uparrow x_{j+1}) = E_{j+1}'(\downarrow x_{j+1}) + 2k\zeta E_{j+1}(\downarrow x_{j+1}), \tag{4.13}$$

$$E_{n_j}(\uparrow x_{j+1}) = E_{n_{j+1}}(\downarrow x_{j+1}), \qquad E_{n_j}'(\uparrow x_{j+1}) = E_{n_{j+1}}'(\downarrow x_{j+1}), \tag{4.14}$$

$$E_j(\uparrow x_{j+1}) = E_{n_j}(\uparrow x_{j+1}), \qquad E_{j+1}(\uparrow x_{j+2}) = E_{n_{j+1}}(\uparrow x_{j+2}). \tag{4.15}$$

The first line shows the conditions that E_j and E_{j+1} are solutions of the Helmholtz equation (4.1), cf. (4.3) or (Deutsch *et al.* 1995), the second line denotes Fresnel's equations for the transition between two dielectrics. In the third line, finally, we demand that the plane wave solutions of (4.1) agree with the fields inside the dielectrics at positions x_{j+1} and x_{j+2}. This leads to the required, successive coupling between ζ, the distances $d_j = x_j - x_{j-1}$ and d_{j+1}, and some indices n_j, n_{j+1}.

Solving (4.13)-(4.15) under the assumption (4.12) and demanding solutions independent of the field amplitudes results in two conditions, for $j = 1, \ldots, N-1$

$$\frac{n_j \sin(kd_j)}{\sin(kn_j d_j)} = \frac{n_{j+1} \sin(kd_{j+1})}{\sin(kn_{j+1} d_{j+1})}, \tag{4.16}$$

$$\zeta = \frac{1}{2} \left[\frac{\cos(kd_j) - \cos(n_j kd_j)}{\sin(kd_j)} + \frac{\cos(kd_{j+1}) - \cos(n_{j+1} kd_{j+1})}{\sin(kd_{j+1})} \right]. \tag{4.17}$$

One can easily check that these conditions give the known relation (4.6) in the equidistant case where $d_j = d_{j+1} \equiv d_0$ and $n_j = n_{j+1} \equiv n$. Unfortunately, we were not able to find solutions with finite values of $d_j \neq d_{j+1}$ for both conditions. Inspired from (4.6) one may try

$$n_j = \frac{1}{d_j k} \arccos\big(\cos(d_j k) - \zeta \sin(d_j k)\big). \tag{4.18}$$

to find that this approach satisfies (4.17), but not (4.16). However, choosing ζ as in (4.6), writing $d_j = d_0(1 + \Delta_j/d_0)$, and taking the continuous limit $N \to \infty$ with $\Delta_j/d_0 \to u'(x)$ (4.9) alters (4.18) to

$$\widetilde{n}(x) = \sqrt{\frac{n^2 + u'(x)}{1 + u'(x)}}, \tag{4.19}$$

satisfying both (4.16) and (4.17). With the given inhomogeneous refractive index we can compute the electric field inside a strained, 1D dielectric by solving

$$\left(\partial_x^2 + \widetilde{n}^2(x) k^2\right) E(x) = 0 \tag{4.20}$$

numerically. A comparison with the field computed via the transfer matrix method described in (4.4) shows excellent agreement, for sufficiently large N.

Another way to approximate the optical field is to expand the transfer matrices in (4.4) for small local deformations Δ_j and then perform the continuous limit. This analytical approximation works sufficiently well for the typically small strain u' obtained in the scope of parameters used in this work. The lengthy results of this approach are presented in appendix 4.B, equation (4.60).

Inserting the relation between strain and density modifications (4.10) we finally obtain

$$\widetilde{n}^2 = \frac{(n^2+1)\,\rho - \widetilde{\rho}(x)}{2\rho - \widetilde{\rho}(x)} \simeq n^2 + \left(n^2 - 1\right) \frac{\widetilde{\rho}(x) - \rho}{\rho}, \tag{4.21}$$

where we assumed $(\widetilde{\rho} - \rho)/\rho \ll 1$ for the final expansion.

4.2.1 Computing the reflection and transmission amplitudes

To find solutions for the fields inside the medium with refractive index distribution $\widetilde{n}(x)$, one needs to specify initial values. As discussed for the discrete system in (4.5), the medium can be described in terms of a transfer matrix such that

$B_0 = r_\mathrm{l} A_0 + t D_0$ and $C_L = t A_0 + r_\mathrm{r} D_L$, if the electric fields outside the medium are given as $E(x) = A_0 \exp(ikx) + B_0 \exp(-ikx)$ for $x \leq 0$ and $E(x) = C_L \exp(ik(x - L)) + D_L \exp(-ik(x - L))$ for $x \geq L$. The amplitudes A_0 and D_L are determined by the intensities $I_{l,r}$ and phases $\phi_{l,r}$ of the fields incident from the left and right and the displacement u, as

$$A_0 = \sqrt{\tfrac{2I_\mathrm{l}}{\varepsilon_0 c}} e^{i\phi_\mathrm{l}} e^{iku(0)} \qquad \text{and} \qquad D_L = \sqrt{\tfrac{2I_\mathrm{r}}{\varepsilon_0 c}} e^{i\phi_\mathrm{r}} e^{-ik(L+u(L))}. \tag{4.22}$$

Therefore, the initial conditions for solutions of (4.20) are $E(0) = A_0 + B_0$ and $E'(0) = ik(A_0 - B_0)$.

But obviously, the reflection and transmission coefficients r_l, r_r and t strongly depend on the refractive index $\tilde{n}(x)$. To calculate those one can either use some approximations, cf. appendix 4.B, equation (4.59), or solve the field equation (4.20) for specially chosen boundary values, e.g.

$$\begin{aligned} E^{[1]}(0) = iE^{[1]\prime}(0)/k = tD_L \quad &\Rightarrow \quad E^{[1]}(L) = D_L(r_\mathrm{r} + 1),\ E^{[1]\prime}(L) = ikD_L(r_\mathrm{r} - 1), \\ E^{[2]}(L) = -iE^{[2]\prime}(L)/k = tA_0 \quad &\Rightarrow \quad E^{[2]}(0) = A_0(1 + r_\mathrm{l}),\ E^{[2]\prime}(0) = ikA_0(1 + r_\mathrm{l}), \end{aligned} \tag{4.23}$$

allowing the easy computation of r_l, r_r and t.

It is easy to see that if $\tilde{n}(x)$ is symmetric, i.e. $\tilde{n}(x) = \tilde{n}(L - x)$, $x \in [0, L]$, then a beam entering from the left experiences the same medium as one from the right and hence $r_\mathrm{l} = r_\mathrm{r}$. Note that for the homogeneous case where $u' = 0$ and $\tilde{n} = n$, we recover the usual (Born *et al.* 1993)

$$\begin{aligned} t_\mathrm{h} &= \frac{2n}{2n\cos(nkL) - i(n^2+1)\sin(nkL)}, \\ r_\mathrm{h} &= \frac{i(n^2-1)\sin(nkL)}{2n\cos(nkL) - i(n^2+1)\sin(nkL)}. \end{aligned} \tag{4.24}$$

4.3 Light forces in an inhomogeneous medium

In general, the total electromagnetic force on an object embedded in vacuum is given by (Jackson 1999)

$$\mathrm{F}_\alpha = \oint_\mathcal{A} \sum_\beta \mathrm{T}_{\alpha\beta}\, \mathrm{n}_\beta \, \mathrm{d}A, \tag{4.25}$$

where $\mathcal{A}$ denotes the surface of the object, n is the normal to $\mathcal{A}$ and $\mathrm{T}_{\alpha\beta}$ is the Maxwell stress tensor

$$\mathrm{T}_{\alpha\beta} = \varepsilon_0 \mathrm{E}_\alpha \mathrm{E}_\beta + \tfrac{1}{\mu_0} \mathrm{B}_\alpha \mathrm{B}_\beta - \tfrac{1}{2}\delta_{\alpha,\beta}\left(\varepsilon_0 \mathrm{E}^2 + \tfrac{1}{\mu_0}\mathrm{B}^2\right). \tag{4.26}$$

Using two planes orthogonal to the direction of propagation (i.e. the x-axis) as integration surfaces and the plane wave fields defined in (4.2), the time-averaged optical force per area (pressure) on the j^th slice simply reads (Xuereb *et al.* 2009)

$$F_j = \frac{\varepsilon_0}{2}\Big(|A_j|^2 + |B_j|^2 - |C_j|^2 - |D_j|^2\Big). \tag{4.27}$$

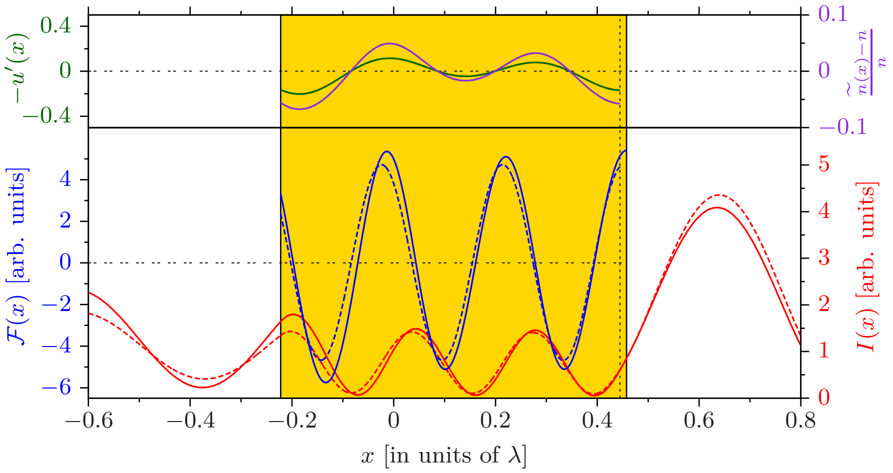

Figure 4.3 Illustration of the influence of a given strain u' (green) on the optical force density (blue) and the local intensity (red). The dotted lines show the homogeneous case $u' = 0$, the continuous lines represent the perturbations computed using the refractive index distribution $\widetilde{n}(x)$ (purple). The reflection and transmission amplitudes here change from $r_{\mathrm{h}} \simeq -0.29 - 0.29i$, $t_{\mathrm{h}} \simeq -0.64 + 0.59i$ to $r_{\mathrm{l}} \simeq -0.20 - 0.21i$, $r_{\mathrm{r}} \simeq -0.15 - 0.24i$, $t \simeq -0.76 + 0.51i$. Please note that in this case the strain is not chosen such that it balances the optical forces as in (4.39).

Following the beam splitter relation in (4.3) we rewrite $C_j = (1 + i\zeta)A_j + i\zeta B_j$ and $D_j = -i\zeta A_j + (1 - i\zeta)B_j$ to obtain

$$F_j = -\varepsilon_0\Big(|\zeta(A_j + B_j)|^2 - \mathrm{Im}[\zeta(A_j + B_j)(A_j - B_j)^*]\Big). \tag{4.28}$$

The naive limit $\lim_{N\to\infty} F_j$ would give a vanishing force per slice as $\lim_{N\to\infty} \zeta = 0$, cf. equation (4.6) with $d_0 = L/(N-1)$. But assigning each slice to one N^{th} of the object's total length L we can define a force density $\mathcal{F}(x) := \lim_{N\to\infty} NF_j/L$ and use

$$\lim_{N\to\infty} \tfrac{N}{L}\zeta = k\tfrac{n^2-1}{2}. \tag{4.29}$$

Following the derivation of the inhomogeneous refractive index (4.19) we can replace $A_j + B_j = E_j(\uparrow x_{j+1}) = E_{n_j}(\uparrow x_{j+1}) \to E(x)$ (4.15) and in the continuous limit it is reasonable to set $A_j - B_j = -iE_j'(\uparrow x_{j+1})/k \to -iE'(x)/k$, if $E(x)$ is a solution of the wave equation (4.20). Hence we obtain the local optical force density

$$\mathcal{F}(x) = \tfrac{\varepsilon_0}{2}\,\mathrm{Re}\left[(n^2-1)E(x)(E'(x))^*\right], \tag{4.30}$$

where we used the algebraic limit theorem for $\lim_{N\to\infty} N|\zeta|^2/L = 0$. Again, the results from the formula above are fully consistent with forces computed using a large but finite number of slices (4.4) and (4.27) as well as an analytical approximation presented in appendix 4.B, equation (4.63).

In figure 4.3 we compare the intensity and optical forces in a medium with homogeneous refractive index n to fields and forces obtained by solving (4.20) and (4.30), respectively, for a given strain u'.

4.3.1 Identification of radiation pressure and dipole force components inside a homogeneous dielectric

In the case of a medium with uniform refractive index n, i.e. with $u' \equiv 0$, the force density computed from (4.30) can be identified with established expressions for optical forces on dielectric test particles. There, the time-averaged force on a dipole at position x_0 in the external field $E(x,t) = \mathrm{Re}\{E(x)\exp(-i\omega t)\}$ with $E(x) = |E(x)|\exp(-i\varphi(x))$ reads (Cohen-Tannoudji 1992)

$$F_\mathrm{L} = \tfrac{1}{4}\partial_x |E(x_0)|^2 \,\mathrm{Re}\,\alpha - \tfrac{1}{2}|E(x_0)|^2 \partial_x \varphi(x_0)\,\mathrm{Im}\,\alpha\,, \tag{4.31}$$

where α is the polarizability of the dipole. The first term proportional to $\mathrm{Re}\,\alpha$ is often referred to as *dipole* or *gradient force*, the (dissipative) term proportional to $\mathrm{Im}\,\alpha$ is called *radiation pressure* or *scattering force* (Cohen-Tannoudji 1992).

Inside a homogeneous dielectric we may write the spatial component of the electric field as $E(x) = G\exp(ink(x-x_0)) + H\exp(-ink(x-x_0))$, where the amplitudes G and H are chosen such that Fresnel's conditions at the boundary of the object are met. Using this field and rewriting (4.31) into a force density on particles with volume density η_V located at x_0 leads to

$$\mathcal{F}_\mathrm{L}(x_0) = -\eta_\mathrm{V} k\,\mathrm{Im}\{GH^*\}\,\mathrm{Re}\{\alpha n^*\} + \tfrac{k}{2}\eta_\mathrm{V}\big(|G|^2 - |H|^2\big)\,\mathrm{Im}\{\alpha n^*\}. \tag{4.32}$$

As the coupling parameter in (4.1) is defined as $\zeta = k\eta_\mathrm{A}\alpha/(2\varepsilon_0)$, with η_A denoting the areal particle density in each of the N slices, we may write using (4.6) and (4.29)

$$\eta_\mathrm{V}\alpha = \lim_{N\to\infty} \tfrac{N}{L}\eta_\mathrm{A}\alpha = \lim_{N\to\infty} 2\tfrac{N}{kL}\varepsilon_0\zeta = \varepsilon_0(n^2-1). \tag{4.33}$$

This relation also resembles the Lorentz-Lorenz relation for the case of a thin gas (Born *et al.* 1993), where the individual dipoles do not directly interact with each other.

It can easily be checked that the force density in (4.32) together with the Lorentz-Lorenz relation (4.33) gives exactly the same result as the force computed from (4.30), if we insert the same field for a homogeneous dielectric. This demonstrates that our approach to calculate fields and forces from multiple scatterers is consistent with well known results derived from more general assumptions.

4.3.2 Integrated force and trap formation

To compute the total force on an extended dielectric in a standing wave we can use the same derivation as for the force on an infinitesimal slice in (4.27) and get

$$F_\mathrm{tot} = \frac{\varepsilon_0}{2}\Big(|A_0|^2 + |r_\mathrm{l}A_0 + tD_L|^2 - |r_\mathrm{r}D_L + tA_0|^2 - |D_L|^2\Big), \tag{4.34}$$

with A_0 and D_L denoting the amplitudes at the object's left and right boundaries, as given in (4.22). Defining the position of the centre of the object $x_0 = (u(0) + L + u(L))/2$, we can express the total force in terms of $\xi := x_0 + (\phi_\mathrm{l} - \phi_\mathrm{r})/(2k)$

$$F_\mathrm{tot}(\xi) = \tfrac{1}{c}\left(I_\mathrm{l} s_\mathrm{l} - I_\mathrm{r} s_\mathrm{r} + 2v\sqrt{I_\mathrm{l} I_\mathrm{r}}\cos(2k\xi + \psi)\right), \tag{4.35}$$

with $s_\mathrm{l} = 1 + |r_\mathrm{l}|^2 - |t|^2$, $s_\mathrm{r} = 1 + |r_\mathrm{r}|^2 - |t|^2$, $v = |r_\mathrm{l} t^* - r_\mathrm{r}^* t|$, $\psi = \arg(r_\mathrm{l} t^* - r_\mathrm{r}^* t)$.

If $4 I_\mathrm{l} I_\mathrm{r} v^2 \geq (I_\mathrm{l} s_\mathrm{l} - I_\mathrm{r} s_\mathrm{r})^2$, the force vanishes at every position $\xi_0 \in \Xi_+ \cup \Xi_-$ where

$$\begin{aligned} &\Xi_+ := \left\{\tfrac{m\pi}{k} + \widehat{\xi}_0, m \in \mathbb{Z}\right\} \qquad \text{and} \qquad \Xi_- := \left\{\tfrac{m\pi - \psi}{k} - \widehat{\xi}_0, m \in \mathbb{Z}\right\}, \\ &\widehat{\xi}_0 := \frac{1}{2k}\left(\arccos\left[\frac{I_\mathrm{r} s_\mathrm{r} - I_\mathrm{l} s_\mathrm{l}}{2v\sqrt{I_\mathrm{l} I_\mathrm{r}}}\right] - \psi\right). \end{aligned} \tag{4.36}$$

Using some trigonometric properties one can show that stable trapping positions are those defined in the set Ξ_+. For $\xi_0 \in \Xi_-$ we find $F'_\mathrm{tot}(\xi_0) > 0$ and hence Ξ_- is a set of unstable trapping position. Linearizing the total force in (4.35) around stable trapping positions $\xi_0 \in \Xi_+$ leads to a trap stiffness of

$$\kappa = \tfrac{2k}{c}\sqrt{4 I_\mathrm{l} I_\mathrm{r} v^2 - (I_\mathrm{l} s_\mathrm{l} - I_\mathrm{r} s_\mathrm{r})^2}. \tag{4.37}$$

Since the reflection and transmission coefficients strongly depend on the object's size, one finds that the parameter ψ can change its sign abruptly for certain values of L. This leads to sudden jumps between a low- and high-field-seeking behaviour for a trapped object (Čižmár *et al.* 2006; Sonnleitner *et al.* 2011; Stilgoe *et al.* 2008; Zemánek *et al.* 2003). Figure 4.5 shows how trap position and trap stiffness is changed by the strain induced on the object by optical forces.

4.4 Self-consistent balancing of optical force and elastic back-action

In the previous sections 4.2 and 4.3 we found expressions for the local fields and the local optical force densities in deformed, dielectric media. But depending on the given elastic properties, the strain will result in stress which typically tries to compensate the external volumetric forces.

In this section we will investigate the behaviour of a linear elastic, dielectric object subjected to the optical forces described by (4.30). More precisely, we will provide a framework to compute the equilibrium configuration between the optical forces and the elastic counter reaction in a self-consistent manner. In our computations we will assume only optical forces and neglect thermal or piezoelectric effects as well as surface tension.

Mechanical equilibrium between some general volume force density f and the resulting stress denoted by the tensor σ is given by Cauchy's equilibrium equation (Lautrup 2005)

$$f_i + \sum_j \partial_j \sigma_{ij} = 0, \tag{4.38}$$

for i, j denoting the coordinates of the system. Since the model discussed here considers only one relevant dimension, this equilibrium equation simplifies to $f + \partial_x \sigma = 0$. The constitutive relation for a linear elastic, 1D object simply reads $\sigma = \mathcal{E} u'$, where $\mathcal{E}$ is Young's modulus and u' is the local strain (Lautrup 2005).

Hence we see that an equilibrium between the optical force density and the elastic strain requires

$$\mathcal{F}(x) + \mathcal{E} u''(x) = 0, \tag{4.39}$$

at every position $x \in [0, L]$, with $\mathcal{F}$ being a solution of (4.30). Note that the electric field computed from (4.20) also depends on the amplitudes at the edges of the object and therefore also on the displacement u, cf. (4.22).

Solving (4.39) for an equilibrium requires boundary conditions on the displacement u and the strain u' which are determined by the given setup. The displacement is fixed by the assumed trapping mechanism, e.g. if the object is trapped by a standing wave, we have to fulfil $(u(0) + L + u(L))/2 \in \Xi_+$. But note that $\widehat{\xi_0}$ depends on the reflection and transmission coefficients and hence also on the deformation u', cf. (4.36).

The strain has to be chosen such that the stress $\sigma = \mathcal{E} u'$ at each surface balances external *surface* forces (Lautrup 2005). Assuming for the moment an object subjected to volumetric optical forces only, we integrate the equilibrium equation (4.39) at obtain

$$0 = \int_0^L (\mathcal{F}(x) + \sigma'(x)) \mathrm{d}x = F_{\mathrm{tot}} + \sigma(L) - \sigma(0). \tag{4.40}$$

For an object trapped by light fields, we get $F_{\mathrm{tot}} = 0$ and $\sigma(0) = \sigma(L) = 0$, due to the lack of surface pressure. In section 4.5.2, however, we fix the slab by an external mechanism balancing the total optical force via surface interaction. Hence if the left boundary of the slab is retained at $x = 0$ (i.e. $u(0) = 0$), then $\sigma(L) = 0$ and $\sigma(0) = F_{\mathrm{tot}}$.

To solve equation (4.39) numerically, we use an iterative approach where the equilibrium condition is rewritten in the form

$$\mathcal{F}(x)[u_i, u_i'] + \mathcal{E} u_{i+1}''(x) = 0, \tag{4.41}$$

with u_i and u_i' denoting the displacement and strain obtained by the ith iteration step and $\mathcal{F}(x)[u_i, u_i']$ is the force density computed using u_i and u_i'. The updated u_{i+1}' and u_{i+1} can then be obtained by simple numerical integration, with integration constants chosen in accordance to the boundary conditions of the used setup. With the updated optical force densities $\mathcal{F}(x)[u_{i+1}, u_{i+1}']$ one can compute the next step of the iteration. An obvious choice for initial values is a homogeneously shifted distribution (i.e. a constant u_0) with a given starting length L and refractive index n.

This iterative scheme proved to be sufficiently exact but significantly faster compared to other methods of solving nonlinear equations, such as Newton's method. We also confirmed our computations with force densities obtained from the transfer matrix approach in (4.4) and the analytic approximation described in appendix 4.B, respectively.

4.5 Examples and physical interpretation

In our basic considerations above we always assumed the object to be exposed to two counterpropagating laser beams of the same, linear polarization forming a standing wave. These results can easily be extended to describe situations with only one incident beam or with two counterpropagating beams of different polarization. In the latter case, one has to calculate the intensities and forces separately for each polarization direction.

In this section we will present four showcase examples to give insight into the large variety of possible results. The first two examples deal with the case where an object is trapped by two counterpropagating beams. The latter examples will treat the case where the object is illuminated by only one beam and externally fixed at one end. For each of the given examples one has to specify the boundary conditions for u and u', as discussed in section 4.4.

For all considered setups we will see that the interaction between optical forces and elastic back-action strongly depends on the ratio between the initial length L and the wavelength of the deformation beam in the unperturbed medium, $\lambda/\operatorname{Re}[n]$. Concerning the intensity and the elastic properties of the medium we find that all results grow linearly in $(I_\mathrm{l} + I_\mathrm{r})/(\mathcal{E}c)$, at least in the scope of parameters where a solution of the equilibrium equation (4.39) could be obtained within a reasonable error tolerance. That is why the local intensities, $I(x) = \varepsilon_0 c|E(x)|^2/2$, and force densities are given in units proportional to $\mathcal{E}$ in the upcoming figures. Note that the numbers used in the simulations are unrealistic in order to exaggerate the effects, since an intensity of $I = 0.1\mathcal{E}c$ would imply $I \simeq 30\mathrm{W}/\mu\mathrm{m}^2$ for $\mathcal{E} \sim 1\mathrm{MPa}$.

4.5.1 Example: object trapped by two counterpropagating beams

As argued above, an object with initial length L subjected to optical forces will in general experience local deformations and an overall length change. Figure 4.4 shows the relative length change $\Delta L = (\widetilde{L} - L)/L$ for different initial lengths L in the cases where an object is trapped in a standing wave (blue lines) or by two beams of orthogonal polarization (red curves) and equal intensity. Obviously, both configurations are symmetric regarding an inversion of x at the centre of the object and therefore we find $r_\mathrm{l} = r_\mathrm{r}$, as mentioned in section 4.2.1.

Surprisingly, in the standing wave case we observe abrupt switching from strong compressive to stretching behaviour around certain initial lengths. A comparison with section 4.3.2 and earlier discussions in (Sonnleitner *et al.* 2011) shows that these switches are concurrent with jumps of the stable trapping position ξ_0. Generally speaking, objects with small values of kL are trapped at local maxima of the intensity in the standing wave. But for larger objects, the term ψ in (4.36) abruptly changes its sign and the object seeks positions centred around intensity minima. As indicated by the dotted grid lines, these jumps occur at lengths of minimal reflection $|r_\mathrm{h}|^2$ and maximal transmission $|t_\mathrm{h}|^2$ (4.24), i.e. at $L = m\lambda/(2\operatorname{Re}[n])$, $m \in \mathbb{N}$.

For larger objects we observe a slight decay of the maximal relative length change,

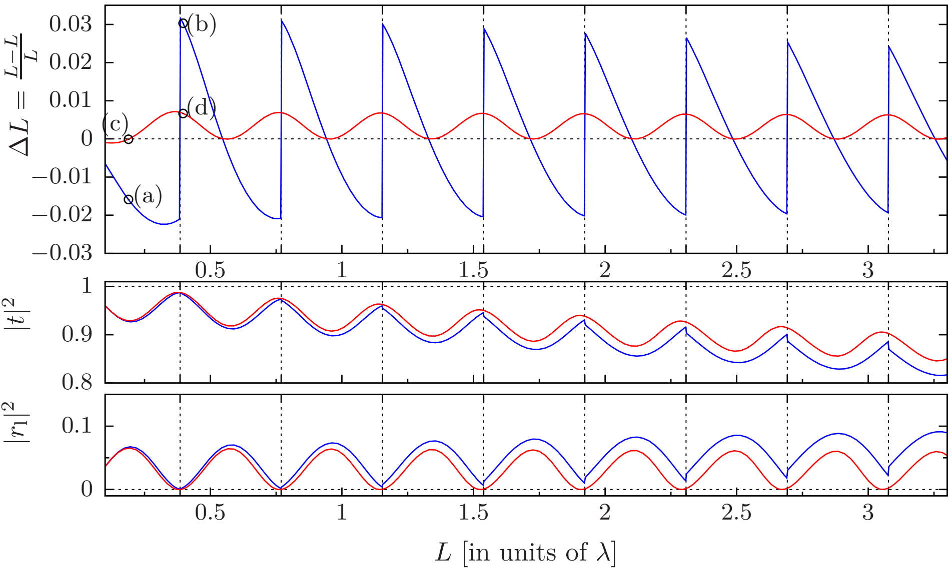

Figure 4.4 Relative length change, transmission $|t|^2$ and reflection $|r_\mathrm{l}|^2$ for a dielectric slab trapped by two plane waves forming a standing wave (blue) or having orthogonal directions of polarization (red lines). The incoming intensities and Young's modulus are related as $I_\mathrm{l} = I_\mathrm{r} = 0.05\mathcal{E}c$, where c is the speed of light in vacuum; the refractive index is chosen as $n = 1.3 + 0.0025i$. The discontinuities in the standing-wave case stem from abrupt jumps in the stable trapping positions at $L = m\lambda/(2\,\mathrm{Re}[n])$, $m \in \mathbb{N}$ (grid lines). The circles indicate the values used for the examples in figure 4.6 and 4.7.

which is found also for computations with $\mathrm{Im}[n] = 0$ and thus is not caused by additional radiation pressure only. However, a glance at the reflectivity and transmission shows that the self consistent deformation prevents configurations with zero reflectivity which would usually result in maximum elongation or compression. For the given standing wave trap we generally observe that deformations computed with the steady state equation (4.39) tend to increase reflectivity and decrease transitivity compared to a homogeneous medium, for both $\mathrm{Im}[n] = 0$ or $\mathrm{Im}[n] \neq 0$.

In figure 4.5 we compare the trap stiffness κ from (4.37) and the trapping position $\widehat{\xi}_0$ from (4.36) between unperturbed and self-consistently deformed objects. We find that the deformation significantly increases the trap stiffness, even if the total size of the object remains unchanged, cf. figure 4.4. An elastic object in a standing wave therefore assists in enforcing its own trap, just like a rabbit who starts to dig when captured in a pit. Note that for a compressible slab in a standing wave there is no critical length of zero trap stiffness, but deformation always leads to a stable trapping position.

Two examples for optical force densities and the associated deformation in the standing wave setup are shown in figure 4.6. There we see that the strain is negative (i.e. the material density is increased) at positions where the force density changes from positive values, denoting a force pushing to the right, to negative values

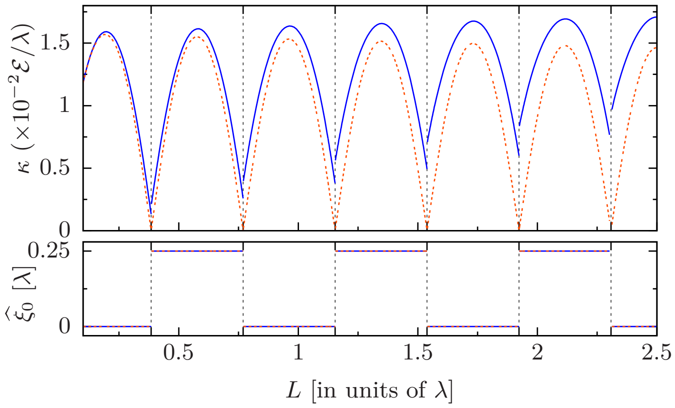

Figure 4.5 Trap stiffness κ (4.37) and stable trapping position $\widehat{\xi}_0 \in \Xi_+$ (4.36) for an object trapped in a standing wave. The same parameters are used as in fig. 4.4, i.e. $I_\mathrm{l} = I_\mathrm{r} = 0.05\mathcal{E}c$ and $n = 1.3 + 0.0025i$. A comparison of the blue curves denoting equilibrium solutions of (4.39) with the orange, dashed lines computed for the homogeneous objects shows that the deformation induced by optical forces significantly increases the total trapping strength. For the given case where $I_\mathrm{l} = I_\mathrm{r}$, the trap positions remain unchanged.

associated with a force pushing to the left. One can clearly see the difference between the compressive situation (a) where the object is trapped at maximal intensity and situation (b), where the trapping occurs at minimal intensity and the object experiences a stretching force.

To trap a dielectric slab with two non-interfering plane waves of orthogonal polarization, the intensities of said beams have to be equal, i.e. $I_\mathrm{l} = I_\mathrm{r}$. In this case there are certain starting lengths $L \simeq (2m+1)/(4\,\mathrm{Re}[n])$, $m \in \mathbb{N}_0$, for which the intensities inside the unperturbed object add up to a constant value. Hence for these specific lengths the dominant gradient forces add up to zero and the object's length remains unchanged. Apart from that we find an expanding behaviour for $L > \lambda/(4\,\mathrm{Re}[n])$, as can also be seen in the examples in figure 4.7.

In the case of non-interfering beams, figure 4.4 also shows that the reflectivity and transitivity is no longer periodic in the object's length L. For the reflectivity we find that the zeros are shifted from $L = m\lambda/(2\,\mathrm{Re}[n])$, $m \in \mathbb{N}$, towards smaller lengths and no longer coincide with lengths of maximal elongation.

4.5.2 Example: object fixed at the left boundary and illuminated by one beam

Figure 4.8 shows the relative length change in the case where the left edge of a dielectric slab is fixed by some external mechanism. Here we observe a striking difference whether the object is illuminated from the left (blue) or right hand side (red curves). In the first case we find only stretching behaviour with minor oscillations of the relative length change ΔL. However, if the object is illuminated from the right hand side (i.e. the beam is incident on the free surface) we again find both

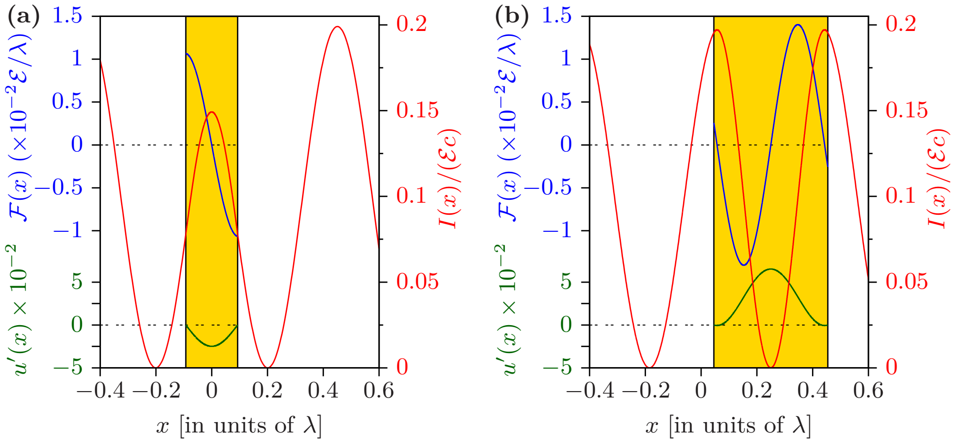

Figure 4.6 Dielectric objects trapped in a standing wave configuration with $I_\mathrm{l} = I_\mathrm{r} = 0.05\mathcal{E}c$. The initial lengths are chosen as $L \simeq 0.19\lambda$ (a) and $L \simeq 0.4\lambda$ (b); $n = 1.3 + 0.0025i$. As mentioned in (4.10), positive strain $u'(x)$ (green curves) denotes larger distances between the particles and hence a reduction of material density. The density is increased at positions where the force density (blue lines) $\mathcal{F}$ is zero and $\mathcal{F}' < 0$, i.e. where the light intensity (depicted red) has a maximum value. As indicated by the marks in figure 4.4 and verifiable from the signs of $u'(x)$, the object on the left gets squeezed whereas the right hand side example shows a stretched object.

compression and elongation, depending on the initial length L.

Furthermore we observe a stronger impact of absorption than for the previous case with two counterpropagating beams. Now we see that if $\mathrm{Im}[n] \neq 0$, then ΔL increases (light incident from the left, radiation pressure pushing the object to the right) or decreases (light incident from the right) for larger initial lengths L. As we see from the dash-dotted lines, the length change continues to oscillate around a constant value also for large values of L, if $\mathrm{Im}[n] = 0$.

For the reflectivity [transmitivity], the self consistent strain again results in a shift of the minimal [maximal] values to the left of $L = m\lambda/(2\,\mathrm{Re}[n])$, $m \in \mathbb{N}$. Note that for the given, asymmetric setup $r_\mathrm{l} \neq r_\mathrm{r}$, but the difference in the total reflectivity $|r_\mathrm{l}|^2 - |r_\mathrm{r}|^2$ remains very low for the given parameters.

To explain the different results for left and right incident beams, we take a closer look at the interface where a single beam exits the slab, e.g. at hand of figure 4.9. Let us assume a beam entering from the left and $I_\mathrm{r} = 0$. Then the intensity is not only constant on the right of the object, but Fresnel's formulae also tell us (for a homogeneous object)

$$\frac{d}{dx}I(L) = 0 \quad \text{and} \quad \frac{d^2}{dx^2}I(L) = k^2 I(L)\left(1 - 2\,\mathrm{Re}[n]^2 + 2\,\mathrm{Im}[n]^2\right) \leq 0, \tag{4.42}$$

and hence the intensity has a local maximum at the edge where the beam exits the slab. For the usually dominant gradient force $\mathcal{F}_\mathrm{gr}(x) \sim \frac{d}{dx}I(x)$ we thus find $\mathcal{F}_\mathrm{gr}(L) = 0$ and $\mathcal{F}_\mathrm{gr} > 0$ left of the surface. Considering the steady state equation (4.39) and

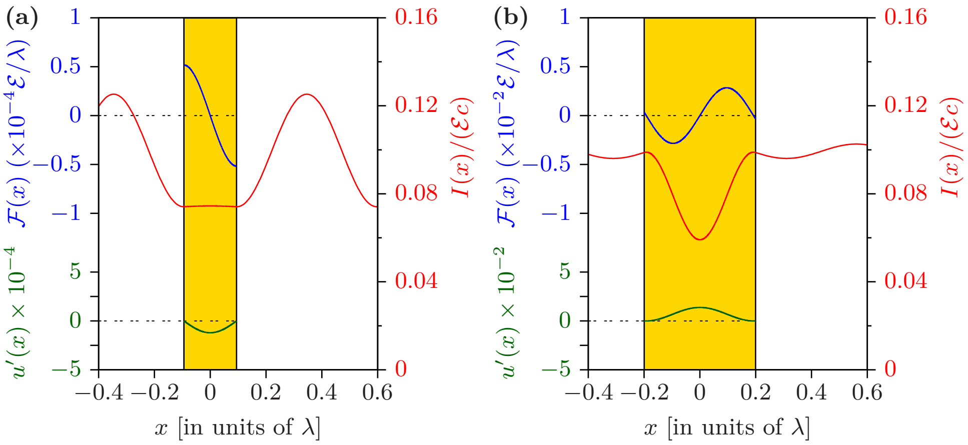

Figure 4.7 Dielectric objects trapped by two counterpropagating beams with orthogonal polarization and $I_{\mathrm{l}} = I_{\mathrm{r}} = 0.05\mathcal{E}c$. As in figure 4.6, the initial lengths are $L \simeq 0.19\lambda$ (a) and $L \simeq 0.4\lambda$ (b); $n = 1.3 + 0.0025i$. As can be seen from figure 4.4, the length of the first example is chosen such that the intensities (red curves) inside the medium almost add up to a constant value. Hence the force densities (blue curves) and the self-consistent deformation (green lines) practically vanish (please note the changed scale on the axes). For the second example we obtain a stretching of $\Delta L \simeq 6.6 \times 10^{-3}$.

omitting the scattering force shows that

$$\mathcal{F}(L) + \mathcal{E}u''(L) \simeq \mathcal{F}_{\mathrm{gr}}(L) + \mathcal{E}u''(L) = 0 \tag{4.43}$$

and hence the strain u' has a local minimum at the right edge $x = L$. If light enters only from the right hand side we find analogous behaviour for the left edge $x = 0$. Since minimal strain corresponds to a maximum in local material density (4.10), we conclude that the gradient force tends to accumulate material at the surface where a single light beam exits the object. A similar statement holds for the aforementioned case with two counterpropagating beams oscillating in orthogonal polarizations, but then one has to add up the forces generated by the two beams.

In total, the constraints on the strain as derived from (4.42), (4.43) and section 4.4 are found as

$$\text{left incidence only}, I_{\mathrm{r}} = 0: \quad u'(0) = \mathcal{F}_{\mathrm{tot}}/\mathcal{E} \geq 0;\ u'(L) = 0 \text{ is a minimum}, \tag{4.44}$$

$$\text{right incidence only}, I_{\mathrm{l}} = 0: \quad u'(0) = \mathcal{F}_{\mathrm{tot}}/\mathcal{E} \leq 0 \text{ is a minimum};\ u'(L) = 0. \tag{4.45}$$

So if $I_{\mathrm{l}} = 0$, the strain is fixed at a minimum with negative value on the left edge, at zero on the right edge, and oscillates proportional to the intensity in between. So in total we find both negative (compressive) and positive (expanding) deformation, depending on the length and refractive index of the object. For $I_{\mathrm{r}} = 0$ we see a positive strain at the left edge and a minimum with $u'(L) = 0$ at the right boundary. Hence the deformations oscillate between zero and some positive value and always lead to a total stretching behaviour.

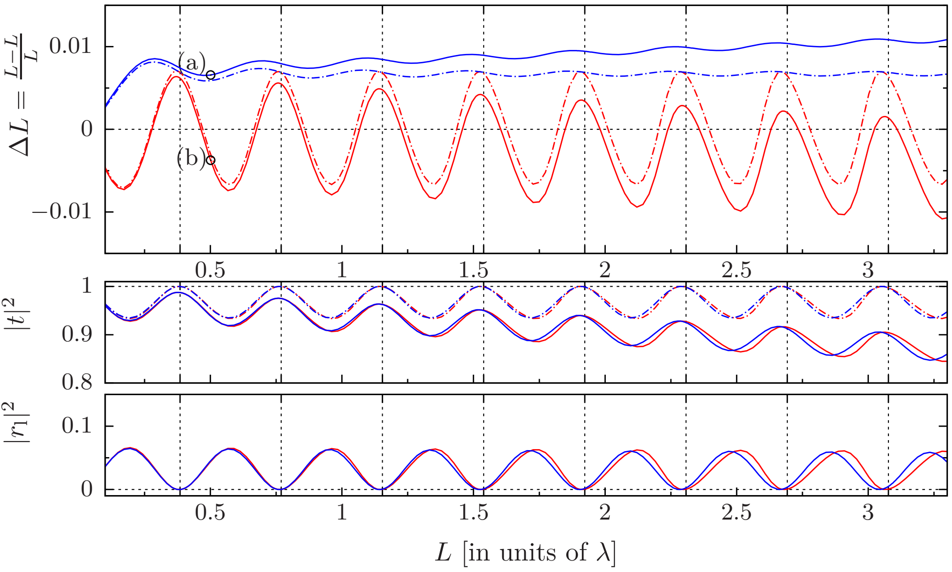

Figure 4.8 Relative length change, transmission $|t|^2$ and left reflection $|r_\mathrm{l}|^2$ for a dielectric slab fixed at the left edge and illuminated by only one beam incident from the left (blue) or right (red curves) hand side, respectively. The initial refractive index is chosen as $n = 1.3 + 0.0025i$, the dash-dotted lines show the results for the non-absorptive case $n = 1.3$ (in the third plot for $|r_\mathrm{l}|^2$ the additional lines were omitted to avoid ambiguity). The beams are of intensity $I_{\mathrm{l,r}} = 0.1\mathcal{E}c$, the circles indicate the values used in figure 4.9. The grid lines mark the locations of the minima [maxima] of the reflectivity [transmitivity] in the homogeneous case at $L = m\lambda/(2\,\mathrm{Re}[n])$, $m \in \mathbb{N}$.

4.5.3 Identifying length changes by probing the reflectivity

As one can see from figures 4.4 and 4.8, the relative length change ΔL obtained for a given ratio of total intensity to Young's modulus can be imperceptibly small, especially if the original length is not chosen in an optimal relation to the vacuum wavelength of the trapping beam, λ. But one possibility to detect minor stretching or squeezing for arbitrary initial lengths can be found in the use of a second, weaker laser probing the change in the reflectivity of the medium: assuming a non-dispersive medium, a probe laser with a vacuum wavelength matching the Fabry-Pérot condition

$$\lambda_\mathrm{p} \simeq \frac{2L\,\mathrm{Re}\,n}{m}, \quad m \in \mathbb{N}, \tag{4.46}$$

will travel through a slab of length L without being reflected, i.e. $|r_\mathrm{h}(\lambda_\mathrm{p})|^2 \simeq 0$. Turning on a powerful laser will deform the object and hence also change the reflectivity for the weak probe beam. Figure 4.10 shows the relative change of reflectivity

$$\delta R = \frac{|r_\mathrm{l}|^2 - |r_\mathrm{h}|^2}{|r_\mathrm{l}|^2 + |r_\mathrm{h}|^2} \tag{4.47}$$

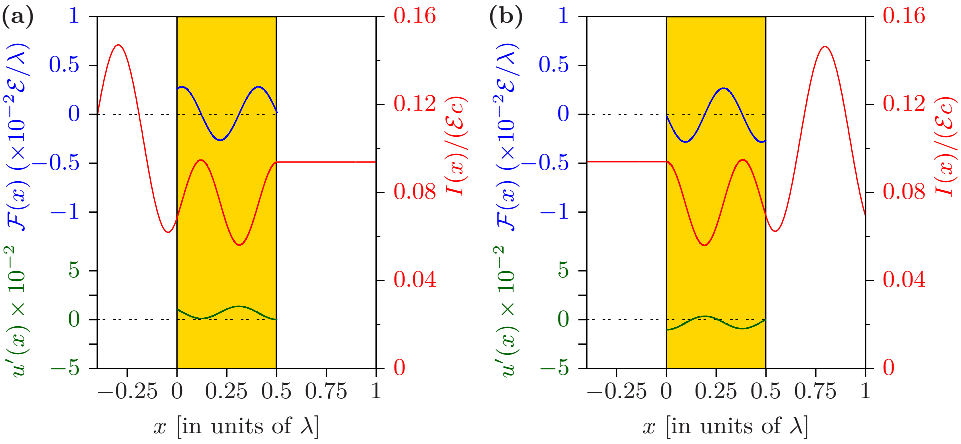

Figure 4.9 Two dielectric objects fixed at the left edge and illuminated from the left (a) or from the right hand side only (b), with $I_{\mathrm{l,r}} = 0.1\mathcal{E}c$. As predicted from (4.42), the intensity (red) is locally maximal and the force densities (blue lines) are (almost) zero at the interface where light exits the slab. For left incidence we observe only positive (i.e. stretching) strain u' (green lines) whereas both elongating and compressive deformation is feasible for right illumination.

between the unperturbed and the strained medium for different wavelengths of the probe laser beam. We can see that as λ_{p} crosses values defined in (4.46), δR changes from negative to positive values if the object is compressed (i.e. $\Delta L < 0$) and vice versa if $\Delta L > 0$.

4.6 Estimating the deformation by computing the photon momentum transfer on a surface

There exist numerous experimental and theoretical papers reporting optical stretching of deformable objects, such as biological cells (Guck *et al.* 2001; Rancourt-Grenier *et al.* 2010), or light induced outward bending of liquid-gas surfaces (Ashkin *et al.* 1973; Casner *et al.* 2001). In the mentioned publications, the light-induced deformation is estimated by considering an effective photon momentum change at the transition from one medium to another. In this context, the optical forces emerge as surface forces, acting on the interface between two regions of different refractive index. Since the considered materials are incompressible, the refractive index in each region remains constant.

Let us try here a similar approach to estimate the deformation of an elastic object and put our results in context with these earlier works. But note that the very different physical properties of a linear elastic medium as compared to incompressible water, plane waves instead of Gaussian beams and a wave description instead of geometric optics, do not allow a straightforward comparison of the results. But nevertheless we can investigate whether our findings based on a volumetric description of optical

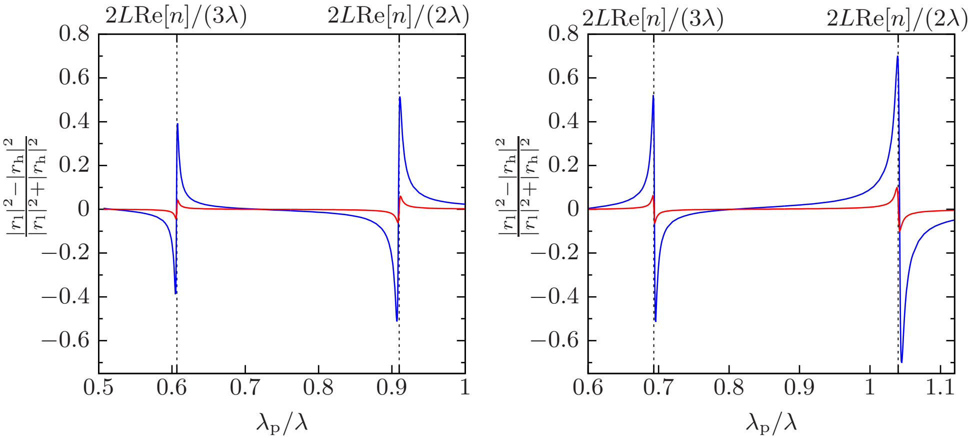

Figure 4.10 Relative change in the reflectivity of a strained object for different probe laser wavelengths λ_p, for slabs trapped in a standing wave pattern with $I_\mathrm{l} = I_\mathrm{r} = 0.0005\mathcal{E}c$ (red) and $I_\mathrm{l} = I_\mathrm{r} = 0.005\mathcal{E}c$ (blue curves), $n = 1.3 + 0.0025i$. In the left frame we used an initial length $L = 0.7\lambda$ and obtained compressive behaviour with $\Delta L \simeq -0.2 \times 10^{-3}$ (red) and $\Delta L \simeq -2.0 \times 10^{-3}$ (blue). The results on the right indicate stretching with $\Delta L \simeq 0.3 \times 10^{-3}$ (red) and $\Delta L \simeq 3.1 \times 10^{-3}$ (blue) for $L = 0.8\lambda$.

forces are compatible with a concept of surface forces due to photon momentum exchange.

Following the line of (Ashkin *et al.* 1973; Guck *et al.* 2001; Rancourt-Grenier *et al.* 2010) one estimates the time averaged force per area on an interface separating two regions with different indices of refraction $n_1 \neq n_2 \in \mathbb{R}$ and fields $E(x) = A\exp(in_1kx) + B\exp(-in_1kx)$, $x \leq 0$, and $E(x) = C\exp(in_2kx)$, $x > 0$, as

$$F_{1,2} = \frac{\Delta p}{\Delta t} = \frac{I_\mathrm{inc}(p_1(1+R) - p_2T)}{\hbar kc}. \tag{4.48}$$

Here $I_\mathrm{inc} = n_1c\varepsilon_0|A|^2/2$ is the total energy-flux density entering the system, $R = |B|^2/|A|^2$ and $T = n_2|C|^2/(n_1|A|^2)$ is the reflected and transmitted fraction the energy-flux and $p_i = \hbar kn_i$ describes the momentum of a single photon in a medium with index n_i, $i = 1, 2$. As in (Ashkin *et al.* 1973; Guck *et al.* 2001; Rancourt-Grenier *et al.* 2010) we here used Minkowski's version of the momentum of light in dielectric media. Out of curiosity about simple but puzzling arguments on stretching or compression of media in connection with the Abraham-Minkowski controversy (Ashkin *et al.* 1973; Barnett *et al.* 2010; Mansuripur 2010; Pfeifer *et al.* 2007) we also included results computed by naively inserting Abraham's result for the photon momentum, $p_i = \hbar k/n_i$, in figure 4.11. One must note, however, that Abraham's stress tensor would also require a material tensor component. A thorough calculation should always give the same results, independent of the used version of stress tensor (Barnett *et al.* 2010; Pfeifer *et al.* 2007).

Neglecting internal reflections, the force on an extended object with index n_2 embedded in a medium n_1 and subjected to a single beam is estimated to give

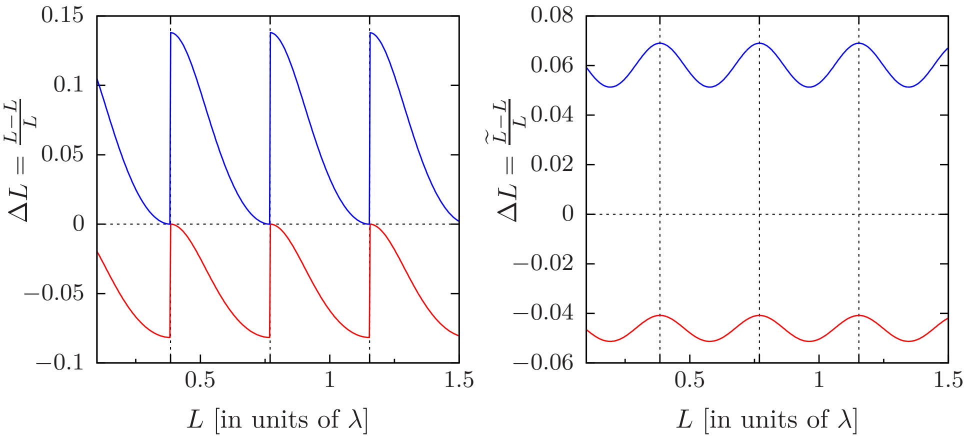

Figure 4.11 Expected deformation due to the change in photon momentum at the interfaces between vacuum and a homogeneous dielectric of refractive index $n = 1.3$, as obtained from (4.50). For the blue lines we used Minkowski's photon momentum $p = \hbar kn$, the red curves are computed using Abraham's $p = \hbar k/n$. The left figure shows the situation where a homogeneous object is trapped by a sanding wave with $I_\mathrm{l} = I_\mathrm{r} = 0.05\mathcal{E}c$. As in figure 4.4, the deformation changes abruptly, if the object switches from a low-field to a high-field seeking behaviour. The right hand figure depicts the relative length change for an object illuminated from only one side with $I_\mathrm{l} = 0.1\mathcal{E}c$, $I_\mathrm{r} = 0$. In both situations we find that Minkowski's momentum only leads to stretching, whereas the naive adaption of Abraham's photon momentum would solely result in compression.

$F_\mathrm{tot} = F_{1,2} + TF_{2,1}$. The deformation of such an object is then simply the difference in the two forces on the surfaces, reading $F_\mathrm{def} = TF_{2,1} - F_{1,2}$. Assuming a linear elastic medium with Young's modulus $\mathcal{E}$, the relative length-change can be estimated by $\Delta L = F_\mathrm{def}/\mathcal{E}$. For the values used in the previous examples $n_1 = 1$, $n_2 = 1.3$, $I_0 = 0.1\mathcal{E}c$, we obtain $\Delta L \simeq 0.059$ when using Minkowski's momentum and $\Delta L \simeq -0.046$ for Abraham. These deformations have about the same order of magnitude as our full self-consistent computations, depicted e.g. in figure 4.8, but do not depend on the length of the object.

Formally one can refine these calculations from (4.48) and include also light incident from the right such that $E(x) = C\exp(in_2kx) + D\exp(-in_2kx)$, $x > 0$ to obtain

$$F_{1,2} = \frac{\varepsilon_0 n_1 p_1}{2\hbar k}\left(|A|^2 + |B|^2\right) - \frac{\varepsilon_0 n_2 p_2}{2\hbar k}\left(|C|^2 + |D|^2\right). \tag{4.49}$$

For $D = 0$ this reduces to (4.48) and for $n_1 = n_2 = 1$ and $p_1 = p_2 = \hbar k$ we recover the force derived previously with the Maxwell stress tensor (4.27). This allows us to formulate a generic wave optics extension for the deformation estimated above in the scope of geometric optics, now also including size dependent reflection and transmission. The total deformation pressure on an object with length L and homogeneous refractive index $n \in \mathbb{R}$ surrounded by vacuum then reads

$$F_{\mathrm{def}} = \frac{\varepsilon_0 n p_n}{\hbar k} \left(|G|^2 + |H|^2\right) - \frac{\varepsilon_0}{2} \left(|A|^2 + |B|^2 - |C|^2 - |D|^2\right) \tag{4.50}$$

where the amplitudes inside the medium are computed using Fresnel's relations $G = ((n+1)A + (n-1)B)/(2n)$, $H = ((n-1)A + (n+1)B)/(2n)$, the amplitudes outside are connected by the homogeneous reflection and transmission coefficients (4.24), $B = r_{\mathrm{h}} A + t_{\mathrm{h}} D$, $C = t_{\mathrm{h}} A + r_{\mathrm{h}} D$, and the incoming A and D are given in (4.22). As expected, a similar calculation for the total force F_{tot} gives the same result as we obtained previously in (4.34).

The resulting relative length change $\Delta L = F_{\mathrm{def}}/\mathcal{E}$ is presented in figure 4.11. There we find that the estimations using optical surface forces even qualitatively differ from the results we obtained with the present description using the full, volumetric optical forces, cf. figures 4.4 or 4.8, even if the force on the surface is adapted to include interference due to internal reflections.

An intuitive example is the object of length $L = \lambda/(2n)$ where $r_{\mathrm{h}} = 0$ and $t_{\mathrm{h}} = 1$. In a standing wave trap with $I_l = I_r$ this object is then trapped at $\xi_0 = x_0 + (\phi_{\mathrm{l}} - \phi_{\mathrm{r}})/(2k) = 0$, cf. section 4.3.2 or figure 4.5. Using Minkowski's $p_n = \hbar k n$ we then find that the force due to photon momentum transfer vanishes at each surface and hence $\Delta L = 0$ in figure 4.11.

But from the examples in figure 4.6 we deduce that the intensity at the *surface* is zero, yet the object will contract due to the intensity maximum at its central position. This is because the dipole force pulls each volume element towards the next local maximum of intensity, regardless of whether this volume element is located at the surface or in the bulk of the medium.

In fact, none of our calculations or simulations showed any distinctive effects suggesting a surface force at the boundaries of a dielectric (Sonnleitner *et al.* 2011). This is supported by computations on large but finite stacks of polarizable slices where the forces on the first or last slice qualitatively do not differ from those on the second or next to last, respectively. We therefore conclude that optical forces have to be treated as real volumetric forces (Mansuripur 2010; Rinaldi *et al.* 2002) and that a description using the change of photon momentum at the surface of a medium is inappropriate, regardless of using Abraham's or Minkowski's momentum.

4.7 Conclusions

Using an implicit calculation of optical fields and forces allows to self-consistently determine the stationary local deformations of an elastic object, where the local stress balances the local light forces by elastic back action. These solutions show a surprisingly variable and nonlinear dependence on the chosen parameters. Generally we see a length and illumination dependent, spatially quasiperiodic strain pattern, which can lead to length stretching as well as compression. As expected, standing wave configurations yield the strongest forces and effective length changes with a clear resonant structure for special ratios of initial object length L and trap beam wavelength λ. In the standing wave setup, variations in the trap wavelength λ lead to discrete jumps of the stable trapping positions. At $L = m\lambda/(2\,\mathrm{Re}[n])$, $m \in \mathbb{N}$, the particle switches from a position centred around an intensity maximum to one around a field node, which is associated with changes from compression to elongation of the object. Interestingly, in particular close to these instability points, this generally leads to an increase in trap stiffness. We expect that this indicates possible bistability between high and low field seeking behaviour for certain lengths very close to $L = m\lambda/(2\,\mathrm{Re}[n])$.

Although the calculations presented here were performed in the scope of elastic media, we believe that the model can be extended to deformable but incompressible media like water or even dilute gases. Here in particular stability thresholds for the homogeneous solutions should prove physically very interesting, as they could lead to stationary flows, periodic density oscillations or light induced density pattern formation and particle ordering in a gas.

Here we limited our considerations to the case, where a steady state solution can be found. As for other nonlinear dynamical effects (Asbóth *et al.* 2008), there are of course regions in parameter space, were no stationary solutions exist and we find self sustained oscillations or even disintegration of the material. Indications of this behaviour appear e.g. in a non-converging iteration procedure. At this point we leave this to future work.

Acknowledgements

We thankfully acknowledge support via ERC Advanced Grant (catchIT, 247024) and the Austrian Science fund FWF grant S4013.

Appendix 4.A General features of transfer matrices

In equation (4.3) we already used the concept of a transfer matrix to couple the plane wave amplitudes left and right of a beam splitter. Let us generally define the set of transfer matrices as

$$\mathcal{T} := \left\{ \mathrm{T} \in \mathbb{C}^{2\times 2} \;\middle|\; \exists\, r_1, r_2, t \in \mathbb{C} : \mathrm{T} = \frac{1}{t}\begin{pmatrix} t^2 - r_1 r_2 & r_2 \\ -r_1 & 1 \end{pmatrix} \equiv \mathrm{T}(r_1, r_2, t) \right\}. \tag{4.51}$$

One can easily show that $\mathrm{T}_1 \cdot \mathrm{T}_2 \in \mathcal{T}$ for all $\mathrm{T}_1, \mathrm{T}_2 \in \mathcal{T}$ and $\cdot$ here denoting the usually omitted matrix multiplication. Since also

$$[\mathrm{T}(r_1, r_2, t)]^{-1} = \frac{1}{t}\begin{pmatrix} 1 & r_1 \\ -r_2 & t^2 - r_1 r_2 \end{pmatrix} \in \mathcal{T} \tag{4.52}$$

we conclude that $(\mathcal{T}, \cdot)$ is a group.

To motivate definition (4.51), let us consider two plane waves $E_\mathrm{l}(x) = A\exp(ik(x)) + B\exp(-ik(x))$, $x \le 0$, and $E_\mathrm{r}(x) = C\exp(ik(x-L)) + D\exp(-ik(x-L))$, $x \ge L$, left and right of a dielectric with a homogeneous refractive index n. Hence their amplitudes are coupled as

$$\begin{pmatrix} C \\ D \end{pmatrix} = \mathrm{S}_{n,1} \cdot \mathrm{P}_{nL} \cdot \mathrm{S}_{1,n} \begin{pmatrix} A \\ B \end{pmatrix}. \tag{4.53}$$

where S_{n_1,n_2} couples the amplitudes at the intersection from a region with refractive index n_1 to a region with index n_2 and P_d denotes the propagation matrix over a distance d, i.e.

$$\mathrm{S}_{n_1,n_2} = \frac{1}{2n_2} \begin{pmatrix} n_2 + n_1 & n_2 - n_1 \\ n_2 - n_1 & n_2 + n_1 \end{pmatrix} \quad \text{and} \quad \mathrm{P}_d = \begin{pmatrix} e^{ikd} & 0 \\ 0 & e^{-ikd} \end{pmatrix}. \tag{4.54}$$

One can easily show that $\mathrm{S}_{n,1} \cdot \mathrm{P}_{nL} \cdot \mathrm{S}_{1,n} = \mathrm{T}(r_\mathrm{h}, r_\mathrm{h}, t_\mathrm{h})$, with r_h and t_h as given in (4.24). But the attempt to construct a total transfer matrix for stacked media such as $\mathrm{S}_{n_K,1} \cdot \mathrm{P}_{n_K d_K} \cdot \mathrm{S}_{n_{K-1},n_K} \cdots \mathrm{S}_{n_2,n_1} \cdot \mathrm{P}_{n_1 d_1} \cdot \mathrm{S}_{1,n_1}$ with arbitrary n_i, d_i, $i = 1, \ldots, K$, will show that one reflection coefficient is not enough. However, such a system can be described by a more general $T(r_1, r_2, t) \in \mathcal{T}$ such that $B = r_1 A + tD$ and $C = r_2 D + tA$.

Appendix 4.B Analytical approximations for electric fields and forces for small deformations

In section 4.2 and in an earlier work (Sonnleitner *et al.* 2011) we showed that for equally spaced slices the amplitudes of the electric fields are related as $(A_{j+1}, B_{j+1})^T = {\mathrm{T}_\mathrm{h}}^j (A_1, B_1)^T$, with $\mathrm{T}_\mathrm{h} := \mathrm{P}_{d_0} \mathrm{M}_\mathrm{BS}$. Choosing the coupling ζ as in (4.6), the eigenvalues of T_h read $\exp(\pm inkd_0)$. This leads to

$$\lim_{N\to\infty} {\mathrm{T}_\mathrm{h}}^{j-1} =: \mathrm{T}(x) = \frac{1}{2n} \begin{pmatrix} f(-x) + g(-x) & f(x) - g(x) \\ f(-x) - g(-x) & f(x) + g(x) \end{pmatrix} \tag{4.55}$$

where $x = \lim_{N\to\infty} L(j-1)/(N-1)$ and

$$\begin{aligned} f(x) &= n\cos(nkx) - i\sin(nkx), \\ g(x) &= n\cos(nkx) - in^2\sin(nkx). \end{aligned} \tag{4.56}$$

Allowing small local density variations $\tilde{d}_j - d_0 = \Delta_j$ we may use $\mathrm{P}_{d_j} \simeq \mathrm{P}_{d_0} + ik\Delta_j \sigma_z \mathrm{P}_{d_0}$ to expand the relation between the field amplitudes from (4.4) as

$$\begin{pmatrix} A_{j+1} \\ B_{j+1} \end{pmatrix} \simeq \left[{\mathrm{T}_\mathrm{h}}^j + ik \sum_{m=1}^{j} \Delta_m {\mathrm{T}_\mathrm{h}}^{j-m} \sigma_z {\mathrm{T}_\mathrm{h}}^m \right] \begin{pmatrix} A_1 \\ B_1 \end{pmatrix}, \tag{4.57}$$

where $\sigma_z = \mathrm{diag}(1, -1)$. In the limit of infinitely many slices within a finite length L, the sum above can be rewritten to an integral and we obtain

$$\begin{pmatrix} A(x) \\ B(x) \end{pmatrix} \simeq \left[\mathrm{T}(x) + ik \int_0^x u'(y) \mathrm{T}(x-y) \sigma_z \mathrm{T}(y) \, \mathrm{d}y \right] \begin{pmatrix} A(0) \\ B(0) \end{pmatrix}. \tag{4.58}$$

Since $\lim_{N\to\infty} \mathrm{M}_{\mathrm{BS}} = \mathrm{id}_2$, the total reflection and transmission coefficients for the displaced object can be read off and expanded in linear order of u' from equations (4.5) and (4.58)

$$\begin{aligned} t &\simeq t_{\mathrm{h}} + \frac{2ik}{(f(L)+g(L))^2} \int_0^L u'(y)\,(f(y)f(L-y)+g(y)g(L-y))\,\mathrm{d}y, \\ r_{\mathrm{l}} &\simeq r_{\mathrm{h}} + \frac{2ik}{(f(L)+g(L))^2} \int_0^L u'(y)\left(f(L-y)^2-g(L-y)^2\right)\mathrm{d}y, \\ r_{\mathrm{r}} &\simeq r_{\mathrm{h}} + \frac{2ik}{(f(L)+g(L))^2} \int_0^L u'(y)\left(f(y)^2-g(y)^2\right)\mathrm{d}y. \end{aligned} \tag{4.59}$$

Here r_{h} and t_{h} denote the reflection and transmission amplitudes of a homogeneous medium with length L and refractive index n, as given in (4.24). As mentioned in section 4.2.1 we find that symmetric local strain, i.e. $u'(x) = u'(L-x)$, $x \in [0, L]$, results in $r_{\mathrm{l}} \simeq r_{\mathrm{r}}$ and antisymmetric strain gives $t \simeq t_{\mathrm{h}}$ and $r_{\mathrm{l}} - r_{\mathrm{h}} \simeq r_{\mathrm{h}} - r_{\mathrm{r}}$.

Using the reflection and transmission amplitudes from (4.59) to replace $B(0) = r_{\mathrm{l}}A(0) + tD(L)$ in (4.58) leads to analytical approximations for the local field amplitudes inside a deformed medium

$$\begin{aligned} A(x) &\simeq a_{\mathrm{h}}(x) + \int_0^x u'(y)a_{\mathrm{x}}(x,y)\,\mathrm{d}y + \int_0^L u'(y)a_{\mathrm{L}}(x,y)\,\mathrm{d}y, \\ B(x) &\simeq b_{\mathrm{h}}(x) + \int_0^x u'(y)b_{\mathrm{x}}(x,y)\,\mathrm{d}y + \int_0^L u'(y)b_{\mathrm{L}}(x,y)\,\mathrm{d}y, \end{aligned} \tag{4.60}$$

with the individual terms reading

$$\begin{aligned} a_{\mathrm{h}}(x) &= \frac{A_0(f(L-x)+g(L-x)) + D_L(f(x)-g(x))}{f(L)+g(L)}, \\ b_{\mathrm{h}}(x) &= \frac{A_0(f(L-x)-g(L-x)) + D_L(f(x)+g(x))}{f(L)+g(L)}, \\ a_{\mathrm{x}}(x,y) &= \frac{ik}{n(f(L)+g(L))}\Big(A_0(f(L-y)f(y-x)+g(L-y)g(y-x)) + \\ &\qquad + D_L(f(y)f(y-x)-g(y)g(y-x))\Big), \\ b_{\mathrm{x}}(x,y) &= \frac{-ik}{n(f(L)+g(L))}\Big(A_0(f(L-y)f(x-y)-g(L-y)g(x-y)) + \\ &\qquad + D_L(f(y)f(x-y)+g(y)g(x-y))\Big), \\ a_{\mathrm{L}}(x,y) &= \frac{ik(f(x)-g(x))}{n(f(L)+g(L))^2}\Big(A_0(f(L-y)^2-g(L-y)^2) + \\ &\qquad + D_L(f(y)f(L-y)+g(y)g(L-y))\Big), \\ b_{\mathrm{L}}(x,y) &= \frac{ik(f(x)+g(x))}{n(f(L)+g(L))^2}\Big(A_0(f(L-y)^2-g(L-y)^2) + \\ &\qquad + D_L(f(y)f(L-y)+g(y)g(L-y))\Big). \end{aligned} \tag{4.61}$$

The functions f and g are given in (4.56), the amplitudes at the boundary $A_0 \equiv A(0)$ and $D_L \equiv D(L)$ are determined by the incoming intensities and the displacement and can be read off from (4.22).

To obtain an approximation for the forces we use (4.28), take the limit $\mathcal{F}(x) := \lim_{N\to\infty} NF_j/L$ with $\lim_{N\to\infty} N\zeta/L = k(n^2-1)/2$ and insert the amplitudes from (4.60) to find

$$\begin{aligned} \mathcal{F}(x) &= \tfrac{k\varepsilon_0}{2} \operatorname{Im}\left\{(n^2-1)\big(A(x)+B(x)\big)\big(A(x)-B(x)\big)^*\right\} \\ \mathcal{F}(x) &\simeq \mathcal{F}_{\mathrm{h}}(x) + \int_0^x u'(y)\mathcal{F}_{\mathrm{x}}(x,y)\,\mathrm{d}y + \int_0^L u'(y)\mathcal{F}_{\mathrm{L}}(x,y)\,\mathrm{d}y, \end{aligned} \tag{4.62}$$

where

$$\begin{aligned} \mathcal{F}_{\mathrm{h}}(x) =\ & \tfrac{2k\varepsilon_0}{|(f(L)+g(L)|^2} \operatorname{Im}\Big\{(n^2-1)\big(A_0 f(L-x) + D_L f(x)\big)\times \\ & \qquad\qquad\qquad \times\big(A_0 g(L-x) - D_L g(x)\big)^*\Big\} \\ \mathcal{F}_{\mathrm{x}}(x) =\ & \tfrac{k\varepsilon_0}{2} \operatorname{Im}\Big\{(n^2-1)\Big[\big(a_{\mathrm{h}}(x)-b_{\mathrm{h}}(x)\big)^*\big(a_{\mathrm{x}}(x,y)+b_{\mathrm{x}}(x,y)\big)+ \\ & \qquad\qquad + \big(a_{\mathrm{h}}(x)+b_{\mathrm{h}}(x)\big)\big(a_{\mathrm{x}}(x,y)-b_{\mathrm{x}}(x,y)\big)^*\Big]\Big\} \\ \mathcal{F}_{\mathrm{L}}(x) =\ & \tfrac{k\varepsilon_0}{2} \operatorname{Im}\Big\{(n^2-1)\Big[\big(a_{\mathrm{h}}(x)-b_{\mathrm{h}}(x)\big)^*\big(a_{\mathrm{L}}(x,y)+b_{\mathrm{L}}(x,y)\big)+ \\ & \qquad\qquad + \big(a_{\mathrm{h}}(x)+b_{\mathrm{h}}(x)\big)\big(a_{\mathrm{L}}(x,y)-b_{\mathrm{L}}(x,y)\big)^*\Big]\Big\} \end{aligned} \tag{4.63}$$

with the terms a_{X} and b_{X} as given above in (4.61).

Just like the field amplitudes in (4.60) and the reflection and transmission coefficients in (4.59), the above result is only an approximation for the case of small deformation u'. That is, we neglect products of $\Delta_l\Delta_m$ in (4.57) and hence also correlations of type $\iint u'(y_1)u'(y_2)\ldots \mathrm{d}y_1\mathrm{d}y_2$. But a comparison of the approximated results in the continuous limit with solutions of the wave equation (4.20) or numerical computations for a large but finite number of beam splitters confirmed that this first order expansion is sufficient for the scope of parameters used in this work.

5 Preprint

Scattering approach to two-colour light forces and self-ordering of polarizable particles

S. Ostermann, M. Sonnleitner* and H. Ritsch

Collective coherent scattering of laser light by an ensemble of polarizable point particles creates long-range interactions, whose properties can be tailored by choice of injected laser powers, frequencies and polarizations. We use a transfer matrix approach to study the forces induced by non-interfering fields of orthogonal polarization or different frequencies in a 1D geometry and find long-range self-ordering of particles without a prescribed order. Adjusting laser frequencies and powers allows tuning of inter-particle distances and provides a wide range of possible dynamical couplings not accessible in usual standing light wave geometries with prescribed order. In this work we restrict the examples to two frequencies and polarisations but the framework also allows to treat multicolour light beams with random phases. These dynamical effects should be observable in existing experimental setups with effective 1D geometries such as atoms or nanoparticles coupled to the field of an optical nanofibre or transversely trapped in counterpropagating Gaussian beams.

arXiv: 1310.6246v3 [quant-ph] (2013)
Accepted for publication in *New Journal of Physics*

---

[*] The author of the present thesis contributed to this work primarily in an intensive advisory role, discussing the model, the computational methods and the scientific conclusions. All the primary calculations and simulations were performed by S. Ostermann.

5.1 Introduction

Coherent interference of light scattered from different particles in an extended ensemble of polarizable, point-like particles leads to important modifications of the forces on the particles as well as to new inter-particle light-forces, even if the light fields are far detuned from any optical resonance (Bender *et al.* 2010; Courteille *et al.* 2010). While a full 3-D treatment certainly leads to a very rich and complex dynamics (Douglass *et al.* 2012), key physical effects can already by discussed in effective 1D geometries. One particularly interesting example are atoms in or close to 1D optical micro structures (Vetsch *et al.* 2010; Zoubi *et al.* 2010) as e.g. an optical nanofibre, where even a single atom can strongly modify light propagation and forces (Domokos *et al.* 2002; Horak *et al.* 2003). In a milestone experiment Rauschenbeutel and coworkers recently managed to trap cold atoms alongside a tapered optical fibre (Vetsch *et al.* 2010) and related setups predict and demonstrate strong back-action and inter-particle interaction (Chang *et al.* 2012a; Goban *et al.* 2012; Lee *et al.* 2013) leading to the formation of periodical self-ordered arrays (Chang *et al.* 2013; Grießer *et al.* 2013). Alternatively, in free space interesting dynamical effects of collective light scattering were recently predicted and studied in standard 1D optical lattices of sufficient optical density (Asbóth *et al.* 2008; Deutsch *et al.* 1995). One could also consider arrays of optical membranes to study such effects.

In this work we extend an existing model (Asbóth *et al.* 2008; Deutsch *et al.* 1995; Sonnleitner *et al.* 2011, 2012) towards light configurations with multiple frequencies and polarizations of the fields illuminating the particles. In particular, this includes a new class of geometries where crystalline order can be dynamically generated and sustained even without prescribing a standing wave lattice geometry. As a generic example the polarizations of two counter-propagating fields can be chosen orthogonally, such that incident and scattered fields do not directly interfere. Light scattering thus occurs for both fields independently and the forces on the particles can simply be added up. However, any structure forming by the scattering of one field component will be seen by all other fields and thus change their scattering properties and the induced forces. On the one hand this mediates nonlinear interaction between the different fields while on the other hand it generates inter particle interactions throughout the sample, inducing a wealth of nonlinear complex dynamical effects. Besides such dynamic self-ordering phenomena, we also study the possibilities to induce tailored long-range interactions via multicolour illumination and collective scattering of particles trapped in prescribed optical lattice potentials.

This work is organized as follows: First we introduce the basic definitions and dynamical equations of the well-established generalized multiple scattering model for light forces (Asbóth *et al.* 2008; Deutsch *et al.* 1995; Sonnleitner *et al.* 2011, 2012) and extend this framework to support multiple polarizations and frequencies. This formalism is then applied to an orthogonal beam trap consisting of an array of particles modelled as beam splitters irradiated by two counter-propagating beams of orthogonal polarization and possibly different wavenumbers, cf. figure 5.1a. For two beam splitters we analytically derive conditions for the intensity ratios and

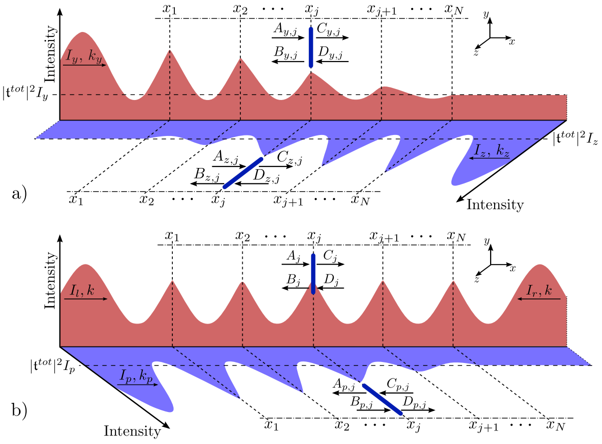

Figure 5.1 Sketch of the intensity distribution of two light fields of orthogonal polarization and different colour propagating through a 1D array of thin beam splitters located at positions $x_1, \ldots, x_N$. The upper graph (a) shows illumination from two sides with beams of orthogonal polarization, while the lower graph (b) shows a symmetric standing wave trap (red) perturbed by an extra field with orthogonal polarization (blue).

wavenumbers to trap or stabilize them at a given separation. These results are then numerically extended to higher particle numbers.

As a generalization and connection to usual experimental setups for optical lattices we then analyze how an additional beam polarized orthogonally to a prescribed standing wave perturbs the trapped particles and induces peculiar interaction patterns in 1D optical lattices, cf. figure 5.1b.

5.2 Multiple scattering approach to multicolour light propagation in linearly polarizable media

It is now well established that propagation of far detuned light through a one dimensional atomic lattice or an array of dielectric membranes can be well described in a plane wave approximation with multiple scattering by a corresponding series of beam splitters (Asbóth *et al.* 2008; Deutsch *et al.* 1995; Sonnleitner *et al.* 2011, 2012). A very analogous situation arises when the light is transversely strongly confined by optical structures so that scattering dominantly occurs along a preferred direction.

The spatial dynamics of the electric field $E(x,t) = E(x)\exp(-i\omega t)$ is then described by the 1D Helmholtz-equation

$$\left(\partial_x^2 + k^2\right) E(x) = -2k\zeta\, E(x) \sum_{j=1}^{N} \delta(x - x_j), \tag{5.1}$$

where N denotes the total number of beam splitters at positions $x_1, \ldots, x_N$; $\zeta := k\eta\alpha/(2\varepsilon_0)$ is a dimensionless parameter proportional to the atomic polarizability α, the wavenumber $k = \omega/c$ and the density of particles combined to a single beam splitter, η. The plane wave solution between two beam splitters, $x \in (x_j, x_{j+1})$, then reads

$$E(x) = C_j e^{ik(x-x_j)} + D_j e^{-ik(x-x_j)} \equiv A_{j+1} e^{ik(x-x_{j+1})} + B_{j+1} e^{-ik(x-x_{j+1})}, \tag{5.2}$$

the amplitudes A_j, B_j left and C_j, D_j right of the beam splitter at position x_j (cf. figure 5.1) are related by the linear transformation matrix M_{BS}, with

$$\begin{pmatrix} C_j \\ D_j \end{pmatrix} = \begin{pmatrix} 1+i\zeta & i\zeta \\ -i\zeta & 1-i\zeta \end{pmatrix} \begin{pmatrix} A_j \\ B_j \end{pmatrix} =: M_{BS} \cdot \begin{pmatrix} A_j \\ B_j \end{pmatrix}. \tag{5.3}$$

From (5.2) we read off the propagation matrix

$$\begin{pmatrix} A_{j+1} \\ B_{j+1} \end{pmatrix} = \begin{pmatrix} e^{ik(x_{j+1}-x_j)} & 0 \\ 0 & e^{-ik(x_{j+1}-x_j)} \end{pmatrix} \begin{pmatrix} C_j \\ D_j \end{pmatrix} =: M_p(x_{j+1}-x_j) \cdot \begin{pmatrix} C_j \\ D_j \end{pmatrix} \tag{5.4}$$

The values of the electric fields then are fixed by the incoming beam amplitudes A_1 and D_N. The total reflection and transmission coefficients are calculated from the total transfer matrix of the setup and give the remaining amplitudes at the boundaries as $B_1 = \mathfrak{r}_1^{tot} A_1 + \mathfrak{t}^{tot} D_N$ and $C_N = \mathfrak{r}_2^{tot} A_1 + \mathfrak{t}^{tot} D_N$ self-consistently (Sonnleitner *et al.* 2012). Using Maxwell's stress tensor (Jackson 1999) yields the time averaged force per unit area on the jth beam splitter as (Asbóth *et al.* 2008)

$$\mathcal{F}_j = \frac{\epsilon_0}{2} \left(|A_j|^2 + |B_j|^2 - |C_j|^2 - |D_j|^2 \right). \tag{5.5}$$

This simple but powerful formalism to calculate the fields and forces on single atoms, atom clouds or other dielectric media such as membranes or elastic dielectrics allows to describe complex dynamics such as self-organization or even laser cooling in any effective 1D geometry (Chang *et al.* 2012b; Ni *et al.* 2012; Xuereb *et al.* 2009; Xuereb *et al.* 2012).

Previous approaches were limited to a single frequency and polarization in a counter-propagating geometry. Here we show that it is straightforward to generalize the beam splitter method to allow for multiple frequencies and polarizations. The field propagating in the x-direction shall then be written as

$$\mathbf{E}(x,t) = E_y(x) \exp(-i\omega_y t) \mathbf{e}_y + E_z(x) \exp(-i\omega_z t) \mathbf{e}_z, \tag{5.6}$$

where $E_y(x)$ $[E_z(x)]$ is defined as the component polarized in the direction of $\mathbf{e}_y$ $[\mathbf{e}_z]$ oscillating with frequency $\omega_y = k_y c$ $[\omega_z = k_z c]$. We want to emphasize that writing the total field as a sum of linearly polarized fields in (5.6) is an arbitrary choice. None of the upcoming conclusions would change if we chose another orthogonal basis system (e.g. circular polarizations).

The main assumption of this work is that the particles do not scatter photons from one mode into the other. As long as this is fulfilled, the beam splitter model can be employed for each component independently. This assumption is obviously correct if the beam splitters are made of non-birefringent materials as they are used in many optomechanical experiments.

If the beam splitters are assumed to be single atoms one has to take additional care as these typically have tensor polarizabilities. In this case one would choose counterpropagating circularly polarized waves in equation (5.6) because the two modes then address different atomic transitions. If we additionally assume sufficiently large detuning for each field, we can also neglect mixing due to spontaneous emissions into other Zeeman-levels. The polarizability then loses all spin and polarization dependencies resulting in a scalar quantity

This is why the coupling parameter ζ introduced in equation (5.1) is proportional to a linear atomic polarizability and the wavenumber. For a generalization of the beam splitter method to multi-level atoms with tensor polarizability we refer to a work by Xuereb et al. (Xuereb *et al.* 2010). In this work we will assume that the atomic polarizability α is the same for k_y and k_z, hence $\zeta_z = \zeta_y k_z/k_y$. Of course, a more realistic scenario is easily possible within our framework but it would add unnecessary complexity here. Our central goal is the study of multiple scattering dynamics and not the effect of optical pumping and polarization gradients.

In the following chapters we will study how the introduction of different frequency fields provides new prospects to manipulate arrays of particles, ranging from equidistant lattices to individually tuned inter-particle distances as well as the design and control of motional couplings.

5.3 Light forces in counter-propagating beams with orthogonal polarization

In this section we explore forces and dynamics of a 1D lattice geometry modelled by a chain of beam splitters at distances $d_j := x_{j+1} - x_j$ irradiated from both sides by light with orthogonal polarizations ($\mathbf{e}_y$ and $\mathbf{e}_z$) and possibly distinct frequencies (ω_y and ω_z), cf. figure 5.1a. In contrast to a standard optical lattice setup as treated before (Asbóth *et al.* 2008; Deutsch *et al.* 1995) no a priori intensity modulation due to wave interference is present and we start with a fully translation invariant field configuration. Hence the light field itself does not prescribe any local ordering and only multiple light scattering from the particles themselves creates local trapping forces. Due to the translation invariance of the setup no stable particle configuration can be expected. However, the coupled particle field dynamics still induce relative order. Hence our central goal is to find conditions, when the light forces induced by two non-interfering beams are nevertheless sufficient to obtain stationary stable particle arrays and how this spontaneous crystal formation arises.

5.3.1 Stability conditions for two beam splitters

To get some first insight, we start with the simplest nontrivial example of two beam splitters at a distance $d = x_2 - x_1$. The intensities from the left and right beam

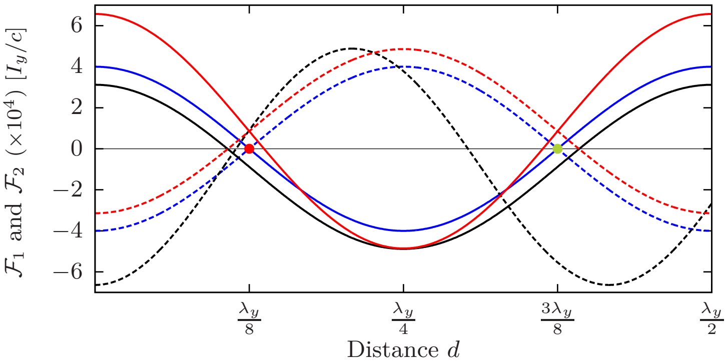

Figure 5.2 Light force onto the left (5.7) (solid lines) and right beam splitter (5.8) (dashed lines) as function of their distance d for $\zeta = 0.01$ and $k = k_y = k_z = 2\pi/\lambda$. For equal intensity $\mathcal{P} = I_z/I_y = 1$ and frequency (blue curves) the two forces add to zero and vanish at distances $d = \lambda/8$ and $d = 3\lambda/8$. For asymmetric intensities $\mathcal{P} = 0.7$ (red curves) we find distances with equal forces $\mathcal{F}_1 = \mathcal{F}_2$ but a net centre of mass force remains. The black curve shows a similar behaviour occurring for different wavenumbers $k_/k_y = 1.2$ of same power $\mathcal{P} = 1$. The red (green) dot marks unstable (stable) stationary points.

are given as $I_y = \frac{c\varepsilon_0}{2}\,|A_{y,1}|^2$ and $I_z = \frac{c\varepsilon_0}{2}\,|D_{z,2}|^2$, respectively. Here we chose the convention that all variables with index y correspond to light polarized in direction of $\mathbf{e}_y$ which is injected from the left (negative x-axis) and index z corresponds to $\mathbf{e}_z$ polarized light injected from the right. The individual beam splitters are counted from left to right with integer indices, hence, for example $B_{z,2}$ is the B-amplitude of the light field polarized parallel to $\mathbf{e}_z$ at the second beam splitter, cf. (5.2).

Using (5.3) and (5.4) to compute the fields for any given distance d, it is straightforward to obtain the total force on each beam splitter by simply adding the forces generated by the light in each polarization, i.e. $\mathcal{F}_1 = \mathcal{F}_{y,1} + \mathcal{F}_{z,1}$ and $\mathcal{F}_2 = \mathcal{F}_{y,2} + \mathcal{F}_{z,2}$. The individual forces $\mathcal{F}_{y,1}$, $\mathcal{F}_{z,1}$, $\mathcal{F}_{y,2}$ and $\mathcal{F}_{z,2}$ are obtained from (5.5).

Despite the simple physical situation the corresponding general analytic solution already is rather unhandy. Thus we first restrict ourselves to real valued ζ neglecting absorption in the beam splitter or equivalently neglecting spontaneous emission in an atom fibre system. Assuming small values of ζ and dropping terms of $\mathcal{O}(\zeta^3)$ and higher, we then find the following approximate formulas for the force on the two particles:

$$\mathcal{F}_1 = \frac{2}{c}\left(\frac{I_y\,\zeta^2\left(4\cos^2(dk_y)-1\right)}{1+4\zeta^2\cos^2(dk_y)} - \frac{I_z\left(\frac{k_z}{k_y}\zeta\right)^2}{1+4\left(\frac{k_z}{k_y}\zeta\right)^2\cos^2(dk_z)}\right), \tag{5.7}$$

$$\mathcal{F}_2 = \frac{2}{c}\left(\frac{I_y\,\zeta^2}{1+4\zeta^2\cos^2(dk_y)} - \frac{I_z\left(\frac{k_z}{k_y}\zeta\right)^2\left(4\cos^2(dk_z)-1\right)}{1+4\left(\frac{k_z}{k_y}\zeta\right)^2\cos^2(dk_z)}\right). \tag{5.8}$$

For a given set of control parameters, i.e. the intensity ratio $\mathcal{P} := I_z/I_y$ and the wavenumbers k_y and k_z, the beam splitters will settle at a distance d_0 for which the two forces are equal, i.e., $\mathcal{F}_1|_{d=d_0} = \mathcal{F}_2|_{d=d_0}$, and the configuration is stable ($\partial_d \mathcal{F}_1|_{d=d_0} > 0$, $\partial_d \mathcal{F}_2|_{d=d_0} < 0$). In this case, the system can still exhibit centre of mass motion but the particles keep a constant distance. From (5.7) and (5.8) we see that a stable configuration in the special case of equal wavenumbers, $k = k_y = k_z$ requires

$$\Delta \mathcal{F} = \mathcal{F}_1 - \mathcal{F}_2 = \frac{4\zeta^2 \cos(2d_0 k)}{1 + 4\zeta^2 \cos^2(d_0 k))} \frac{(I_y + I_z)}{c} = 0. \tag{5.9}$$

Independent of the injected laser intensities, which just appear as a multiplicative factor, this corresponds to a pair distance $d_0^s = (2n+1)\pi/(4k)$ $(n \in \mathbb{N})$. Here the solutions for odd n correspond to a stable configuration, while even n leads to unstable behaviour. As numerical example we plot the full distance dependent forces for three typical sets of parameters in figure 5.2, where stationary distances of equal force can be read off the intersection points. If these occur at zero force, the centre of mass is stationary as well. For small ζ these distances of zero force on each particle can be approximated by

$$d_1^{\pm} = \frac{1}{k_y} \left[\arccos \left(\pm \frac{1}{2k_y} \sqrt{\frac{k_y^2 I_y + k_z^2 I_z}{I_y + (k_z/k_y)^2 \zeta^2 \left(I_y - I_z\right)}} \right) + n_1 \pi \right] \qquad n_1 \in \mathbb{Z}, \tag{5.10}$$

$$d_2^{\pm} = \frac{1}{k_z} \left[\arccos \left(\pm \frac{1}{2k_z} \sqrt{\frac{k_y^2 I_y + k_z^2 I_z}{I_z - \zeta^2 \left(I_y - I_z\right)}} \right) + n_2 \pi \right] \qquad n_2 \in \mathbb{Z}. \tag{5.11}$$

Conditions (5.10) and (5.11) imply $\mathcal{F}_1|_{d=d_1^{\pm}} = 0$ and $\mathcal{F}_2|_{d=d_2^{\pm}} = 0$, respectively. Any solution fulfilling $d_1^- = d_2^-$ thus gives a stable and stationary configuration, where the forces on both beam splitters vanish and small perturbations induce a restoring force, as shown in figure 5.2. In general, such solutions can only be determined numerically and are not guaranteed to exist for every set of parameters. In appendix 5.A we show that the line of argument can also be reversed and one can calculate the intensity ratios and wavenumbers needed to obtain a stable configuration for a desired distance d. This allows precise distance control of the particles via intensities and frequencies.

Let us now exhibit some more of the intrinsic complexity of the system in a numerical example. In figure 5.3a we first plot the forces on the two beam splitters as function of distance and relative wavenumber for fixed equal intensity from both sides. Clearly the intersection of the two force surfaces exhibits a complex pattern with a multitude of stationary distances which can be controlled e.g. via the chosen frequency ratio.

In an alternative approach we can numerically find a stable stationary distance of the two beam splitters as function of intensity and wavenumber ratio by time integration of their motion with some damping added, cf. figure 5.3b. We see that depending on the parameters for a given initial condition the system can settle to a large range of different stationary distances, exhibiting rather abrupt jumps at certain critical parameter values. Generally a numerical evaluation requires very little effort and can be easily performed for large parameter ranges. Despite the fact

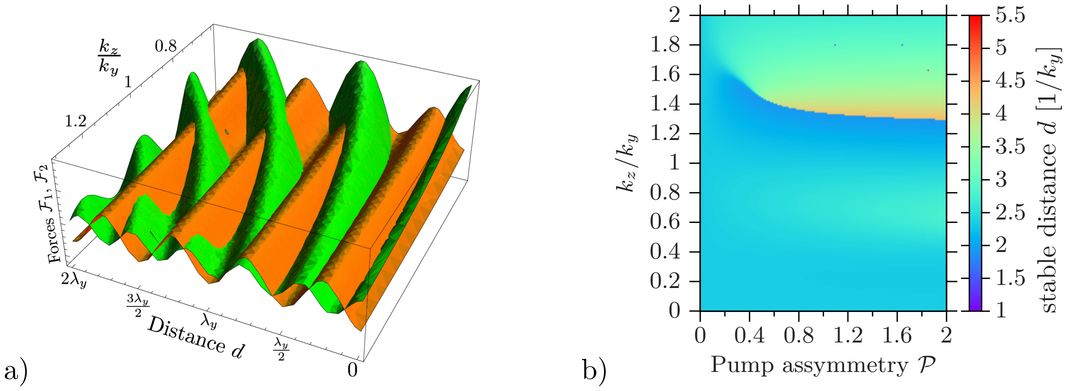

Figure 5.3 a) Force on left (orange) and right beam splitter (green) as function of the wavenumber ratio k_z/k_y and distance for two partly absorbing beam splitters with $\zeta = 1/12 - i/150$ and $\mathcal{P} = 1$ (left figure). b) Stationary distance of two beam splitters with $\zeta = 0.01$ as function of the wavenumber ratio k_z/k_y and the intensity ratio $\mathcal{P}$ obtained by numerical integration of their equation of motion including an effective friction term.

that there is no externally prescribed order, the particles mostly tend to arrange at configurations with stationary distance.

5.3.2 Self-ordering dynamics for higher numbers of beam splitters

In principle, determining stationary states for a larger number of beam splitters is straightforward by first solving (5.3) and (5.4) for the fields and using these to calculate the forces. However, to determine a completely stationary configuration of N beam splitters for a given input field configuration, we have to solve N nonlinear equations to guarantee a vanishing force at each particle as function of the $N-1$ relative distances. This problem can have no or infinitely many solutions. Often one does not get an exact solution, but solutions with vanishingly small centre of mass force.

As a rather tractable example we plot the zero force lines as function of the two relative distances for the case of three beam splitters illuminated by light of equal power, $\mathcal{P} = 1$, but different colour, $k_z/k_y = 1.1$, in figure 5.4. One finds many intersections of these lines, where two forces vanish, but only for a few distances we get triple intersections where the forces on all three particles vanish and stationary order can be achieved. These solutions then still have to be checked for stability against small perturbations to find a stable steady state.

To investigate the dynamics of a higher number of beam splitters it is more instructive to solve the dynamical equations of motion for various initial conditions until an equilibrium configuration is reached. To arrive at a stationary solution we assign a mass to the beam splitters and add an effective friction coefficient μ in the

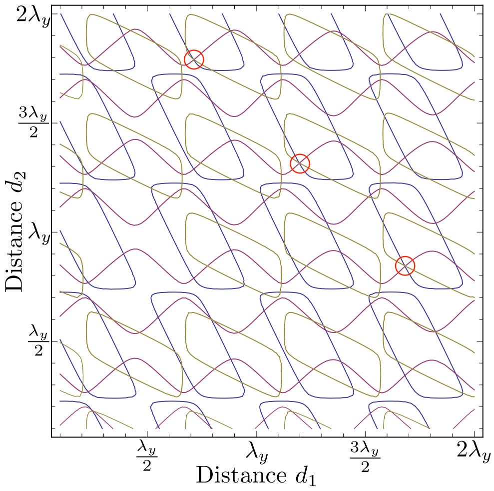

Figure 5.4 Zero-force lines for three beam splitters as function of the two distances for $k_z/k_y = 1.1$, $\zeta = 0.1$ and equal power $\mathcal{P} = 1$. Common crossings of all three lines (red circles) denote a stationary (but possibly unstable) configuration with no centre of mass motion.

classical Newtonian equations of motion,

$$m\ddot{x}_j = -\mu\dot{x}_j + F_j(x_1, ..., x_N). \tag{5.12}$$

In the following simulations we assume that the system is in the so called over damped regime, meaning that the characteristic time scale of undamped cloud motion, i.e. the oscillation period, is much smaller than the relaxation time of the cloud's velocity towards a constant value due to viscous friction. Under this assumption the equations of motion (5.12) reduce to a set of differential equations of first order (Asbóth *et al.* 2008),

$$\mu\dot{x}_j = F_j(x_1, ..., x_N). \tag{5.13}$$

In figure 5.5 we show the solutions of (5.13) for ten beam splitters in a simple orthogonal beam trap with $I_z = I_y$ and $k_z = k_y = k$. In a traditional standing wave trap, the beam splitters would settle at the chosen initial equidistant spacing $d_{OL} \approx \lambda/2$, cf. equation (5.23), which can be determined self-consistently (Asbóth *et al.* 2008). However, for two trap beams of orthogonal polarization no prescribed periodicity is present and the particles themselves create field configurations which confine their motion through multiple scattering. Our simulations show that for a large range of operating conditions the light forces generated by two counter-propagating beams with orthogonal polarizations will indeed induce an ordering of the particles, i.e. multiple scattering between the beam splitters is sufficiently strong to generate a stable configuration.

Interestingly, the final distances $d_1 = d_2 = \cdots = d_N$ converge to the same result as obtained for the standing wave optical lattice as the number of beam splitters

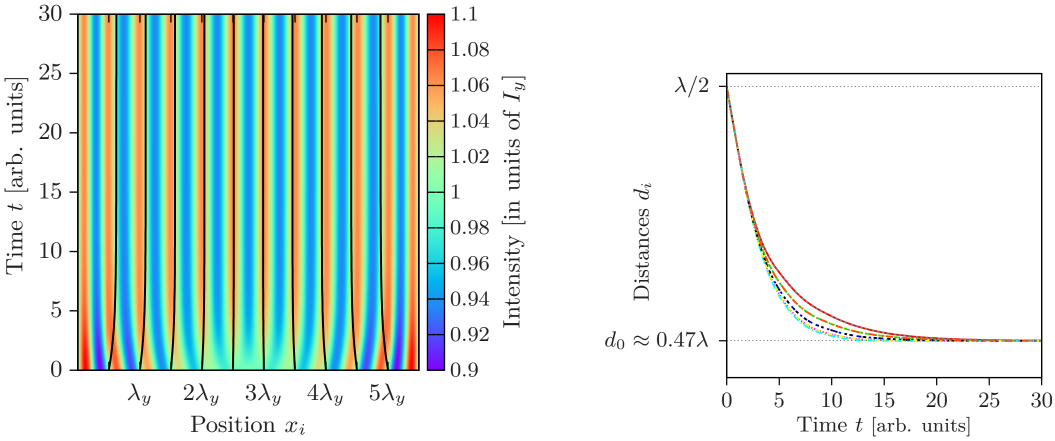

Figure 5.5 Trajectories of $N = 10$ beam splitters for $\mathcal{P} = 1$, $k_y = k_z$ and $\zeta = 0.01$ (left figure) started from a regular array of distance $\lambda/2$. The colour coding in the background shows the corresponding evolution of the total field intensity $I_{tot} := I_y + I_z$. The figure on the right depicts the change of the relative distances $d_i := x_{i+1} - x_i$ which converge towards a stable equidistant order of reduced distance.

N is increased, cf. figure 5.6. Thus orthogonally polarized trap beams have the same trapping properties as a standing wave setup, as $N \to \infty$. The beam splitters themselves then form an effective Bragg reflector to synthesize a standing wave configuration, which traps the particles.

A substantially more complex behaviour is found for the case of two colour illumination with different intensities, $I_y \neq I_z$. The trajectories for some representative cases can be found in figure 5.7. Interestingly, there is still a wide range of parameters where one obtains stationary patterns, but we generally get a non-equidistant spacing, cf. figure 5.8, and a finite centre of mass force. As above for two beam splitters, this force can be controlled via the intensity ratio to stabilize the centre of mass or induce controlled motion. Of course, the configuration not only depends on the operating conditions, but also on the initial conditions allowing for a multitude of different stationary configurations.

In summary we conclude that the particles prefer to form crystalline structures held in place by collective multiple scattering. The more particles we have, the more complex these patterns can get and the more different solutions can exist. The complexity of the problem increases further, if one allows for a variation of the individual coupling parameters ζ, e.g. to represent number fluctuations of the atoms trapped at each lattice site or size variation of trapped beads. Note that although appearing similar at first sight, the mechanism is different from standard optical binding of polarizable beads, which works on transverse shaping of the incoming light with the particles acting as small lenses (Dholakia *et al.* 2010), which we neglected in our model.

Let us finally note that analogous results should be obtained for a setup using two

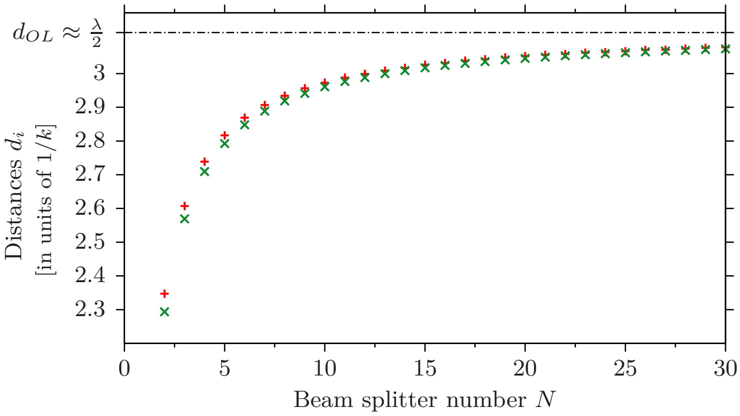

Figure 5.6 Dependence of the relative distances d_i (given in units of $1/k$) on the beam splitter number N. The parameters are chosen symmetric i.e. $\mathcal{P} = 1$, $k = k_y = k_z$, resulting in a equidistant lattice cf. figure 5.5. For large N we observe asymptotic convergence towards the effective lattice constant as found for a standing wave configuration, cf. equation (5.23) or (Asbóth *et al.* 2008). For the red dots we use $\zeta = 0.01$. A small imaginary part of zeta (green dots) $\zeta = 0.01 + i0.001$ decreases the distances but still yields stable configurations.

counter-propagating beams of equal polarization, but sufficiently different frequencies, such that scattering between the different colours is suppressed. From the particles point of view, the interference pattern of the combined fields then oscillates so rapidly that they cannot follow and the two forces stemming from the two fields can be calculated independently. Such frequency shifts are a common method to generate 3D optical lattices by using a different frequency in each dimension. But in contrast to those cases, here we get a mutual interaction between the light intensities of the different frequency components. During the evolution the spatial shifts of the beam splitters induced by one field are seen by all other fields and influences their propagation.

5.4 Tailored long-range interactions in a bichromatic optical lattice

Optical lattices for ultracold atoms are of course an extremely well established and controllable technology. In general, parameters are chosen in a way to avoid back-action of the particles on the fields. The underlying physics helps here to achieve this goal as particles tend to accumulate in zero force regions, where their influence on the lattice light is minimized (Asbóth *et al.* 2008; Deutsch *et al.* 1995). This is radically changed in the orthogonally polarized beam setup described above, where trapping forces are only created by the back-action of the particles on the two beams and interactions in the lattice occur via multiple collective scattering.

In the following chapter we will consider a second generic example to generate

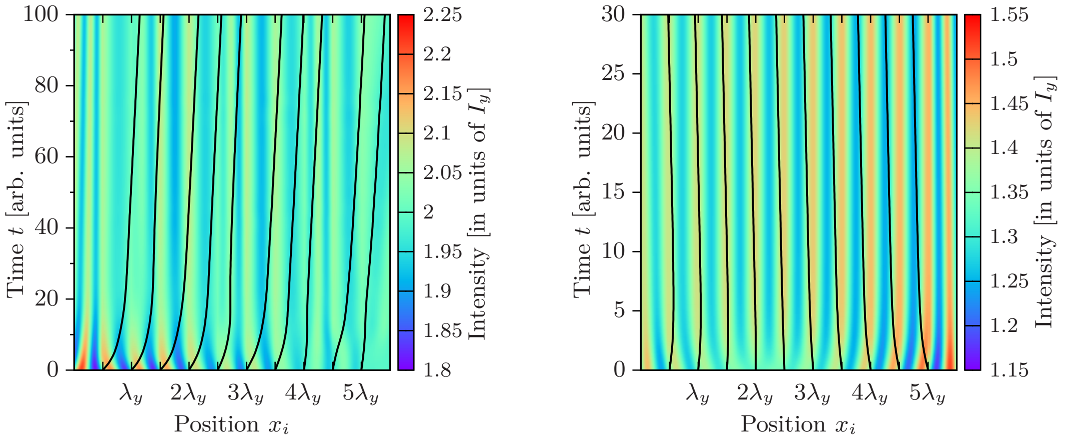

Figure 5.7 Trajectories of $N = 10$ beam splitters for $\mathcal{P} = 1$, $k_z/k_y = 1.3$ and $\zeta = 0.01$ (left figure). The colour coding in the background shows the total field intensity $I_{tot} := I_y + I_z$ during the reorganization process of the system. On the right hand side the trajectories ($N = 10$) for $\mathcal{P} = 1.3$, $k_y = k_z$ are shown. In both cases we observe a finite centre of mass force in the long time limit, while the pattern formed is stable but is no longer equidistant.

tailored long-range interactions in an optical lattice. In particular we study the extra forces introduced by a second perturbation field of different wavelength in a given optical lattice formed by two strong counter-propagating beams of equal wavenumber k and polarization $\mathbf{e}_y$, cf. figure 5.1b. By adding an extra beam of different wavenumber k_p and polarization $\mathbf{e}_z$ we can introduce tailored perturbations and couplings, as its gradient is generally non-zero at the positions of the original lattices sites.

For generality we allow intensity asymmetries for the dominant standing wave field $\mathcal{P} := I_r/I_l$ where the first indices l and r stand for *left* and *right* suggesting the direction of incidence. The intensity of the additional perturbing field is called I_p. The same index notation will also be used for the corresponding field amplitudes.

5.4.1 Two beam splitters in an bichromatic optical lattice

The first relevant system to study interactions and couplings introduced by an additional field of different frequency are two beam splitters trapped at a distance d_{sw}, cf. equation (5.23), in a far detuned optical lattice at stable positions $x_1^0 = x_0 - d_{\text{sw}}/2$ and $x_2^0 = x_0 + d_{\text{sw}}/2$. Here x_0 denotes the centre of mass coordinate calculated following (Sonnleitner *et al.* 2012), via

$$x_0 = \frac{1}{2k}\left(\arccos\left[\frac{(I_r - I_l)\left(1 + |\mathfrak{r}|^2 - |\mathfrak{t}|^2\right)}{2|\operatorname{Im}(\mathfrak{r}\mathfrak{t}^*)|\sqrt{I_l I_r}}\right] - \frac{\pi}{2}u\right) + \frac{n\pi}{k}, \quad n \in \mathbb{Z} \qquad (5.14)$$

with $u = \operatorname{sgn}[\operatorname{Im}(\mathfrak{r}\mathfrak{t}^*)]$.

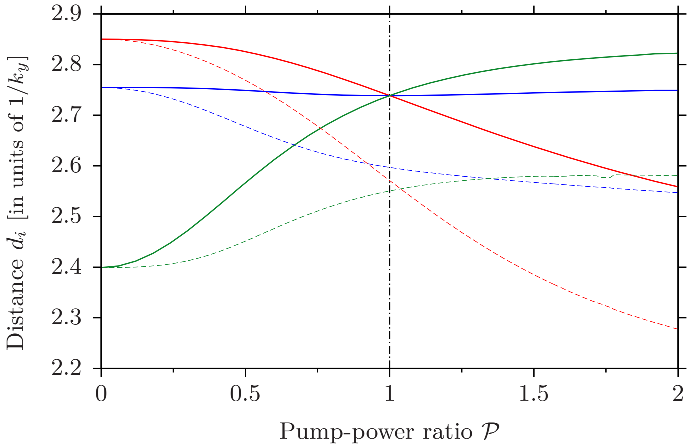

Figure 5.8 Relative distances $d_i := x_{i+1} - x_i$ between $N = 4$ beam splitters, after the system has reorganized and stabilised, as function of intensity ratio $\mathcal{P}$. If we assume $k = k_y = k_z$ there is only one point ($\mathcal{P} = 1$) where d_1 (red curve), d_2 (blue curve) and d_3 (green curve) have the same values. This corresponds to a formation of an equally spaced lattice. The dashed lines show the relative distances for $k_z/k_y = 1.1$, where no equidistant configuration can be realized.

The reflection and transmission coefficients $\mathfrak{r}$ and $\mathfrak{t}$ of the total system derived from the total transfer matrix are

$$\mathfrak{t} = \frac{e^{ik(x_2-x_1)}}{\zeta^2\left(e^{2ik(x_2-x_1)}-1\right)-2i\zeta+1}, \tag{5.15}$$

$$\mathfrak{r} = -\frac{\zeta\left((\zeta-i)e^{2ik(x_2-x_1)}-\zeta-i\right)}{\zeta^2\left(e^{2ik(x_2-x_1)}-1\right)-2i\zeta+1}. \tag{5.16}$$

The incident field amplitudes of the standing wave component are assumed as $A_l = \sqrt{2I_l/(\varepsilon_0 c)}\exp(ikx_1)$ and $D_r = \sqrt{2I_r/(\varepsilon_0 c)}\exp(-ikx_2)$ so that the remaining amplitudes at the boundaries are $B_l = \mathfrak{r}A_l + \mathfrak{t}D_r$, $C_r = \mathfrak{t}A_l + \mathfrak{r}D_r$. This allows to calculate the lattice forces on the first and second particle,

$$\mathcal{F}_1 = \frac{\epsilon_0}{2}\left[|A_l|^2 + |B_l|^2 - |(1+i\zeta)A_l + i\zeta B_l|^2 - |i\zeta A_l - (1-i\zeta)B_l|^2\right], \tag{5.17}$$

$$\mathcal{F}_2 = \frac{\epsilon_0}{2}\left[|(1+i\zeta)A_l + i\zeta B_l|^2 + |i\zeta A_l - (1-i\zeta)B_l|^2 - |C_r|^2 - |D_r|^2\right]. \tag{5.18}$$

The additional perturbation field is described by $A_p = \sqrt{2I_p/(\varepsilon_0 c)}\exp(ik_p x_1)$, $B_p = \mathfrak{r}A_p$ and $C_p = \mathfrak{t}A_p$ and generates the additional forces ($\zeta_p = k/k_p\,\zeta$)

$$\mathcal{F}_{1p} = \frac{\epsilon_0}{2}\left[|A_p|^2 + |B_p|^2 - |(1+i\zeta_p)A_p + i\zeta_p B_p|^2 - |i\zeta_p A_p - (1-i\zeta_p)B_p|^2\right], \tag{5.19}$$

$$\mathcal{F}_{2p} = \frac{\epsilon_0}{2}\left[|(1+i\zeta_p)A_{p,z} + i\zeta_p B_p|^2 + |i\zeta_p A_p - (1-i\zeta_p)B_p|^2 - |C_p|^2\right]. \tag{5.20}$$

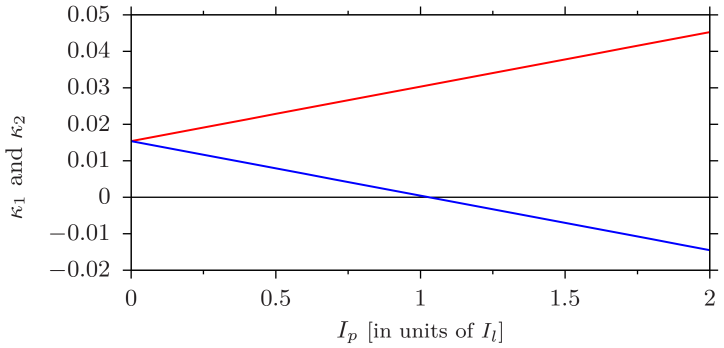

Figure 5.9 Dependence of the coupling constants κ_1 (blue) and κ_2 (red) on the perturbation field intensity I_p for $\zeta = \zeta_p = 0.1$, $k = k_p$ and $\mathcal{P} = 1$. As soon as the perturbation field is switched on, the constants differ.

Here we restrict the corresponding added dynamics of the two beam splitters to small, time dependent perturbations $\Delta x_1(t), \Delta x_2(t) << d_{\mathrm{sw}}$ from the equilibrium positions x_0 given in (5.14). Using $x_1(t) = x_0 - d_{\mathrm{sw}}/2 + \Delta x_1(t)$ and $x_2(t) = x_0 + d_{\mathrm{sw}}/2 + \Delta x_2(t)$ and linearising the forces for small $\Delta x_1(t)$ and $\Delta x_2(t)$ yields to the following coupled equations of motion

$$\begin{aligned} m\Delta\ddot{x}_1(t) &= -K\Delta x_1 + \kappa_1(\Delta x_2(t) - \Delta x_1(t)) + F_{ext}, \\ m\Delta\ddot{x}_2(t) &= -K\Delta x_2 - \kappa_2(\Delta x_2(t) - \Delta x_1(t)) + F_{ext}. \end{aligned} \tag{5.21}$$

A detailed calculation of the coefficients K, κ_1, κ_2 and F_{ext} is shown in appendix 5.B. The equations above correspond to two coupled harmonic oscillators driven by an external force F_{ext}.

The solution of the system (5.21) can be calculated analytically yielding

$$\begin{pmatrix} \Delta x_1(t) \\ \Delta x_2(t) \end{pmatrix} = \begin{pmatrix} 1 \\ 1 \end{pmatrix} \left(a_1 \cos(\omega_1 t + \varphi_1) + \frac{F_{ext}}{K} \right) + a_2 \begin{pmatrix} -\frac{\kappa_1}{\kappa_2} \\ 1 \end{pmatrix} \cos(\omega_2 t + \varphi_2) \tag{5.22}$$

with $\omega_1 = \sqrt{K/m}$ and $\omega_2 = \sqrt{(K + \kappa_1 + \kappa_2)/m}$.

Note that the coupling constants κ_1 and κ_2 here are not necessarily equal, cf. also figure 5.9, as there is no energy conservation enforced for the motion of the two beam splitters. Since the parameters can be chosen in a way so that the coupling constant κ_1 is equal to zero, one-sided couplings can be achieved. This means that only the motion of beam splitter number two is coupled to beam splitter number one, which does not couple to the rest of the system. The direction of this effect is governed by the direction of incidence of the perturbation beam. Besides, $\kappa_2 > 0$ holds for all values of I_p, meaning that no antisymmetric modes can be obtained if $\kappa_1 < 1$,cf. equation (5.22). Generally we find that tuning the perturbation field intensity offers a variety of different dynamics not accessible with traditional standing wave setups. This motivates a more detailed treatment of this system, using numerical methods.

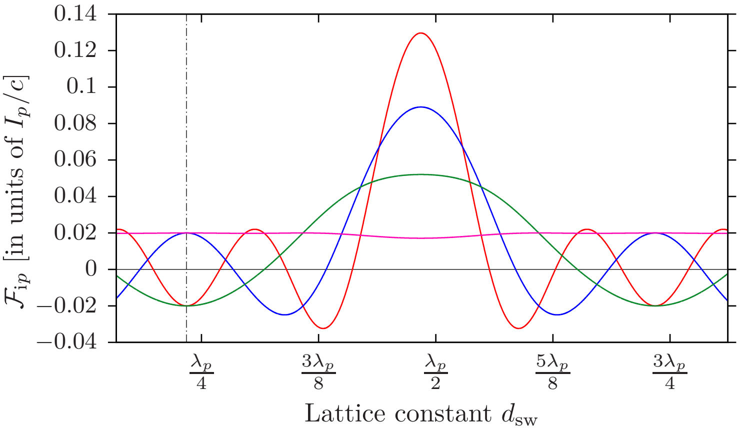

Figure 5.10 Perturbation induced force $\mathcal{F}_{ip}$ on $N = 4$ beam splitters at their unperturbed equilibrium positions in an optical lattice as function of the lattice constant d for $\zeta = 0.1$. The red line corresponds to the force $\mathcal{F}_{1p}$, the blue line to $\mathcal{F}_{2p}$, the green line to $\mathcal{F}_{3p}$ and the magenta line to $\mathcal{F}_{4p}$.

5.4.2 Long-range coupling of beam splitters in an optical lattice

As shown in (Asbóth *et al.* 2008) the effective self-consistent lattice constant in a standing wave with asymmetry $\mathcal{A} := (I_l - I_r)/\sqrt{I_l I_r}$, with $I_l := \frac{\epsilon_0}{c}|A_l|^2$, $I_r := \frac{\epsilon_0}{c}|D_r|^2$ adjusts to

$$d_{\mathrm{sw}} = \frac{\lambda}{2}\left(1 - \frac{1}{\pi}\arccos\left[\frac{-\zeta^2\sqrt{4+\mathcal{A}^2} + \sqrt{4-\zeta^2\mathcal{A}^2}}{2(1+\zeta^2)}\right]\right). \tag{5.23}$$

In an optical lattice, multiple scattering induces long-range interactions between the particles in the form of collective oscillation modes. In the self-consistent configuration the particles arrange at intensity maxima at minimal field gradients, so that this interaction is strongly suppressed for small perturbations. Adding, however, a second, perturbative field by a single running wave beam of wavenumber k_p injected from one side induces an additional force on each particle perturbing the regular periodic order. This perturbation then acts back on the original standing wave field. Note that a single plane wave by itself would only add a constant force, but this force is modified by multiple scattering depending on the particle distances. As an instructive example we show these perturbing force acting on $N = 4$ beam splitters in figure 5.10. We see that the additional force is different for all the particles and changes as a function of the lattice constant relative to the wavelength of the perturbing light. Hence, by a proper choice of parameters almost any combination of magnitudes and signs of forces on the different beam splitters can be achieved.

This can be exploited for different purposes to control and study lattice dynamics. As a first and direct application it is possible to tailor a specific field to induce oscillations of selected particles in the optical lattice by deflecting them from their

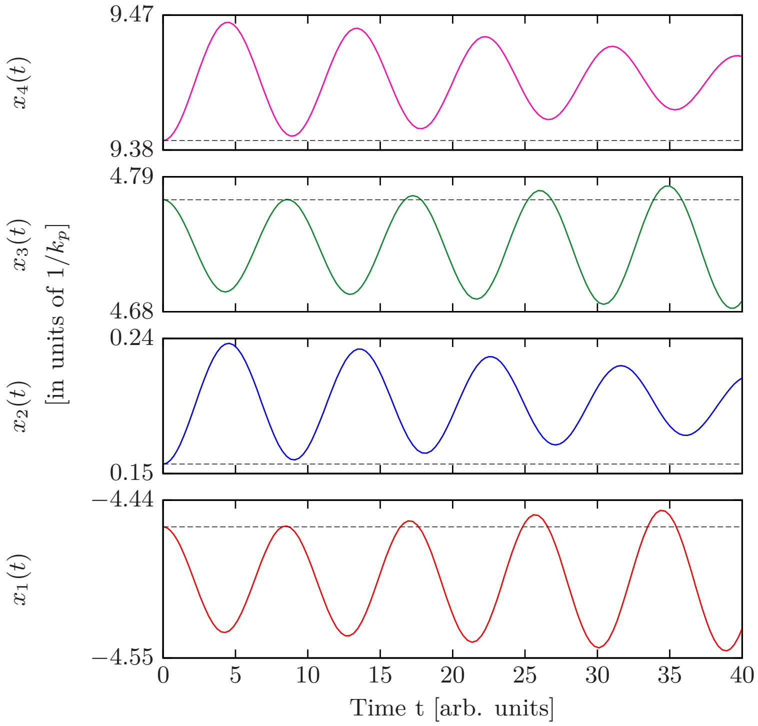

Figure 5.11 Correlated oscillatory motion of $N = 4$ beam splitters in a lattice induced by an additional perturbation field with intensity $I_p = I_l = I_r$, wavenumber $k_p = k$, $\zeta = \zeta_p = 0.1$ and damping parameter $\mu = 0.01$. The black, dashed lines show the initial unperturbed trapping positions $x_i = n_i d_0 - x_0$ ($n_i \in \{1, 2, \ldots, 4\}$) for $d_0 = 0.23\lambda_p$.

equilibrium position. As shown in figure 5.10, the force on the individual beam splitters depends strongly on the prescribed lattice constant. This means that there is a wide range of realizable dynamics as long as the lattice constant can be tuned, cf. equation (5.23). This can be potentially refined by the simultaneous use of several perturbation frequencies.

For example, using the parameters from figure 5.10 we anticipate interesting behaviour for a lattice with spacing $d_{\mathrm{sw}} \approx 0.23\lambda_p + m\pi$, $m \in \mathbb{N}$ as in that case $\mathcal{F}_{1p} = \mathcal{F}_{3p} = -\mathcal{F}_{2p} = -\mathcal{F}_{4p}$ (cf. dash-dotted line in figure 5.10). This behaviour is verified by calculating the trajectories via (5.12), the results are shown in figure 5.11. Obviously it is possible to correlate the motion of distant beam splitters in an optical lattice via the additional beam. After switching on the perturbation at $t = 0$, particles number one and three show amplified oscillations, while the other's oscillations are damped.

In a second approach the additional field is designed to enhance interactions between selected distant areas in the lattice. As shown in figure 5.12, exciting an oscillation of one particle weakly coupled to the standing wave field will usually have little effect on the other trapped particles. But after adding a perturbative field

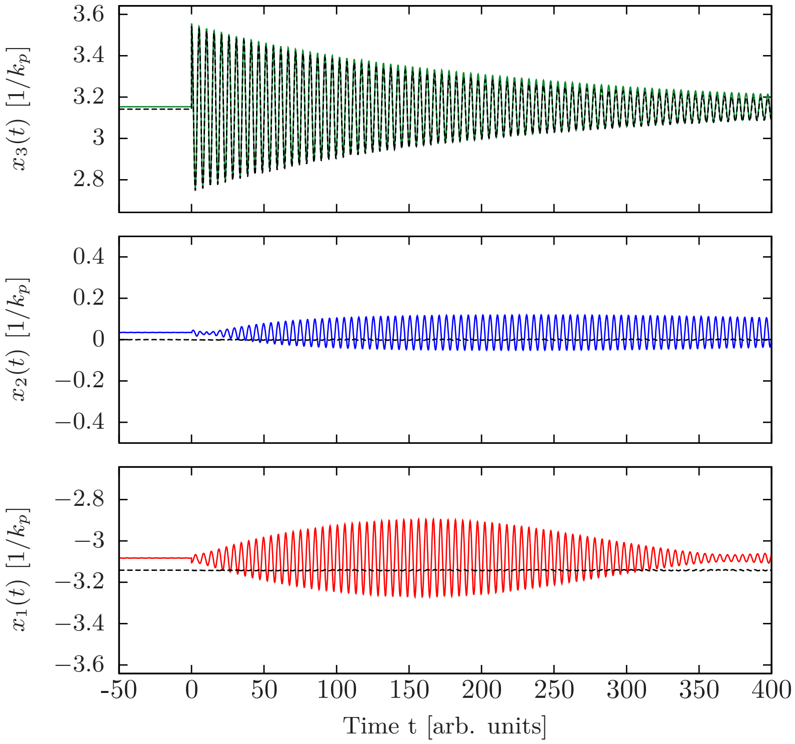

Figure 5.12 Example plot for the resonant coupling of three beam splitters, trapped in a standing wave configuration with $d_0 = \lambda_p/2$. We used $\zeta = 0.01$, $\zeta_p = 0.1$, $I_l = I_r = 20 I_p$ and $k/k_p = 0.99$. The rightmost beam splitter is displaced from the equilibrium position at $t = 0$, resulting in a damped oscillation (damping parameter $\mu = 0.01$). The black curves show the resulting dynamics for $I_p = 0$. The green ($x_3(t)$), blue ($x_2(t)$) and red ($x_1(t)$) curves show the dynamics if the coupling field is switched on. Note the resonant coupling between x_1 and x_3.

with carefully chosen parameters, this oscillation can be transferred to the other particles, forcing them to move along. Note that due to the fact that the additional perturbation (coupling) field is imposed from only one side, this coupling effect is not symmetric and excitations can flow in a desired direction. For example, a perturbing field entering from the left hand side will maximally transfer the motion of the rightmost beam splitter. This setup allows one to correlate the motion of particles and can even be used as a channel to transfer e.g. quantum information through the lattice, very much like phonons in ion crystals.

5.5 Conclusions

We have shown that even in the case of non-interfering counter-propagating light fields of different polarization and frequency, stable lattice configurations of particles held in space by multiple coherent scattering are possible. In contrast to conventional optical lattices the light here plays a decisive dynamical role as multiple scattering is essential to form and stabilize the structure. Compared to prescribed optical lattices the physics is much closer to the case of solids, where lattice dynamics in form of phonons not only keep the atoms in place, but also mediate long-range interactions. Interestingly, in conventional optical lattices such interactions can be tailored by adding additional coupling fields of suitable frequency and polarization. While we have performed our calculations only for 1D geometries, where a semi-analytic scattering approach can be used, similar effects should be present in 3D geometries as well.

In general, for very far detuned optical fields these effects will be rather small but their importance will grow with the size of the lattice as well as in transversely confined fields. Particularly strong effects can be expected in fields guided by nano-optical devices such as nano fibres or hollow core fibres. Here even for a few particles strong interactions can be expected.

In this work we have restricted ourselves to the bichromatic case for sake of simplicity. Nevertheless one can expect even more complex dynamics for an increasing number of input fields as the forces show a more complex distance dependence. Note that here we have ignored any internal optical resonances of the particles. Working close to such resonances certainly should strongly increase the effects but also will complicate the analysis.

Let us finally mention here that the system not necessarily requires a fixed set of beam splitters as a starting point. As an alternative we can consider each beam splitter to be formed by a small sub-ensemble of atoms in a 1D beam configuration, as it has been proposed before (Asbóth *et al.* 2008; Deutsch *et al.* 1995). In our case of non-interfering counter-propagating beams, one can expect that under suitable conditions the cold atoms arrange in small groups forming at local field intensity maxima (Grießer *et al.* 2013). Groups of atoms at certain spatial sites then commonly form beam splitters shaping a self-consistent lattice structure.

In contrast to conventional lattices, back-action of the particles onto the fields is an essential part of the dynamics and the field thus strongly mediates collective interactions. Light scattering on one end of the lattice influences the lattice depth at the other end, which opens a completely new branch of ultracold atom optical lattice physics. Note that also atoms trapped in optical resonator fields (Ritsch *et al.* 2013) exhibit similar dynamical coupling effects but in that case the back-action is strongly restricted by the resonator geometry limiting the available interaction wavenumbers.

Acknowledgements

We thank A. Rauschenbeutel, M. Aspelmeyer, N. Kiesel and H. J. Kimble for stimulating discussions. We acknowledge support via the Austrian Science Fund grant SFB F40 and ERC Advanced Grant (catchIT, 247024).

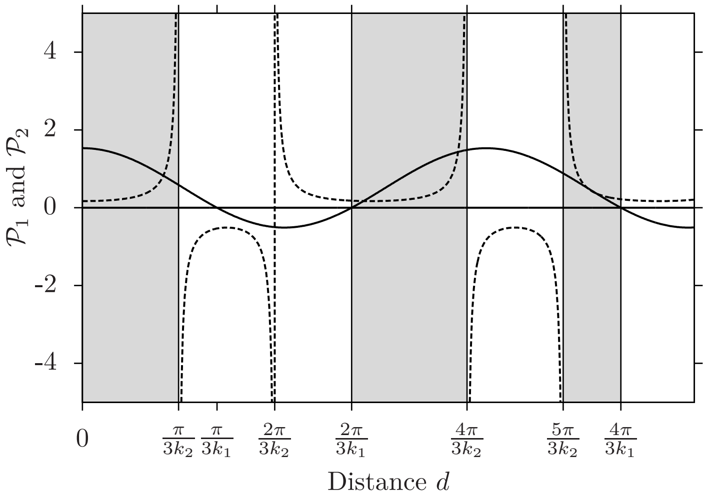

Figure 5.13 Intensity ratio leading to stable solutions (5.24) (solid line) and (5.25) (dashed line) for a prescribed distance d for $\zeta = 0.01$ and $k_z/k_y = 1.4$. The grey regions mark the physically allowed regions $\mathcal{P}_1 > 0$ and $\mathcal{P}_2 > 0$. It impossible to find intensity configurations so that particles can be trapped at distances outside of these regions.

Appendix 5.A Distance control for two particles

In section 5.3.1 we saw that distances with vanishing force on both beam splitters, leading to a stable or trapped configuration for given intensity ratios and wavenumbers for the special case $k = k_y = k_z$ require equal intensity from left and right. If we reverse the line of argument and ask for intensity ratios and wavenumbers where the two beam splitters can be trapped at a given distance d, the result allows us to study the full system, i.e. different polarizations *and* frequencies. In this case precise distance control is possible.

First we need to find the zeros of (5.7) and (5.8) with respect to $\mathcal{P}$.

$$\mathcal{P}_1 = \frac{\left(4\cos^2(dk_y) - 1\right)\left(k_y^2 + 4k_z^2\,\zeta^2\cos^2(dk_z)\right)}{k_y^2\left(1 + 4\zeta^2\cos^2(dk_y)\right)} \tag{5.24}$$

$$\mathcal{P}_2 = \frac{k_y^2 + 4k_z^2\,\zeta^2\cos^2(dk_z)}{k_y^2\left(1 + 4\zeta^2\cos^2(dk_y)\right)\left(4\cos^2(dk_z) - 1\right)} \tag{5.25}$$

Both solutions $\mathcal{P}_1$ and $\mathcal{P}_2$ have to be positive, which is not valid for all values of d, cf. figure 5.13.

To obtain a trapping condition for the wavenumbers, i.e. wavenumbers where the total force $\mathcal{F}_1 + \mathcal{F}_2$ vanishes, we solve $\mathcal{P}_1 = \mathcal{P}_2$, finding

$$k_z^{\pm} = \frac{1}{d}\arccos\left(\pm\frac{\sqrt{\cos(2dk_y)}}{\sqrt{2(1 + 2\cos(2dk_y))}}\right) + 2\pi n, \qquad n \in \mathbb{Z}. \tag{5.26}$$

Equation (5.26) allows us to calculate the needed wavenumbers to trap the beam splitters at a given distance d. The associated intensity ratio can be calculated via (5.24) or (5.25).

Obviously there exists a wide range of parameters which allow stable and trapped configurations of beam splitters in multicolour light beams with orthogonal polarizations (or sufficiently different wavenumbers).

Appendix 5.B Linearisation of the forces on two beam splitters in a bichromatic optical lattice

In section 5.3.1 we calculate the equations of motion for two beam splitters in a standing-wave geometry perturbed by an additional field with orthogonal polarization. For that purpose we use linearised forces (5.17), (5.18), (5.19) and (5.20). Here we want to show how this linearisation is done and how the constants K, κ_1, κ_2 and F_{ext} can be calculated.

The force $\mathcal{F}_1$ depends only on the positions $x_1(t)$ and $x_2(t)$ of the two beam splitters. Replacing these variables via $x_1(t) = x_0 - d_{\mathrm{sw}}/2 + \Delta x_1(t)$ and $x_2(t) = x_0 + d_{\mathrm{sw}}/2 + \Delta x_2(t)$ results in a force dependent on $\Delta x_1(t)$ and $\Delta(t) := \Delta x_2(t) - \Delta x_1(t)$. Assuming small $\Delta x_1(t)$ and $\Delta(t)$ we perform a 2D Taylor approximation to first order resulting in

$$\mathcal{F}_1 = a + b\Delta x_1 + c(\Delta x_2(t) - \Delta x_1(t)) \tag{5.27}$$

where we defined real constants a,b and c which are lengthy expressions depending on the system's parameters.

The same method works for the remaining forces $\mathcal{F}_2$, $\mathcal{F}_{1p}$ and $\mathcal{F}_{2p}$, where the latter two only depend on the relative distance $\Delta(t)$.

$$\mathcal{F}_2 = u + v\Delta x_2 + w(\Delta x_2(t) - \Delta x_1(t)) \tag{5.28}$$

$$\mathcal{F}_{1p} = K_{1p} + K_{2p}(\Delta x_2(t) - \Delta x_1(t)) \tag{5.29}$$

$$\mathcal{F}_{2p} = K_{3p} + K_{4p}(\Delta x_2(t) - \Delta x_1(t)) \tag{5.30}$$

Performing these tedious calculations we find that some of the obtained constants are zero ($a = u = 0$) while others have the same values. We define $-K := b = v$, $\kappa_1 := K_{2p} + c$, $-\kappa_2 := K_{4p} + w$ with $c = w$ and $F_{ext} := K_{1p} = K_{3p}$. With this results result we get the forces used in the equations of motion (5.21).

Part II

Light forces induced by sources of thermal radiation

6 Background: forces on atoms in thermal radiation fields

Since the early proposal by Ashkin (Ashkin 1970) the mechanical interaction of atoms or molecules and electromagnetic fields are typically explored using coherent and narrow-band radiation from lasers. These allow for fascinating and groundbreaking research including, amongst others, cooling and trapping of single atoms or atomic clouds in optical lattices, resonators and optical tweezers (Ashkin 2000; Chu *et al.* 1986; Cohen-Tannoudji 1992; Ritsch *et al.* 2013; Wineland *et al.* 1979).

As explained in chapter 1, the intra-atomic processes induced by the optical fields and resulting in "optical forces" are the absorption and spontaneous emission of photons leading to *radiation pressure* and an induced shift of the atomic levels causing the *dipole* or *gradient force*. Obviously, both mechanisms are not exclusive to coherent or narrow-band radiation: the absorption of ambient radiation is a continuous and omnipresent process; the dynamic Stark shifts due to thermal radiation is more subtle but is nevertheless a source of error in precision spectroscopy (Farley *et al.* 1981; Gallagher *et al.* 1979; Jentschura *et al.* 2008; Safronova *et al.* 2010).

The most prominent force in connection with thermal fields is radiation pressure. In astrophysics it plays a crucial role, e.g. for the internal stability of stars, the formation of star systems and galaxies or in the dynamics of comets and their tails (Carroll *et al.* 1996; Evans 1993; Robertson 1937). Surprisingly—at least to our knowledge—the gradient force has not been studied yet in this context.

In the following sections we will therefore briefly review the dynamic Stark shift for atoms in isotropic thermal fields where, due to symmetry, no forces are expected. However, this changes once a finite source of radiation, such as a hot sphere, is considered in section 6.2. A comparison with radiation pressure shows that the overlooked gradient force actually dominates for a wide range of parameters. The publication (Sonnleitner *et al.* 2013) presented in chapter 7 is based on the findings of this introductory chapter. Further calculations are presented in chapter 8.

6.1 The dynamic Stark shift for an atom in a thermal bath

The effect of a weak electromagnetic field on an atom shall be described as a perturbation in the electric dipole approximation (Bransden *et al.* 1983),

$$V(t) = e\mathbf{r} \cdot \mathbf{E}(\mathbf{x}, t) e^{\eta t}, \tag{6.1}$$

where e is the elementary charge, $\mathbf{r}$ is the electron's position operator[1] and $\mathbf{E}(\mathbf{x}, t)$ is the electric field at the atom's position $\mathbf{x}$. The factor $\exp(\eta t)$ is introduced to account for a slowly increasing perturbation starting at a time $t_0 \to -\infty$ and will vanish as we take the limit $\eta \to 0$.

The incoming electric field can be written as a superposition of plane waves of frequency $\omega = c|\mathbf{k}| \in [0, \infty]$ incident from a solid angle $\Omega(\mathbf{x})$,

$$\mathbf{E}(\mathbf{x}, t) = \int_0^\infty \int_{\Omega(\mathbf{x})} |\boldsymbol{\mathcal{E}}_\omega| \cos(\omega t + \phi_\mathbf{k}) \left(\mathbf{e_k}^{[1]} \cos(\alpha_\mathbf{k}) + \mathbf{e_k}^{[2]} \sin(\alpha_\mathbf{k}) \right) \mathrm{d}\Omega \mathrm{d}\omega. \tag{6.2}$$

Here $|\boldsymbol{\mathcal{E}}_\omega|$ is the field's amplitude in the spectral region $[\omega, \omega + \mathrm{d}\omega]$; $\mathbf{e_k}^{[1]}$ and $\mathbf{e_k}^{[2]}$ span the plane of polarization orthogonal to a wavevector $\mathbf{k}$ coming in from a region of solid angle $[\Omega, \Omega + \mathrm{d}\Omega]$. The variables $\alpha_\mathbf{k}$ and $\phi_\mathbf{k}$ describe the polarization and phase of the electric field and will be chosen randomly from the interval $[0, 2\pi)$ to account for the unpolarized and incoherent nature of the thermal light field, respectively.

From time-dependent perturbation theory, cf. appendix 6.A, one can define the quantity[2]

$$\Delta_n = \langle n| V(t) |n\rangle - \tfrac{i}{\hbar} \sum_{m \neq n} \int_{-\infty}^{t} e^{i(\omega_n - \omega_m)(t-t')} \langle n| V(t) |m\rangle \langle m| V(t') |n\rangle \, \mathrm{d}t' \tag{6.3}$$

associated with the level shift ΔE_n and the additional line width Γ_n of the atomic eigenstate $|n\rangle$ via

$$\Delta_n = \Delta E_n - \tfrac{i\hbar}{2} \Gamma_n. \tag{6.4}$$

To calculate the mean value of Δ_n we have to deal with terms involving different stochastic processes, e.g. $\langle \cos(\omega t + \phi_\mathbf{k}) \cos(\omega' t' + \phi_{\mathbf{k}'}) \rangle$. The assumed incoherent light field allows us to perform the averaging independently for $\mathbf{k} \neq \mathbf{k}'$ such that we find

$$\begin{aligned} &\langle \cos(\omega t + \phi_\mathbf{k}) \cos(\omega' t' + \phi_{\mathbf{k}'}) \rangle = \\ &\qquad = \begin{cases} \langle \cos(\omega t + \phi_\mathbf{k}) \cos(\omega t' + \phi_\mathbf{k}) \rangle = \cos(\omega(t - t'))/2 & \text{for } \mathbf{k} = \mathbf{k}', \\ \langle \cos(\omega t + \phi_\mathbf{k}) \rangle \langle \cos(\omega' t' + \phi_{\mathbf{k}'}) \rangle = 0 & \text{else.} \end{cases} \end{aligned} \tag{6.5}$$

A similar procedure for the randomised directions of polarization finally leads to an average shift of

$$\begin{aligned} \langle \Delta_n \rangle = -\tfrac{ie^2}{4\hbar} \sum_{m \neq n} \int_0^\infty \int_{\Omega(\mathbf{x})} |\boldsymbol{\mathcal{E}}_\omega|^2 \left(|\langle m| \mathbf{r} \cdot \mathbf{e_k}^{[1]} |n\rangle|^2 + |\langle m| \mathbf{r} \cdot \mathbf{e_k}^{[2]} |n\rangle|^2 \right) \times \\ \times \int_{-\infty}^{t} \cos(\omega(t - t')) e^{i\omega_{nm}(t-t')} e^{\eta(t+t')} \mathrm{d}t' \mathrm{d}\Omega \mathrm{d}\omega, \end{aligned} \tag{6.6}$$

---

[1] For a multi-electron atom or molecule $\mathbf{r}$ is the sum of the positions of all N_e electrons, i.e., $\mathbf{r} = \sum_{k=1}^{N_e} \mathbf{r}_k$.

[2] The sum is here understood to be a sum over discrete as well as an integral over the continuous eigenstates $|m\rangle$ of the unperturbed atomic Hamiltonian. Also, $|n\rangle$ is assumed to be nondegenerate.

where we set $\omega_{nm} := \omega_n - \omega_m$. The time integral gives

$$\int_{-\infty}^{t} \cos(\omega(t-t'))e^{i\omega_{nm}(t-t')}e^{\eta(t+t')}\mathrm{d}t' = \frac{ie^{2\eta t}}{2}\left(\frac{1}{\omega_{nm}+\omega+i\eta}+\frac{1}{\omega_{nm}-\omega+i\eta}\right). \tag{6.7}$$

Using that $\lim_{\eta\to 0}(x+i\eta)^{-1} = \mathcal{P}x^{-1} + i\pi\delta(x)$ and identifying the terms in equation (6.4) with the real and imaginary party of Δ_n we finally obtain a mean level shift

$$\langle \Delta E_n(\mathbf{x})\rangle = \frac{e^2}{8\hbar}\sum_{m\neq n}\mathcal{P}\int_0^\infty\int_{\Omega(\mathbf{x})}|\boldsymbol{\mathcal{E}}_\omega|^2\left(|\langle m|\,\mathbf{r}\cdot\mathbf{e_k}^{[1]}\,|n\rangle|^2 + |\langle m|\,\mathbf{r}\cdot\mathbf{e_k}^{[2]}\,|n\rangle|^2\right)\times$$
$$\times\left(\frac{1}{\omega_{nm}+\omega}+\frac{1}{\omega_{nm}-\omega}\right)\mathrm{d}\Omega\,\mathrm{d}\omega, \tag{6.8}$$

where $\mathcal{P}$ denotes the Cauchy principal value integral, and an additional effective line width

$$\langle \Gamma_n(\mathbf{x})\rangle = \frac{e^2\pi}{4\hbar^2}\sum_{m\neq n}\int_0^\infty\int_{\Omega(\mathbf{x})}|\boldsymbol{\mathcal{E}}_\omega|^2\Big(|\langle m|\,\mathbf{r}\cdot\mathbf{e_k}^{[1]}\,|n\rangle|^2 +$$
$$+ |\langle m|\,\mathbf{r}\cdot\mathbf{e_k}^{[2]}\,|n\rangle|^2\Big)\delta(|\omega_{nm}|-\omega)\,\mathrm{d}\Omega\,\mathrm{d}\omega. \tag{6.9}$$

One can easily see that this perturbative approach breaks down if $|\omega_{nm}| \simeq \omega$. In this case we have to solve the problem in the dressed-state picture (Haas *et al.* 2006). Farley and Wing (Farley *et al.* 1981), however, argue that a full, non-perturbative treatment will finally, after integrating over the resonance, give the same result.

Equation (6.8) can be simplified for the special case of an atom immersed in an isotropic, incoherent electric field, where $\Omega(\mathbf{x}) = 4\pi$. To connect the polarization vectors $\mathbf{e_k}^{[1]}$ and $\mathbf{e_k}^{[2]}$ with the spherical coordinates used to parametrise the solid angle element, i.e. $\mathrm{d}\Omega = \sin\vartheta\,\mathrm{d}\vartheta\,\mathrm{d}\varphi$, we set

$$\mathbf{k} = \frac{\omega}{c}\begin{pmatrix}-\cos\varphi\,\sin\vartheta\\ -\sin\varphi\,\sin\vartheta\\ -\cos\vartheta\end{pmatrix}, \qquad \mathbf{e_k}^{[1]} = \begin{pmatrix}-\cos\varphi\,\cos\vartheta\\ -\sin\varphi\,\cos\vartheta\\ \sin\vartheta\end{pmatrix} \quad\text{and}\quad \mathbf{e_k}^{[2]} = \begin{pmatrix}-\sin\varphi\\ \cos\varphi\\ 0\end{pmatrix}. \tag{6.10}$$

The squared matrix elements in equation (6.8) then read, for instance,

$$|\langle m|\,\mathbf{r}\cdot\mathbf{e_k}^{[1]}\,|n\rangle|^2 = \left(|\langle m|\,x\,|n\rangle|^2\cos^2\varphi + |\langle m|\,y\,|n\rangle|^2\sin^2\varphi\right)\cos^2\vartheta +$$
$$+ |\langle m|\,z\,|n\rangle|^2\sin^2\vartheta + \langle n|\,x\,|m\rangle\,\langle m|\,y\,|n\rangle\cos\varphi\,\sin\varphi\,\cos^2\vartheta + \ldots \tag{6.11}$$

but after integrating over the unit sphere, the mixed terms $\sim \langle n|\,x\,|m\rangle\,\langle m|\,y\,|n\rangle$ etc. vanish and only

$$\int_0^{2\pi}\int_0^{\pi}\left(|\langle m|\,\mathbf{r}\cdot\mathbf{e_k}^{[1]}\,|n\rangle|^2 + |\langle m|\,\mathbf{r}\cdot\mathbf{e_k}^{[2]}\,|n\rangle|^2\right)\sin\vartheta\,\mathrm{d}\vartheta\,\mathrm{d}\varphi =$$
$$= \frac{8\pi}{3}\left(|\langle m|\,x\,|n\rangle|^2 + |\langle m|\,y\,|n\rangle|^2 + |\langle m|\,z\,|n\rangle|^2\right) = \frac{8\pi}{3}|\langle m|\,\mathbf{r}\,|n\rangle|^2 \tag{6.12}$$

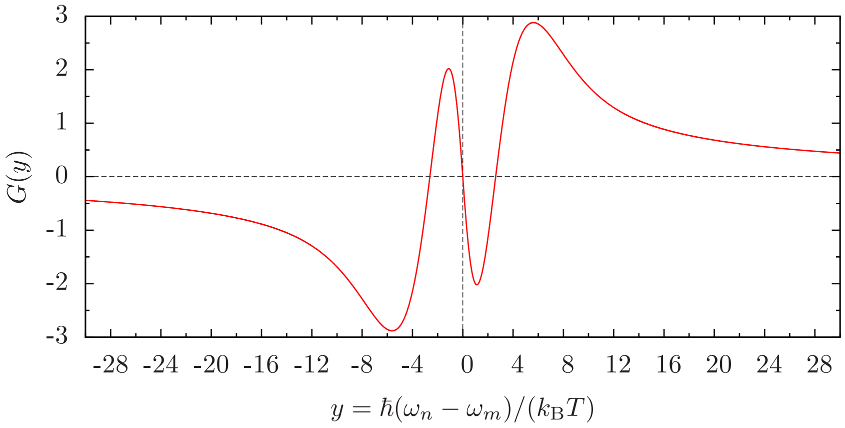

Figure 6.1 Numerical computation of the integral $G(y)$ as defined in equation (6.16) and its continuation to negative values as $G(-y) = -G(y)$.

remains. Defining $|\mathbf{r}_{mn}|^2 := |\langle m|\,\mathbf{r}\,|n\rangle|^2$ the mean energy shift is then simply given by

$$\Delta E_n = \frac{e^2\pi}{3\hbar}\sum_{m\neq n}|\mathbf{r}_{mn}|^2\mathcal{P}\int_0^\infty |\boldsymbol{\mathcal{E}}_\omega|^2\left(\frac{1}{\omega_{nm}+\omega}+\frac{1}{\omega_{nm}-\omega}\right)\mathrm{d}\omega. \tag{6.13}$$

If the isotropic electromagnetic field is the result of a thermal bath of temperature T and differential energy density u_ω, cf. appendix 6.B,

$$u_\omega = \frac{\hbar}{\pi^2c^3}\frac{\omega^3}{e^{\frac{\hbar\omega}{k_{\mathrm{B}}T}}-1} \tag{6.14}$$

we can use $u_\omega = 2\pi\varepsilon_0|\boldsymbol{\mathcal{E}}_\omega|^2$, cf. appendix 6.C, to reproduce the formula given in (Farley *et al.* 1981), reading

$$\Delta E_n = \frac{e^2}{6\pi^2\varepsilon_0c^3}\left(\frac{k_{\mathrm{B}}T}{\hbar}\right)^3\sum_{m\neq n}G\left(\frac{\hbar(\omega_n-\omega_m)}{k_{\mathrm{B}}T}\right)|\mathbf{r}_{mn}|^2. \tag{6.15}$$

Here we used (Farley *et al.* 1981)

$$G(y) = \mathcal{P}\int_0^\infty \frac{x^3}{e^x-1}\left(\frac{1}{y+x}+\frac{1}{y-x}\right)\mathrm{d}x, \tag{6.16}$$

which has to be computed numerically and is drawn in figure 6.1.

Introducing the *oscillator strengths*[3] defined as (Bethe *et al.* 1977; Bransden *et al.* 1983; Sakurai *et al.* 2011)

$$f_{mn} := \frac{2m_e(\omega_m-\omega_n)}{3\hbar}|\langle m|\,\mathbf{r}\,|n\rangle|^2 \tag{6.17}$$

---

[3] This dimensionless number is positive for processes where $\omega_m > \omega_n$ and obeys the neat Thomas-Reiche-Kuhn sum rule as $\sum_m f_{mn} = N_e$, with N_e being the number of electrons in the atom. It is related to Einstein's absorption coefficient as $B_{mn} = e^2\pi/(2m_e\varepsilon_0\hbar)f_{mn}/(\omega_m-\omega_n)$ (Bransden *et al.* 1983; Einstein 1917; Hilborn 2002).

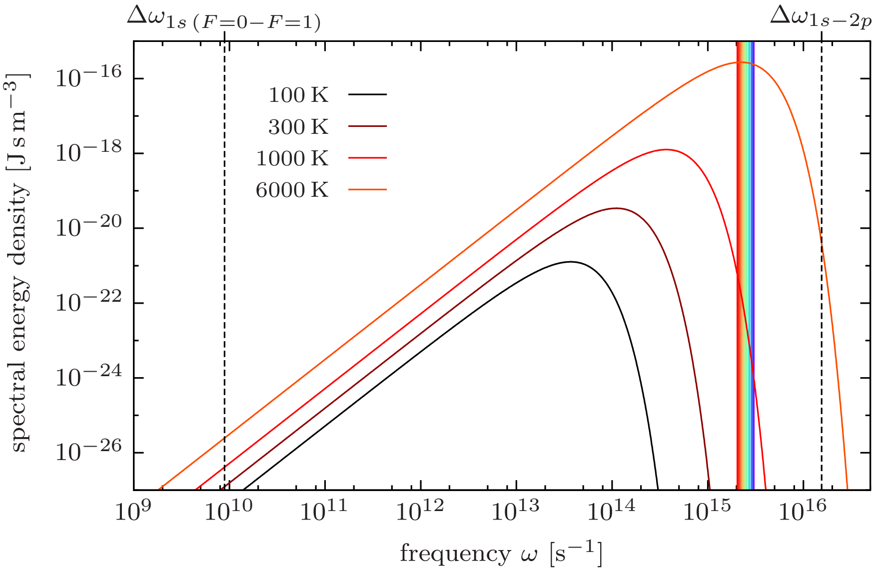

Figure 6.2 The Planckian energy density (6.14) for different temperatures, the rainbow highlights the range of optical frequencies. The dashed vertical lines indicate the frequencies of the first two transitions of atomic hydrogen in the ground state: the hyperfine $1s(F = 0 - F = 1)$ line and the $1s - 2p$ transition. The numerical values for the transition frequencies were taken from (Wiese *et al.* 2009) and are displayed in table 6.1.

the energy shift (6.15) can be rewritten as

$$\Delta E_n = \frac{e^2(k_\mathrm{B}\,T)^3}{4\pi^2\varepsilon_0 c^3 m_e \hbar^2}\sum_{m\neq n} G\left(\frac{\hbar(\omega_n-\omega_m)}{k_\mathrm{B}\,T}\right)\frac{f_{mn}}{\omega_m-\omega_n}. \tag{6.18}$$

From equations (6.15) or (6.18) combined with figure 6.1 we can infer the sign of the energy shift: for a particle in the ground state all oscillator strengths f_{m0} are positive and G is negative for $k_\mathrm{B}T \ll \hbar(\omega_m - \omega_0)$. Therefore we expect a negative energy shift, $\Delta E_0 < 0$, for atoms in their ground state.

On the other hand, highly excited atoms have the strongest transitions to lower levels, hence transitions with $\omega_n - \omega_m > 0$ will dominate and for moderate temperatures the numerical integral G will adopt positive values. These atoms will therefore experience a positive energy shift.

For example we use the numbers given in (Farley *et al.* 1981) to confirm our estimates as, e.g. for hydrogen we find $\Delta E_{1s}/\hbar \approx -0.26\,\mathrm{Hz}$ or for Rubidium $\Delta E_{5s}/\hbar \approx -17.5\,\mathrm{Hz}$, for $T = 300\,\mathrm{K}$. We also find that the absolute value of the frequency shift is much larger for Rydberg atoms than for atoms in the ground state, e.g. for hydrogen $\Delta E_{14p}/\hbar \approx 11.6\,\mathrm{kHz}$ or for Rubidium $\Delta E_{19s}/\hbar \approx -16.4\,\mathrm{kHz}$, again at $T = 300\,\mathrm{K}$. This can be easily understood as Rydberg atoms have far stronger transition lines.

For some elements, especially for atomic hydrogen in the ground state, the frequency of the first optical transition is far above the bulk of the black-body power spectrum, cf. figure 6.2. Therefore the AC Stark shift can be well approximated by the static (DC) shift reading (Bransden *et al.* 1983)

$$\Delta E^{\mathrm{DC}} = -\frac{\alpha_X}{2} \langle \mathbf{E}(\mathbf{x})^2 \rangle, \tag{6.19}$$

where α_X is the static polarizability of the atomic species X and $\langle \mathbf{E}(\mathbf{x})^2 \rangle$ denotes the average squared electric field. For isotropic irradiance of energy density u_ω this reads

$$\langle \mathbf{E}(\mathbf{x})^2 \rangle = 4\pi \int_0^\infty \tfrac{1}{2} |\boldsymbol{\mathcal{E}}_\omega|^2 \mathrm{d}\omega = \frac{1}{\varepsilon_0} \int_0^\infty u_\omega \, \mathrm{d}\omega. \tag{6.20}$$

For blackbody radiation we find $\int_0^\infty u_\omega \mathrm{d}\omega = \pi^2 (k_\mathrm{B} T)^4 / (15 c^3 \hbar^3)$, cf. equation (6.14). The static polarizability for atomic hydrogen in the $1s$ ground state reads (Bransden *et al.* 1983)

$$\alpha_H = \tfrac{9}{2} 4\pi\varepsilon_0 a_0^3, \tag{6.21}$$

with the Bohr radius $a_0 = \hbar/(m_e \alpha c)$ and the fine-structure constant $\alpha = e^2/(4\pi\varepsilon_0\hbar) \approx 1/137$. Hence the energy shift for ground-state hydrogen in a thermal bath of temperature T can be approximated by (Jentschura *et al.* 2008)

$$\Delta E_{1s}(T) \approx -\frac{3\pi^3 k_\mathrm{B}^4 T^4}{5\alpha^3 m_\mathrm{e}^3 c^6}. \tag{6.22}$$

6.2 The dynamic Stark shift for an atom close to a hot sphere

Obviously, the Stark shift induced by an isotropic thermal bath, cf. equation (6.15), is again isotropic and will not accelerate an atom initially at rest. Hence we shall discuss the simple anisotropic case of an atom in the vicinity of a spherical blackbody.

As shown in figure 6.3, a sphere of radius R at a distance $r > R$ appears like a disk of radius $R_\mathrm{d} = R\sqrt{r^2 - R^2}/r$ at distance $r_d = (r^2 - R^2)/r$ (Guess 1962). In the spherical coordinates consistent with the notation introduced in equation (6.10) this corresponds to a region $\varphi \in [0, 2\pi)$, $\vartheta \in [0, \arctan(R_d/r_d)]$ or a solid angle

$$\Omega_\odot = 2\pi \left(1 - \frac{\sqrt{r^2 - R^2}}{r} \right). \tag{6.23}$$

Starting again from equation (6.8) we now find that the terms with the squared matrix elements are more evolved and read

$$\begin{aligned}
&\int_{\Omega_\odot} \left(|\langle m| \mathbf{r} \cdot \mathbf{e_k}^{[1]} |n\rangle|^2 + |\langle m| \mathbf{r} \cdot \mathbf{e_k}^{[2]} |n\rangle|^2 \right) \mathrm{d}\Omega = \\
&\quad = \frac{4\pi}{3} \left(1 - \frac{\sqrt{r^2 - R^2}}{r} \right) \left(|\langle m| x |n\rangle|^2 + |\langle m| y |n\rangle|^2 + |\langle m| z |n\rangle|^2 \right) + \\
&\qquad + \frac{\pi}{3} \frac{R^2 \sqrt{r^2 - R^2}}{r^3} \left(|\langle m| x |n\rangle|^2 + |\langle m| y |n\rangle|^2 - 2|\langle m| z |n\rangle|^2 \right).
\end{aligned} \tag{6.24}$$

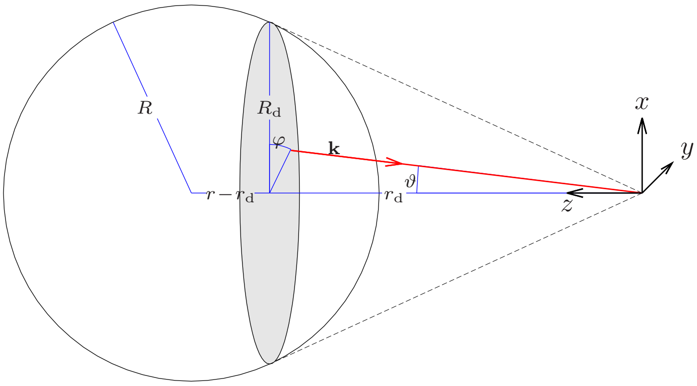

Figure 6.3 Sketch of an atom at distance r from a radiating sphere of radius R. As explained in (Guess 1962) the sphere then appears as a disc of radius R_d at distance r_d corresponding to a solid angle $\Omega_\odot$ as given in equation (6.23). The individual light rays propagate along wavevectors $\mathbf{k}$, cf. equation (6.10).

After using $|\boldsymbol{\mathcal{E}}_\omega|^2 = u_\omega/(2\pi\varepsilon_0)$, cf. appendix 6.C, inserting the blackbody relation given in (6.14) and using again $G(y)$ defined in (6.16) we obtain the total energy shift caused by a hot sphere,

$$\begin{aligned}\Delta E_n^{\odot} = {} & \frac{e^2}{48\pi^2 c^3 \varepsilon_0}\left(\frac{k_\mathrm{B}\,T}{\hbar}\right)^3 \sum_{m\neq n} G\left(\frac{\hbar(\omega_n-\omega_m)}{k_\mathrm{B}\,T}\right) \times \\ & \times \left[4\left(1-\frac{\sqrt{r^2-R^2}}{r}\right)\left(|\langle m|\,x\,|n\rangle|^2 + |\langle m|\,y\,|n\rangle|^2 + |\langle m|\,z\,|n\rangle|^2\right) + \right. \\ & \left. + \frac{R^2\sqrt{r^2-R^2}}{r^3}\left(|\langle m|\,x\,|n\rangle|^2 + |\langle m|\,y\,|n\rangle|^2 - 2|\langle m|\,z\,|n\rangle|^2\right)\right]. \qquad (6.25)\end{aligned}$$

As long as the atom is not oriented along some external magnetic field, no quantisation axis is defined and the term proportional to $(|x_{nm}|^2 + |y_{nm}|^2 - 2|z_{nm}|^2)$ vanishes. In this case we obtain the intuitive result where the shift for an atom close to a hot sphere is linked to the shift in an isotropic field as

$$\Delta E_n^{\odot} = \frac{1}{2}\left(1-\frac{\sqrt{r^2-R^2}}{r}\right)\Delta E_n = \frac{\Omega_\odot}{4\pi}\Delta E_n. \qquad (6.26)$$

Here we emphasise that the geometric prefactor is nothing but the ratio between the solid angle occupied by the radiation source and the whole 4π environment.

The gradient or dipole force is then given as $F_n^{\odot}(r) = -\partial_r \Delta E_n^{\odot}$ or

$$F_n^{\odot}(r) = \frac{\Delta E_n}{2R}\,\frac{R^3}{r^2\sqrt{r^2-R^2}}. \qquad (6.27)$$

6.3 Absorption rate and radiation pressure induced by blackbody radiation

As discussed in appendix 6.A, a perturbation such as the interaction with a light field will not only shift the energy levels of an atom, but also trigger transitions to other atomic states. From equations (6.9) and (6.14) we find that for the case of isotropic thermal radiation the natural line width of a state $|n\rangle$ will be broadened by an additional term (Farley *et al.* 1981; Jentschura *et al.* 2008)

$$\Gamma_n = \frac{e^2}{3\pi\hbar\varepsilon_0 c^3} \sum_{m\neq n} |\mathbf{r}_{mn}|^2 \frac{|\omega_n - \omega_m|^3}{e^{\frac{\hbar|\omega_n-\omega_m|}{k_\mathrm{B}T}} - 1}, \tag{6.28}$$

or, in terms of the oscillator strength f_{mn} defined in (6.17),

$$\Gamma_n = \frac{e^2}{2\pi m_e \varepsilon_0 c^3} \sum_{m\neq n} |f_{mn}| \frac{|\omega_n - \omega_m|^2}{e^{\frac{\hbar|\omega_n-\omega_m|}{k_\mathrm{B}T}} - 1}. \tag{6.29}$$

For an atom in the ground state, a transition to another (i.e. higher) state implies the absorption of a photon and the transfer of momentum. To estimate the effect of this *radiation pressure* we use that $\Gamma_n = \sum_{m\neq n} \tau_{nm}{}^{-1}$ where τ_{nm} is the transition time for the process of absorption of a photon of momentum $\hbar|\omega_n - \omega_m|/c$. The momentum transferred per unit time is proportional[4] to the radiation pressure which thus reads

$$F_n^{\mathrm{rp}}(r) \simeq \frac{e^2\hbar}{2\pi m_e \varepsilon_0 c^4} \frac{R^2}{4r^2} \sum_{m\neq n} |f_{mn}| \frac{|\omega_n - \omega_m|^3}{e^{\frac{\hbar|\omega_n-\omega_m|}{k_\mathrm{B}T}} - 1}. \tag{6.30}$$

Note that equation (6.28) was derived for the case of *isotropic* irradiance which is why we had to include the geometric factor $\pi R^2/r^2$, normalized by 4π, to obtain the radiation pressure from the field emitted by a hot sphere, cf. also equation (6.70) for the corresponding average Poynting vector. The radiation pressure from a hot sphere can also be expressed in terms of a potential energy,

$$V_n^{\mathrm{rp}}(r) = \frac{a_{\mathrm{rp}} R}{r} \qquad \text{with} \quad a_{\mathrm{rp}} = \frac{e^2\hbar}{8\pi m_e \varepsilon_0 c^4} R \sum_{m\neq n} |f_{mn}| \frac{|\omega_n - \omega_m|^3}{e^{\frac{\hbar|\omega_n-\omega_m|}{k_\mathrm{B}T}} - 1}. \tag{6.31}$$

A comparison with the dipole force (6.27) shows that the two forces show a very different distance behaviour.

To compare the relative strengths of the two forces we plot the main contributions to the total radiation pressure (at $r = R$) on a ground-state hydrogen atom in figure 6.4 and compare them to the prefactor of the dipole force as as given in equation (6.27) using the estimation from (6.22). Here we find that the radiation pressure is much

---

[4] For an exact treatment of the radiation pressure we would also have to consider the reemission of a photon. As this will typically be a spontaneous process it will on average not deposit any momentum, but require additional time. The force given here is thus an approximate upper bound for the radiation pressure.

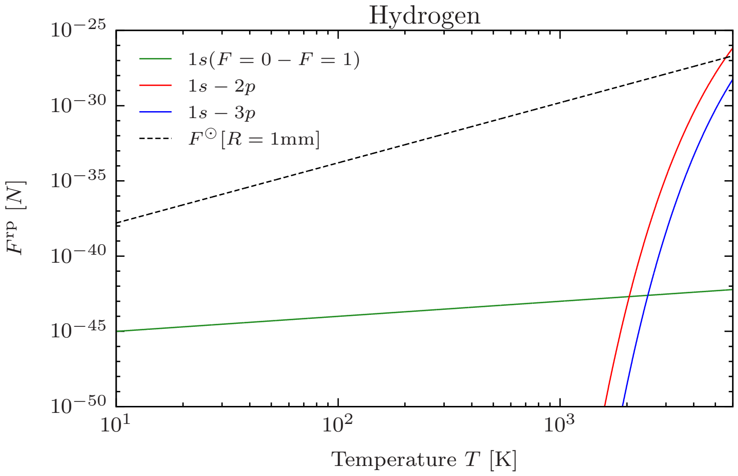

Figure 6.4 Contributions of the $1s-2p$, $1s-3p$ and the hyperfine $1s\,(F=0-F=1)$ transitions to the total radiation pressure on a ground-state hydrogen atom at $r=R$. The comparison with the prefactor for the gradient force $F^{\odot}=\Delta E/(2R)$ shows that radiation pressure can be ignored for $T\lesssim 5000\,\mathrm{K}$ at $R=1\,\mathrm{mm}$. The numbers for the oscillator strengths and transition frequencies were taken from (Wiese *et al.* 2009) and are displayed in table 6.1.

smaller than the dipole force for temperatures less than a few thousand Kelvin. In figure 6.5 a similar plot for lithium shows that radiation pressure there dominates earlier, as the first optical transition energy is only $\hbar\Delta\omega_{2s-3p}\approx 1.85\,\mathrm{eV}$.

However, we point out that these comparisons are only crude estimates since the approximation to use the static polarizability for the dipole force breaks down once a specific transition becomes important, which is exactly when the radiation pressure force comes into play, cf. also figure 6.2.

6.4 Limits of our model

In this section we shall address the validity and the limits of several assumptions we made about the thermal radiation of the hot sphere interacting with an atom.

The first and major assumption is that the sphere is a blackbody. As explained in appendix 6.B, a blackbody is an idealised concept where the absorption and emission coefficient is equal to one for all frequencies. The thermal emission of realistic objects can be connected to the Planckian energy density by introducing the emissivity, a property describing the spectral and directional radiation characteristics of a given material. As the emissivity itself may depend on the temperature, the total power emitted by a non-black body might not scale with the fourth power of temperature as predicted by the Stefan-Boltzmann law (Siegel *et al.* 1992).

Additionally, the derivation of Planck's law, cf. appendix 6.B, uses the assumption of a sufficiently large cavity capable of supporting all relevant wavelengths (Bohren

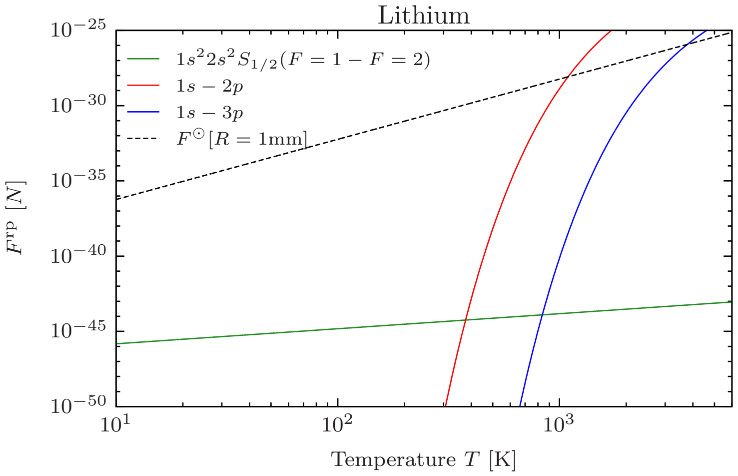

Figure 6.5 Contributions of the $2s-3p$, $2s-4p$ and the hyperfine $2s\,(F=1-F=2)$ transitions to the total radiation pressure on a ground-state lithium atom at $r=R$. The prefactor for the gradient force $F^{\odot}=\Delta E/(2R)$ was computed using the DC Stark shift approximation (6.19) using $\alpha_{\mathrm{Li}}\approx 36.5\alpha_{\mathrm{H}}$ (Yan *et al.* 1996). Note, however, that this approximation breaks down at temperatures of a few hundred Kelvin when the individual transitions become relevant. The numerical values for the oscillator strengths and transition frequencies were taken from (Wiese *et al.* 2009) and are displayed in table 6.1.

et al. 1983; Reiser *et al.* 2013). Therefore this approximation breaks down if one or more dimensions of the object shrinks to sizes comparable to the thermal wavelength $\lambda_{\mathrm{th}}\approx 2.898\times10^{-3}\,\mathrm{m}\cdot\mathrm{K}/T$ (Bransden *et al.* 1983). The thermal radiation from (sub-) micron sized objects is therefore strongly modified by geometric effects and they will typically emit less power than expected from a the Stefan-Boltzmann law (Greffet *et al.* 2002; Martynenko *et al.* 2005; Rosenberg *et al.* 2008; Wuttke *et al.* 2013; Yu *et al.* 2010) although amplified emission is possible too (Reiser *et al.* 2013).

As the main objective of this work is to investigate the basic mechanism of optical forces from thermal radiation sources, we decided to stick to the approximate but nevertheless generic scenario of a small blackbody. For radii larger than a few microns, this assumption should not be too far off.

For an atom in the near-field of an object a wide range of factors have to be considered, such as evanescent thermal fields or interactions of the atom with its own field reflected off the surface. These and other effects are incorporated in the research on van der Waals or Casimir-Polder forces (Antezza *et al.* 2005; Ellingsen *et al.* 2012; Klimchitskaya *et al.* 2009; Obrecht *et al.* 2007) but shall not be discussed here. We expect that a full treatment would show that the forces described in the present work merge with those interactions close to the surface.

Table 6.1 Parameters for the transitions in atomic hydrogen and lithium used for figures 6.2, 6.4 and 6.5 as collected in (Wiese *et al.* 2009). For the hyperfine transition in Li we used $f_{nm} = 2\pi m_e \varepsilon_0 c^3/(\omega_{mn}^2 e^2)\, g_m/g_n\, A_{nm}$ to compute the oscillator strength from the given spontaneous emission coefficient A_{nm} and degeneracies g_m and g_n.

	transition	frequency ω_{mn} [Hz]	osc. strength f_{mn}
H:	$1s - 2p$	1.54948×10^{16}	0.41641
	$1s - 3p$	1.83641×10^{16}	0.079142
	$1s\,{}^2S_{1/2}\,(F = 0 - F = 1)$	8.92467×10^{9}	5.7786×10^{-12}
^{7}Li:	$1s^2 2s - 1s^2 2p$	2.80738×10^{15}	0.74696
	$1s^2 2s - 1s^2 3p$	5.82527×10^{15}	4.711×10^{-3}
	$1s^2 2s\,{}^2S_{1/2}\,(F = 1 - F = 2)$	5.04442×10^{9}	2.71408×10^{-12}

Appendix 6.A Energy shift and decay rate in time-dependent perturbation theory

In this short overview we follow Sakurai (Sakurai *et al.* 2011) to calculate the shift of the eigenenergies of a nondegenerate state $|n\rangle$, $H_0 |n\rangle = \hbar\omega_n |n\rangle$, exposed to a time-dependent, perturbative interaction $\epsilon V(t)$ where $V(t)$ is linear and self-adjoint and a parameter $0 < \epsilon \ll 1$. Inserting a state

$$|\psi(t)\rangle = \sum_m c_m(t) e^{-i\omega_m t} |m\rangle \tag{6.32}$$

into the Schrödinger equation and projecting on a state $e^{-i\omega_n t} |n\rangle$ gives

$$\dot{c}_n(t) = -\epsilon \frac{i}{\hbar} \sum_m c_m(t)\, e^{i(\omega_n - \omega_m)t} \langle n| V(t) |m\rangle , \tag{6.33}$$

which can be solved by a formal integration

$$c_n(t) - c_n(t_0) = -\epsilon \frac{i}{\hbar} \sum_m \int_{t_0}^{t} c_m(t')\, e^{i(\omega_n - \omega_m)t'} \langle n| V(t') |m\rangle \,\mathrm{d}t'. \tag{6.34}$$

Before we continue, note and keep in mind that $\sum_m$ here actually denotes the sum over the discrete and and integral over the continuous eigenstates of H.

Let us assume that our state is initially an eigenstate of H_0, for example, $|\psi(t_0)\rangle = e^{-i\omega_n t_0} |n\rangle$, hence $c_k(t_0) = \delta_{k,n}$. An iterative application of equation (6.34) then gives

$$\begin{aligned} c_n(t) = 1 - \epsilon \frac{i}{\hbar} \int_{t_0}^{t} \langle n| V(t') |n\rangle \,\mathrm{d}t' - \epsilon^2 \frac{1}{\hbar^2} \sum_m \int_{t_0}^{t} \int_{t_0}^{t'} e^{i(\omega_n - \omega_m)t'} \langle n| V(t') |m\rangle \times \\ \times e^{-i(\omega_n - \omega_m)t''} \langle m| V(t'') |n\rangle \,\mathrm{d}t'' \,\mathrm{d}t' + \mathcal{O}(\epsilon^3), \end{aligned} \tag{6.35}$$

and for $k \neq n$ we obtain

$$c_k(t) = -\epsilon \frac{i}{\hbar} \int_{t_0}^{t} e^{-i(\omega_n - \omega_k)t'} \langle k| V(t') |n\rangle \,\mathrm{d}t' + \mathcal{O}(\epsilon^2). \tag{6.36}$$

Let us define

$$\Delta_n := i\hbar \frac{\dot{c}_n(t)}{c_n(t)} \tag{6.37}$$

such that $c_n(t) = \exp(-i \int_{t_0}^{t} \Delta_n(t')\mathrm{d}t'/\hbar)$. If Δ_n turns out to be time independent we find

$$|\psi(t)\rangle = e^{-i(\omega_n t + \Delta_n (t - t_0)/\hbar)}\,|n\rangle + \sum_{m\neq n} c_m(t) e^{-i\omega_m t}\,|m\rangle\,. \tag{6.38}$$

This suggests the interpretation that the real part of Δ_n gives the *energy shift* ΔE_n of our initial state $|n\rangle$, whereas the imaginary part is linked to the induced *decay rate* Γ_n to other states (Farley *et al.* 1981; Haas *et al.* 2006; Sakurai *et al.* 2011), i.e.

$$\Delta_n = \Delta E_n - \tfrac{i\hbar}{2}\Gamma_n. \tag{6.39}$$

Plugging the result from equation (6.35) into our definition (6.37) shows that, up to second order in ϵ and using $\omega_{nm} := \omega_n - \omega_m$,

$$\Delta_n = \epsilon\,\langle n|\,V(t)\,|n\rangle - \epsilon^2 \frac{i}{\hbar} \sum_{m\neq n} \int_{t_0}^{t} e^{i\omega_{nm}(t-t')}\,\langle n|\,V(t)\,|m\rangle\,\langle m|\,V(t')\,|n\rangle\,\mathrm{d}t'. \tag{6.40}$$

Note that the matrix element $\langle n|\,V(t)\,|n\rangle$ does not contribute to the second order term.

To compare our formalism with the results from time-independent perturbation theory let us assume a slowly increasing perturbation $V(t) = V_0 e^{\eta t}$ with $0 < \eta \ll 1$. Let us further set $t_0 \to -\infty$ such that equation (6.35) reads

$$c_n(t) = 1 - \epsilon \frac{i}{\eta\,\hbar}\,\langle n|\,V_0\,|n\rangle\, e^{\eta t} + \epsilon^2 \frac{1}{\eta\,\hbar^2} \sum_m \frac{|\langle m|\,V_0\,|n\rangle|^2 e^{2\eta t}}{2i(\omega_n - \omega_m + i\eta)} + \ldots \tag{6.41}$$

and after using equation (6.40) we get

$$\Delta_n = \epsilon\,\langle n|\,V_0\,|n\rangle\, e^{\eta t} + \epsilon^2 \sum_{m\neq n} \frac{|\langle m|\,V_0\,|n\rangle|^2 e^{2\eta t}}{\hbar(\omega_{nm} + i\eta)}. \tag{6.42}$$

Taking the limit $\eta \to 0$ allows us to compare our interpretations with the results from time-independent perturbation theory. To do so, we use (Sakurai *et al.* 2011)

$$\lim_{\eta\to 0} \frac{1}{x + i\,\eta} = \mathcal{P}\frac{1}{x} - i\pi\delta(x) \tag{6.43}$$

where $\mathcal{P}$ denotes the Cauchy principal value and $\delta(x)$ is Dirac's delta function. Thus we obtain

$$\Delta E_n = \epsilon\,\langle n|\,V_0\,|n\rangle + \epsilon^2 \sum_{m\neq n} \frac{|\langle m|\,V_0\,|n\rangle|^2}{\hbar\,\omega_{nm}}, \tag{6.44}$$

$$\hbar\Gamma_n = -2\,\mathrm{Im}\,\Delta_n = 2\pi\epsilon^2 \sum_{m\neq n} |\langle m|\,V_0\,|n\rangle|^2 \delta(\hbar\,\omega_{nm}), \tag{6.45}$$

and, as expected, this is the same energy shift as we would find in stationary perturbation theory (Sakurai *et al.* 2011).

As another important example we assume an oscillating perturbation $V(t) = V_0 \cos(\omega t) e^{\eta t}$, $0 \leq \eta \ll 1$, and calculate a time-dependent shift as

$$i\hbar \frac{\dot{c}_n(t)}{c_n(t)} = \epsilon \langle n| V_0 |n\rangle \cos(\omega t) + \\ \epsilon^2 \sum_{m \neq n} \frac{|\langle m| V_0 |n\rangle|^2 \cos(\omega t) \left[(\omega_{nm} + i\eta)\cos(\omega t) + i\omega \sin(\omega t)\right]}{\hbar((\omega_{nm} + i\eta)^2 - \omega^2)} + \dots \quad (6.46)$$

where we already set $t_0 \to -\infty$ and $\exp(2\eta t) \to 1$. In many examples the perturbation is an electromagnetic wave with frequencies in the range of 10^{13}Hz to 10^{15}Hz, thus oscillating too fast for atomic time-scales in the order of nanoseconds. Hence the atoms only "feel" an average, effectively time-independent potential and we redefine (with $\tau = 2\pi/\omega$)

$$\Delta_n \simeq \lim_{\eta \to 0} \frac{i\hbar}{\tau} \int_{-\tau/2}^{\tau/2} \frac{\dot{c}_n(t)}{c_n(t)} \mathrm{d}t, \quad (6.47)$$

$$\Delta E_n \simeq \frac{\epsilon^2}{4\hbar} \sum_{m \neq n} |\langle m| V_0 |n\rangle|^2 \left(\frac{1}{\omega_{nm} - \omega} + \frac{1}{\omega_{nm} + \omega} \right), \quad (6.48)$$

$$\Gamma_n \simeq \frac{\epsilon^2 \pi}{2\hbar^2} \sum_{m \neq n} |\langle m| V_0 |n\rangle|^2 \delta(|\omega_{nm}| - \omega). \quad (6.49)$$

Appendix 6.B Planck's law of blackbody radiation

Planck's derivation of the spectral energy density of blackbody radiation and the associated introduction of Planck's constant h marks without doubt one of the greatest milestones in modern physics (Planck 1901). It goes without saying that this crucial topic has been discussed in numerous textbooks, the following short introduction is based on the book by Bransden and Joachain (Bransden *et al.* 1983).

A blackbody is the idealised concept of an object that absorbs all the radiation of all wavelengths. Kirchhoff's law states that if such an object is in thermal equilibrium with its environment of temperature T, it has to reemit the same amount of energy as it absorbs. Stefan could show empirically that the total power emitted per unit area depends only on the temperature as

$$P/A = \sigma T^4, \quad (6.50)$$

where $\sigma = \pi^2 k_\mathrm{B}^4/(60\hbar^3 c^2)$ has later been named the Stefan-Boltzmann constant. By the end of the nineteenth century this and some other characteristics of blackbody radiation were well established, but the spectral energy density remained a mystery. Theoretical derivations by Rayleigh and Jeans predicted infinite energies for high frequencies which obviously were not confirmed by experiments.

Apart from the cosmic microwave background (Fixsen *et al.* 1996), reasonably accurate blackbody radiation can be obtained from a box with a small hole. Imagine the box being made of a well absorbing material and kept at constant temperature. Then light entering the box through the whole might be reflected several times inside the box, but in the end it will certainly be absorbed before it can leave the box. Hence, all the radiation coming out of the whole has been emitted from the walls and therefore should carry blackbody signature.

Inside the box we find standing waves with wavelengths $\lambda = 2L/n$, where L is the length of each edge of our cubic box and

$$n = \sqrt{n_x^2 + n_y^2 + n_z^2}. \tag{6.51}$$

The natural numbers n_i give the numbers of antinodes of the standing waves in each dimension. Obviously, many different combinations of n_x, n_y and n_z give the same total n. Drawing n_x, n_y and n_z in three independent axes shows that for large n or, equivalently, large L the combinations meeting $\sqrt{n_x^2 + n_y^2 + n_z^2} \leq n$ fill one eighth of a sphere of radius n. The total number of modes of wavelengths larger than λ then read

$$N(\lambda) = \frac{1}{8}\frac{4\pi n^3}{3} = \frac{4\pi L^3}{3\lambda^3} \tag{6.52}$$

and the number of modes in an interval $[\lambda, \lambda + \mathrm{d}\lambda]$ is then $\mathrm{d}N_\lambda = N(\lambda) - N(\lambda + \mathrm{d}\lambda) \approx 4\pi L^3/\lambda^4\,\mathrm{d}\lambda$. As described nicely by Reiser and Schächter (Reiser *et al.* 2013) and mentioned in section 6.4, this derivation of the density of states is based on the assumption that the volume is large compared to all wavelengths. Given this assumption the mean spectral energy density is now the number of modes per volume L^3 multiplied by the mean energy of each mode, i.e.

$$u_\lambda \mathrm{d}\lambda = 2\frac{\mathrm{d}N_\lambda}{L^3}\left\langle \epsilon_\lambda \right\rangle. \tag{6.53}$$

The factor of 2 accounts for the two possible polarizations of the standing waves in the box.

Rayleigh and Jeans assumed that each mode could carry any real value of energy $\epsilon_\lambda \equiv \epsilon$, independent of its wavelength. These energies would be distributed according to Boltzmann statistics with $\beta = 1/(k_\mathrm{B}T)$, such that the mean energy reads

$$\langle \epsilon \rangle = \frac{\int_0^\infty \epsilon \exp(-\epsilon\beta)\mathrm{d}\epsilon}{\int_0^\infty \exp(-\epsilon\beta)\mathrm{d}\epsilon} = 1/\beta. \tag{6.54}$$

This mean energy is independent of the wavelength and hence the integrated energy density is proportional to λ^{-4}, resulting in the “ultraviolet catastrophe” mentioned earlier.

Plank’s revolutionary idea was to propose that the energies of the modes take discrete values $\epsilon_\lambda = m\,\epsilon_\mathrm{p}(\lambda)$, with $m \in \mathbb{N}$ and $\epsilon_\mathrm{p}(\lambda)$ yet to be determined. The integrals from equation (6.54) are then replaced by sums as

$$\langle \epsilon_\lambda \rangle = \frac{\sum_{m=0}^\infty m\,\epsilon_\mathrm{p} \exp(-m\,\epsilon_\mathrm{p}\beta)}{\sum_{m=0}^\infty \exp(-m\,\epsilon_\mathrm{p}\beta)} = \frac{\epsilon_\mathrm{p}}{e^{\epsilon_\mathrm{p}\beta} - 1}. \tag{6.55}$$

To comply with an improved version of Wien's approximation stating $u_\lambda = f(\lambda T)/\lambda^5$ (Planck 1900; Wien 1896) with some unknown function f, the energy per light quantum must be

$$\epsilon_\mathrm{p} = hc/\lambda = \hbar\omega \tag{6.56}$$

where $h \approx 6.626 \times 10^{-34}$Js is Planck's constant and $\hbar = h/(2\pi)$. Finally we obtain the spectral energy density of blackbody radiation

$$u_\lambda \,\mathrm{d}\lambda = \frac{8\pi hc}{\lambda^5} \frac{1}{e^{hc/(k_\mathrm{B}T\lambda)} - 1} \,\mathrm{d}\lambda, \tag{6.57}$$

or, using $u_\omega \,\mathrm{d}\omega = u_\lambda \,\mathrm{d}\lambda$ with $\lambda = 2\pi c/\omega$ and $\mathrm{d}\lambda = 2\pi c/\omega^2 \,\mathrm{d}\omega$,

$$u_\omega \,\mathrm{d}\omega = \frac{\hbar}{\pi^2 c^3} \frac{\omega^3}{e^{\hbar\omega/(k_\mathrm{B}T)} - 1} \,\mathrm{d}\omega. \tag{6.58}$$

Appendix 6.C Poynting vectors and energy densities for incoherent electromagnetic fields

In sections 6.1 and 6.2 we need to connect the spectral energy density u_ω with the amplitudes of electric fields, $|\mathcal{E}_\omega|^2$. As this is an error-prone task we shall provide a few examples which might prove useful not only for the topic of thermally radiating spheres.

The energy density u and energy flux density, i.e. Poynting vector, $\mathbf{S}$ are defined as (Jackson 1999)

$$\begin{aligned} u(\mathbf{x},t) &= \tfrac{1}{2}(\mathbf{E}(\mathbf{x},t) \cdot \mathbf{D}(\mathbf{x},t) + \mathbf{B}(\mathbf{x},t) \cdot \mathbf{H}(\mathbf{x},t)), \\ \mathbf{S}(\mathbf{x},t) &= \mathbf{E}(\mathbf{x},t) \times \mathbf{H}(\mathbf{x},t). \end{aligned} \tag{6.59}$$

For fields in vacuum these expressions are simplified as $\mathbf{D} = \varepsilon_0 \mathbf{E}$ and $\mathbf{H} = \mathbf{B}/\mu_0$, $\mu_0 = 1/(\varepsilon_0 c^2)$,

$$\begin{aligned} u(\mathbf{x},t) &= \tfrac{\varepsilon_0}{2} \left(|\mathbf{E}(\mathbf{x},t)|^2 + c^2 |\mathbf{B}(\mathbf{x},t)|^2 \right), \\ \mathbf{S}(\mathbf{x},t) &= \varepsilon_0 \, c^2 \mathbf{E}(\mathbf{x},t) \times \mathbf{B}(\mathbf{x},t). \end{aligned} \tag{6.60}$$

Note that for complex vectors $\mathbf{a}, \mathbf{b} \in \mathbb{C}^3$, the dot product shall be defined as $\mathbf{a} \cdot \mathbf{b} = \sum_i a_i^* b_i$, with z^* denoting the complex conjugate of $z \in \mathbb{C}$.

For plane waves with a wavevector $\mathbf{k} = \omega \boldsymbol{\kappa}/c$ one can easily verify that $\mathbf{B} = \boldsymbol{\kappa} \times \mathbf{E}/c$ and $\boldsymbol{\kappa} \cdot \mathbf{E} = 0$. Using some properties of the cross product we find

$$u(\mathbf{x},t) = \varepsilon_0 |\mathbf{E}(\mathbf{x},t)|^2 \quad \text{and} \quad \mathbf{S}(\mathbf{x},t) = \varepsilon_0 \, c \, |\mathbf{E}(\mathbf{x},t)|^2 \boldsymbol{\kappa} = c \, u(\mathbf{x},t) \boldsymbol{\kappa}. \tag{6.61}$$

When dealing with highly oscillating fields it can be useful to average over a period $\tau = 2\pi/\omega$. Defining $\mathbf{E}(\mathbf{x},t) = \mathrm{Re}[\mathbf{E}(\mathbf{x}) e^{-i\omega t}]$ and $\langle f(t) \rangle_t := \tau^{-1} \int_0^\tau f(t) \,\mathrm{d}t$ leads to

$$\left\langle |\mathbf{E}(\mathbf{x},t)|^2 \right\rangle_t = \frac{1}{4} \left\langle \left(\mathbf{E}(\mathbf{x}) e^{-i\omega t} + \mathbf{E}^*(\mathbf{x}) e^{i\omega t} \right)^2 \right\rangle_t = \frac{1}{2} |\mathbf{E}(\mathbf{x})|^2. \tag{6.62}$$

After averaging over one period of time the energy density and the Poynting vector of equation (6.61) change to

$$u(\mathbf{x}) := \langle u(\mathbf{x},t)\rangle_t = \frac{\varepsilon_0}{2}|\mathbf{E}(\mathbf{x})|^2 \quad \text{and} \quad \mathbf{S}(\mathbf{x}) := \langle \mathbf{S}(\mathbf{x},t)\rangle_t = \frac{\varepsilon_0\, c}{2}|\mathbf{E}(\mathbf{x})|^2\boldsymbol{\kappa}. \tag{6.63}$$

A superposition of plane waves, $\mathbf{E} = \sum_\mathbf{k} \mathbf{E}_\mathbf{k}$ and $\mathbf{B} = \sum_\mathbf{k} \mathbf{B}_\mathbf{k} = \frac{1}{c}\sum_\mathbf{k} \boldsymbol{\kappa} \times \mathbf{E}_\mathbf{k}$, results in an energy density and Poynting vector reading

$$\begin{aligned} u &= \frac{\varepsilon_0}{2}\sum_{\mathbf{k},\mathbf{k}'}\Big((\mathbf{E}_\mathbf{k}\cdot\mathbf{E}_{\mathbf{k}'})(1+\boldsymbol{\kappa}\cdot\boldsymbol{\kappa}') - (\boldsymbol{\kappa}\cdot\mathbf{E}_{\mathbf{k}'})(\boldsymbol{\kappa}'\cdot\mathbf{E}_\mathbf{k})\Big), \\ \mathbf{S} &= \varepsilon_0\, c\sum_{\mathbf{k},\mathbf{k}'}\Big((\mathbf{E}_\mathbf{k}\cdot\mathbf{E}_{\mathbf{k}'})\boldsymbol{\kappa}' - (\mathbf{E}_{\mathbf{k}'}\cdot\boldsymbol{\kappa})\mathbf{E}_\mathbf{k}\Big). \end{aligned} \tag{6.64}$$

For the example of two counter-propagating waves with $\boldsymbol{\kappa}_1 = -\boldsymbol{\kappa}_2$ this simplifies to

$$u = \varepsilon_0\left(|\mathbf{E}_{\mathbf{k}_1}|^2 + |\mathbf{E}_{\mathbf{k}_2}|^2\right) \quad \text{and} \quad \mathbf{S} = \varepsilon_0\, c\left(|\mathbf{E}_{\mathbf{k}_1}|^2 - |\mathbf{E}_{\mathbf{k}_2}|^2\right)\boldsymbol{\kappa}_1. \tag{6.65}$$

To describe a superposition of incoherent waves we set

$$\mathbf{E}_\mathbf{k}(\mathbf{x},t) = |\boldsymbol{\mathcal{E}}_\mathbf{k}|\cos(\omega t + \phi_\mathbf{k})(\mathbf{e}_\mathbf{k}{}^{[1]}\cos(\alpha_\mathbf{k}) + \mathbf{e}_\mathbf{k}{}^{[2]}\sin(\alpha_\mathbf{k})) \tag{6.66}$$

where $\phi_\mathbf{k} \in [0, 2\pi)$ describes the phase and $\alpha_\mathbf{k} \in [0, 2\pi)$ fixes the direction of polarization in the plane spanned by the unitvectors $\mathbf{e}_\mathbf{k}{}^{[1]}$ and $\mathbf{e}_\mathbf{k}{}^{[2]}$. Averaging over the uncorrelated phases and polarizations then results in

$$\langle \mathbf{E}_\mathbf{k}(\mathbf{x},t)\cdot\mathbf{E}_{\mathbf{k}'}(\mathbf{x},t)\rangle_{\phi_\mathbf{k},\phi_{\mathbf{k}'},\alpha_\mathbf{k},\alpha_{\mathbf{k}'}} = |\boldsymbol{\mathcal{E}}_\mathbf{k}|^2\,\delta(\mathbf{k}-\mathbf{k}')/2. \tag{6.67}$$

For incoherent radiation received from a direction Ω we may write $\mathbf{E}(\mathbf{x},t) = \int \mathbf{E}_\mathbf{k}\,\mathrm{d}^3k \equiv \iint \mathbf{E}_\mathbf{k}(\mathbf{x},t)\,\mathrm{d}\Omega\,\mathrm{d}\omega$ and this results in simple expressions for the averaged energy density and flux as

$$\langle u\rangle = \frac{\varepsilon_0}{2}\iint |\boldsymbol{\mathcal{E}}_\mathbf{k}|^2\,\mathrm{d}\Omega\,\mathrm{d}\omega \quad \text{and} \quad \langle \mathbf{S}\rangle = \frac{\varepsilon_0\, c}{2}\iint |\boldsymbol{\mathcal{E}}_\mathbf{k}|^2\boldsymbol{\kappa}\,\mathrm{d}\Omega\,\mathrm{d}\omega. \tag{6.68}$$

If the field's amplitude only depends on the frequency and not on the direction of incidence, i.e. $\boldsymbol{\mathcal{E}}_\mathbf{k} \equiv \boldsymbol{\mathcal{E}}_\omega$, and if we assume isotropic irradiance we obtain

$$\langle u\rangle = \frac{\varepsilon_0}{2}4\pi\int_0^\infty |\boldsymbol{\mathcal{E}}_\omega|^2\,\mathrm{d}\omega \quad \text{and} \quad \langle \mathbf{S}\rangle = 0. \tag{6.69}$$

Defining the spectral energy density via $\langle u\rangle = \int_0^\infty u_\omega\,\mathrm{d}\omega$ we finally see that $u_\omega = 2\pi\varepsilon_0|\boldsymbol{\mathcal{E}}_\omega|^2$.

If the radiation is not isotropic but originates from a sphere of radius R at distance $r > R$ we find, using the notation introduced in figure 6.3,

$$\begin{aligned} \langle u\rangle &= \frac{\varepsilon_0}{2}\Omega_\odot\int_0^\infty |\boldsymbol{\mathcal{E}}_\omega|^2\,\mathrm{d}\omega = \frac{1}{2}\left(1 - \frac{\sqrt{r^2-R^2}}{r}\right)\int_0^\infty u_\omega\,\mathrm{d}\omega, \\ \langle \mathbf{S}\rangle &= \frac{\varepsilon_0\, c}{2}\int_{\Omega_\odot}\boldsymbol{\kappa}\,\mathrm{d}\Omega\int_0^\infty |\boldsymbol{\mathcal{E}}_\omega|^2\,\mathrm{d}\omega = -\mathbf{e}_z\frac{R^2 c}{4\,r^2}\int_0^\infty u_\omega\,\mathrm{d}\omega. \end{aligned} \tag{6.70}$$

7 Publication

Attractive optical forces from blackbody radiation

M. Sonnleitner*, M. Ritsch-Marte and H. Ritsch

Blackbody radiation around hot objects induces ac Stark shifts of the energy levels of nearby atoms and molecules. These shifts are roughly proportional to the fourth power of the temperature and induce a force decaying with the third power of the distance from the object. We explicitly calculate the resulting attractive blackbody optical dipole force for ground state hydrogen atoms. Surprisingly, this force can surpass the repulsive radiation pressure and actually pull the atoms against the radiation energy flow towards the surface with a force stronger than gravity. We exemplify the dominance of the "blackbody force" over gravity for hydrogen in a cloud of hot dust particles. This overlooked force appears relevant in various astrophysical scenarios, in particular, since analogous results hold for a wide class of other broadband radiation sources.

Phys. Rev. Lett. **111**, 023601 (2013) doi: 10.1103/PhysRevLett.111.023601

Light forces on particles microscopically arise from the basic physics of absorption and redistribution of photon momentum. For light far detuned from any optical resonance, the interaction is dominated by coherent scattering and can be attributed to an optical potential corresponding to the dynamic Stark shift of the involved atomic energy levels. Red-detuned light induces a negative Stark shift on low energy states so that particles are high-field seekers drawn towards regions of higher radiation intensity. From precision experiments in atomic spectroscopy it has been known for at least half a century that blackbody radiation also induces Stark shifts of atomic states. In particular the ground state is shifted towards lower energy (Angstmann

---

*The author of the present thesis performed all of the calculations in this publication.

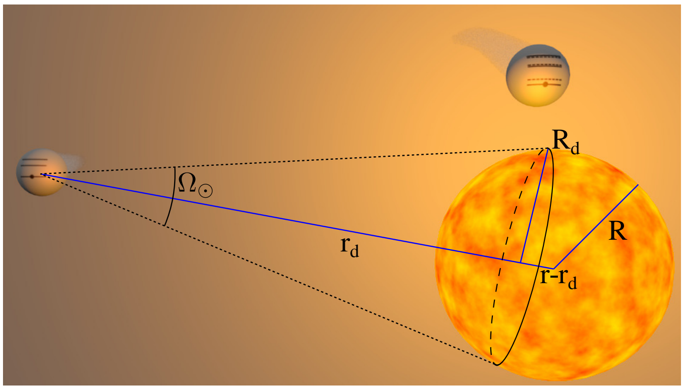

Figure 7.1 An artist's view of the interaction between an atom and a hot sphere of radius R. From a distance r it appears as a disk of effective radius R_d at distance r_d.

et al. 2006; Farley *et al.* 1981; Gallagher *et al.* 1979; Itano *et al.* 1982; Jentschura *et al.* 2008; Mitroy *et al.* 2009; Porsev *et al.* 2006; Safronova *et al.* 2010). Albeit a small shift, it constitutes an important perturbation of precision spectroscopy proportional to the radiated blackbody intensity (Parthey *et al.* 2011) growing with the fourth power of temperature. Obviously, for a thermal source of finite size the radiation field intensity decays with distance from the surface inducing a spatially varying Stark shift. Our central claim now is that this shift constitutes a spatially varying optical potential exerting an effective optical dipole force on neutral atoms.

In this Letter we study the surprising and peculiar properties of this—so far overlooked—optical force for the simple but generic example of individual hydrogen atoms interacting with "hot" spheres. Since the first electronic excitation of hydrogen is in the far UV region, the largest part of a typical blackbody radiation spectrum is below the first optically coupled atomic excited state, i.e., the $2p$ state. Thus it induces an attractive dispersive dipole force analogous to the dominant force in optical tweezers (Ashkin *et al.* 1986). Of course, at the same time some narrow high frequency components are resonantly absorbed and spontaneously reemitted generating a repulsive radiation pressure. The relative size of these two components depends on temperature. As shown below, for hydrogen these forces can be explicitly calculated by generalizing known derivations of the Stark shift (Farley *et al.* 1981; Jentschura *et al.* 2008) exhibiting a surprising dominance of the attractive dipole force up to a limiting temperature. Geometrical considerations as shown in Fig. 7.1 reveal that in the far field the blackbody intensity decays with the second inverse power of the distance r of the atom, implying an unusual $1/r^3$ effective attractive force.

Let us mention here that for an atom very close to a (hot) surface additional interactions of similar magnitude such as van der Waals forces or forces arising from zero-point and thermal fluctuations of the electromagnetic field appear (Antezza *et al.* 2005; Obrecht *et al.* 2007). These are also mostly attractive and depend on the detailed material properties of the surface. We will not consider these in our generic calculations.

In the following we will briefly review the calculation of the temperature-dependent Stark shift in a thermal field and then generalize it to the case of radiation emitted from a finite-size spherical blackbody. The corresponding potential and forces are then evaluated as a function of the radius R and the temperature T of the sphere. The resulting forces are then compared to other forces (possibly) acting on the particle, such as gravity or attraction by a dc Stark shift from a charged sphere. We finally apply the model to atomic hydrogen moving close to a cloud of small thermal particles, where the "blackbody optical force" turns out to surpass the effect of gravity.

Let us recall some important results on polarizability and the Stark shift of light atoms and, in particular, hydrogen. The static polarizability $\alpha_H = (9/2)4\pi\varepsilon_0 a_0^3$ of ground state hydrogen atoms was calculated almost a century ago (Buckingham 1937; Epstein 1916), with a_0 being the Bohr radius. As atomic hydrogen has its first radiative transition at an energy of $E_{2p} - E_{1s} \approx 10.2\,\mathrm{eV}$, most of the blackbody radiation components are well below this frequency (up to temperatures of a few thousand kelvin). Hence, using this static polarizability the ground state energy shift can roughly be estimated to be $\Delta E = -\alpha_H \langle \mathbf{E}^2 \rangle / 2$, with the time-averaged square of the total electric field $\mathbf{E}$; cf. Eq. (7.3). A quantitatively more reliable calculation requires summation of the perturbative contributions of all higher-lying states including their energies and dipole matrix elements, which has already been carried out by several authors (Farley *et al.* 1981; Jentschura *et al.* 2008).

The perturbative expression of the dynamic Stark shift of an energy level $|n\rangle$ in an isotropic thermal bath explicitly reads (Farley *et al.* 1981; Jentschura *et al.* 2008)

$$\Delta E_n = \frac{e^2 (k_\mathrm{B} T)^3}{6\pi^2 \varepsilon_0 (c\hbar)^3} \sum_{i;\, m \neq n} f\left(\frac{\hbar(\omega_n - \omega_m)}{k_\mathrm{B} T}\right) |\langle n| \, r_i \, |m\rangle|^2, \tag{7.1}$$

where $\hbar\omega_n$ denotes the energy of the unperturbed state $|n\rangle$, r_i is the electron-core distance operator, and $f(y)$ is Cauchy's principal value integral

$$f(y) = \mathcal{P} \int_0^\infty \frac{x^3}{e^x - 1} \left(\frac{1}{y + x} + \frac{1}{y - x}\right) \mathrm{d}\,x. \tag{7.2}$$

In general, the sign and magnitude of the Stark shift depend on the chosen atomic or molecular state and on the radiation field temperature T (Farley *et al.* 1981; Jentschura *et al.* 2008). However, it will mostly cause a negative energy shift for the ground state. For the $1s$ state of hydrogen it can be approximated by (Jentschura *et al.* 2008)

$$\Delta E_{1s}(T) \approx -\frac{3\pi^3 (k_\mathrm{B} T)^4}{5\alpha^3 (m_\mathrm{e} c^2)^3}, \tag{7.3}$$

which gives a small shift of $\Delta E_{1s}/\hbar \approx -1\,\mathrm{Hz}$ for $T = 400\,\mathrm{K}$. For higher excited atomic states the blackbody shift is much larger, reaching a few kHz (Farley *et al.* 1981). For these states, however, the resonant absorption and emission processes discussed below also become important.

One arrives at similar expressions for radiation-induced absorption and stimulated transition rates between different levels resulting in an effective line width given by (Farley *et al.* 1981; Jentschura *et al.* 2008)

$$\Gamma_n = \frac{e^2}{3\pi\, c^3 \hbar \varepsilon_0} \sum_{i;m\neq n} |\langle n|\, r_i\, |m\rangle|^2 \frac{|\omega_n - \omega_m|^3}{\exp\left(\frac{\hbar|\omega_n-\omega_m|}{k_\mathrm{B}\, T}\right) - 1}. \tag{7.4}$$

This gives a good estimate for the expected radiation pressure force. For hydrogen in its $1s$ ground state, the temperature-dependent transition time to the $2p$ state given via $\tau_{1s\to 2p}(T) = 1/W_{1s\to 2p}(T)$ and $\Gamma_n = \sum_{m\neq n} W_{n\to m}$ is extremely long, yielding $\tau_{1s\to 2p}(300\,\mathrm{K}) \approx 10^{162}\,\mathrm{s}$ and $\tau_{1s\to 2p}(1000\,\mathrm{K}) \approx 10^{42}\,\mathrm{s}$. Note, however, that one gets a very rapid increase of this absorption with temperature, over several tens of orders of magnitude, giving $\tau_{1s\to 2p}(6000\,\mathrm{K}) \approx 0.2\,\mathrm{s}$ around the solar temperature, where the force thus changes from attraction to repulsion.

For the sake of completeness let us also include the hyperfine transition within the hydrogen ground state manifold, i.e., the famous 21-cm line. For this radio transition we use the Rayleigh-Jeans approximation for the thermal energy density and the known relations between Einstein's absorption and emission coefficients to obtain the absorption rate $W_{F0\to F1}(T) = 3\hbar\,\omega_{21} A_{21}/(k_B T)$ with $\omega_{21} \approx 8.9\,\mathrm{GHz}$ being the angular frequency of the transition and $A_{21} \approx 2.87 \times 10^{-15}\,\mathrm{s}^{-1}$ (Lequeux 2005). We see that these rates grow linearly in temperature but are typically very small, i.e., $W_{F0\to F1}(100\,\mathrm{K}) \approx 1.26 \times 10^{-11}\,\mathrm{s}^{-1}$. Hence, transitions take several thousand years and only deposit negligible momentum. This shows that resonant excitations due to thermal radiation can be neglected for neutral hydrogen in the ground state, at least up to temperatures of a few thousand K. In this regime the force induced by the ac Stark shift will dominate.

In an isotropic thermal bath, due to symmetry, the blackbody field cannot have any directional effect on the movement of the atom, but can only induce friction and diffusion. Thermal light radiated from a *finite* source, however, creates a spatially varying Stark potential giving rise to a net force. As a generic example we consider a hot sphere of radius R with an atom located at a distance $r \geq R$ from its center. As depicted in Fig. 7.1 (cf. also (Guess 1962)) the atom then sees radiation from the projection of the sphere as a disk of radius R_d at distance r_d, with $R_\mathrm{d} = R\sqrt{1-(R/r)^2}$ and $r_\mathrm{d} = (r^2 - R^2)/r$ covering a solid angle of

$$\Omega_\odot = 2\pi \left(1 - \frac{r_\mathrm{d}}{\sqrt{r_\mathrm{d}^2 + R_\mathrm{d}^2}}\right) = 2\pi \left(1 - \frac{\sqrt{r^2 - R^2}}{r}\right). \tag{7.5}$$

After a somewhat lengthy calculation to integrate over all incoherent contributions of the electric field radiated from a hot sphere, we finally arrive at a simple and intuitive result for the spatial dependence of the induced Stark shift,

$$\Delta E_n^\odot(r) = \frac{1}{2}\left(1 - \frac{\sqrt{r^2 - R^2}}{r}\right)\Delta E_n = \frac{\Omega_\odot}{4\pi}\Delta E_n, \tag{7.6}$$

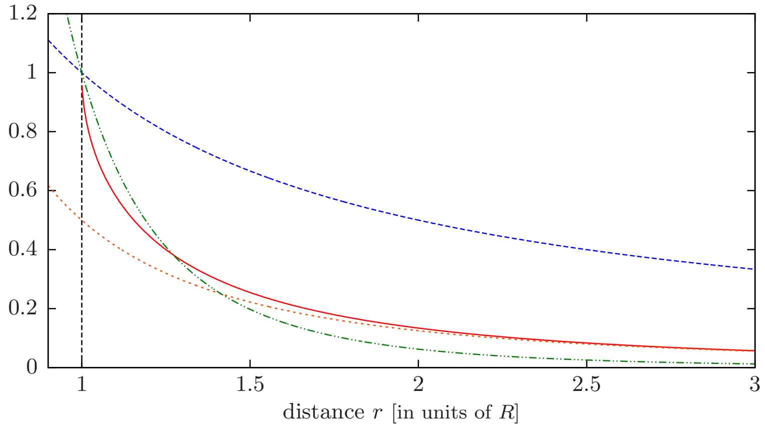

Figure 7.2 Comparison of the spatial decay of various interaction strengths between an atom and a hot sphere of radius R: blackbody ($1-\sqrt{r^2-R^2}/r$, red solid line), gravity (R/r, blue dashed line) and electrostatic potential (R^4/r^4, green dash-dotted line), cf. also Eq. (7.10). The orange dashed line extrapolates the asymptotic inverse quadratic long-range radiation potential, $R^2/(2r^2)$.

where ΔE_n is the isotropic shift for a state $|n\rangle$ computed from Eq. (7.1). The increasing ac Stark shift for an atom approaching a hot sphere thus induces the rapidly growing dipole force

$$F_n^{\odot}(r) = -\partial_r \Delta E_n^{\odot}(r) = \frac{\Delta E_n}{2}\frac{R^2}{r^2\sqrt{r^2-R^2}}. \tag{7.7}$$

For negative ΔE_n, as, e. g., for an atom in the ground state, the atom is pulled towards the sphere. Directly at the surface, where the validity of our model ends, the force diverges, but the potential energy remains finite: $\Delta E_n^{\odot}(R) = \Delta E_n/2$. This shift corresponds to illumination by half of the full 4π solid angle. The spatial dependence of the different potentials in Eq. (7.10) is shown in Fig. 7.2 with the blackbody potential falling off as $\sim R^2/(2r^2)$ for $r \gg R$.

In the derivation above we set the ambient temperature around the sphere and the atom to zero. If $T_{\mathrm{amb}} \neq 0$, the radiation from the sphere coming in from a solid angle $\Omega_{\odot}$ will add up with background radiation from $4\pi - \Omega_{\odot}$. Equation (7.7) will thus change to $F_n^{\odot}(r) = (\Delta E_n(T) - \Delta E_n(T_{\mathrm{amb}}))R^2/(2r^2\sqrt{r^2-R^2})$. The effects of a surrounding temperature bath are thus of the order of $T^4 - T_{\mathrm{amb}}^4$ and will be ignored in the upcoming simple examples.

This "new" attractive force is rather unexpected and—so far at least in principle—quite intriguing. In order to assess the practical importance, however, as a next step we will compare the forces created by the blackbody Stark shift to other atom-sphere interactions, such as gravitational forces or forces induced by electrostatic shifts. Gravitational forces may be derived from the potential

$$V_{\mathrm{G}}(r) = -G\frac{m\,M_{\odot}}{r} = -G\frac{4\,\pi\,m\,\rho\,R^3}{3\,r} = -\frac{a_{\mathrm{G}}R}{r}, \tag{7.8}$$

with $M_\odot$ being the mass of the sphere of density ρ and m the mass of the atom, which for atomic hydrogen is $m \approx m_{\text{proton}}$.

If the central sphere carries a surface charge of density σ_Q, defined as $4\pi R^2 \sigma_Q = Q$, the atom will experience an additional electrostatic Stark shift, which for the ground state of atomic hydrogen is found to be (Bransden *et al.* 1983)

$$\Delta E_{1s}^{[\mathrm{Q}]} = -\frac{9a_0^3 Q^2}{16\pi\,\varepsilon_0 r^4} = -\frac{9\pi a_0^3 \sigma_Q^2 R^4}{\varepsilon_0 r^4} = -\frac{a_{\mathrm{Q}} R^4}{r^4}. \tag{7.9}$$

In total, a neutral atom interacting with a hot sphere of radius R, mass density ρ, temperature T, and surface charge density σ_Q thus sees the total potential

$$V(r) = -\frac{a_{\mathrm{G}} R}{r} - \frac{a_{\mathrm{Q}} R^4}{r^4} - a_{\mathrm{BB}} \left(1 - \frac{\sqrt{r^2 - R^2}}{r}\right), \tag{7.10}$$

where we have set $a_{\mathrm{BB}} = |\Delta E_n|/2$. If the energy shift is positive, we must change the sign to get a repulsive interaction.

As forces following power laws have no natural length scale, we will use the radius R of the sphere as a reference length and first compare the potential energies generated by these different interactions at the surface. Figure 7.3 displays the different prefactors for different temperatures and surface charge densities as a function of sphere radius. Here, for a_{BB} we have used the approximated Eq. (7.3).

As the blackbody potential at the surface is independent of the sphere size, it clearly dominates gravity for small objects ($R \ll 1\mathrm{m}$). For an interplanetary dust particle of $R = 1\,\mu\mathrm{m}$, $\rho = 2\,\mathrm{g/cm^3}$ radiating at $T = 100\,\mathrm{K}$ (Evans 1993), we obtain $a_{\mathrm{BB}} \approx 1.7 \times 10^8 a_{\mathrm{G}}$. For an adult human, i.e., a sphere of water with a total mass of 70 kg, radiating at $T = 300\,\mathrm{K}$, $a_{\mathrm{BB}} \approx 0.42\, a_{\mathrm{G}}$. For larger masses the blackbody potential only yields a weak perturbation; e. g., for our sun (with $R = 6.96 \times 10^8\,\mathrm{m}$, $\rho = 1.408\,\mathrm{g/cm^3}$, $T = 5778\,\mathrm{K}$ (Lequeux 2005)) we get $a_{\mathrm{BB}} \approx 5.5 \times 10^{-15} a_{\mathrm{G}}$. Hence, blackbody radiation can dominate over gravity and perturb particle orbits in a way that Kepler ellipses change to rosettes or spiral trajectories towards the surface.

Note that aberrational effects due to the relative motion of atom and sphere generate an additional weak friction force of a different nature, leading to the known Poynting-Robertson drag on dust particles orbiting a star (Guess 1962; Lequeux 2005). For fast atoms an analogous effect should be added to the gradient forces described here.

For the sake of brevity we also ignored the fact that thermal radiation from micron-sized particles will certainly not follow Planck's law (Odashima *et al.* 2009). A more elaborate calculation would therefore produce somewhat different numbers without changing the basic physical mechanisms and their magnitude.

The above considerations show that particularly strong effects can be expected from *hot and light objects.* As a simple, but striking example we model a hot cloud as the integral effect of a dilute random ensemble of thermally radiating small particles. For a mass density ρ and a spherically symmetric Gaussian particle distribution of

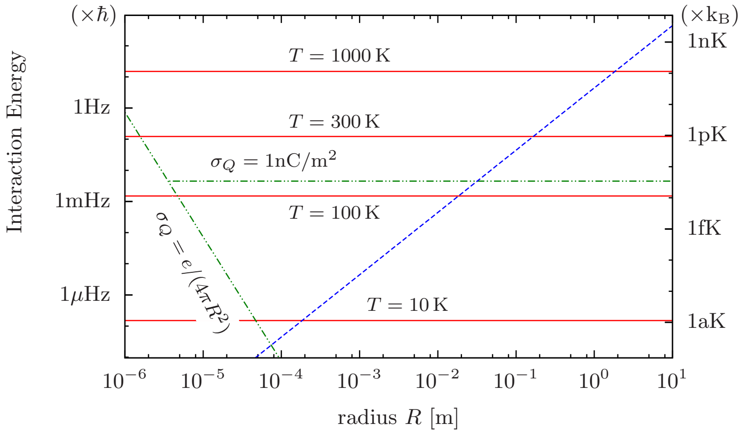

Figure 7.3 Comparison of the energy shift of the hydrogen ground state induced by blackbody radiation (a_{BB}, red lines), the electrostatic interaction (a_{Q}, green dash-dotted) and the gravitational potential energy (a_{G}, blue dashed line) at the sphere surface as function of the radius R for a mass density $\rho = 1\,\mathrm{g/cm^3}$.

width σ, $g(r) = \exp[-r^2/(2\sigma^2)]/[(2\pi)^{3/2}\sigma^3]$, the mean gravitational potential can be computed explicitly to give

$$\langle V_{\mathrm{G}}(r)\rangle = -\frac{N\,a_{\mathrm{G}}\,R}{r}\,\mathrm{erf}\left(\frac{r}{\sqrt{2}\,\sigma}\right) \tag{7.11}$$

with the error function $\mathrm{erf}(x) = 2/\sqrt{\pi}\int_0^x \exp(-t^2)\mathrm{d}t$. For the blackbody contribution we use the approximation $V_{\mathrm{BB}}(r \gg R) \simeq -a_{\mathrm{BB}}R^2/(2r^2)$ to obtain

$$\langle V_{\mathrm{BB}}(r)\rangle = -\frac{\pi\,N\,a_{\mathrm{BB}}\,R^2}{r}\mathcal{P}\int_0^\infty s\,g(s)\ln\left(\frac{r+s}{|r-s|}\right)\mathrm{d}s. \tag{7.12}$$

At the center of the cloud we get the simple expressions

$$\langle V_{\mathrm{G}}(0)\rangle = -\frac{N\,a_{\mathrm{G}}R}{\sqrt{\pi/2}\,\sigma} \quad \text{and} \quad \langle V_{\mathrm{BB}}(0)\rangle = -\frac{N\,a_{\mathrm{BB}}R^2}{2\sigma^2}. \tag{7.13}$$

The blackbody radiation induced interaction will dominate for parameters satisfying $\langle V_{\mathrm{BB}}(0)\rangle/\langle V_{\mathrm{G}}(0)\rangle > 1$ or, making use of Eq. (7.3), when

$$\frac{\sigma}{R} < \frac{\sqrt{\pi}a_{\mathrm{BB}}}{2\sqrt{2}a_{\mathrm{G}}} \simeq \frac{9\pi^{5/2}(k_{\mathrm{B}}T)^4}{80\sqrt{2}\alpha^3 G\,\rho\,(m_{\mathrm{e}}c^2)^3\,m_{\mathrm{p}}\,R^2}. \tag{7.14}$$

As illustrated in Fig. 7.4, we thus arrive at the quite surprising result that even for “large” dust clouds with $\sigma = 10, \ldots, 100\,\mathrm{m}$, gravitational interaction with hydrogen is not only assisted but even dominated by blackbody induced dipole forces.

While the idea of an attractive optical force induced by blackbody radiation appears rather exotic and unintuitive at first, we have nevertheless shown that in many cases,

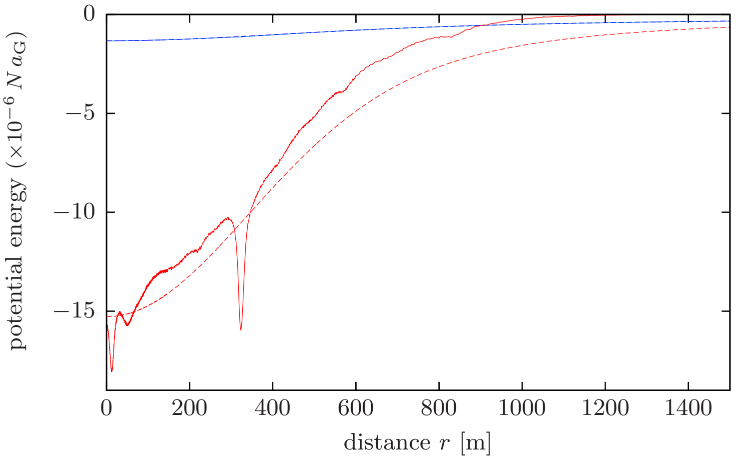

Figure 7.4 Gravitational [blue lines] and blackbody induced [red lines] potential of randomly distributed spheres of size $R = 5\,\mu$m and temperature $T = 300\,$K such that $a_{\mathrm{BB}} \approx 1.1 \times 10^9\, a_{\mathrm{G}}$ for $\rho = 1\,\mathrm{g/cm}^3$. The dashed lines show the potentials calculated in Eqs. (7.11) and (7.12) using a distribution of width $\sigma = 300\,$m. The solid lines are the result of a random sample of $N = 8000$ Gaussian distributed spheres.

as, e. g., for ground state hydrogen atoms, the "blackbody force" dominates the repulsive radiation pressure. For small objects it can even be stronger than the gravitational interaction. Despite its outgoing radiative energy flow, a hot finite-size sphere thus attracts neutral atoms and molecules, a force, which to the best of our knowledge, has been overlooked so far. Although in many cases it will be very weak and challenging to measure in the lab, one can think of many tailored or astrophysical scenarios, which should be revisited in the context of these findings. Let us note here that at sufficiently high temperatures radiation pressure dominates and the total force changes its sign. Hence, only above a critical, rather high, temperature hydrogen atoms will be repelled by blackbody radiation as intuitively expected. Note that the dipole force is state selective and can induce spatial separation of atoms in different long-lived states.

Our results actually go beyond the case of blackbody radiation and basically also hold for other broadband incoherent light sources, with narrower frequency distributions but higher photon flux compared to blackbody radiation. This potentially generates much stronger forces which are strongly species specific. On the microscopic scale it is also important to note that the precise shape of the hot particle surface will be decisive and strong enhancement effects could be expected near tips, grooves, and edges. Hence, our findings could go much beyond the originally intended scope, e. g., towards the effect of hot microstructured surfaces in vacuum chambers or the total energy shift induced by cosmic background radiation.

Acknowledgements

We thank Sabine Schindler and Josef Stöckl for stimulating discussions, Miles Padgett and Jean Dalibard for helpful comments and acknowledge support by the ERC Advanced Grant (Project No. 247024 catchIT).

8 Additional calculations on optical forces from blackbody radiation

The following chapter contains some additional results on the dynamics generated by optical forces from finite sources of thermal radiation. Most of these calculations were performed after the publication of the paper presented in chapter 7.

First we present a simple estimation on how the cross section for atom-sphere collisions change if an additional blackbody force is incorporated. This is followed by a short discussion of the radiation forces on Rayleigh scatterers in the thermal field of a larger hot sphere.

In section 8.3 we elaborate on the forces generated by an ensemble of hot spheres as shortly mentioned in the previous chapter, cf. figure 7.4. Apart from spherically symmetric sphere configurations we also introduce a scenario in toroidal symmetry.

In section 8.4 we finally develop a framework to calculate the coupled dynamics of an ensemble of spheres and a gas of atoms. We also explore whether the additional radiative interaction influences the stability of this dynamic mixture of two types of particles in section 8.4.2.

8.1 Estimating the scattering cross section for atom-sphere collisions

Consider a particle of mass m and initial velocity v_0 entering a radially symmetric potential energy landscape $V(r)$ from $r_0 = \sqrt{x_0^2 + b^2} \to \infty$, where b is the (finite) impact parameter. For a monotonic $V(r)$ with $\lim_{r\to\infty} V(r) = 0$ we can compute a critical impact parameter $b_{r'}(v_0)$ for which the closest distance of the particle to the origin is $r_{\min}[b_{r'}(v_0)] = r'$:

From energy conservation we know that $E_{\mathrm{kin}}(r_0 \to \infty) = E_{\mathrm{kin}}(r') + V(r')$ or $v' = \sqrt{v_0^2 - 2\,V(r')/m}$. On the other hand, conservation of angular momentum gives $b_{r'}(v_0)\,v_0 = r'\,v'$ such that

$$b_{r'}(v_0) = r'\sqrt{1 - 2V(r')/(m\,v_0^2)}. \tag{8.1}$$

If the source of the interaction is a sphere of radius R then $b_R(v_0)$ gives the impact parameter for which the particle scratches along the surface of said sphere. Any particle with an impact parameter $b \leq b_R(v_0)$ will therefore hit the sphere and thus the collisional cross section is given by

$$\sigma_c(v_0) = \pi\,b_R(v_0)^2 = \pi\,R^2\left(1 - 2\frac{V(R)}{m\,v_0^2}\right). \tag{8.2}$$

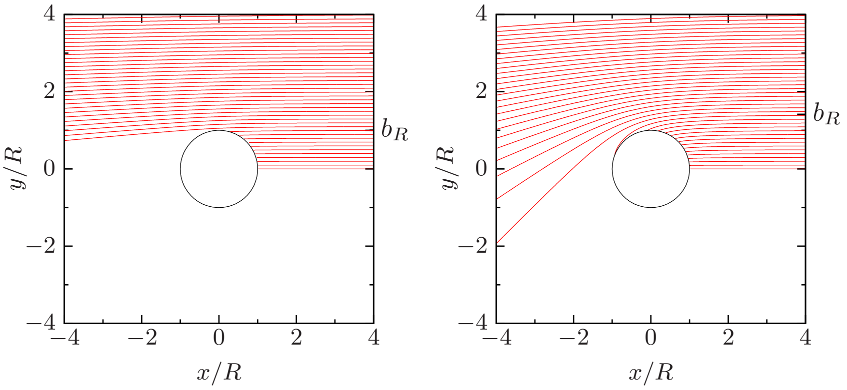

Figure 8.1 Comparison of $2D$ atom-sphere scattering without (left figure) and with (right figure) an attractive blackbody potential. Atoms (trajectories drawn red) are incident from the far right and interact with the spheres (indicated by the black circles) via the potential $V(r) = -a_\mathrm{G} R/r - a_\mathrm{BB}(1 - \sqrt{r^2 - R^2}/r)$; left figure: $a_\mathrm{G} = E_\mathrm{kin}(r_0)/10$, $a_{BB} = 0$, right figure: $a_{BB} = E_\mathrm{kin}(r_0) = 10\, a_\mathrm{G}$ with an initial kinetic energy $E_\mathrm{kin}(r_0)$ at $r_0 \gg R$. Notice how the critical impact factor for collisions b_R changes, cf. also equation (8.2).

Using the notation introduced in chapter 7, figure 8.1 shows the trajectories of atoms scattering from a massive and thermally radiating sphere generating a potential energy $V(r) = -a_\mathrm{G} R/r - a_\mathrm{BB}(1 - \sqrt{r^2 - R^2}/r)$, such that $V(R) = -a_\mathrm{G} - a_\mathrm{BB}$. For a very small initial relative velocity v_0 we see a modified scattering behaviour as $b_R(v_0)$ is visibly larger than R.

If the atom is part of an ensemble where the velocity follows a Maxwell-Boltzmann distribution such that $m \left\langle v_0^2 \right\rangle /2 = k_\mathrm{B} T/2$, the averaged collisional cross section reads

$$\langle \sigma_c \rangle = \pi\, R^2 \left(1 + 2 \frac{a_\mathrm{G} + a_\mathrm{BB}}{k_\mathrm{B} T} \right). \tag{8.3}$$

8.2 Estimating the radiation forces between a hot and a cold dust particle

As can be seen from figure 7.3, the energies for the interaction between a hot blackbody and an atom are vanishingly small. But although the arguments in the introductory chapter 6 are at first based on the atomic Stark-shifts, the final estimation using the static polarizability (cf. equation (6.19)) is valid for atom clusters or nanoparticles as well.

If the particle in the vicinity of a hot sphere is not an atom but a small Rayleigh scatterer of radius $\widetilde{R}$ and refractive index n, its reaction to an external field can again be described by a scalar polarizability

$$\alpha = 4\pi\varepsilon_0 \widetilde{R}^3 \frac{n^2 - 1}{n^2 + 2}. \tag{8.4}$$

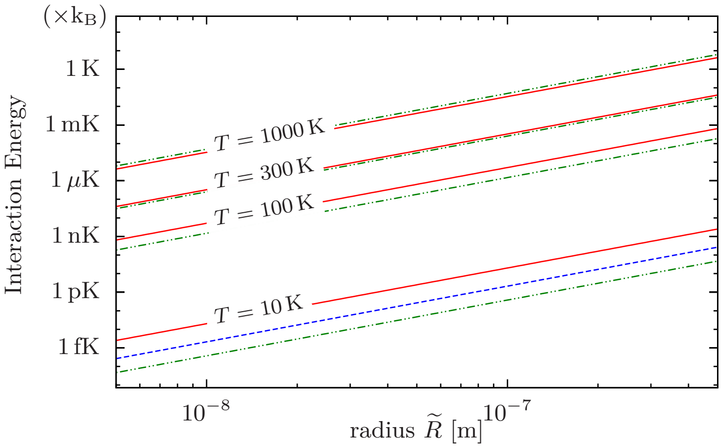

Figure 8.2 Comparison of the prefactors for the gravitational potential, a_{G} (blue dashed line), the dipole force, a_{BB} (red solid lines) and the radiation pressure, a_{rp} (green dash dotted lines) for the interaction of a sphere of radius $R = 5\,\mu$m with a Rayleigh scatterer of variable radius $\widetilde{R}$ and the complex refractive index of ice (data taken from (Warren 1984)). Both spheres are assumed to have a mass density of $1\mathrm{g/cm}^3$. We see that the repulsive radiation pressure is stronger than the attractive gradient force for $T > 300\,$K, both are much stronger than gravity. Note that the radius of the central sphere enters in the expression for a_{rp}, cf. equation (8.7), a larger blackbody will therefore repel the Rayleigh particle even stronger.

Of course, the complex refractive index of any material changes drastically in the range of frequencies covered by typical blackbody radiation. Adopting equations (6.19) and (6.26) to our case we find that the attractive potential for a Rayleigh particle next to a sphere of radius R and temperature T is given by

$$V_{\mathrm{BB}}(r) = -\left(1 - \frac{\sqrt{r^2 - R^2}}{r}\right) \pi \widetilde{R}^3 \int_0^\infty u_\lambda \,\mathrm{Re}\left[\frac{n(\lambda)^2 - 1}{n(\lambda)^2 + 2}\right] \mathrm{d}\lambda, \tag{8.5}$$

where $u_\lambda \,\mathrm{d}\lambda$ is the differential energy density for blackbody radiation for wavelengths in the range $[\lambda, \lambda + \mathrm{d}\lambda]$, see also (6.57). The terms behind the brackets with the spatial dependence can be combined to a coupling strength a_{BB}. Figure 8.2 shows a comparison of this a_{BB} with the prefactors for the gravitational potential, a_{G}, and the repulsive radiation pressure, a_{rp}, cf. equation (8.7), respectively.

Increasing the attractive gradient force here also implies that the repulsive radiation pressure is strongly enhanced. This force is proportional to the imaginary part of the polarizability α and the wavevector $\mathbf{k} = 2\pi/\lambda\,\boldsymbol{\kappa}$ of the incident light, $\mathbf{F}_{\mathrm{rp}}(r) = \mathrm{Im}[\alpha]\mathbf{k}\,\langle \mathbf{E}(r)^2\rangle$. In the thermal light field at distance r from a hot sphere of radius R and temperature T we thus use the expression for the Poynting vector (6.70) to obtain a radiation pressure

$$F_{\mathrm{rp}}(r) = \frac{\pi R^2}{r^2} \widetilde{R}^3 \int_0^\infty \frac{2\pi u_\lambda}{\lambda} \,\mathrm{Im}\left[\frac{n(\lambda)^2 - 1}{n(\lambda)^2 + 2}\right] \mathrm{d}\lambda. \tag{8.6}$$

Integration gives the corresponding potential $V_{\mathrm{rp}}(r) = a_{\mathrm{rp}}R/r$ with

$$a_{\mathrm{rp}} = \pi R \widetilde{R}^3 \int_0^\infty \frac{2\pi u_\lambda}{\lambda} \operatorname{Im}\left[\frac{n(\lambda)^2 - 1}{n(\lambda)^2 + 2}\right] \mathrm{d}\lambda. \tag{8.7}$$

Of course, these estimates only hold for sufficiently small particles. Once the particle's radius $\widetilde{R}$ is comparable to the thermal wavelength one has to use Mie scattering techniques.

8.3 Averaged interactions for ensembles of small spheres

The gravitational and radiative interaction between an individual atom and a single sphere are, of course, very small. In the following we shall therefore discuss the cumulative effect of N hot spheres distributed according to a density function $g(\mathbf{r})$ with $\int g(\mathbf{r})\,\mathrm{d}^3 r = 1$. If a sphere at position $\mathbf{r}'$ generates a potential $V(|\mathbf{r} - \mathbf{r}'|)$, then the averaged cumulative potential is given by

$$\langle V(\mathbf{r})\rangle = N \int_{\mathbb{R}^3} V(|\mathbf{r} - \mathbf{r}'|) g(\mathbf{r}')\,\mathrm{d}^3 r'. \tag{8.8}$$

From now on we will only consider the gravitational interaction, $V_{\mathrm{G}}(\mathbf{r}) = -a_{\mathrm{G}}R/\mathbf{r}$, and the gradient force induced by hot radiating spheres, $V_{\mathrm{BB}}(\mathbf{r}) \simeq -a_{\mathrm{BB}}R^2/(2|\mathbf{r}|^2)$. The radiation pressure induced by blackbody radiation described in equation (6.30), $V_{\mathrm{rp}}(\mathbf{r}) = a_{\mathrm{rp}}R/|\mathbf{r}|$, is—at least for atoms—typically much weaker than the gradient force and shall be ignored here. If needed, its effects can be obtained from the result for gravity by replacing a_{G} by $-a_{\mathrm{rp}}$.

The mean potential defined in equation (8.8) suffers from two assumptions: First, we don't take into account that our point of observation must not lie inside one of the spheres of radius R which corresponds to the requirement $|\mathbf{r} - \mathbf{r}'| > R$. But for small spheres distributed over a wide volume this would obviously have a very little effect on the total result. The same is true for the error we introduce by using a the approximations for $|\mathbf{r}| \gg R$ for the radiation induced interactions. In figure 8.3 the mean potentials calculated via equation (8.8) are compared to the average potentials using the correct distance behaviour and show very good agreement.

In equation (8.8) we assumed that the potentials of all individual spheres can be simply added up. This is certainly true for gravitational interactions but for the radiative interactions this might not be the case: the assumption is valid only if the electromagnetic field emitted from a sphere at position $\mathbf{r}'$ and measured at a position $\mathbf{r}$ is not absorbed by other blackbodies (partly) blocking the solid angle $\Omega_\odot(\mathbf{r} - \mathbf{r}')$ (cf. equation (6.23)) and if the light is not scattered away or absorbed by some background gas.

The arguments above boil down to the requirement of a dilute distribution of spheres. A good indicator whether the spheres are too closely packed is if the maximum of the mean potential exceeds the value for a thermal bath, cf. equation (6.26).

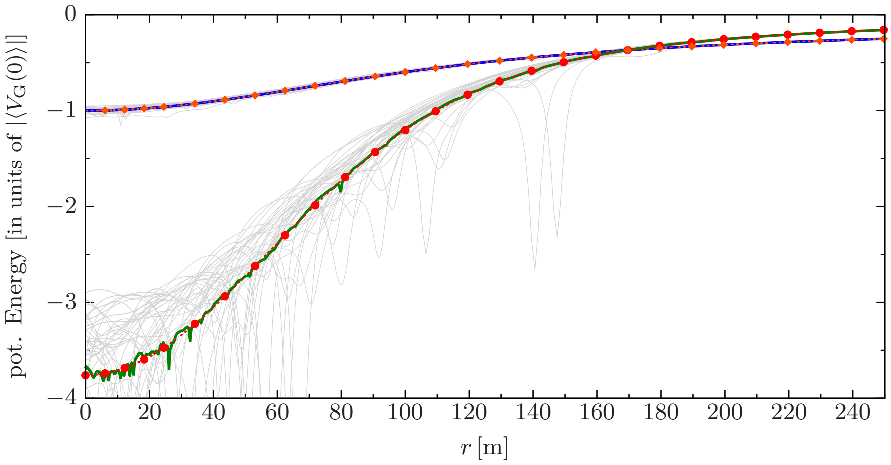

Figure 8.3 Calculated averaged gravitational (orange diamonds) and blackbody potential (red circles) for a spherically symmetric Gaussian distribution of hot spheres, cf. equations (8.12) and (8.15). The blue and green solid lines show the mean potentials obtained by averaging over 800 ensembles, 35 potentials are shown as examples in grey. We see a very good agreement between the mean results despite the fact that the calculated results use the approximation where $V_{\mathrm{BB}} \sim r^{-2}$ which is valid only for $r \gg R$. The parameters used are $R = 10\,\mu\mathrm{m}$, $a_{\mathrm{BB}} = 3 \times 10^7 a_{\mathrm{G}}$; the width of the Gaussian distribution is $\sigma = 50\,\mathrm{m}$; the total number of spheres $N = 1000$.

As this must not be the case we require

$$\min_{\mathbf{r}\in\mathbb{R}^3} \langle V_{\mathrm{BB}}(\mathbf{r})\rangle < \Delta E(T) = -2\, a_{\mathrm{BB}} \tag{8.9}$$

8.3.1 Average interactions in spherical symmetry

Assume N hot spheres spread according to a spherically symmetric particle distribution $g(r) = 4\pi\rho(r)$ with $\int_0^\infty \rho(r) r^2\,\mathrm{d}r = 1$. Choosing w.l.o.g. that $\mathbf{r} = r\mathbf{e}_z$ and after integrating over the polar angle we obtain an average gravitational potential

$$\langle V_{\mathrm{G}}(r)\rangle = -\frac{N a_{\mathrm{G}} R}{2} \int_0^\infty \int_0^\pi \frac{\rho(r')}{\sqrt{r^2 + r'^2 - 2rr'\cos\vartheta'}} r'^2 \sin\vartheta'\,\mathrm{d}\vartheta'\mathrm{d}r'. \tag{8.10}$$

The integral over the azimuthal angle ϑ' gives

$$\int_0^\pi \frac{\sin\vartheta'}{\sqrt{r^2 + r'^2 - 2rr'\cos\vartheta'}}\mathrm{d}\vartheta' = \begin{cases} 2/r & \text{for } r' < r, \\ 2/r' & \text{for } r' > r. \end{cases} \tag{8.11}$$

such that

$$\langle V_{\mathrm{G}}(r)\rangle = -N a_{\mathrm{G}} R \left(\tfrac{1}{r} \int_0^r \rho(r') r'^2\,\mathrm{d}r' + \int_r^\infty \rho(r') r'\,\mathrm{d}r' \right) \tag{8.12}$$

for $r > 0$. At the origin we obtain $\langle V_{\mathrm{G}}(0)\rangle = -N a_{\mathrm{G}} R \int_0^\infty \rho_X(t, r') r'\,\mathrm{d}r'$.

The potential from the gradient force induced by the blackbody radiation of the spheres decays as $\sim |\mathbf{r}-\mathbf{r}'|^{-2}$ and hence we find after integrating over the polar angle

$$\langle V_{\mathrm{BB}}(r)\rangle = -\frac{N a_{\mathrm{BB}} R^2}{4}\int_0^\infty \int_0^\pi \frac{\rho(r')}{r^2 + r'^2 - 2rr'\cos\vartheta'} r'^2 \sin\vartheta' \,\mathrm{d}\vartheta' \,\mathrm{d}r'. \tag{8.13}$$

Subsequent integration over the azimuthal angle gives

$$\int_0^\pi \frac{\sin\vartheta'}{r^2 + r'^2 - 2rr'\cos\vartheta'} \mathrm{d}\vartheta' = \frac{1}{rr'}\ln\left(\frac{r+r'}{|r-r'|}\right). \tag{8.14}$$

The remaining radial integral has a singularity at $r' = r$ but for smooth particle distributions the Cauchy principal value integral

$$\langle V_{\mathrm{BB}}(r)\rangle = -\frac{N a_{\mathrm{BB}} R^2}{4}\mathcal{P}\int_0^\infty \rho(r')\frac{r'}{r}\ln\left(\frac{r+r'}{|r-r'|}\right)\mathrm{d}r' \tag{8.15}$$

exists for $r > 0$. At the origin we use

$$\lim_{r\to 0}\frac{r'}{r}\ln\left(\frac{r+r'}{|r-r'|}\right) = 2 \tag{8.16}$$

to compute that $\langle V_{\mathrm{BB}}(0)\rangle = -N a_{\mathrm{BB}} R^2/2\int_0^\infty \rho(r')\,\mathrm{d}r'$.

In the publication presented in chapter 7 we introduced a Gaussian particle distribution, i.e. $\rho(r) = 4\pi/(2\pi\sigma^2)^{3/2}\exp(-r^2/(2\sigma^2))$. The averaged potential energy of the blackbody radiation induced dipole force then has a minimum at $r = 0$ with $\langle V_{\mathrm{BB}}(0)\rangle = -N a_{\mathrm{BB}} R^2/(2\sigma^2)$. Using the requirement for a dilute distribution given in equation (8.9) we find that the number of radiating spheres is bounded by $N < 4\sigma^2/R^2$. This corresponds to a maximal particle density

$$N\frac{\rho(0)}{4\pi} = \frac{N}{(\sqrt{2\pi}\sigma)^3} < \frac{1}{\sqrt{8\pi^5}R^2\sigma}, \tag{8.17}$$

or approximately $0.2\,\mathrm{cm}^{-3}$ for $R = 10\,\mu\mathrm{m}$ and $\sigma = 1\,\mathrm{km}$. If the particles have a mass density of $2000\,\mathrm{kg/m}^3$ this corresponds to a maximal total mass $M < 3.4\times 10^5\mathrm{kg}$.

In figure 8.4 we see the averaged effect of a Gaussian cloud of spheres on atomic trajectories, cf. also figure 8.1 for scattering events of a single sphere.

8.3.2 Average interactions in a special toroidal setup

As a second example let us assume that the radiating spheres are distributed according to a special toroidal symmetry

$$g(r,\vartheta) = \frac{1}{2\pi S^3\sigma^2}\rho(\vartheta)e^{-\frac{r^2}{2\sigma^2 S^2}}. \tag{8.18}$$

As shown in figure 8.5, the particles are scattered around a ring of radius S from the origin. Radially, their density decays like a Gaussian of width σS. Note that

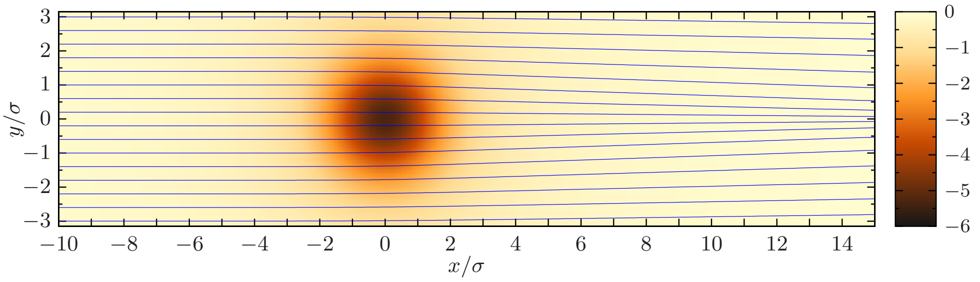

Figure 8.4 Trajectories (blue lines) of atoms travelling from left to right through a Gaussian cloud of radiating spheres. The background colour shows the total potential $\langle V_{\mathrm{BB}}\rangle + \langle V_{\mathrm{G}}\rangle$ in units of $|\langle V_G(0)\rangle| = Na_G R/(\sqrt{\pi/2}\sigma)$ and calculated using equations (8.12) and (8.15). Used parameters are $R = 10\,\mu\mathrm{m}$, $a_G \approx 3.6 \times 10^{-9} a_{BB}$ (i.e. $T = 300\,\mathrm{K}$ for $\rho = 1\,\mathrm{g/cm}^3$); the $N = 6 \times 10^{14}$ spheres are distributed with a width $\sigma = 400\,\mathrm{m}$; the atoms' initial kinetic energy is $E_{\mathrm{kin}}(r_0) = 5\,a_{BB}$.

the notation here is different from the previous example where σ had the dimension of a length, here it is a dimensionless parameter, typically $\sigma \ll 1$. The angular distribution along the torus is given by $\rho(\vartheta)$ which is normalized to ensure that

$$\int_0^\infty \int_0^{2\pi} \int_0^{2\pi} g(r,\vartheta)\, r\,(S + r\cos\varphi)\,\mathrm{d}\vartheta\,\mathrm{d}\varphi\mathrm{d}r = \int_0^{2\pi} \rho(\vartheta)\,\mathrm{d}\vartheta = 1. \tag{8.19}$$

The toroidal coordinates are linked to the Cartesian ones via $x = (S + r\cos\varphi)\cos\vartheta$, $y = (S + r\cos\varphi)\sin\vartheta$ and $z = r\sin\varphi$; $r \geq 0$, $\vartheta \in [0, 2\pi)$, $\varphi \in [0, 2\pi)$.

For simplicity we restrict our analysis to the one dimensional dynamics in the centre of the torus where $r = 0$. The calculated potentials and forces will therefore only affect the movement along the ϑ-direction.

The average gravitational potential at a position $\mathbf{r} = (S\cos\vartheta, S\sin\vartheta, 0)$ generated by a particle density g defined in equation (8.18) then reads

$$\langle V_{\mathrm{G}}(\vartheta)\rangle = -Na_{\mathrm{G}}R \int_0^\infty \int_0^{2\pi} \int_0^{2\pi} \frac{g(r',\vartheta')}{\Delta(r',\vartheta-\vartheta',\varphi')} r'(S + r'\cos\varphi')\,\mathrm{d}\vartheta'\mathrm{d}\varphi'\mathrm{d}r' \tag{8.20}$$

where $\Delta(r,\vartheta,\varphi) := \left[2S^2(1-\cos(\vartheta)) + r^2 + 2Sr\cos(\varphi)(1-\cos(\vartheta))\right]^{1/2}$ such that the distance between a point $\mathbf{r}' = ((S + r'\cos\varphi')\cos\vartheta', (S + r'\cos\varphi')\sin\vartheta', r'\sin\varphi')$ and $\mathbf{r}$ in toroidal coordinates is $\Delta(r',\vartheta-\vartheta',\varphi')$. Introducing $s' = r'/S$ we find

$$\langle V_{\mathrm{G}}(\vartheta)\rangle = -\frac{Na_{\mathrm{G}}R}{2\pi S\sigma^2} \int_0^{2\pi} \int_0^\infty \rho(\vartheta')\, s' e^{-\frac{s'^2}{2\sigma^2}}\, I_{\mathrm{G}}^{\varphi}\left(s', 1-\cos(\vartheta-\vartheta')\right)\,\mathrm{d}s'\mathrm{d}\vartheta', \tag{8.21}$$

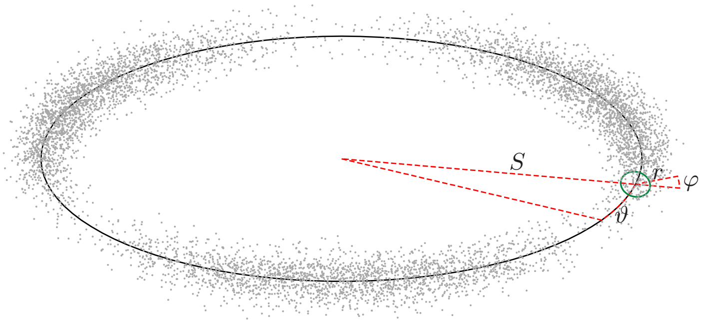

Figure 8.5 Schematic illustration of a toroidal particle density as given in equation (8.18). Here $N \approx 7000$ particles (grey dots) are distributed with $\rho(\vartheta) \sim 0.05 + \sin^2(3\vartheta/2)$. The green circle has a radius of σS which is also the width of the Gaussian distribution along r (here $\sigma = 1/20$). For the dynamics we restrict ourselves to a one dimensional movement along a circle of radius S at $r = 0$, here drawn in black.

where we defined

$$\begin{aligned} I_{\mathrm{G}}^{\varphi}(s,\gamma) &:= \int_0^{2\pi} \frac{1 + s\cos\varphi}{\sqrt{s^2 + 2\gamma + 2s\gamma\cos\varphi}}\,\mathrm{d}\varphi \\ &= \frac{2}{\gamma\sqrt{s^2 + 2\gamma(s+1)}}\Bigg[\Big(s^2 + 2\gamma(s+1)\Big)\,E\left(\tfrac{4\gamma s}{s^2+2\gamma(s+1)}\right) - \\ &\qquad\qquad - s^2 K\left(\tfrac{4\gamma s}{s^2+2\gamma(s+1)}\right)\Bigg], \end{aligned} \tag{8.22}$$

with the complete elliptic integrals of first and second kind,

$$K(k) = \int_0^{\pi/2} \frac{1}{\sqrt{1 - k^2\sin\vartheta}}\,\mathrm{d}\vartheta \quad \text{and} \quad E(k) = \int_0^{\pi/2} \sqrt{1 - k^2\sin\vartheta}\,\mathrm{d}\vartheta. \tag{8.23}$$

The subsequent radial integration can be carried out numerically and we define

$$I_{\mathrm{G}}(\sigma,\vartheta) := \int_0^{\infty} s\,e^{-\frac{s^2}{2\sigma^2}}\, I_{\mathrm{G}}^{\varphi}\left(s, 1 - \cos(\vartheta)\right)\,\mathrm{d}s \tag{8.24}$$

such that the mean gravitational potential in a toroidal setup in given by a periodic one-dimensional convolution integral

$$\langle V_{\mathrm{G}}(\vartheta)\rangle = -\frac{N a_{\mathrm{G}} R}{2\pi S\sigma^2}\int_0^{2\pi} \rho(\vartheta') I_{\mathrm{G}}(\sigma, \vartheta - \vartheta')\,\mathrm{d}\vartheta'. \tag{8.25}$$

Similarly, the mean potential due to thermal radiation in the long-distance approximation can be written as

$$\langle V_{\mathrm{BB}}(\vartheta)\rangle = -\frac{N a_{\mathrm{BB}} R^2}{2}\int_0^{\infty}\int_0^{2\pi}\int_0^{2\pi} \frac{g(r',\vartheta')}{\Delta^2(r',\vartheta-\vartheta',\varphi')} r'(S + r'\cos\varphi')\,\mathrm{d}\vartheta'\mathrm{d}\varphi'\mathrm{d}r'. \tag{8.26}$$

The angular and radial integration can be carried out similarly to the gravitational case with

$$\begin{aligned} I_{\mathrm{BB}}^{\varphi}(s,\gamma) &:= \int_0^{2\pi} \frac{1+s\cos\varphi}{s^2+2\gamma+2s\gamma\cos\varphi}\,\mathrm{d}\varphi \\ &= \frac{\pi}{\gamma}\left(1-\frac{s^2}{\sqrt{s^4-4s^2\gamma(\gamma-1)+4\gamma^2}}\right) \end{aligned} \tag{8.27}$$

and

$$I_{\mathrm{BB}}(\sigma,\vartheta) = \int_0^{\infty} s\,e^{-\frac{s^2}{2\sigma^2}}\,I_{\mathrm{BB}}^{\varphi}\left(s,1-\cos(\vartheta)\right)\,\mathrm{d}s. \tag{8.28}$$

Hence we obtain another one-dimensional convolution for the potential induced by the dipole interaction with thermally radiation spheres

$$\langle V_{\mathrm{BB}}(\vartheta)\rangle = -\frac{N a_{\mathrm{BB}} R^2}{4\pi S^2\sigma^2}\int_0^{2\pi}\rho(\vartheta')I_{\mathrm{BB}}(\sigma,\vartheta-\vartheta')\,\mathrm{d}\vartheta' \tag{8.29}$$

The averaged forces in the ϑ-direction due to these potentials then read $\langle F(\vartheta)\rangle = -\frac{1}{S}\,\partial_\vartheta\,\langle V(\vartheta)\rangle$.

8.4 Coupled dynamics of gas and hot dust

Up to now we always analysed the influence of a single or a group of small hot spheres on the dynamics of a *single* atom, molecule or nanoparticle. The next logic step is to explore the mutual interactions between a cloud of small spheres and an ensemble of atoms. Of special interest is the possibility of self-organisation due to the electromagnetic forces, as it has been described for polarizable particles in a cavity (Grießer *et al.* 2010).

The following chapter will treat this matter in a simplified setup where small spheres, now called *dust*, with a particle distribution $g_{\mathrm{d}}(t,\mathbf{r})$ generate a gravitational and blackbody potential for an atomic gas of distribution $g_{\mathrm{g}}(t,\mathbf{r})$. The gas in turn also acts gravitationally on the dust and, of course, both ensembles also see their own gravitational potentials.

Both ensembles are assumed to be sufficiently rarefied such that collisions can be neglected. We will therefore describe the dynamics of the phase space distribution $f_X(t,\mathbf{r},\mathbf{v})$ with $g_X(t,\mathbf{r}) = \int f_X(t,\mathbf{r},\mathbf{v})\,\mathrm{d}^n v$ for $X \in \{\mathrm{g},\mathrm{d}\}$ by a pair of collisionless Boltzmann equations reading

$$\partial_t f_X(t,\mathbf{r},\mathbf{v}) + \mathbf{v}\cdot\nabla_{\mathbf{r}} f_X(t,\mathbf{r},\mathbf{v}) - \tfrac{1}{m_X}\nabla_{\mathbf{r}} V_X(t,\mathbf{r})\cdot\nabla_{\mathbf{v}} f_X(t,\mathbf{r},\mathbf{v}) = 0. \tag{8.30}$$

Here m_{g} (or m_{d}) describes the mass of an individual gas (or dust) particle and V_{g} (or V_{d}) is the potential acting on this particle. As the potentials are generated by the particles themselves they obviously depend on both distributions g_{g} and g_{d} and are therefore time dependent. More details on the shape of the potentials is given in the upcoming example in section 8.4.1.

The collisionless Boltzmann equation is often also called *Vlasov* equation, especially in plasma physics. For electrostatic or gravitational interactions the potential obeys a Poisson equation, $\nabla_{\mathbf{r}}^2 V(t,\mathbf{r}) \propto g(t,\mathbf{r})$, and we would call equation (8.30) a *Vlasov-Poisson* system.

Of course, the coupled Boltzmann equation above conserve mass

$$\partial_t g_X(t,\mathbf{r}) + \nabla_{\mathbf{r}} \cdot \int_{\mathbb{R}^n} \mathbf{v} f_X(t,\mathbf{r},\mathbf{v})\, \mathrm{d}^n v = 0, \qquad X \in \{\mathrm{g},\mathrm{d}\}, \tag{8.31}$$

and for gravitational or electrostatic interactions energy, too. In our case, however, the radiating spheres loose energy to the radiation field which in turn interacts with the gas. To recover energy conservation we would therefore have to include the dynamics of the radiation field as well as the process heating the dust particles such that they maintain their constant temperature.

We can not deny that the following calculations are motivated by the interaction of gas and dust in astrophysical scenarios ranging from planetary rings, to protoplanetary discs or molecular clouds. Although these systems differ strongly in size, kinetic energies, density and other parameters, they have in common that diluted atomic or molecular gas interacts with cosmic dust particles ranging from a few nanometres to several millimetres or beyond. Our idea mentioned also in the publication presented in the previous chapter 7 was that an additional force from the thermal radiation of the dust particles could play a role in one of these scenarios.

Having said that, let us also clarify that the model and assumptions employed here are actually not suitable to realistically describe any of these systems. That is firstly because we believe that the characteristics of the blackbody interaction should be studied in an abstract, generic framework before going into the full detail of some specific setup. But secondly we also came to the conclusion that the blackbody interaction is far too weak to modify a natural system where dust interacts with an atomic gas with kinetic energies in the order of several tens to hundreds of Kelvin. More promising is a scenario where hot dust grains interact with smaller particles in the scale of nanometres as described in section 8.2, but still this interaction is in reality more complex than the simplified models in this work.

The calculations presented here are therefore a first attempt to study the generic effects and shall not be misunderstood to realistically describe a specific astrophysical scenario.

8.4.1 Coupled dynamics of gas and hot dust in a toroidal symmetry

In section 8.3.2 we introduced a simplified particle distribution following a toroidal symmetry and derived the potentials for periodic movement along the angle ϑ. Here we will explore the coupled dynamics of gas and dust each distributed according to equation (8.18) but possibly with different widths such that

$$g_{\mathrm{g}}(t,r,\vartheta) = \frac{1}{2\pi S^3 \sigma_{\mathrm{g}}^2}\, \rho_{\mathrm{g}}(t,\vartheta)\, e^{-\frac{r^2}{2\sigma_{\mathrm{g}}^2 S^2}} \tag{8.32}$$

and vice versa for $g_\mathrm{d}(t,r,\vartheta)$. The radius S of the main ring shall be equal for both species.

The coupled Boltzmann equations in toroidal symmetry with movement restricted in the ϑ-direction then read for both $X \in \{\mathrm{g},\mathrm{d}\}$

$$\partial_t f_X(t,\vartheta,v_\vartheta) + \tfrac{v_\vartheta}{S}\,\partial_\vartheta f_X(t,\vartheta,v_\vartheta) - \tfrac{1}{m_X S}\,\partial_\vartheta V_X(t,\vartheta)\,\partial_{v_\vartheta} f_X(t,\vartheta,v_\vartheta) = 0, \tag{8.33}$$

where we used the potential energies from section 8.3.2 to construct

$$V_\mathrm{g}(t,\vartheta) = \left\langle V_\mathrm{G}^{\mathrm{g,g}}(t,\vartheta)\right\rangle + \left\langle V_\mathrm{G}^{\mathrm{d,g}}(t,\vartheta)\right\rangle + \left\langle V_\mathrm{BB}^{\mathrm{d,g}}(t,\vartheta)\right\rangle, \tag{8.34a}$$

$$V_\mathrm{d}(t,\vartheta) = \left\langle V_\mathrm{G}^{\mathrm{g,d}}(t,\vartheta)\right\rangle + \left\langle V_\mathrm{G}^{\mathrm{d,d}}(t,\vartheta)\right\rangle. \tag{8.34b}$$

The upper indices indicate which species generates a certain potential, for example $\langle V_\mathrm{G}^{\mathrm{g,d}}\rangle$ denotes the mean gravitational potential generated by the gas and acting on the dust, i.e.

$$\left\langle V_\mathrm{G}^{\mathrm{g,g}}(t,\vartheta)\right\rangle = -G\frac{m_\mathrm{g}\,M_\mathrm{g}}{2\pi S\sigma_\mathrm{g}^2}\int_0^{2\pi} \rho_\mathrm{g}(t,\vartheta')I_\mathrm{G}(\sigma_\mathrm{g},\vartheta-\vartheta')\,\mathrm{d}\vartheta', \tag{8.35a}$$

$$\left\langle V_\mathrm{G}^{\mathrm{g,d}}(t,\vartheta)\right\rangle = -G\frac{m_\mathrm{d}\,M_\mathrm{g}}{2\pi S\sigma_\mathrm{g}^2}\int_0^{2\pi} \rho_\mathrm{g}(t,\vartheta')I_\mathrm{G}(\sigma_\mathrm{g},\vartheta-\vartheta')\,\mathrm{d}\vartheta', \tag{8.35b}$$

$$\left\langle V_\mathrm{G}^{\mathrm{d,g}}(t,\vartheta)\right\rangle = -G\frac{m_\mathrm{g}\,M_\mathrm{d}}{2\pi S\sigma_\mathrm{d}^2}\int_0^{2\pi} \rho_\mathrm{d}(t,\vartheta')I_\mathrm{G}(\sigma_\mathrm{d},\vartheta-\vartheta')\,\mathrm{d}\vartheta', \tag{8.35c}$$

$$\left\langle V_\mathrm{G}^{\mathrm{d,d}}(t,\vartheta)\right\rangle = -G\frac{m_\mathrm{d}\,M_\mathrm{d}}{2\pi S\sigma_\mathrm{d}^2}\int_0^{2\pi} \rho_\mathrm{d}(t,\vartheta')I_\mathrm{G}(\sigma_\mathrm{d},\vartheta-\vartheta')\,\mathrm{d}\vartheta'. \tag{8.35d}$$

These potentials are derived from equation (8.25) but here we introduced the total mass of a species, $M_X = N_X m_X$, and used that $a_\mathrm{G} = G\,m_\mathrm{g} m_\mathrm{d}/R$ with the gravitational constant G.

As derived in section 8.3.2, the gradient-force component of the blackbody interaction between dust and gas reads

$$\left\langle V_\mathrm{BB}^{\mathrm{d,g}}(t,\vartheta)\right\rangle = -\frac{N_\mathrm{d} a_\mathrm{BB} R^2}{4\pi S^2\sigma_\mathrm{d}^2}\int_0^{2\pi} \rho_\mathrm{d}(t,\vartheta')I_\mathrm{BB}(\sigma_\mathrm{d},\vartheta-\vartheta')\,\mathrm{d}\vartheta'. \tag{8.35e}$$

Note that the potentials depend on the densities $\rho_X(t,\vartheta) = \int_\mathbb{R} f_X(t,\vartheta,v_\vartheta)\,\mathrm{d}v_\vartheta$ hence each species moves in the fields generated by its own particle density while it is influenced by the interaction with the other species, too.

To obtain dimensionless potentials we define

$$\begin{aligned}\mathcal{V}_\mathrm{g}(t,\vartheta) = \int_0^{2\pi} \rho_\mathrm{g}(t,\vartheta')I_\mathrm{G}(\sigma_\mathrm{g},\vartheta-\vartheta')\,\mathrm{d}\vartheta' + \frac{M_\mathrm{d}\sigma_\mathrm{g}^2}{M_\mathrm{g}\sigma_\mathrm{d}^2}\int_0^{2\pi} \rho_\mathrm{d}(t,\vartheta')I_\mathrm{G}(\sigma_\mathrm{d},\vartheta-\vartheta')\,\mathrm{d}\vartheta' + \\ + \frac{N_\mathrm{d} a_\mathrm{BB} R^2\sigma_\mathrm{g}^2}{2G m_\mathrm{g} M_\mathrm{g} S\sigma_\mathrm{d}^2}\int_0^{2\pi} \rho_\mathrm{d}(t,\vartheta')I_\mathrm{BB}(\sigma_\mathrm{d},\vartheta-\vartheta')\,\mathrm{d}\vartheta',\end{aligned} \tag{8.36a}$$

$$\mathcal{V}_\mathrm{d}(t,\vartheta) = \int_0^{2\pi} \rho_\mathrm{g}(t,\vartheta')I_\mathrm{G}(\sigma_\mathrm{g},\vartheta-\vartheta')\,\mathrm{d}\vartheta' + \frac{M_\mathrm{d}\sigma_\mathrm{g}^2}{M_\mathrm{g}\sigma_\mathrm{d}^2}\int_0^{2\pi} \rho_\mathrm{d}(t,\vartheta')I_\mathrm{G}(\sigma_\mathrm{d},\vartheta-\vartheta')\,\mathrm{d}\vartheta'. \tag{8.36b}$$

such that

$$V_{\mathrm{g}}(t,\vartheta) = -G\frac{m_{\mathrm{g}}M_{\mathrm{g}}}{2\pi S\sigma_{\mathrm{g}}^2}\mathcal{V}_{\mathrm{g}}(t,\vartheta) \quad \text{and} \quad V_{\mathrm{d}}(t,\vartheta) = -G\frac{m_{\mathrm{d}}M_{\mathrm{g}}}{2\pi S\sigma_{\mathrm{g}}^2}\mathcal{V}_{\mathrm{d}}(t,\vartheta). \tag{8.37}$$

Finally, after introducing the constants[1]

$$t^* = \sqrt{\frac{4\pi^2(\sigma_{\mathrm{g}}S)^3}{GM_{\mathrm{g}}}} \quad \text{and} \quad v_\vartheta^* = \frac{2\pi\sigma_{\mathrm{g}}S}{t^*} \tag{8.38}$$

we define $\tau := t/t^*$ and $u := v_\vartheta/v_\vartheta^*$ to obtain a dimensionless set of equations for $X \in \{\mathrm{g},\mathrm{d}\}$

$$\partial_\tau f_X(\tau,\vartheta,u) + 2\pi\sigma_{\mathrm{g}}u\,\partial_\vartheta f_X(\tau,\vartheta,u) + \partial_\vartheta\mathcal{V}_X(\tau,\vartheta)\,\partial_u f_X(\tau,\vartheta,u) = 0. \tag{8.39}$$

Figure 8.6 shows the result of a self-consistent numerical simulation of the coupled dynamics of a “gas” consisting of small Rayleigh scatterers and dust in a toroidal setup. In these simulations we initialise the phase-space densities of the two species as $f_X(0,\vartheta,u) \simeq \rho_X(0,\vartheta)\exp(-u^2/(2\widetilde{u}_X^2))$, where $\widetilde{u}_X$ is the dimensionless thermal velocity of species $X \in \{\mathrm{g},\mathrm{d}\}$. The initial spatial distribution $\rho_X(0,\vartheta)$ is then chosen to have a slight inhomogeneity, the resulting forces then reshape the distributions of the two interacting species. A short overview over the used numeric method is given in the following section.

The example in figure 8.6 shows that the small scatterers are pushed away from the hot spheres by the radiation pressure, which is modelled as described in section 8.2 using the complex refractive index of ice, cf. figure 8.2. As mentioned before, the radiation pressure on a Rayleigh particle has the same distance behaviour as the gravitational interaction. Its effect can therefore be included in the dynamics by adding a term

$$\left\langle V_{\mathrm{rp}}^{\mathrm{d,g}}(t,\vartheta)\right\rangle = \frac{N_{\mathrm{d}}a_{\mathrm{rp}}R}{2\pi S\sigma_{\mathrm{d}}^2}\int_0^{2\pi}\rho_{\mathrm{d}}(t,\vartheta')I_{\mathrm{G}}(\sigma_{\mathrm{d}},\vartheta-\vartheta')\,\mathrm{d}\vartheta' \tag{8.40}$$

to the total potential for the gas in equation (8.34a). Note that this potential is repulsive and, as shown in figure 8.2, it is much stronger than the gravitational interaction between a dust particle and a Rayleigh scatterer. However, one should keep in mind that the range of the radiation pressure would be reduced by absorption in optically thick media, an effect which is not included in this setup.

A numerical model for the coupled dynamics in toroidal symmetry

To solve the coupled dynamics of gas and dust in this toroidal setup we use a numerical simulation to propagate the distribution functions along characteristic

---

[1] According to Kepler’s third law, t^* corresponds to one “year” on a cyclic orbit around a mass M_{g} at a distance $\sigma_{\mathrm{g}}S$.

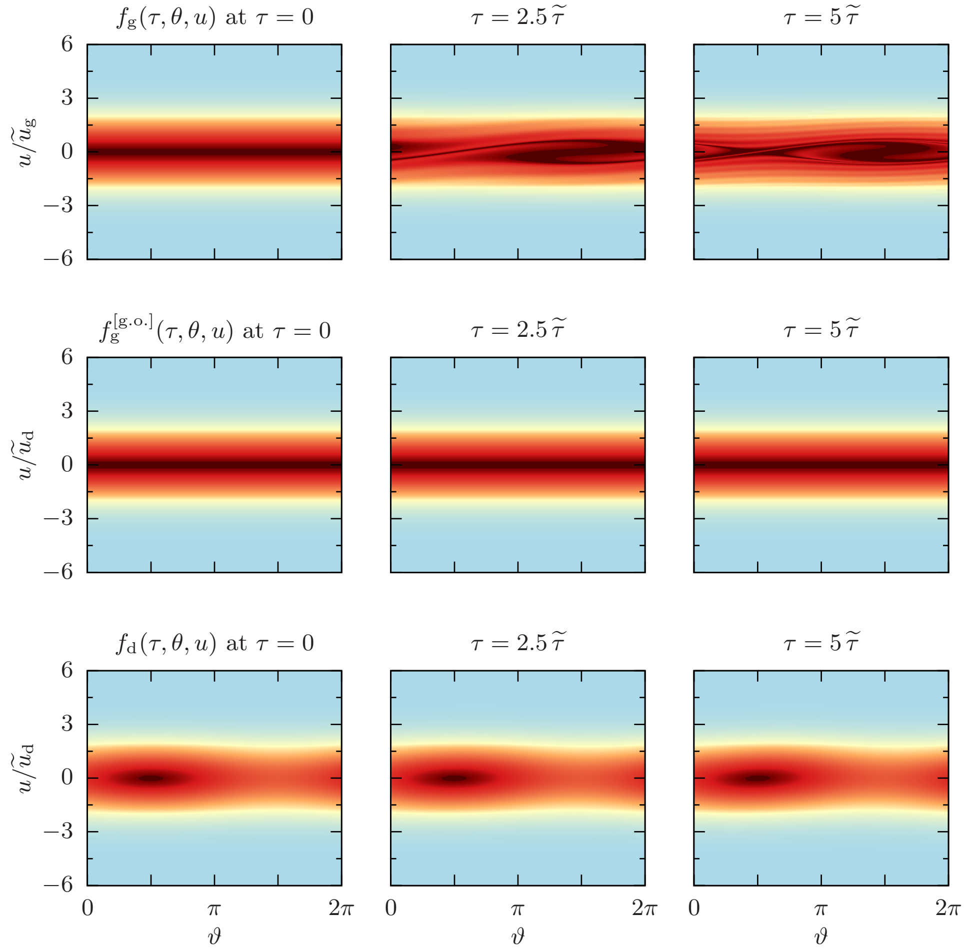

Figure 8.6 Evolution of the phase-space densities for two types of particles: heavy and hot dust particles with density $f_{\rm d}$ and small Rayleigh scatterers (“gas”) with density $f_{\rm g}$. The first and the third row show the evolution of $f_{\rm g}$ and $f_{\rm d}$ according to the collisionless Boltzmann equation (8.39) when radiation forces are included; the second row shows how $f_{\rm g}$ would evolve if only gravity is accounted for; the colours range from blue (zero density) to dark red (maximal density). We see that the small particles start to cluster if blackbody forces are present, the heavy particles however remain in their initial distribution. The species travel on a ring of radius $S = 10^{11}$m with distributions of widths $\sigma_{\rm g} = \sigma_{\rm d} = 10^{-4}$, their initial kinetic energy is $E_{\rm kin} = 50\,k_{\rm B}{\rm K}$ and the initial spatial distributions are homogeneous for the “gas” and $\rho_{\rm d}(\vartheta) \sim 1 + 0.1\sin\vartheta$. The hot dust particles have a radius $R = 5\,\mu{\rm m}$, radiate at $T = 100\,{\rm K}$, have a mass $m_{\rm d} \approx 5 \times 10^{-10}\,{\rm g}$ and do not react to their own radiation. The “gas” particles have the complex refractive index profile of ice, cf. figure 8.2, radius $\widetilde{R} = 10\,{\rm nm}$, mass $m_{\rm g} = 4 \times 10^{-18}\,{\rm g}$ and a total number of $N_{\rm g} \approx 10^{35}$ particles which corresponds to an average particle density of $500\,{\rm cm}^{-3}$. The total mass ratio is $M_{\rm g} = 10\,M_{\rm d}$. The scaling factors are $\widetilde{\tau} = 1/(\sigma_{\rm g}\widetilde{u}_{\rm g})$ and the dimensionless thermal velocity $\widetilde{u}_{\rm g} = \sqrt{E_{\rm kin}/m_{\rm g}}/v_{\vartheta}^{*}$.

curves using a time splitting method described in the following paragraphs (Filbet *et al.* 2003; Grießer *et al.* 2010; Sonnendrücker *et al.* 1999).

First, we recall that the collisionless Boltzmann equation

$$\partial_t f(t,x,v) + v\,\partial_x f(t,x,v) + a(t,x)\,\partial_v f(t,x,v) = 0 \tag{8.41}$$

can be transformed into a set of ordinary differential equations

$$\frac{\mathrm{d}f}{\mathrm{d}t} = \frac{\partial f}{\partial t} + \frac{\mathrm{d}x}{\mathrm{d}t}\frac{\partial f}{\partial x} + \frac{\mathrm{d}v}{\mathrm{d}t}\frac{\partial f}{\partial v} = 0 \quad \text{with} \quad \frac{\mathrm{d}x}{\mathrm{d}t} = v \quad \text{and} \quad \frac{\mathrm{d}v}{\mathrm{d}t} = a. \tag{8.42}$$

Therefore, a distribution f is constant along the characteristic curves $x(t)$ and $v(t)$ solving the differential equations above, i.e. $f(t_1, x(t_1), v(t_1)) = f(t_0, x_0, v_0)$, if $x(t_0) = x_0 \simeq x(t_1) - v(t_0)\,(t_1 - t_0)$ and $v(t_0) = v_0 \simeq v(t_1) - a(t_0, x_0)\,(t_1 - t_0)$.

The method of characteristics with time splitting then uses the following procedure to evolve one time step Δt from a solution at $t = t^n$ (Sonnendrücker *et al.* 1999):

1. half an Euler time step in x-direction: $f^{[1]}(x,v) = f\left(t^n, x - v\Delta t/2, v\right)$,
2. a full Euler time step along the characteristic in v-direction using the acceleration at time $t = t^n + \Delta t/2$: $f^{[2]}(x,v) = f^{[1]}\left(x, v - a(t^n + \Delta t/2, x)\Delta t\right)$,
3. a half Euler time step in x-direction: $f\left(t^{n+1}, x, v\right) = f^{[2]}\left(x - v\Delta t/2, v\right)$.

Since the origins of the characteristic curves will typically not lie on a grid point one needs to perform a 2D-interpolation once at each of the three steps.

In our case we have two Boltzmann equations coupled by a mutual interaction such that $a \equiv \partial_\vartheta \mathcal{V}_X$ depends on both distributions, cf. equation (8.36). Therefore we have to use the distributions $f_\mathrm{g}^{[1]}(\vartheta, u)$ and $f_\mathrm{h}^{[1]}(\vartheta, u)$ to compute the accelerations needed for the second part of each time step.

8.4.2 Linear stability of gas and dust distributions with mutual gravitational and radiative interaction

Describing the interaction of gas and dust in terms of coupled collisionless Boltzmann equations (8.30) allows us to explore whether the additional blackbody interaction is suitable to modify, enhance or trigger structure formation within the gas-dust mixture. To do so we will employ the marginal stability criterion (Binney *et al.* 2008; Chavanis *et al.* 2009) which we introduce in a more general form before applying it to the toroidal case described in the previous section.

General marginal stability criterion for two interacting species

Consider the following pair of coupled collisionless Boltzmann equations for two ensembles of particles with phase space distributions f and h, respectively, moving along a single spatial dimension x

$$\partial_t f(t,x,v) + v\,\partial_x f(t,x,v) - \partial_x \phi[f,h](t,x)\,\partial_v f(t,x,v) = 0, \tag{8.43a}$$

$$\partial_t h(t,x,v) + v\,\partial_x h(t,x,v) - \partial_x \psi[f,h](t,x)\,\partial_v h(t,x,v) = 0. \tag{8.43b}$$

The distributions $\rho_f(t,x) = \int_{-\infty}^{\infty} f(t,x',v)\mathrm{d}v$ and $\rho_h(t,x) = \int_{-\infty}^{\infty} h(t,x',v)\mathrm{d}v$ are assumed to be periodic in space with $\rho_f(t,x) = \rho_f(t,x{+}L)$ and $\rho_h(t,x) = \rho_h(t,x{+}L)$.[2]

The potentials for the mutual interactions shall be generated by a convolution of the spatial distributions with some periodic functions a, b, c and d,

$$\phi[f,h](t,x) = \int_0^L a(x-x')\rho_f(t,x')\,\mathrm{d}x' + \int_0^L b(x-x')\rho_h(t,x')\,\mathrm{d}x', \tag{8.44a}$$

$$\psi[f,h](t,x) = \int_0^L c(x-x')\rho_f(t,x')\,\mathrm{d}x' + \int_0^L d(x-x')\rho_h(t,x')\,\mathrm{d}x'. \tag{8.44b}$$

A trivial solution of the system (8.43) is a pair of time independent and homogeneous distributions[3] $f(v)$ and $h(v)$. Now, the system shall be called *unstable* if small perturbations $\delta f(t,x,v)$ and $\delta h(t,x,v)$ of the homogeneous solutions start to grow in time. If that is the case, the system will rather be found in some inhomogeneous state. This means, the interactions are strong enough to concentrate the particles in certain locations.

Expanding equations (8.43) in linear order of these perturbations leads to

$$\partial_t \delta f(t,x,v) + v\,\partial_x \delta f(t,x,v) - \partial_x \phi[\delta f,\delta h](t,x)\, f'(v) = 0, \tag{8.45a}$$

$$\partial_t \delta h(t,x,v) + v\,\partial_x \delta h(t,x,v) - \partial_x \psi[\delta f,\delta h](t,x)\, h'(v) = 0. \tag{8.45b}$$

As mentioned, we assume that the distributions are periodic in x such that we can use the Fourier series with $k = 2\pi/L$

$$\delta f(t,x,v) = \sum_{n=-\infty}^{\infty} \widehat{f}_n(t,v)e^{inkx}, \qquad \delta h(t,x,v) = \sum_{n=-\infty}^{\infty} \widehat{h}_n(t,v)e^{inkx}, \tag{8.46}$$

$$\phi(t,x) = \sum_{n=-\infty}^{\infty} \widehat{\phi}_n(t)e^{inkx}, \qquad \psi(t,x) = \sum_{n=-\infty}^{\infty} \widehat{\psi}_n(t)e^{inkx}, \tag{8.47}$$

to obtain a new form of the linearised coupled Boltzmann equations, for all $n \in \mathbb{Z}$,

$$\partial_t \widehat{f}_n(t,v) + inkv\,\widehat{f}_n(t,v) - ink\,\widehat{\phi}_n(t)\,f'(v) = 0, \tag{8.48a}$$

$$\partial_t \widehat{h}_n(t,v) + inkv\,\widehat{h}_n(t,v) - ink\,\widehat{\psi}_n(t)\,h'(v) = 0. \tag{8.48b}$$

An additional Laplace transformation $\widehat{f}_n(t,v) \to \widetilde{f}_n(\omega,v)\exp(-i\omega t)$, $\omega \in \mathbb{C}$, allows us to simplify equations (8.43) even further for $n \neq 0$

$$\widetilde{f}_n(\omega,v) = \frac{nk\widetilde{\phi}_n(\omega)f'(v)}{nkv-\omega}, \qquad \widetilde{h}_n(\omega,v) = \frac{nk\widetilde{\psi}_n(\omega)h'(v)}{nkv-\omega}. \tag{8.49}$$

---

[2] The restriction on periodic functions is in anticipation of the toroidal case discussed later and is not a general requirement for the stability analysis in these systems.

[3] Note that a homogeneous distribution actually is not a stable solution in a self-gravitating system. This inconsistency is the reason why typically the so called *Jeans' swindle* is adopted, where the gravitational contribution of the homogeneous density is ignored and only local inhomogeneities generate forces (Binney *et al.* 2008).

As mentioned above, we are interested in solutions δf and δg growing in time. In the Laplace-transformed versions this is equivalent to solutions with $\operatorname{Im}\omega > 0$. Solutions with $\operatorname{Im}\omega < 0$ damp out in time and thus correspond to stable homogeneous configurations. Solutions to (8.49) with real valued ω represent the thin line between stable and unstable solutions and are thus called *marginally stable*.

In equations (8.44) we introduced the potentials as convolutions which is particularly useful for Fourier series as

$$\widehat{\phi}_n(t) = 2\pi\widehat{a}_n \int_{-\infty}^{\infty} \widehat{f}_n(t,v)\mathrm{d}v + 2\pi\widehat{b}_n \int_{-\infty}^{\infty} \widehat{h}_n(t,v)\mathrm{d}v \tag{8.50}$$

and similarly for $\widehat{\psi}_n(t)$, with $\widehat{a}_n$ denoting the Fourier components of $a(x)$ etc. Using equations (8.49) we then obtain a system of linear equations for $\widetilde{\phi}_n(\omega)$ and $\widetilde{\psi}_n(\omega)$,

$$\widetilde{\phi}_n(\omega) = 2nk\pi\widehat{a}_n\widetilde{\phi}_n(\omega) \int_{-\infty}^{\infty} \frac{f'(v)}{nkv-\omega}\,\mathrm{d}v + 2nk\pi\widehat{b}_n\widetilde{\psi}_n(\omega) \int_{-\infty}^{\infty} \frac{h'(v)}{nkv-\omega}\,\mathrm{d}v, \tag{8.51a}$$

$$\widetilde{\psi}_n(\omega) = 2nk\pi\widehat{c}_n\widetilde{\phi}_n(\omega) \int_{-\infty}^{\infty} \frac{f'(v)}{nkv-\omega}\,\mathrm{d}v + 2nk\pi\widehat{d}_n\widetilde{\psi}_n(\omega) \int_{-\infty}^{\infty} \frac{h'(v)}{nkv-\omega}\,\mathrm{d}v. \tag{8.51b}$$

The integral terms will be abbreviated as

$$F_n(\omega) := \int_{-\infty}^{\infty} \frac{f'(v)}{nkv-\omega}\,\mathrm{d}v \quad \text{and} \quad H_n(\omega) := \int_{-\infty}^{\infty} \frac{h'(v)}{nkv-\omega}\,\mathrm{d}v. \tag{8.52}$$

With (8.51) we transformed a system of partial differential equations (8.43) to homogeneous linear equations. These have nontrivial solutions only if their determinant vanishes, i.e.

$$\Big(2nk\pi\widehat{a}_nF_n(\omega)-1\Big)\Big(2nk\pi\widehat{d}_nH_n(\omega)-1\Big) - 4n^2k^2\pi^2\widehat{b}_n\widehat{c}_nF_n(\omega)H_n(\omega) = 0, \tag{8.53}$$

and since this is a relation between ω and k this criterion is called *dispersion relation* (Chavanis *et al.* 2009). If the coupling interactions are turned off, i.e. $\widehat{b}_n = \widehat{c}_n = 0$, we find the typical marginal stability conditions for a single species.

If a, b, c and d are even functions, their Fourier coefficients will be real valued and the real and imaginary parts of the dispersion relation (8.53) read

$$\begin{aligned} 4n^2k^2\pi^2\Big(\widehat{a}_n\widehat{d}_n - \widehat{b}_n\widehat{c}_n\Big)\Big(\operatorname{Re}F_n\operatorname{Re}H_n - \operatorname{Im}F_n\operatorname{Im}H_n\Big) - {}& \\ - 2nk\pi\Big(\widehat{a}_n\operatorname{Re}F_n + \widehat{d}_n\operatorname{Re}H_n\Big) + 1 &= 0, \end{aligned} \tag{8.54a}$$

$$\begin{aligned} 4n^2k^2\pi^2\Big(\widehat{a}_n\widehat{d}_n - \widehat{b}_n\widehat{c}_n\Big)\Big(\operatorname{Re}F_n\operatorname{Im}H_n + \operatorname{Im}F_n\operatorname{Re}H_n\Big) - {}& \\ - 2nk\pi\Big(\widehat{a}_n\operatorname{Im}F_n + \widehat{d}_n\operatorname{Im}H_n\Big) &= 0. \end{aligned} \tag{8.54b}$$

As explained above we are interested in marginal stability solutions with $\operatorname{Im}\omega = 0$. Setting $\omega = \omega_r + i\omega_i$ we apply the Sokhotski–Plemelj theorem already used in chapter 6 to the integral terms (8.52) to find

$$\lim_{\omega_i\to 0} F_n(\omega) = \mathcal{P}\int_{-\infty}^{\infty} \frac{f'(v)}{nkv-\omega_r}\,\mathrm{d}v + \frac{i\pi}{nk} f'\left(\omega_r/(nk)\right), \tag{8.55}$$

a similar result holds for $H_n(\omega_r)$.

Equation (8.54b) is satisfied if $\operatorname{Im} F_n = \operatorname{Im} H_n = 0$. In the case of real valued ω, this corresponds to $f'(\omega_r/(nk)) = h'(\omega_r/(nk)) = 0$. In the following we will assume that the trivial solutions $f(v)$ and $g(v)$ follow a Maxwell-Boltzmann distribution with $\beta_X = k_\mathrm{B} T_\mathrm{kin}/m_X$

$$f(v) = \frac{1}{L\sqrt{2\pi\beta_f}} e^{-\frac{v^2}{2\beta_f}}, \quad \text{and} \quad h(v) = \frac{1}{L\sqrt{2\pi\beta_h}} e^{-\frac{v^2}{2\beta_h}}. \tag{8.56}$$

They thus have maximal values at $v = 0$ and hence $\operatorname{Im} F_n = \operatorname{Im} H_n = 0$ is true only if $\omega_r = 0$. We note therefore that there exist no stable oscillatory perturbations where $\omega_i = 0$ and $\omega_r \neq 0$. From equation (8.55) we find that $\operatorname{Re} F_n(0) = -(nkL\beta_f)^{-1}$ and similarly, $\operatorname{Re} H_n(0) = -(nkL\beta_h)^{-1}$.

After inserting these results into equation (8.54a) the condition of marginal stability for a system of coupled collisionless Boltzmann equations reads

$$\left(\frac{2\pi\,\widehat{a}_n}{L\beta_f} + 1\right)\left(\frac{2\pi\,\widehat{d}_n}{L\beta_h} + 1\right) - \frac{4\pi^2\,\widehat{b}_n\,\widehat{c}_n}{L^2\beta_f\beta_h} = 0. \tag{8.57}$$

If the interaction is purely gravitational we use the Poisson equation $\nabla^2\phi[\delta f, \delta h] = \kappa\, G(M_f\delta\rho_f + M_h\delta\rho_h)$, where κ is some prefactor depending on the chosen geometry.[4] From a comparison with equation (8.50) we find that $\widehat{a}_n = \widehat{c}_n = -\kappa\, GM_f/(2\pi n^2 k^2)$ and $\widehat{b}_n = \widehat{d}_n = -\kappa\, GM_h/(2\pi n^2 k^2)$. Then, as expected, equation (8.57) gives Jeans' instability criterion for the gravitational collapse of a two-species gas,[5]

$$k_J^2 := n^2 k^2 = \frac{\kappa\, G}{k_\mathrm{B} T_\mathrm{kin}} \left(\bar{\rho}_f m_f + \bar{\rho}_h m_h\right), \tag{8.58}$$

with m_f being the mass of a single particle of species f, $\bar{\rho}_f = M_f/L$ and the velocities obey a Maxwell distribution with $\beta_f = k_\mathrm{B} T_\mathrm{kin}/m_f$.

To discuss some further general properties we use the well established form for a single species in a gravitational form and define

$$m(k) = 1 - G\alpha/k^2 \tag{8.59}$$

with the gravitational constant G and all other parameters included in $\alpha > 0$. The marginal stability criterion $m(k_J) = 0$ thus defines the Jeans wavenumber for the given system. Obviously, $m(k)$ takes values in the range $(-\infty, 1]$ and since a homogeneous particle distribution should be stable for vanishingly small interactions, the limit of $\lim_{G\to 0} m(k) = 1$ corresponds to a stable solution. As mentioned before, the marginal stability criterion marks the border between stable (i.e. $\operatorname{Im}\omega < 0$) and unstable (i.e. $\operatorname{Im}\omega > 0$) solutions. We note that (i) $m(k) = 1$ is stable and

---

[4] In setup where ρ_f describes the particle density along a single dimension, κ as the units of length^{-2}.

[5] The better known one-species version can be obtained by averaging $\bar{\rho} m := \bar{\rho}_f m_f + \bar{\rho}_h m_h$, the version given above can be found in the appendix of (Sopik *et al.* 2005).

(*ii*) $m(k) = 0$ is the border of stability and hence we conclude that $1 \geq m(k) > 0$ defines the region of stable solutions. For the Jeans instability this has the intuitive consequence that small-scale fluctuations with $k > k_J$ will *not* lead to a gravitational collapse but large scale inhomogeneities with $k < k_J$ will (Binney *et al.* 2008).

In section 8.2 we mentioned the radiation pressure which has the same distance behaviour as gravity. The effect of this repulsive interaction can thus be assessed by switching $G \to -G$ in equation (8.59). We then find that $m(k) \geq 1$ and the marginal stability criterion can therefore not be fulfilled once a repulsive interaction dominates.

Application of the marginal stability criterion to a toroidal setup

In section 8.4.1 we discussed the effective one dimensional, periodic dynamics of interacting gas and dust in a special toroidal configuration. Using the more general formalism given above one can easily derive a marginal stability criterion for this toroidal system.

Comparing the underlying collisionless Boltzmann equations (8.39) and (8.43) we identify the potentials $\phi[f_G, f_D] \equiv -\mathcal{V}_{\rm g}$ with (cf. equation (8.36))

$$a(\vartheta) = -I_{\rm G}(\sigma_{\rm g}, \vartheta), \quad b(\vartheta) = -\frac{M_{\rm d}\sigma_{\rm g}^2}{M_{\rm g}\sigma_{\rm d}^2} I_{\rm G}(\sigma_{\rm d}, \vartheta) - \frac{N_{\rm d} a_{\rm BB} R^2 \sigma_{\rm g}^2}{2G m_{\rm g} M_{\rm g} S \sigma_{\rm d}^2} I_{\rm BB}(\sigma_{\rm d}, \vartheta), \tag{8.60a}$$

and $\psi[f_G, f_D] \equiv -\mathcal{V}_{\rm d}$ where

$$c(\vartheta) = -I_{\rm G}(\sigma_{\rm g}, \vartheta), \quad d(\vartheta) = -\frac{M_{\rm d}\sigma_{\rm g}^2}{M_{\rm g}\sigma_{\rm d}^2} I_{\rm G}(\sigma_{\rm d}, \vartheta). \tag{8.60b}$$

After writing the phase-space densities and potentials as Fourier series with $L = 2\pi$ we can replace equation (8.49) by

$$\widetilde{f}_{X,n}(\omega, u) = -\frac{n\widetilde{\mathcal{V}}_{X,n}(\omega)\, f'_X(u)}{2n\pi\sigma_{\rm g} u - \omega} \tag{8.61}$$

for both species, $X \in \{\mathrm{g}, \mathrm{d}\}$. The factor $2\pi\sigma_{\rm g}$ comes from the prefactor in the dimensionless toroidal Boltzmann equation (8.39).

For the dispersion relation (8.53) we thus find

$$\Big(2n\pi\widehat{a}_n F_{\mathrm{g},n}(\omega) - 1\Big)\Big(2n\pi\widehat{d}_n F_{\mathrm{d},n}(\omega) - 1\Big) - 4n^2\pi^2\widehat{b}_n\widehat{c}_n\, F_{\mathrm{g},n}(\omega)\, F_{\mathrm{d},n}(\omega) = 0 \tag{8.62}$$

with $F_{X,n}(\omega) = \int f'_X(u)/(2n\pi\sigma_{\rm g} u - \omega)\,\mathrm{d}u$ defined in analogy to equation (8.52).

Using again a Maxwellian velocity profile for the initial homogeneous distribution $f_X(u) = 1/(2\pi\sqrt{2\pi\beta_X})\exp\big[-u^2/(2\beta_X)\big]$ we find after adapting equation (8.55) that $\operatorname{Re} F_{X,n}(0) = -(4n\pi^2\sigma_{\rm g}\beta_X)^{-1}$.

Inserting this into the real part of equation (8.62) we finally obtain a marginal stability criterion for the toroidal setup:

$$\left(\frac{\widehat{a}_n}{2\pi\sigma_{\rm g}\beta_{\rm g}} + 1\right)\left(\frac{\widehat{d}_n}{2\pi\sigma_{\rm g}\beta_{\rm d}} + 1\right) - \frac{\widehat{b}_n\widehat{c}_n}{4\pi^2\sigma_{\rm g}^2\beta_{\rm g}\beta_{\rm d}} = 0. \tag{8.63}$$

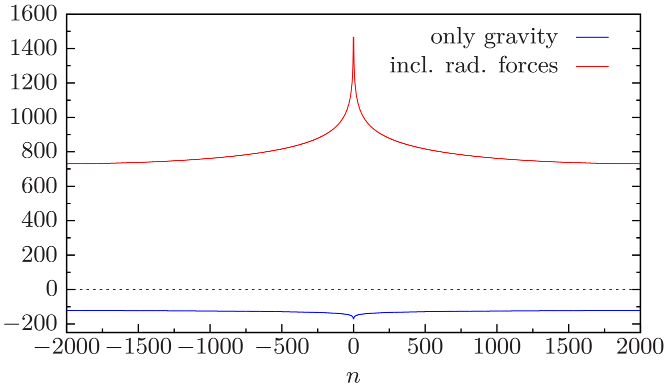

Figure 8.7 The left hand side of the marginal stability equation (8.63) for different Fourier components without (blue line) and with (red line) the thermal radiation potentials. As discussed below equation (8.59), negative values in combination with an attractive potential indicate that small perturbations of a homogeneous initial state grow exponentially. In this case the repulsive interaction due to radiation pressure dominates, which can be seen from the large positive values of the red curve. The setup here is the same as in figure 8.6 where the radiation forces clearly trigger unstable behaviour while the instabilities due to gravity are not seen in the timescales shown there.

The Fourier components needed for this stability criterion can be computed numerically from the known functions I_{G} and I_{BB}, cf. equations (8.22) and (8.28). Figure 8.7 shows an example where large hot and small cold particles interact gravitationally and via thermal radiation forces. The parameters used there are the same as for figure 8.6 and result in a dominant repulsive interaction due to radiation pressure between the large and small particles. This radiation pressure obviously triggers strong instabilities which are visible sooner than the instabilities expected from a pure gravitational model.

To calculate the Fourier coefficients for the gravitational potentials we could in principle also use the Poisson relation $\nabla^2_{\mathbf{r}} V_{\mathrm{G}}(r,\vartheta,\varphi) = -4\pi G m M g(r,\vartheta)$. The Laplace operator in toroidal coordinates gives a lengthy expression

$$\nabla^2_{\mathbf{r}} V = \frac{1}{r(S + r\cos\varphi)} \left[\frac{\partial}{\partial r}\left(r(S + r\cos\varphi) \frac{\partial}{\partial r} V \right) + \frac{r}{S + r\cos\varphi} \frac{\partial^2}{\partial \vartheta^2} V + \right. \\ \left. + \frac{\partial}{\partial \varphi}\left(\frac{S + r\cos\varphi}{r} \frac{\partial}{\partial \varphi} V \right) \right] \tag{8.64}$$

which can be greatly simplified as we are only interested in the values at the singular ring where $r = 0$, cf. figure 8.5. On this axis we can argue that, due to symmetry, all derivatives with respect to φ must vanish, i.e. $\left[\partial^n_\varphi V\right]_{r=0} = 0$. We may also assume that $\left[\partial_r V\right]_{r=0} = 0$, because the particle distribution $g(r,\theta)$ is also flat at $r = 0$, cf. equation (8.18). However, this cannot be assumed for the second partial derivative with respect to r and hence we obtain

$$\left[\nabla_{\mathbf{r}}^2 V\right]_{r=0} = \left[\partial_r^2 V\right]_{r=0} + \frac{1}{S^2}\left[\partial_\vartheta^2 V\right]_{r=0}. \tag{8.65}$$

To compute the Fourier components of the gravitational potentials on the $r = 0$ axis we would therefore need $\partial_r^2 V$, which we did not calculate. Therefore it is more reasonable to stick to the numerical values used also for the example in figure 8.7.

In conclusion we find that the stability criterion introduced in equation (8.57) can be used to qualitatively predict the dynamics of a mixture between micron and nanometre-sized particles. Especially the example in figure 8.6 shows that these dynamics are strongly modified by the presence of radiation forces originating in the blackbody radiation emitted by hot dust particles. Although the model used here is very generic it serves as a motivation for further studies of the versatile optical forces from thermal radiation.

Curriculum Vitae

Matthias Sebastian Karl Sonnleitner

Date of birth: 27. August 1984
Place of birth: Hallein, Salzburg, Austria
Citizenship: Austrian

Education

1990 - 1994	Elementary school: Übungsvolksschule, Salzburg
1994 - 2002	High school: Akademisches Gymnasium, Salzburg
Oct. 2002	Start of studies: Physics and Philosophy, University of Innsbruck, Austria
Oct. 2009	MSc degree (Mag. rer. nat.) in Physics with distinction Diploma Thesis: *Rank-Two Perturbations of a Hamiltonian*, supervised by Univ.-Prof. Dr. Gebhard Grübl, Institute for Theoretical Physics, University of Innsbruck
since Jan. 2010	PhD student in the groups of Univ.-Prof. Dr. Helmut Ritsch, Institute for Theoretical Physics, University of Innsbruck, and Univ.-Prof. Dr. Monika Ritsch-Marte, Div. of Biomedical Physics, Medical University of Innsbruck

Published articles and preprint

- M. Sonnleitner, M. Ritsch-Marte, H. Ritsch: *Optical forces, trapping and strain on extended dielectric objects*, EPL (Europhys. Lett.) **94**, 34005 (2011)
- M. Sonnleitner, M. Ritsch-Marte, H. Ritsch: *Optomechanical deformation and strain in elastic dielectrics*, New J. Phys. **14**, 103011 (2012)
- M. Sonnleitner, M. Ritsch-Marte, H. Ritsch: *Attractive optical forces from blackbody radiation*, Phys. Rev. Lett. **111**, 023601 (2013)
- S. Ostermann, M. Sonnleitner, H. Ritsch: *Scattering approach to two-colour light forces and self-ordering of polarizable particles*, arXiv:1310.6246 [quant-ph] (2013) (accepted for publication in New J. Phys.)

Bibliography

Anderson, M. H., Ensher, J. R., Matthews, M. R., Wieman, C. E. and Cornell, E. A., *Observation of Bose-Einstein condensation in a dilute atomic vapor*, Science **269**, 198 (1995).

Angstmann, E. J., Dzuba, V. A. and Flambaum, V. V., *Frequency shift of the cesium clock transition due to blackbody radiation*, Phys. Rev. Lett. **97**, 040802 (2006).

Antezza, M., Pitaevskii, L. P. and Stringari, S., *New asymptotic behavior of the surface-atom force out of thermal equilibrium*, Phys. Rev. Lett. **95**, 113202 (2005).

Asbóth, J. K., Ritsch, H. and Domokos, P., *Optomechanical coupling in a one-dimensional optical lattice*, Phys. Rev. A **77**, 063424 (2008).

Ashkin, A., *Acceleration and trapping of particles by radiation pressure*, Phys. Rev. Lett. **24**, 156 (1970).

Ashkin, A. and Dziedzic, J. M., *Radiation pressure on a free liquid surface*, Phys. Rev. Lett. **30**, 139 (1973).

Ashkin, A., Dziedzic, J. M., Bjorkholm, J. E. and Chu, S., *Observation of a single-beam gradient force optical trap for dielectric particles*, Opt. Lett. **11**, 288 (1986).

Ashkin, A., *History of optical trapping and manipulation of small-neutral particle, atoms, and molecules*, IEEE J. Sel. Top. Quantum Electron. **6**, 841 (2000).

Ashkin, A., *Optical trapping and manipulation of neutral particles using lasers: a reprint volume with commentaries* (World Scientific, 2006).

Aspelmeyer, M., Kippenberg, T. J. and Marquardt, F., *Cavity optomechanics*, arXiv:1303.0733 [cond-mat.mes-hall] (2013).

Barnett, S. M. and Loudon, R., *The enigma of optical momentum in a medium*, Philos. Trans. R. Soc. London Ser. A **368**, 927 (2010).

Bender, H., Stehle, C., Slama, S., Kaiser, R., Piovella, N., Zimmermann, C. and Courteille, P. W., *Observation of cooperative Mie scattering from an ultracold atomic cloud*, Phys. Rev. A **82**, 011404 (2010).

Bethe, H. A. and Salpeter, E. E., *Quantum mechanics of one- and two-electron atoms* (Plenum, 1977).

Bhattacharya, M. and Meystre, P., *Multiple membrane cavity optomechanics*, Phys. Rev. A **78**, 041801 (2008).

Binney, J. and Tremaine, S., *Galactic dynamics* (Princeton University Press, 2008), second edition.

Bloch, I., *Ultracold quantum gases in optical lattices*, Nat. Phys. **1**, 23 (2005).

Bohren, C. F. and Huffman, D. R., *Absorption and Scattering of Light by Small Particles* (Wiley, 1983).

Born, M. and Wolf, E., *Principles of Optics, Electromagentic Theory of Propagation, Interference and Diffraction of Light* (Pergamon Press, Oxford, 1993), sixth edition.

Bransden, B. H. and Joachain, C. J., *Physics of Atoms and Molecules* (Longman, 1983).

Buckingham, R. A., *The quantum theory of atomic polarization. I. Polarization by a uniform field*, Proc. R. Soc. London, Ser. A **160**, 94 (1937).

Carroll, B. W. and Ostlie, D. A., *An introduction to modern astrophysics* (Addison-Wesley Publishing, 1996).

Casner, A. and Delville, J. P., *Giant deformations of a liquid-liquid interface induced by the optical radiation pressure*, Phys. Rev. Lett. **87**, 54503 (2001).

Chang, D. E., Jiang, L., Gorshkov, A. V. and Kimble, H. J., *Cavity QED with atomic mirrors*, New J. Phys. **14**, 063003 (2012).

Chang, D. E., Ni, K. K., Painter, O and Kimble, H. J., *Ultrahigh-Q mechanical oscillators through optical trapping*, New J. Phys. **14**, 045002 (2012).

Chang, D. E., Cirac, J. I. and Kimble, H. J., *Self-organization of atoms along a nanophotonic waveguide*, Phys. Rev. Lett. **110**, 113606 (2013).

Chavanis, P. H. and Delfini, L., *Dynamical stability of systems with long-range interactions: application of the Nyquist method to the HMF model*, Eur. Phys. J. B **69**, 389 (2009).

Chu, S., Bjorkholm, J. E., Ashkin, A. and Cable, A., *Experimental Observation of Optically Trapped Atoms*, Phys. Rev. Lett. **57**, 314 (1986).

Čižmár, T., Šiler, M., Scaronerý, M., Zemánek, P., Garcés-Chávez, V. and Dholakia, K., *Optical sorting and detection of submicrometer objects in a motional standing wave*, Phys. Rev. B **74**, 035105 (2006).

Čižmár, T., Dávila Romero, L. C., Dholakia, K. and Andrews, D. L., *Multiple optical trapping and binding: new routes to self-assembly*, J. Phys. B **43**, 102001 (2010).

Cohen-Tannoudji, C., *Atomic motion in laser light*, in: *Fundamental Systems in Quantum Optics, Proceedings of the Les Houches Summer School, Session LIII* ed. by J. Dalibard, J.-M. Raimond and J. Zinn-Justin (Elsevier Science Publishers, 1992).

Courteille, P. W., Bux, S., Lucioni, E., Lauber, K., Bienaime, T., Kaiser, R. and Piovella, N., *Modification of radiation pressure due to cooperative scattering of light*, Eur. Phys. J. D **58**, 69 (2010).

Dalibard, J. and Cohen-Tannoudji, C., *Laser cooling below the Doppler limit by polarization gradients: simple theoretical models*, J. Opt. Soc. Am. B **6**, 2023 (1989).

Davis, K. B., Mewes, M.-O., Andrews, M., Van Druten, N. J., Durfee, D. S., Kurn, D. M. and Ketterle, W., *Bose-Einstein condensation in a gas of sodium atoms*, Phys. Rev. Lett. **75**, 3969 (1995).

Deutsch, I. H., Spreeuw, R. J. C., Rolston, S. L. and Phillips, W. D., *Photonic band gaps in optical lattices*, Phys. Rev. A **52**, 1394 (1995).

Dholakia, K. and Zemánek, P., *Colloquium: gripped by light: optical binding*, Rev. Mod. Phys. **82**, 1767 (2010).

Domokos, P., Horak, P. and Ritsch, H., *Quantum description of light-pulse scattering on a single atom in waveguides*, Phys. Rev. A **65**, 033832 (2002).

Domokos, P. and Ritsch, H., *Mechanical effects of light in optical resonators*, J. Opt. Soc. Am. B **20**, 1098 (2003).

Douglass, K. M., Sukhov, S. and Dogariu, A., *Superdiffusion in optically controlled active media*, Nat. Photonics **6**, 834 (2012).

Eichenfield, M., Camacho, R., Chan, J., Vahala, K. J. and Painter, O., *A picogram- and nanometre-scale photonic-crystal optomechanical cavity*, Nature **459**, 550 (2009).

Einstein, A., *On the quantum theory of radiation*, Phys. Z **18**, 121 (1917).

Ellingsen, S. Å., Buhmann, S. Y. and Scheel, S., *Casimir-Polder energy-level shifts of an out-of-equilibrium particle near a microsphere*, Phys. Rev. A **85**, 022503 (2012).

Epstein, P. S., *Zur Theorie des Starkeffektes*, Ann. Phys. (Berlin) **355**, 489 (1916).

Evans, A., *The dusty universe* (Ellis Horwood, New York, 1993).

Farley, J. W. and Wing, W. H., *Accurate calculation of dynamic Stark shifts and depopulation rates of Rydberg energy levels induced by blackbody radiation. Hydrogen, helium, and alkali-metal atoms*, Phys. Rev. A **23**, 2397 (1981).

Filbet, F. and Sonnendrücker, E., *Comparison of eulerian Vlasov solvers*, Comput. Phys. Commun. **150**, 247 (2003).

Fixsen, D. J., Cheng, E. S., Gales, J. M., Mather, J. C., Shafer, R. A. and Wright, E. L., *The cosmic microwave background spectrum from the full COBE FIRAS data set*, Astrophys. J. **473**, 576 (1996).

Gallagher, T. F. and Cooke, W. E., *Interactions of blackbody radiation with atoms*, Phys. Rev. Lett. **42**, 835 (1979).

Goban, A., Choi, K. S., Alton, D. J., Ding, D., Lacroûte, C., Pototschnig, M., Thiele, T., Stern, N. P. and Kimble, H. J., *Demonstration of a state-insensitive, compensated nanofiber trap*, Phys. Rev. Lett. **109**, 33603 (2012).

Gordon, J. P. and Ashkin, A., *Motion of atoms in a radiation trap*, Phys. Rev. A **21**, 1606 (1980).

Grass, D., *Optical Trapping and Transport of Nanoparticles with Hollow Core Photonic Crystal Fibers*, MA thesis, University of Vienna, 2013.

Greffet, J.-J., Carminati, R., Joulain, K., Mulet, J.-P., Mainguy, S. and Chen, Y., *Coherent emission of light by thermal sources*, Nature **416**, 61 (2002).

Grießer, T., Ritsch, H., Hemmerling, M. and Robb, G. R. M., *A Vlasov approach to bunching and selfordering of particles in optical resonators*, Eur. Phys. J. D **58**, 349 (2010).

Grießer, T. and Ritsch, H., *Light-induced crystallization of cold atoms in a 1d optical trap*, Phys. Rev. Lett. **111**, 055702 (2013).

Guck, J., Ananthakrishnan, R., Mahmood, H., Moon, T. J., Casey Cunningham, C. and Käs, J., *The Optical Stretcher: A Novel Laser Tool to Micromanipulate Cells*, Biophys. J. **81**, 767 (2001).

Guess, A. W., *Poynting-Robertson effect for a spherical source of radiation*, Astrophys. J. **135**, 855 (1962).

Haas, M., Jentschura, U. D. and Keitel, C. H., *Comparison of classical and second quantized description of the dynamic Stark shift*, Am. J. Phys. **74**, 77 (2006).

Hänsch, T. W. and Schawlow, A. L., *Cooling of gases by laser radiation*, Opt. Commun. **13**, 68 (1975).

Hilborn, R. C., *Einstein coefficients, cross sections, f values, dipole moments, and all that*, arXiv:physics/0202029 (2002).

Horak, P., Domokos, P. and Ritsch, H., *Giant Lamb shift of atoms near lossy multimode optical micro-waveguides*, EPL (Europhys. Lett.) **61**, 459 (2003).

Itano, W. M., Lewis, L. L. and Wineland, D. J., *Shift of* $^2S_{1/2}$ *hyperfine splittings due to blackbody radiation*, Phys. Rev. A **25**, 1233 (1982).

Jackson, J. D., *Classical Electrodynamics* (Wiley, New York, 1999), third edition.

Jayich, A. M., Sankey, J. C., Zwickl, B. M., Yang, C., Thompson, J. D., Girvin, S. M., Clerk, A. A., Marquardt, F. and Harris, J. G. E., *Dispersive optomechanics: a membrane inside a cavity*, New J. Phys. **10**, 095008 (2008).

Jentschura, U. D. and Haas, M., *Reexamining blackbody shifts for hydrogenlike ions*, Phys. Rev. A **78**, 042504 (2008).

Jessen, P. S. and Deutsch, I. H., *Optical lattices*, Adv. At. Mol. Opt. Phys. **37**, 95 (1996).

Kepler, J., *De cometis libelli tres* (1619).

Kippenberg, T. J. and Vahala, K. J., *Cavity optomechanics: back-action at the mesoscale*, Science **321**, 1172 (2008).

Klimchitskaya, G. L., Mohideen, U. and Mostepanenko, V. M., *The Casimir force between real materials: experiment and theory*, Rev. Mod. Phys. **81**, 1827 (2009).

Landau, L. D. and Litschitz, E. M., *Theory of Elasticity* (Pergamon Press, 1986), third edition.

Lautrup, B., *Physics of Continuous Matter* (IoP Publishing, 2005).

Lebedev, P., *Untersuchungen über die Druckkräfte des Lichtes*, Ann. Phys. (Berlin) **311**, 433458 (1901).

Lee, G. Y. H. and Lim, C. T., *Biomechanics approaches to studying human diseases*, Trends Biotechnol. **25**, 111 (2007).

Lee, J., Park, D. H., Mittal, S., Dagenais, M. and Rolston, S. L., *Integrated optical dipole trap for cold neutral atoms with an optical waveguide coupler*, New J. Phys. **15**, 043010 (2013).

Lequeux, J., *The Interstellar Medium* (Springer, 2005).

Mansuripur, M., *Radiation pressure and the linear momentum of the electromagnetic field*, Opt. Express **12**, 5375 (2004).

Mansuripur, M., *Resolution of the Abraham-Minkowski controversy*, Opt. Commun. **283**, 1997 (2010).

Martynenko, Y. V. and Ognev, L., *Thermal radiation from nanoparticles*, Tech. Phys. **50**, 1522 (2005).

Mitroy, J., Zhang, J. Y., Bromley, M. W. J. and Rollin, K. G., *Blackbody radiation shift of the* Al^+ *clock transition*, Eur. Phys. J. D **53**, 15 (2009).

Ni, K.-K., Norte, R., Wilson, D. J., Hood, J. D., Chang, D. E., Painter, O. and Kimble, H. J., *Enhancement of mechanical Q factors by optical trapping*, Phys. Rev. Lett. **108**, 214302 (2012).

Nichols, E. F. and Hull, G. F., *A preliminary communication on the pressure of heat and light radiation*, Phys. Rev. **13**, 307 (1901).

Obrecht, J. M., Wild, R. J., Antezza, M., Pitaevskii, L. P., Stringari, S. and Cornell, E. A., *Measurement of the temperature dependence of the Casimir-Polder force*, Phys. Rev. Lett. **98**, 063201 (2007).

Odashima, H., Tachikawa, M. and Takehiro, K., *Mode-selective thermal radiation from a microparticle*, Phys. Rev. A **80**, 041806 (2009).

Ostermann, S., Sonnleitner, M. and Ritsch, H., *Scattering approach to two-colour light forces and self-ordering of polarizable particles*, arXiv:1310.6246 [quant-ph] (2013).

Padgett, M. and Di Leonardo, R., *Holographic optical tweezers and their relevance to lab on chip devices*, Lab Chip **11**, 1196 (2011).

Parthey, C. G., Matveev, A., Alnis, J., Bernhardt, B., Beyer, A., Holzwarth, R., Maistrou, A., Pohl, R., Predehl, K., Udem, T., Wilken, T., Kolachevsky, N., Abgrall, M., Rovera, D., Salomon, C., Laurent, P. and Hänsch, T. W., *Improved Measurement of the Hydrogen 1S–2S Transition Frequency*, Phys. Rev. Lett. **107**, 203001 (2011).

Pfeifer, R. N. C., Nieminen, T. A., Heckenberg, N. R. and Rubinsztein-Dunlop, H., *Colloquium: Momentum of an electromagnetic wave in dielectric media*, Rev. Mod. Phys. **79**, 1197 (2007).

Phillips, W. D., *Laser cooling and trapping of neutral atoms*, Rev. Mod. Phys. **70**, 721 (1998).

Planck, M., *Ueber eine Verbesserung der Wien'schen Spectralgleichung*, Verh. Dtsch. phys. Ges. 202 (1900).

Planck, M., *Ueber das Gesetz der Energieverteilung im Normalspectrum*, Ann. Phys. (Berlin) **309**, 553 (1901).

Porsev, S. G. and Derevianko, A., *Multipolar theory of blackbody radiation shift of atomic energy levels and its implications for optical lattice clocks*, Phys. Rev. A **74**, 020502 (2006).

Rancourt-Grenier, S., Wei, M. T., Bai, J. J., Chiou, A., Bareil, P. P., Duval, P. L. and Sheng, Y., *Dynamic deformation of red blood cell in dual-trap optical tweezers*, Opt. Express **18**, 10462 (2010).

Reiser, A. and Schächter, L., *Geometric effects on blackbody radiation*, Phys. Rev. A **87**, 033801 (2013).

Rinaldi, C. and Brenner, H., *Body versus surface forces in continuum mechanics: Is the Maxwell stress tensor a physically objective Cauchy stress?*, Phys. Rev. E **65**, 036615 (2002).

Ritsch, H., Domokos, P., Brennecke, F. and Esslinger, T., *Cold atoms in cavity-generated dynamical optical potentials*, Rev. Mod. Phys. **85**, 553 (2013).

Robertson, H. P., *Dynamical effects of radiation in the solar system*, Mon. Not. R. Astron. Soc. **97**, 423 (1937).

Rosenberg, M., Smirnov, R. D. and Pigarov, A. Y., *On thermal radiation from heated metallic dust grains*, J. Phys. D **41**, 015202 (2008).

Safronova, M. S., Jiang, D., Arora, B., Clark, C. W., Kozlov, M. G., Safronova, U. I. and Johnson, W. R., *Black-body radiation shifts and theoretical contributions to atomic clock research*, IEEE Trans. Ultrason. Ferroelectr. Freq. Control **57**, 94 (2010).

Sakurai, J. J. and Napolitano, J., *Modern Quantum Mechanics* (Pearson, 2011), second edition.

Schneeweiss, P., Dawkins, S. T., Mitsch, R., Reitz, D., Vetsch, E. and Rauschenbeutel, A., *A nanofiber-based optical conveyor belt for cold atoms*, Appl. Phys. B **110**, 279 (2013).

Siegel, R. and Howell, J. R., *Thermal radiation heat transfer* (Hemisphere Publishing Corp, 1992), third edition.

Singer, W., Frick, M., Haller, T., Dietl, P., Bernet, S. and Ritsch-Marte, M., *Combined optical tweezers and optical stretcher in microscopy*, in: *European Conference on Biomedical Optics* International Society for Optics and Photonics (2001), 227.

Singer, W., Frick, M., Bernet, S. and Ritsch-Marte, M., *Self-organized array of regularly spaced microbeads in a fiber-optical trap*, J. Opt. Soc. Am. B **20**, 1568 (2003).

Sonnendrücker, E., Roche, J., Bertrand, P. and Ghizzo, A., *The semi-Lagrangian method for the numerical resolution of the Vlasov equation*, J. Comput. Phys. **149**, 201 (1999).

Sonnleitner, M., Ritsch-Marte, M. and Ritsch, H., *Optical forces, trapping and strain on extended dielectric objects*, EPL (Europhys. Lett.) **94**, 34005 (2011).

Sonnleitner, M., Ritsch-Marte, M. and Ritsch, H., *Optomechanical deformation and strain in elastic dielectrics*, New J. Phys. **14**, 103011 (2012).

Sonnleitner, M., Ritsch-Marte, M. and Ritsch, H., *Attractive optical forces from blackbody radiation*, Phys. Rev. Lett. **111**, 023601 (2013).

Sopik, J., Sire, C. and Chavanis, P.-H., *Self-gravitating Brownian systems and bacterial populations with two or more types of particles*, Phys. Rev. E **72**, 026105 (2005).

Sraj, I., Szatmary, A. C., Marr, D. W. M. and Eggleton, C. D., *Dynamic ray tracing for modeling optical cell manipulation*, Opt. Express **18**, 16702 (2010).

Stevenson, D. J., Gunn-Moore, F. and Dholakia, K., *Light forces the pace: optical manipulation for biophotonics*, J. Biomed. Opt. **15**, 041503 (2010).

Stilgoe, A. B., Nieminen, T. A., Knöener, G., Heckenberg, N. R. and Rubinsztein-Dunlop, H., *The effect of Mie resonances on trapping in optical tweezers*, Opt. Express **16**, 15039 (2008).

Thalhammer, G., Steiger, R., Bernet, S. and Ritsch-Marte, M., *Optical macro-tweezers: trapping of highly motile micro-organisms*, J. Opt. **13**, 044024 (2011).

Thompson, J. D., Zwickl, B. M., Jayich, A. M., Marquardt, F., Girvin, S. M. and Harris, J. G. E., *Strong dispersive coupling of a high-finesse cavity to a micromechanical membrane*, Nature **452**, 72 (2008).

Vetsch, E., Reitz, D., Sagué, G., Schmidt, R., Dawkins, S. T. and Rauschenbeutel, A., *Optical interface created by laser-cooled atoms trapped in the evanescent field surrounding an optical nanofiber*, Phys. Rev. Lett. **104**, 203603 (2010).

Warren, S. G., *Optical constants of ice from the ultraviolet to the microwave*, Appl. Opt. **23** (1984).

Wiederhecker, G. S., Chen, L., Gondarenko, A. and Lipson, M., *Controlling photonic structures using optical forces*, Nature **462**, 633 (2009).

Wien, W., *Ueber die Energievertheilung im Emissionsspectrum eines schwarzen Körpers*, Ann. Phys. (Berlin) **294**, 662–669 (1896).

Wiese, W. L. and Fuhr, J. R., *Accurate atomic transition probabilities for hydrogen, helium, and lithium*, J. Phys. Chem. Ref. Data **38**, 565 (2009).

Wineland, D. J. and Itano, W. M., *Laser cooling of atoms*, Phys. Rev. A **20**, 1521 (1979).

Wuttke, C. and Rauschenbeutel, A., *Thermalization via heat radiation of an individual object thinner than the thermal wWavelength*, Phys. Rev. Lett. **111**, 024301 (2013).

Xuereb, A., Domokos, P., Asbóth, J., Horak, P. and Freegarde, T., *Scattering theory of cooling and heating in optomechanical systems*, Phys. Rev. A **79**, 53810 (2009).

Xuereb, A., Domokos, P., Horak, P. and Freegarde, T., *Scattering theory of multilevel atoms interacting with arbitrary radiation fields*, Phys. Scr. **2010**, 014010 (2010).

Xuereb, A., Genes, C. and Dantan, A., *Strong coupling and long-range collective interactions in optomechanical arrays*, Phys. Rev. Lett. **109**, 223601 (2012).

Xuereb, A., Genes, C. and Dantan, A., *Collectively enhanced optomechanical coupling in periodic arrays of scatterers*, Phys. Rev. A **88**, 053803 (2013).

Yan, Z.-C., Babb, J. F., Dalgarno, A. and Drake, G. W. F., *Variational calculations of dispersion coefficients for interactions among H, He, and Li atoms*, Phys. Rev. A **54**, 2824 (1996).

Yu, S.-J., Youn, S. J. and Kim, H., *Size effect of thermal radiation*, Physica B **405**, 638 (2010).

Zakharian, A., Mansuripur, M. and Moloney, J., *Radiation pressure and the distribution of electromagnetic force in dielectric media*, Opt. Express **13**, 2321 (2005).

Zemánek, P., Jonáš, A., Jákl, P., Ježek, J., Šerý, M. and Liška, M., *Theoretical comparison of optical traps created by standing wave and single beam*, Opt. Commun. **220**, 401 (2003).

Zoubi, H. and Ritsch, H., *Hybrid quantum system of a nanofiber mode coupled to two chains of optically trapped atoms*, New J. Phys. **12**, 103014 (2010).